université PARIS-SACLAY

NNT : 2018SACLN032

Thèse de doctorat

école normale supérieure paris–saclay

Optical properties of graphene nanoribbons and quantum dots

Thèse de doctorat de l'Université Paris-Saclay
préparée à l'Ecole Normale Supérieure de Cachan
(Ecole Normale Supérieure de Paris-Saclay)

École doctorale n°572 Onde et Matière (EDOM)
Spécialité de doctorat: Nanophysique

Thèse présentée et soutenue à Orsay, le 27 Septembre 2018, par

Shen ZHAO

Composition du Jury :

Andrew Mayne Directeur de recherche, CNRS	Président du jury
Stephanie Reich Professeur, Freïe Universität Berlin (Germany)	Rapporteur
Vincent Jacques Chargé de recherche, CNRS	Rapporteur
Costanza Toninelli Directrice de recherche, INO-CNR (Italy)	Examinateur
Jean-Sébastien Lauret Professeur, Ecole Normale Supérieur de Cachan	Directeur de thèse
Loïc Rondin Maître de conférence, Université Paris-Sud	Invité

Thèse préparée au
Laboratoire Aimé Cotton (UMR 9188)
CNRS, Univ. Paris-Sud, ENS Cachan, Université Paris-Saclay
Bât. 505, 91405 Orsay CEDEX

Acknowledgments

At the time of finishing this manuscript, I would like to in several lines thank all the people who helped me and supported me during my thesis.

First of all, I would like to thank Jean-Sébastian Lauret, my thesis supervisor. Actually I have done a 6-month bachelor internship in this group, which is my first experience of research. This experience let me know how charming the research is. Since then I made up my mind to continue to do research and finally I spent an exciting 3-year PhD thesis. Many inspiring scientific discussions with him and his encourage and patience made me enjoy working in the group and his support was determining in the success of my thesis. I would say I will never regret for making this decision.

The other person who played a major role during my thesis is Loic Rondin. He gave me the most valuable advice in my daily work. His huge passion for science and enthusiasm for the experiments really impressed me and encouraged me. It certainly was a pleasure to work with him.

Besides, I wish to express my deep gratitude to all my colleagues at Laboratoire Aimé Cotton: Géraud, Lucile, Ferdinand, Paul, Timothée, Loic, Baptiste, Magarita, Thomas, Luis, Feriel... And of course, I would like to thank all staff of the lab.

I was very happy to be able to collaborate with the team of Stéphane Campidelli, at CEA Saclay and the team of Christophe Voisin, at LPA. I would like here to name a few people who were particularly helpful: Julien, Christophe and Théo.

I will also thank Vincent Jacques and Stephanie Reich to have accepted to be the referee of my manuscript, as well as Andrew Mayne and Costanza Toninelli for their presence in the jury as examiners.

Since life is not only about the work, I would like to thank my friends: Yang, Yue, Xujun, Yifan, Hui Especially the gaming, basketball and cooking time with them make me feel energetic.

Finally, I really want to thank my parents for their love and the outstanding education they offered to me.

Many thanks also to everybody I might have unintentionally forgotten to mention here.

Contents

Preface

Scientific context

Graphene, i.e. single layer of carbon atoms arranged in a honeycomb lattice, plays a very important part in the domain of nanoscience and nanotechnology. The first experimental realization of graphene was done by Geim and Novoselov through the mechanical exfoliation of graphite in 2004 [1]. Since then, important studies have been done on graphene, revealing many intriguing properties. For example, it has been demonstrated that graphene shows quantum Hall effect even at room temperature [2, 3]. Electron mobility of $\sim 2.5 \times 10^6$ cm^2/V·s has been measured on suspended graphene [4], 1000 times larger than standard silicon. Further, graphene transistors with an intrinsic cut-off frequency as high as 300 GHz has already been achieved [5]. These observations make graphene to be considered as a potentially revolutionary material for future electronic applications [6]. Besides, graphene has revealed other exceptional physical properties such as high thermal conductivity of $3000 - 5000$ W/mK [7, 8] ultrahigh Young's modulus of $\sim$1 TPa and intrinsic tensile strength of $\sim$130 GPa [9], as well as high transparency of 97.7% to incident light for wide wavelength range [10, 11]. Only 6 year after the first isolation of graphene, Geim and Novselov were awarded the Nobel Prize in Physics 2010 "*for groundbreaking experiments regarding the two-dimensional material graphene*".

Despite all these fascinating results, graphene has a significant drawback that is the lack of a bandgap. Due to this, it is difficult to obtain a large enough on-off current ratio (I_{on}/I_{off}) in a graphene field-effect transistor (FET) and thus limits its implementation in conventional integrated logic circuits [6]. Moreover, since graphene has no bandgap, when it is excited by light, the induced carriers rapidly relax to the bottom of the band with no energy left. It thus limits its use as light harvesting devices such as photodetectors and solar cells.

Various strategies have been investigated to open a gap in graphene. For example, it has been demonstrated that by applying a perpendicular electric field on bilayer graphene, the bandgap can be tuned up to 0.25 eV [12]. However, this value only correspond to an I_{on}/I_{off} ratio of $\sim 10^3$, much less than the required 10^6 for operating digital logic devices [13]. Moreover, the preparation of bilayer graphene with the required A-B stacking style is relatively complicated, limiting the practicability of such method. Chemical modifications of graphene (n-type doping by potassium [14], hydrogenation [15] and fluorination [16]) have also been able to open a gap, but at the same time, the electron mobility is severely degraded. Besides, application of uni-axial strain on graphene has been proposed for opening a bandgap [17]. However, to obtain a rational bandgap a global uni-axial strain of 20% is required, which makes it impractical.

Compared to the approaches described above, reduction in the dimensionality of graphene in the form of 1D graphene nanoribbons (GNRs) and 0D graphene quantum dots (GQDs) as shown in Fig. 0.1 is extremely promising. Over the last decades, many theoretical studies have been performed on these two types of low dimensional graphene materials. It is predicted that GNRs and GQDs cannot only have a large bandgap but also display an exceptional degree of tunability of their optoelectronic properties. In principle, a widely tunable bandgap (from semi-metallic to several eV) and the presence or absence of correlated low-dimensional magnetism are determined by the size, sym-

metry and edge structure, i.e. the boundary conditions. In combination with additional controllable parameters such as the presence of heteroatoms, tailored strain and the formation of heterostructure, it would be possible to design the electronic properties of GNRs and GQDs according to our needs.

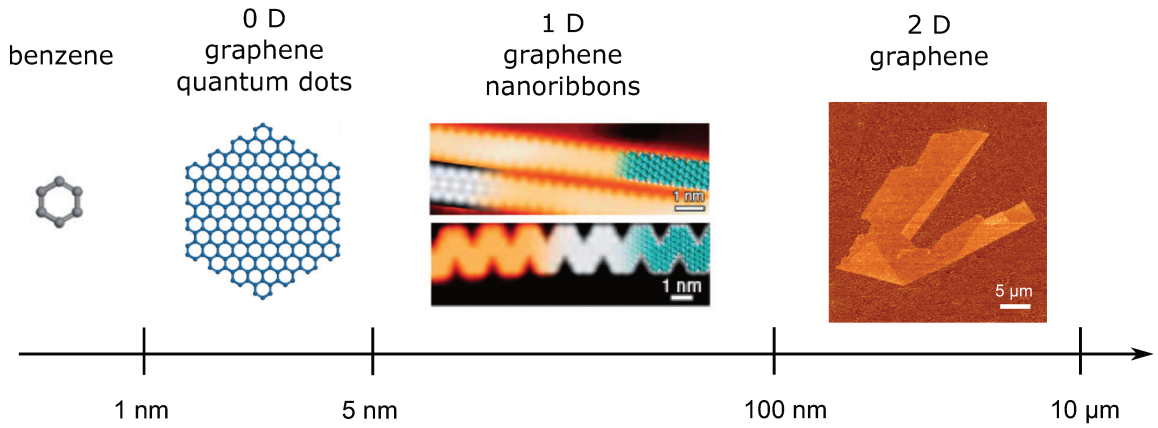

Figure 0.1: Classification of graphenes based on lateral size. 2D graphene (sheets or flakes) exceeds 100 nm in both dimensions. Graphene nanoribbons (GNRs) are quasi-1D graphene strips with a width < 10 nm, while maintaining a *length/width* ratio of > 10. Graphene quantum dots (GQDs, or also called nanographene molecules) are a subset of graphene with size between 1-5 nm (quasi-0D). The scanning tunneling microscopy (STM) images of GNRs are adapted from [18]. The atomic force microscopy (AFM) image of graphene sheet is adapted from [19].

To really benefit from this tunability and harness the opportunities offered by GQDs and GNRs, in the first step one should be able to synthesis them with atomic precision. This now can be achieved by the so called bottom-up chemistry approach. In this approach, starting from the appropriately designed small building blocks (molecule precursors), people let them assemble in a selective way to the final target GNR or GQD structure. By correctly designing specific precursors and the assembly route, bottom-up synthesis approach opens the possibility to obtain a variety of desired structures.

The successful synthesis of GNRs and GQDs with defined structure allows us to go to the second step that is to probe their intrinsic properties and make the link between their structure and intrinsic properties. However, as sp^2 carbon materials, GQDs and GNRs suffer from strong π-π inter-molecular interactions inducing aggregations. This aggregation effect hinders especially the study of their intrinsic optical properties. To date, the photoluminescence (PL) properties of GNRs and GQDs have remained largely underexplored.

Manuscript organization

In this context, my thesis considers the PL spectroscopy of bottom-up synthesized GNRs and GQDs at both ensemble and single-particle levels. The manuscript is organized in 4 chapters:

Chapter I gives a detailed introduction on the current research progress of GNRs and GQDs. I will first explain in theory why the electronic and optical properties of GQDs

and GNRs can be tuned by their structure. The two different synthesis approaches (top-down and bottom-up) are briefly described. Then the characterization results such as STM, XPS and Raman are shown, to suggest the defined structure obtained by the bottom-up approach. The results of optical study results on bottom-up synthesized GNRs and GQDs are also discussed. Finally, the potential applications of GNRs and GQDs are proposed.

Chapter II describes the different experimental techniques employed in this work: optical absorption spectroscopy, photoluminescence spectroscopy and time-resolved photoluminescence for ensemble measurements. Atomic force microscope (AFM), microphotoluminescence and second order photon correlation measurements for single-particle measurements. Finally this chapter describes the suspension preparation protocols as well as the sample preparation procedures for optical microscopy experiments.

Chapter III shows our optical characterization results on the bottom-up synthesized GNRs. In the first section of this chapter, I show the spectroscopy results on two different GNR structures synthesized via the solution-mediated method. I then discuss the nature of the observed emission. Some possible approaches to individualize GNRs are proposed. In the second section, I present our studies on the effect of strain on the optical properties of GNRs. Combing experimental and theoretical results, modulation of the bandgap of GNRs by controlling over the structural distortion is demonstrated. In the third section, I present our optical characterizations of GNRs synthesized by the on-surface approach. Since the grown metal surface is not suitable for the PL measurements, I first describe the transfer procedure to an insulated substrate. Then I present the microPL and AFM results on the transferred sample. We discuss the nature of the unexpected broad emission in the high-energy region. Finally, some distinct Raman features observed on GNRs is also discussed.

In Chapter IV, we study the optical properties of bottom-up synthesized GQDs. In the first part, we show the results of steady-state and time-resolved photoluminescence spectroscopy at ensemble level. These results imply that the individual GQDs are indeed present in the dispersion. In the second part, we go down to the single-particle level by performing microphotoluminescence spectroscopy. The nature of the observed emission from GQDs is discussed, implying that the emission originates from their intrinsic quantum states. Then a detailed study of photophysical properties including second order photon correlation $g^{(2)}$ measurements of GQDs is presented.

Part I

Introduction: GQDs and GNRs

Summary

Introduction

This chapter gives an overview of the state of the art knowledge on the properties of graphene nanoribbons (GNRs) and graphene quantum dots (GQDs), and also their synthesis methods. I will first describe the theoretical works performed on GNRs and GQDs. I will present in theory how the electronic properties of GNRs and GQDs are derived from those of graphene, and how their properties can be tuned via the control of the structure. Secondly, I will present the so-called bottom-up synthesis method, which allows producing GNRs and GQDs with defined structures. Finally, I will discuss the recent results on the structural and electronic characterizations, as well as optical measurements on bottom-up synthesized GNRs and GQDs.

1 Opening a bandgap from graphene

Graphene nanoribbons (GNRs) and Graphene quantum dots (GQDs) can be considered as one-dimensional and zero-dimensional graphene sheets, respectively. In analogy to single wall carbon nanotubes (SWCNTs) [20], the general electronic structure of GNRs and GQDs can be derived from the one-electron model of graphene by applying proper boundary conditions on the wave functions. This simple method is called zone-folding or confinement approximation.

1.1 Tight-binding model of graphene

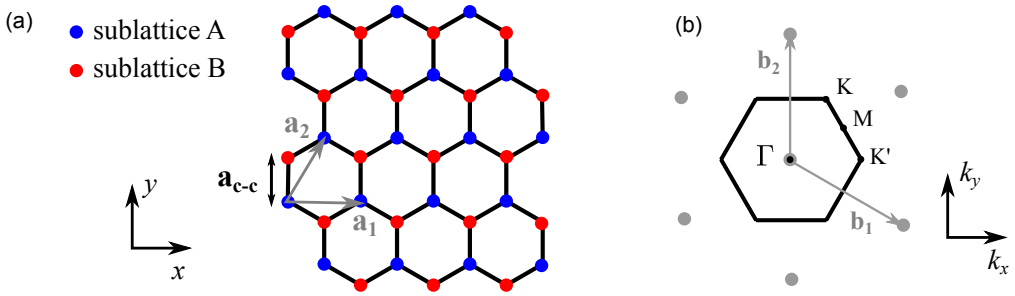

Figure 1.1: (a) - Real-space graphene honeycomb lattice with the two sublattices A and B. $\mathbf{a_1}$ and $\mathbf{a_2}$ are its two primitive vectors with the norm $a = \sqrt{3}a_{\text{C-C}} = 0.246$ nm. (b) - Reciprocal lattice of graphene (grey dots) with $\mathbf{b_1}$ and $\mathbf{b_2}$ the two reciprocal primitive vectors (grey arrows). Its first Brillouin zone (FBZ) is hexagonal (indicated by the black lines). High symmetry points are shown with black dots and labeled as Γ, M, K and K', in which K and K' are the two inequivalent corners.

In a graphene sheet, the carbon atoms arrange in a honeycomb network with a bond distance $a_{\text{C-C}} = 1.42$ nm to their nearest neighbors (see Fig. 1.1). The honeycomb lattice itself is not a Bravais lattice, but it can be considered as a triangular lattice with a basis of two two atoms A and B or two triangular (or hexagonal) sublattices made of atoms A and B, respectively (shown in blue and red). From a crystallographic point of view, A and B are different: atoms A have their nearest neighbors (atoms B) at 0°, 120° and 240°, while atoms B have their nearest neighbors (atoms A) at 60°, 180° and 300°. This

triangular lattice is generated by the primitive basis vectors $\mathbf{a_1}$ and $\mathbf{a_2}$ with

$$\mathbf{a_1} = \begin{pmatrix} a \\ 0 \end{pmatrix} \quad \text{and} \quad \mathbf{a_2} = \begin{pmatrix} \frac{1}{2}a \\ \frac{\sqrt{3}}{2}a \end{pmatrix} \tag{1.1}$$

where the norm of the vectors $a = \sqrt{3}a_{\text{C-C}} = 0.246$ nm.

For a triangular lattice in the real space, the reciprocal lattice is still triangular, which is rotated by 90° with respect to the real space one. The primitive basis vectors of the reciprocal lattice in momentum space are expressed as

$$\mathbf{b_1} = \begin{pmatrix} \frac{2\pi}{a} \\ \frac{2\pi}{\sqrt{3}a} \end{pmatrix} \quad \text{and} \quad \mathbf{b_2} = \begin{pmatrix} 0 \\ \frac{4\pi}{\sqrt{3}a} \end{pmatrix} \tag{1.2}$$

As shown in Fig. 1.1 right, the first Brillouin zone (FBZ) of graphene is the Wigner-Seitz cell of the reciprocal lattice and has a hexagonal shape. It is characterized by four high symmetry points labeled as Γ, M, K and K'. We note that the two corner points K and K' are inequivalent, as they are not connected by a reciprocal lattice vector. We also note that the four other corners of the Brillouin zone can be connected to one of these two points by a vector of the reciprocal lattice. Thus, we have three identical K points and three K' at the corner. Following [21], the positions of K and K' are given by the vectors:

$$\mathbf{K} = \frac{2\pi}{a}\begin{pmatrix} \frac{1}{3} \\ \frac{1}{\sqrt{3}} \end{pmatrix} \quad \text{and} \quad \mathbf{K'} = \frac{2\pi}{a}\begin{pmatrix} \frac{2}{3} \\ 0 \end{pmatrix} \tag{1.3}$$

As we will see later, these two points play an important role for the electronic properties of graphene.

Carbon atom possesses four valence electrons placed into four atomic orbitals: $2s$, $2p_x$, $2p_y$ and $2p_z$. In a graphene sheet, the s-orbitals and in-plane $p_{x,y}$-orbitals of the carbon atoms hybridize to form a strongly bound σ bond (sp_2 hybridization) with an bond angle of 120°. The non hybridized orbital $2p_z$ is perpendicular to this plane. The combination of the p_z orbitals of adjacent carbon atoms give rise to the π bond of graphene. Since the bonding and anti-bonding σ bands are energetically well separated ($\sim$10 eV at the Γ point), it is sufficient to consider only the electrons in π bond to describe the electronic properties of graphene [22].

The band structure of graphene is commonly modeled using a one-electron tight-binding approach [23, 24]. In such approach, the electron-electron interactions is neglected, as well as the curvature effect. Under these hypotheses, the global wavefunction of π electrons $\Psi(\mathbf{r})$ can be expressed as [21]

$$\Psi(\mathbf{r}) = \sum_{\mathbf{R}_A} \Psi_A(\mathbf{R}_A)\Phi_z(\mathbf{r}-\mathbf{R}_A) + \sum_{\mathbf{R}_B} \Psi_B(\mathbf{R}_B)\Phi_z(\mathbf{r}-\mathbf{R}_B) \tag{1.4}$$

where $\Phi_z(\mathbf{r})$ is the wavefunction of the p_z-orbital of a carbon atom located at the origin, $\mathbf{R}_A$ and $\mathbf{R}_B$ are a lattice vector for the sublattice A and B, respectively. Ψ_A and Ψ_B are the corresponding coefficients of Φ_z.

We further restrict the coupling to the nearest neighbor carbon atoms only. We denote the corresponding hopping energy γ_0 and the three vectors τ_l, $l = 1, 2, 3$ that

connect the nearest neighbor carbon atoms:

$$\tau_1 = a\begin{pmatrix} 0 \\ \frac{1}{\sqrt{3}} \end{pmatrix} \quad , \quad \tau_2 = a\begin{pmatrix} -\frac{1}{2} \\ -\frac{1}{2\sqrt{3}} \end{pmatrix} \quad \text{and} \quad \tau_3 = a\begin{pmatrix} \frac{1}{2} \\ -\frac{1}{2\sqrt{3}} \end{pmatrix} \tag{1.5}$$

Neglecting the atomic orbital wavefunction overlap between neighbor atoms A and B, we obtain the linear system for the eigenstates:

$$\begin{aligned} \varepsilon\Psi_A(\mathbf{R}_A) &= -\gamma_0 \sum_{l=1}^{3} \Psi_B(\mathbf{R}_A - \tau_l) \\ \varepsilon\Psi_B(\mathbf{R}_B) &= -\gamma_0 \sum_{l=1}^{3} \Psi_A(\mathbf{R}_B + \tau_l) \end{aligned} \tag{1.6}$$

Applying Bloch's theorem, we decompose the coefficients $\Psi_{A,B}$ in a product of a slowly varying envelope and a planewave component of wavevector $\mathbf{k}$:

$$\Psi_{A,B}(\mathbf{R}_{A,B}) = f_{A,B}(\mathbf{k}) \exp(i\mathbf{k} \cdot \mathbf{R}_{A,B}) \tag{1.7}$$

By combining Eq. 1.7 and 1.6 and performing straightforward simplifications, we obtain the following matrix equation:

$$\begin{pmatrix} 0 & h_{AB}(\mathbf{k}) \\ h_{AB}(\mathbf{k})^* & 0 \end{pmatrix} \begin{pmatrix} f_A(\mathbf{k}) \\ f_B(\mathbf{k}) \end{pmatrix} = \varepsilon \begin{pmatrix} f_A(\mathbf{k}) \\ f_B(\mathbf{k}) \end{pmatrix} \tag{1.8}$$

with

$$h_{AB}(\mathbf{k}) = -\gamma_0 \sum_{l=1}^{3} \exp(-i\mathbf{k} \cdot \tau_l) \tag{1.9}$$

Solving the eigenvalue equation, we finally obtain the energy dispersion of the π electron in graphene:

$$\varepsilon_{\pm}(\mathbf{k}) = \pm\gamma_0 \sqrt{1 + 4\cos\frac{ak_x}{2}\cos\frac{\sqrt{3}ak_y}{2} + 4\cos^2\frac{ak_x}{2}} \tag{1.10}$$

with the nearest neighbor hopping energy $\gamma_0 \approx 2.7$ eV. The band structure of graphene is thus obtained from this formula (Fig. 1.2). It is easily to see that, within the nearest-neighbor approximation, the band structure is symmetric with respect to the zero-energy plane. In addition, the lower band and the upper band touch at each K and K' point at the six corners of the Brillouin zone (i.e., K and K points), showing a six-fold rotation symmetry. In neutral graphene, the lower band is totally filled (valence band), while the upper band is completely empty. As a result, the Fermi Energy E_{F} is located at the touching points K and K' of the two bands, which means $E(\mathbf{K}) = E(\mathbf{K}') = E_{\mathrm{F}} = 0$. Graphene therefore has a zero bandgap, which is called a semi-metal.

Around the K and K' points. The wavevector $\mathbf{k}$ can be rewritten as: $\mathbf{k} = \mathbf{K}^{(\prime)} + \delta\mathbf{k}$, if $|\delta\mathbf{k}|a << 1$. In this condition, the first order Taylor development of the dispersion relation Eq. 1.10 is

$$E(\mathbf{K} + \delta\mathbf{k}) = E(\mathbf{K}' + \delta\mathbf{k}) \simeq \pm\gamma_0 \frac{\sqrt{3}a}{2}|\delta\mathbf{k}| \tag{1.11}$$

So we can see that the dispersion relation is linear with $\delta\mathbf{k}$ around the Fermi level. In contrast, for classical solid, the dispersion is parabolic. This linear dispersion makes the

electrons behave as massless relativistic particles, leading to many remarkable electronic properties, e.g. high electron mobility [4, 25] and quantum fermion properties [3, 26]. One should note that since the dispersion relation is identical near the two inequivalent K and K' points, for the electrons with energy close to the Fermi level there is a double degenerated state. Therefore, in addition to the spin, electrons in graphene has an additional degree of freedom called valley degree of freedom (K and K' valley).

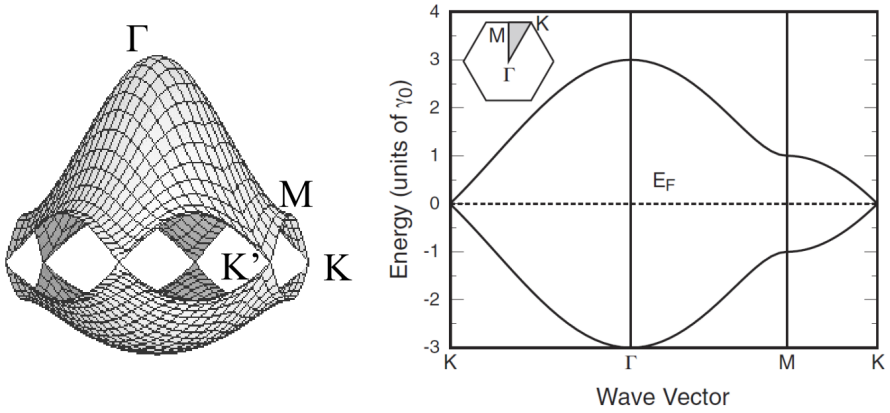

Figure 1.2: Band structure of graphene displayed in a 2-dimensional representation (left) and 1-dimensional cut along the main direction (right). Adapted from [21].

1.2 Zone folding approximation for GNRs and GQDs

For infinite size 2D graphene sheet, the wavevector **k** can vary continuously in the first Brillouin zone. For GNRs and GQDs, due to the presence of boundary conditions (π-electron wave functions on the edges vanish), the wavevectors were further quantized to fulfill the boundary conditions. As a first approximation, the dispersion relations of GNRs and GQDs can be obtained by using the graphene band structure and restricting it to the values of **k** that respect the boundary conditions. This simple method is called zone-folding approximation, and has been used to interpret the electronic structure of carbon nanotubes [20].

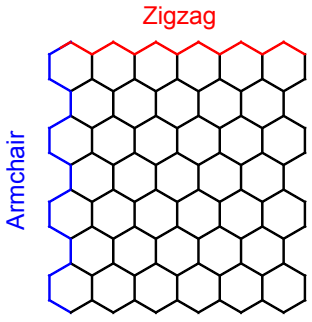

Figure 1.3: Two basic edge structures of nanoscale graphene.

Generally, the edge structure of GNRs and GQDs can be classified into armchair and zigzag types (see Fig. 1.3). According to the edge structure, the way to quantitize wavevector **k** is different and thus the electronic structure is different. We will first look at the electronic structure for armchair edge GNRs and GQDs. For armchair GNRs and GQDs, all the π electrons are paired, thus the total spin is equal to zero and they have a quasi-particle bandgap.

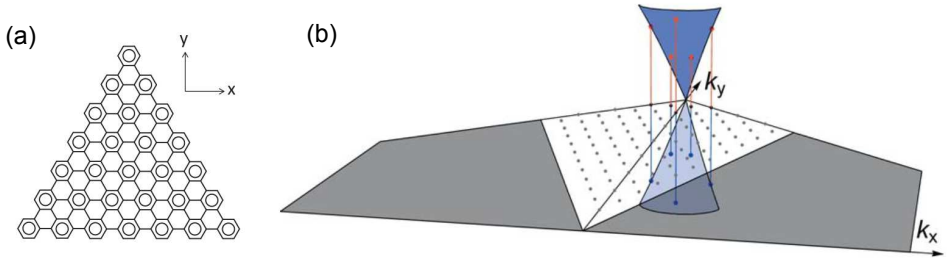

Figure 1.5: (a) - Schematic illustration of triangular shap armchair GQD. (b) - Schematic illustration of the one half of the hexagonal Brillouin zone of 2D graphene sheet. The Dirac cone of the conduction and valence bands of graphene are shown in blue and light blue, respectively. The dots are the allowed **k** values of triangular GQDs with armchair edges, which are also projected onto the Dirac cone. Adapted from [29, 30].

2 Tuning the electronic properties

It is easy to see that depending on the structure of GNRs or GQDs, the boundary conditions will be different and thus the electronic properties will be different. In this section, I will show several ways to tune the electronic properties of GNRs and GQDs, which are proposed by theoretical calculations.

2.1 Tuning through size control

The electronic structure of GNRs and GQDs displays a remarkable dependence on their size. For armchair GNRs, we have seen that the band structure of N-AGNRs can be pictured as a series of cutting lines across the band structure of graphene at N equidistant $k_\perp$ values and these cutting lines are given by Eq. 1.12. As the bandgap of graphene vanishes at the K points, the closer those cutting lines get to the K point, the lower the bandgap of the AGNR will be. From Fig. 1.4 - (b) we can see that by doing the 1D-projection, the K and K' are located at $k_\perp = \frac{1}{3}\frac{2\pi}{a}$ and $k_\perp = \frac{2}{3}\frac{2\pi}{a}$, respectively. The factor 3 in the denominator classify the AGNRs into three families: AGNR with N equal to $3p$, $3p+1$ or $3p+2$ with p an integer, where N is the number of carbon atoms across the width (Fig. 1.4 - (a)). From Eq. 1.12, we can see that for the $3p+2$ family there is always a cutting line going through the K point. Thus, as a first approximation, this family has a zero bandgap. In contrast, for the other two families, there are no cutting lines across the K point. Moreover, the wider the AGNR, the higher value of N, thus the smaller the spacing between the cutting lines and the closer it gets to the K point. As a result, the bandgap is inversely proportional to the width of the ribbon, within each family[1] (see Fig. 2.1 - (a)). One should note that by increasing the ribbon width by just one atom, the electronic properties of GNRs are deeply modified, which implies the importance of the fabrication of GNRs with a atomic precision.

[1]We should note that this tight-binding approach assumes the carbon atoms are equivalent throughout the GNR. As a results, the $3p$ and $3p+1$ families follow a very similar trend and are semiconducting, while the $3p+2$ family are all metallic. However, this assumption is inaccurate for the carbon atoms closer to the edge. Taking into account for the bond length distortions and the associated changes in the hopping energy γ_0, the resulting bandgap values would be changed a lot: opening of a bandgap for the $3p+2$ family, as well as an obvious splitting of the bandgap trends between $3p$ and $3p+1$ families. A more refined *ab initio* calculations thus revealed a relation of $E_g(3p+1) > E_g(3p) > E_g(3p+2)$ of the three different families [31].

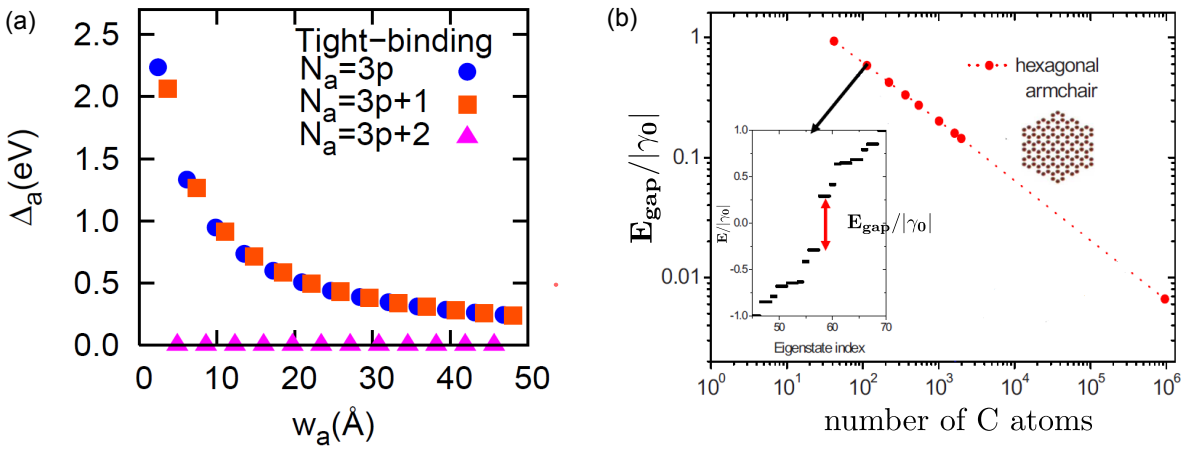

Figure 2.1: (a) - Values of bandgap as a function of the width of armchair GNRs (AGNRs), which are obtained from zone-folding approximation. According to the number of carbon atoms across the width, the AGNRs can be classified into three families: $3p$, $3p+1$ and $3p+2$, showing different trend of bandgap. Adapted from [31]. (b) - Values of bandgap of armchair GQDs as a function of their size (number of C atoms), showing an inverse-square-root relation. Adapted from [32].

For armchair GQDs, according to Eq. 1.13 and 1.14, the states at K point are not allowed. Thus the armchair GQDs always have a non-zero bandgap. In [32], the authors performed an analytic calculations on the hexagonal armchair edge GQDs by a combination of tight-binding approach with a self-consistent Hartree-Fock method (TB-HF). They found that the bandgap values of hexagonal GQDs deduced from their calculations are very similar to the ones obtained by the zone-folding approximation for the triangular GQDs with a similar number of sp^2 carbon atoms. For example, for C222 hexagonal GQD, their calculation leads to $E_g = 0.42\gamma_0$, where γ_0 is the hopping energy, while using Eq. 1.15 the obtained bandgap value of C216 triangular GQD is $E_g \approx 0.46\gamma_0$. This shows that the zone-folding approximation is a relatively efficient approach to predict the bandgap of armchair GQDs. Moreover, the authors indicated that the bandgap of armchair GQDs follows a $1/\sqrt{n}$ scaling, with n the total number of sp^2 carbon atoms (see Fig. 2.1 - (b)).

2.2 Tuning through edge control

As seen from fig. 1.3, GNRs and GQDs can have the so-called zigzag typed edge. Such zigzag GNRs and GQDs have unpaired π electrons present at their edges, which results in the appearance of localized edge states within the bandgap [33,34]. Moreover, due to the presence of unpaired electrons, the total spin of zigzag GNRs and GQDs are non-zero, giving rise to many peculiar spin properties. For example, zigzag GNRs are predicted to show ferromagnetic ordering at each zigzag edge and anti-parallel spin orientation in between [35](see Fig. 2.2 - (a)). By combining alternated zigzag and armchair segments along the ribbon edges, i.e. the chiral edge GNRs (see Fig. 2.2 - (b)), it is possible to further modulate the spin properties of GNRs. Similarly, by designing the shape of zigzag GQDs, their spin properties can also be modulated [36]. These make zigzag GNRs and GQDs very promising for potential applications in spintronics.

In addition to the size and edge structure of GNRs and GQDs, some external parameters such as doping [37, 38], strain [39] and heterostructure formation [40] are also predicted to be able to tune their electronic properties. However, to realize such fine tunability, it is essential to fabricate GNRs and GQDs in a controlled manner and with an atomic precision.

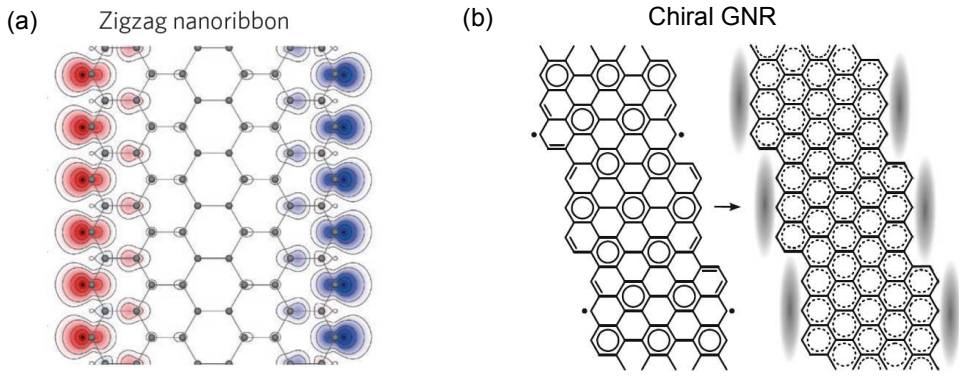

Figure 2.2: (a) - Zigzag GNR predicted to show ferromagnetic ordering at each zigzag edge and anti-parallel spin orientation in between. Adapted from [41]. (b) - Schematic illustration of chiral GNRs, which displays an alternative zigzag and armchair segments along the edges. The spin properties of chiral GNRs are thus different from both armchair and zigzag GNRs. Adapted from [39].

3 Synthesis methods

3.1 Top-down fabrications

Fabrication of GQDs and GNRs has been previously performed through *top-down* methods. This kind of fabrication method can be likened to sculpting from a block of stone. A piece of the base material is gradually eroded until the desired shape is achieved.

As seen from Fig. 3.1 - (a), GQDs can be carved from graphene sheets by means of electron beam lithography. In such approach, by designing the PMMA masks, GQDs with desired geometries can be produced with diameter down to 10 nm. Ponomarenko *et al.* [42] have revealed a confinement bandgap up to 0.5 eV from the GQDs fabricated by this technique. However, nanolithography requires a relative complex processes that hinder applying this technique to a large scale fabrication of GQDs. Due to the irregularities in PMMA, GQDs with diameter smaller than 10 nm cannot be reliably fabricated, and moreover the edge structure can neither be controlled. Another top-down method is the solution-based chemical approaches, which can produce GQDs in a large scale. For instance, GQDs can be derived from carbon fibers [43], graphenes [44], double-walled carbon nanotubes [45] and fullerenes (C60) [46, 47], by cutting these materials via acid or oxidation treatments (Fig. 3.1 - (b)). The GQDs fabricated by these chemical approaches could have a diameter down to several nm with a very good solubility in water and strong photoluminescence, showing the potentials in bioimaging [43] and light-emitting diodes (LEDs) [48]. However, these GQDs obviously do not have a defined structure and severely present defects, which makes it impossible to get access to the intrinsic properties predicted by theoretical calculations.

Similarly, GNRs can be fabricated by cutting of graphene sheets and unzipping of carbon nanotubes (CNTs) (Fig. 3.1 - (c)). Li *et al.* [49] have shown that by sonicating expanded graphite in PmPV conjugated polymer solution, GNRs with various widths between (±2-60 nm) were obtained. The narrowest 2 nm-wide GNR exhibited a bandgap of about ∼0.4 eV and an on-off ratio of 10^6 in a FET configuration. One should note that the width of GNRs resulting from this sonochemical method is not uniform. It is also possible to fabricate uniform GNRs by patterning graphene sheets with nanolithography techniques, e.g. scanning tunneling microscope lithography [50], electron-beam lithography, helium-ion-beam lithography and plasma etching [51]. Similar to the case of GQDs, nanolithography can produce GNRs with width only down to 10 nm. In addition to cutting of graphene, unzipping of CNTs can produce GNRs by solution-based oxidation treatment [52] as well as through plasma etching with PMMA films [53]. Using such approaches, the produced GNRs can have apparently smooth edges and with width between 10-30 nm, showing charge-carrier mobility up to 1500 $cm^2/V.s$. [52]. Nevertheless, smooth edges produced by top-down methods are not precise at the atomic level, i.e. there could be undefined structural disorders and defects of 1 nm or more.

As we have seen in the previous section, GNRs and GQDs are predicted to have an exceptional degree of tunability of their electronic, optical and even magnetic properties via the controlling of the structure, especially when their size and/or width are as narrow as 1-3 nm. To study the link between their intrinsic properties and structure, and eventually engineer the properties in a accurate and reproducible way for optoelectronic and spintronic applications, it is essential to produce nanometer-width/size GNRs and GQDs with an atomic precision. However, realizing such structural precision by means of top-down methods is still highly challenging.

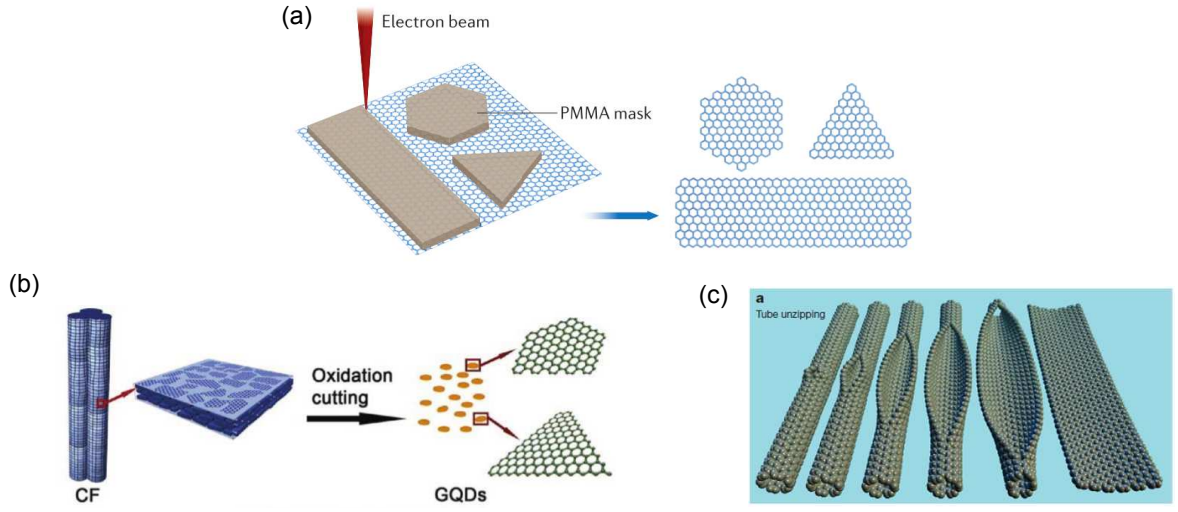

Figure 3.1: Top-down fabrication methods of GNRs and GQDs, including cutting from graphene sheets by lithography (a), solution based oxidation of carbon fibers (b) and unzipping of carbon nanotubes (c). Adapted respectively from [54], [43] and [55].

3.2 Bottom-up syntheses

To this end, *bottom-up* organic synthesis method appears very promising. This method can be likened to building a brick house. Here small molecular precursors (as the bricks)

react in a selective way to obtain final assembled GQDs or GNRs (the house). In principle, by appropriately designing the molecular precursors, it is possible to obtain GQDs and GNRs with desired structure (see Fig. 3.2).

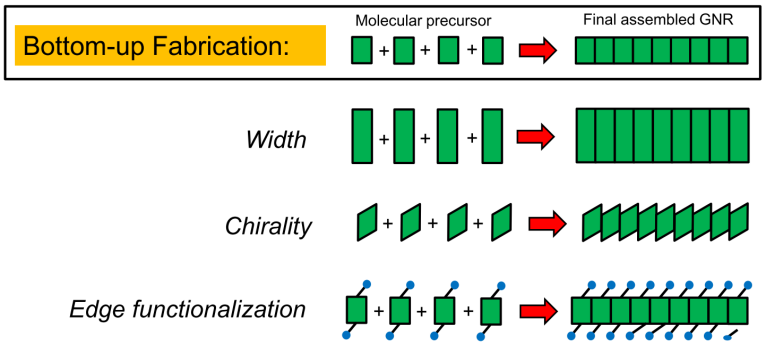

Figure 3.2: Schematic illustration of the principle of bottom-up synthesis method. Adapted from [56].

In-solution approach

As shown in Fig. 3.3 - (a), the bottom-up synthesis of GQDs typically consits in a two-step solution-based chemical reaction route: 1. polymerization of the molecular precursors into intermediate oligophenylenes or polyphenylenes. 2. oxidative intramolecular cyclodehydrogenation (graphitization) of the tailor-made polyphenylenes. A variety of GQDs with defined molecular structures have thus been obtained, ranging from small nanographene molecules such as hexaperi-hexabenzocoronene (HBC, C42) to a larger hexagonal GQD with 222 sp^2 carbons and a diameter of ∼3 nm (C222) [57] (see Fig. 3.3 - (b)

for some examples).[2] Since GQDs tends to stack together due to the strong π-π interactions, alkyl chains are usually installed at the peripheral positions of GQDs to increase the steric hindrance and enhance the solubility. Further edge functionalizations with complex structures have also been reported. Yan *et al.* have shown the attaching of trisubstituted phenyl groups on the edge of two large GQDs (132 and 168 conjugated carbon atoms) [59]. In this way, the GQDs are expected to be shielded from one another in three dimensions, reducing the aggregation effect (Fig. 3.3 - (c)). More recently, atomic precise edge chlorination of GQDs has also been realized [60]. Since the chlorine atoms induce severe steric hindrance, the edge-chlorinated GQDs are non-planar (Fig. 3.3 - (d)) and thus show enhanced solubility. The vast majority of synthesized GQDs have armchair edges as they are chemically stable, but an increasing number of zigzag-edged structures exhibiting distinct properties have recently been reported. For instance, quateranthene (Fig. 3.3 - (e) left), which can be regarded as a short segment of 8-ZGNR, has been synthesized in 2013 [61]. Analyses of this structure revealed indeed the presence of unpaired electrons localized at the zigzag edges as well as ferromagnetic correlation at room temperature. However, such nanographene molecules with zigzag

[2]Unfortunately, the concept of planarizing large oligophenylene precursors to obtain GQDs reaches its limit in solution. Partial cyclodehydrogenation will occur when the size of target GQD is bigger C222, because of poor solubility of precursors, as well as a mismatching of topology for large oligophenylene precursors [58].

edges are often prone to oxidation due to the unpaired electrons, which limits their further investigation and applications. Stable nanographene molecules with zigzag edges but no biradical ground states have also been synthesized. For example, dibenzo[*hi*,*st*] ovalene (DBO) (Fig. 3.3 - (e) right) is highly stable under ambient conditions and exhibits strong red emission [62].

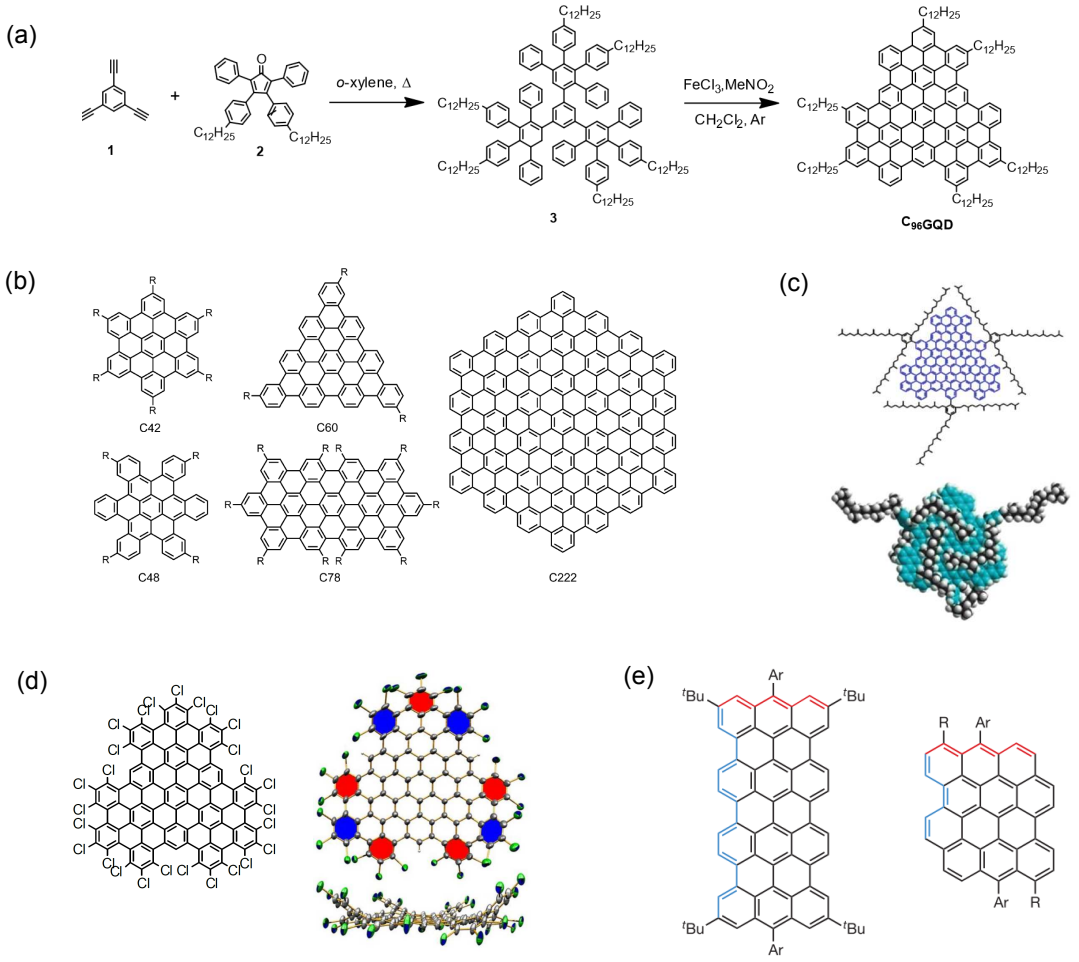

Figure 3.3: (a) - Typical reaction route for producing bottom-up synthesized GQDs. Adapted from [63]. (b) - Examples of bottom-up synthesized armchair-edge GQDs (nanographene molecules). Adapted from [64]. (c) - Edge functionalized GQD with trisubstituted phenyl groups, which fully shield the aromatic core. Adapted from [59]. (d) - Edge-chlorinated GQD, showing non planar structure. (e) - Nanographene molecules with zigzag-typed edges (shown in red). Left: with a biradical ground state. Right: without biradical ground state. Adapted from [61] and [62], respectively.

This bottom-up synthesis can be further applied to produce longitudinally extended GNRs. Similarly to the synthesis of GQDs, the synthesis of GNRs is also based on such in-solution two-step reaction (polymerization and graphitization). There are several different polymerization methods to obtain the intermediate polyphenylenes, for example Diels-Alder [65], Yamamoto [66] and Suzuki [67] polymerizations. These polymerization methods can efficiently prepare appropriate polymer precursors and led to a variety of GNR structures. Among these methods, the DielsAlder polymerization of an AB-type monomer (a cyclopentadienone moiety as the diene and an ethynyl group as the dienophile) could produce polyphenylenes with extremely high molecular weight (up

to 60 kg/mol), which lead to the final GNRs with a width of around 1 nm and an average length >100 nm (Fig. 3.4 - (a)) [65]. Such solution-based synthesis approach is highly scalable, and it has been shown to be possible to prepare over 1 g of GNRs in the laboratory, suggesting the potential for industry-scale production [68]. Moreover, based on the structural defined GNRs, people have also attempted to perform edge functionalization and now it is possible to precisely graft a variety of groups at the edges of GNRs, such as chlorine atoms [60], poly(ethylene oxide) (PEO) chains [69], naphthalene/perylene monoimide [70], porphyrin [71] and more recently a type of spin-bearing radical groups [72], which open the ways to realize the coherent coupling between molecule structures and GNR aromatic cores. One should note that the solution-phase synthesis method finally affords GNRs in powder form. Since the aromatic size of GNRs is much larger than GQDs, they are more difficult to be processed. GNR powders can be dispersed in aqueous surfactants or organic solvents by means of mild sonication. However large portions of the powders often remain undispersed.

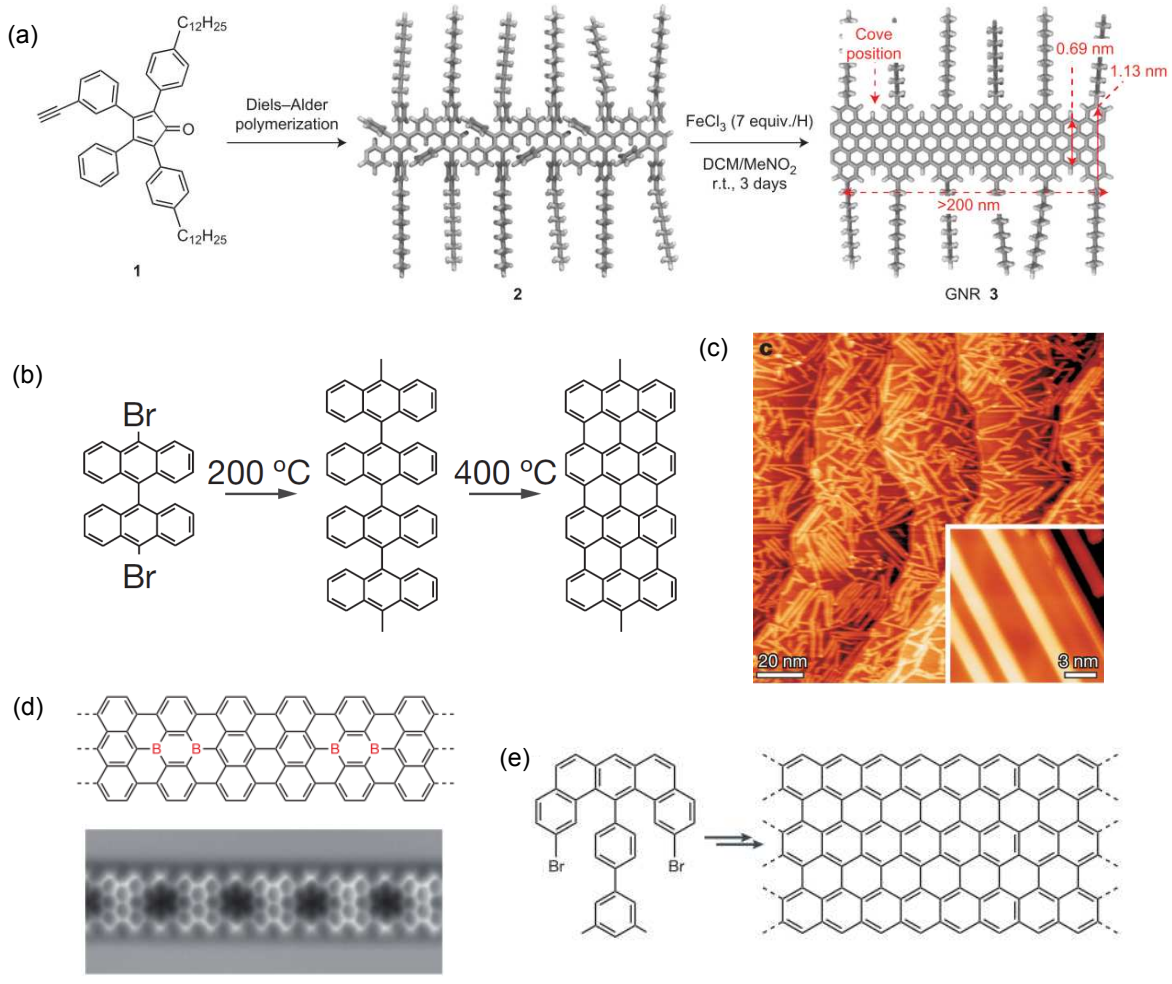

Figure 3.4: (a) - In-solution AB-type Diels-Alder polymerization leads to long graphene nanoribbons. Adapted from [65]. (b) - On-surface reaction scheme for the synthesis of straight GNRs from dihalogen substituted molecular precursors. Adapted from [18]. (c) - *In situ* high-resolution STM image of on-surface synthesized GNRs, showing the defined and uniform GNR sturcture. Adapted from [18]. (d) - Boron-doped GNR and its corresponding non-contact atomic force microscopy (nc-AFM) image. Adapted from [38]. (e) - Synthetic scheme for the fully zigzag edge GNR. Adapted from [73].

On-surface approach

In this regard, the direct synthesis of GNRs on metal (mostly gold) surfaces under ultra-high vacuum (UHV) conditions serves as an alternative approach. Similar to the solution-based approach, the surface-assisted approach also consists in two steps: 1. homocoupling (Ullmann coupling) polymerization of dihalogen substituted precursors. 2. thermally induced and surface-catalyzed cyclodehydrogenation (Fig. 3.4 - (b)). Typically, atomically precise GNRs with a quantity of less than one monolayer coverage (sub-monolayer) can be obtained, flatly lying on the gold surface (Fig. 3.4 - (c)). Their chemical structure can be *in situ* imaged using high-resolution STM (Fig. 3.4 - (c)) and non-contact atomic force microscopy (nc-AFM)(Fig. 3.4 - (d)). The first on-surface synthesis of GNR was realized by Cai *et al.* in 2010 [18]. Since then, a series of armchair-edge GNR with different width (5-, 7-, 9- and 13-AGNR) have been synthesized on gold surfaces by varying the molecular precursors. Besides pristine GNRs, GNRs doped with boron [38, 74], nitrogen [75] or sulfur [76] have also been synthesized with pre-designed molecular precursors (Fig. 3.4 - (d)), providing an additional parameter for tuning the electronic properties of GNRs. Graphene nanoribbon heterojunctions and heterostructures have also been realized in single GNR strands by combining two different molecular precursors [77, 78], which emerges as a promising way to modulate the electronic properties as people have done with inorganic semiconductors [79]. Notably, long-awaited atomically precise zigzag-edge GNR with defined and uniform structures were recently achieved by Ruffieux *et al.* in 2016 [73]. As shown in Fig. 3.4 - (e), they carefully designed an "umbrella"-shape molecule precursor and thus the precursors connects together in an up-and-down configuration forming the full zigzag edge structure. Although a variety of GNRs with different width and edge structures have been synthesized with atomic precision via surface-assisted method, such GNRs need to be transferred from the metal surfaces onto dielectric substrates for further studies on their electronic and optical properties as well as integration into electronic devices. It is thus very necessary to develop an efficient, non-destructive, and clean transfer method.

4 Characterization results on bottom-up synthesized GNRs and GQDs

4.1 Characterization of chemical structure

In principle, bottom-up chemistry method allows us to produce GQDs or GNRs with defined and uniform structure. To support this, there are some characterization techniques that have been employed according to the synthesis approach.

For in-solution synthesized GQDs, since they have defined chemical formula, their structure perfection can be demonstrated directly by matrix-assisted laser desorption/ionization time-of-flight (MALDI-TOF) mass spectrometry (MS). In these measurements, one single intense signal with an ensemble of very narrow peaks is found around the position corresponding to the molecular mass of GQD (Fig. 4.1 - (a)), which means the produced GQDs have the exact structure and there is no detectable amount of side products (unreacted or partially graphitized oligophenylenes) present in the fi-

nal powder product. Besides, liquid-state (for soluble compounds, high resolution) and solid-state (for less soluble compounds, low resolution) ^{1}H NMR measurements can give information on the chemical environment of the groups in intermediate oligophenylenes and final GQDs, and demonstrate the structural perfection of GQDs at an ensemble level (Fig. 4.1 - (b)). Moreover, as we can see in Fig. 4.1 - (c), single GQDs can be visualized using STM by depositing the hot GQD solution [66, 80] or "sublimating" GQD powders [81] on the Au(111) substrate or highly oriented pyrolitic graphite substrate (HOPG). However, to date such measurements have been performed on few GQD structures and most of them have a small core size.

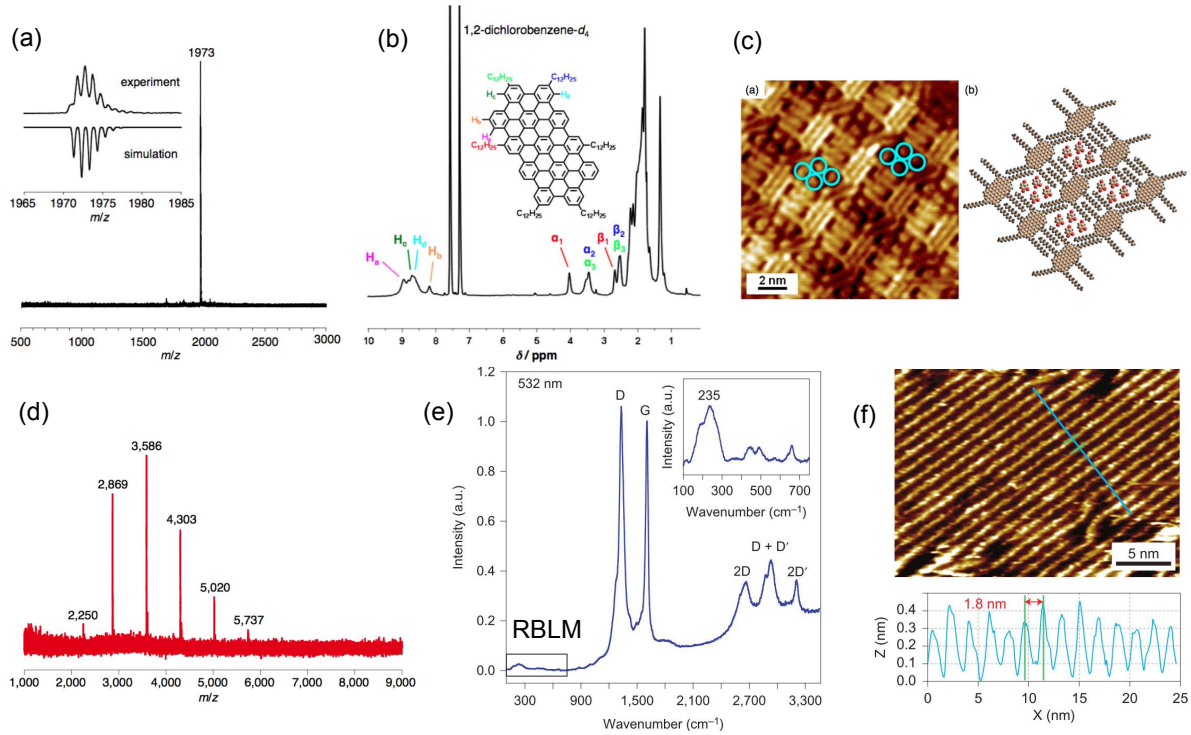

Figure 4.1: (a) - (c): Structural characterizations of bottom-up synthesized GQDs via in-solution method. (a) - Matrix-assisted laser desorption/ionization time-of-flight (MALDI-TOF) mass spectrum (MS) of the GQDs. The obtained spectrum is compared with the simulation, demonstrating the exact structure of the produced GQDs. Adapted from [66]. (b) - Liquide-state ^{1}H NMR of the GQDs. Adapted from [66]. (c) - STM image of the GQDs deposited on the Au(111) substrate. (d) - (e): Structural characterizations of bottom-up synthesized GNRs via in-solution method. (d) - MALDI-TOF mass spectrum of the intermediate polyphenylene precursors, showing a series of equally separated peaks. Adapted from [82]. (e) - Raman spectrum on the GQD powders. Adapted from [65]. (f) - STM image of the GNRs on HOPG, showing a well-organized self-assembled monolayer of straight and uniform nanoribbons. Adapted from [65].

For in-solution synthesized GNRs, since the polymerization step does not control the length of the produced polyphenylenes, the final GNR structure has a certain length distribution. As a result, the MALDI-TOF mass spectrum of GNRs displays a series of peaks with an equal interval corresponding to the mass of one repeating unit (see Fig. 4.1 - (d)).[3] The total absence of the peaks inside the intervals suggests the GNRs are fully

[3]The long GNRs that have high molecular mass cannot be detected by MALDI-TOF MS. To characterize the average length of GNRs, people often uses size-exclusion chromatography (SEC).

graphitized. However, one should note that the MALDI-TOF mass spectra of these in-solution synthesized GNR samples also indicate the presence of a very small amount of short GNR dimer and trimer (can be considered as GQDs), which could have different behaviors, especially a larger bandgap than the sufficient long GNRs. Similar to the case of GQDs, the solid-state ^{1}H NMR spectra of GNRs display some distinct features suggesting their defined structures. Besides, GNRs display distinct vibrational properties, which are directly linked to their structure. Raman spectroscopy measurements on the GNR powders show prominent D and G modes and corresponding second order modes, which are the characteristic features of sp^2 carbon structures. Remarkably, a distinct peak from a width-specific low-frequency mode called radial-breathing-like mode (RBLM) is resolved in the spectrum (see inset of Fig. 4.1 - (e) and for this specific GNR structure, it is at 235 cm^{-1}), indicating high homogeneity of the width of produced GNRs. One should note that this Raman mode has never been observed on the top-down fabricated GNRs [49]. In addition, Fourier transform infrared (FTIR) spectroscopy is also a powerful method to characterize the vibrational properties of sp^2 carbon structures. The FTIR spectra on the final GNR structures always show very different modes compared with the spectra on the intermediate polyphenylenes supporting the successful conversion of polyphenylene precursors into GNRs. STM measurements have also been performed to visualize the in-solution synthesized GNRs. Due to the sever aggregation (π-π stacking) issues of GNRs in suspension, the visualization of GNRs synthesized by in-solution approach becomes extremely hard. To perform STM measurements on such GNRs, the authors in [65] applied a very tricky method, in which they extracted only a tiny amount of short and soluble GNRs from the produced powders using hot TCB solvent and deposited them on the HOPG surface. The STM images of the obtained samples show self-assembled and highly ordered domains of uniform and mostly straight GNRs (see Fig. 4.1 - (f)), which implies the full graphitization of polyphenylene precursors. In addition, several attempts have been performed to visualize single isolated GNRs synthesized by this in-solution approach [83, 84]. However, an efficient and reliable method is still elusive.

For on-surface synthesized GNRs, as they are isolated and extended on gold surface, their chemical structure is usually *in-situ* visualized with STM and nc-AFM under UHV. For molecular visualization with STM, since it is sensitive to the density of states near the Fermi level, which are typically delocalized over the entire molecule, the correlation between bonding structure and STM image contrast is not very straightforward. To solve this problem, simulations of STM images using DFT are usually performed. As we can see in Fig. 4.2 - (a), the very good agreement between the simulated STM image (shown in white) and the experimental results, confirms that the produced GNRs are atomically precise with fully hydrogen-terminated edges. For nc-AFM visualization, the probe is functionalized with a single carbon monoxide (CO) molecule. Since the probe senses the short range forces, the signal is very sensitive to the charge distribution on the sample. Moreover, to reduce the vibration of the measured molecule and to obtain an higher resolution, the measurements are commonly operated at low temperature ($\sim$5 K). As we can see in Fig. 3.4 - (d), the bonding structure of pristine and doped GNRs can be clearly resolved by nc-AFM, which confirms again their structural perfection. X-ray photoemission spectroscopy (XPS) is a powerful technique to study the chemical composition of a material. For on-surface synthesized GNRs, it has been used to monitor the evolution of the chemical compounds and analyze the kinetic during the two-step reaction. Moreover, this technique has been used to study the stability of on-surface

synthesized GNRs (with hydrogenated edges) under ambient conditions. Fig. 4.2 shows the XPS spectrum of the GNR sample after exposure to air, the only peak for carbon atom is at 284.5 eV that corresponds to the sp^2 bonded carbon. There are no signs of carbon in other chemical environments, especially, no CO, C=O or COOH components (indicated by the blue lines), supporting that the GNRs are inert under ambient conditions. Similar to the in-solution synthesized GNRs, the Raman spectra of on-surface synthesized GNRs also display the width specific RBLM mode. Notably, the width of the peak is much narrower than the in-solution GNRs, since the edges are terminated by single hydrogen atoms instead of long alkyl chains [85].

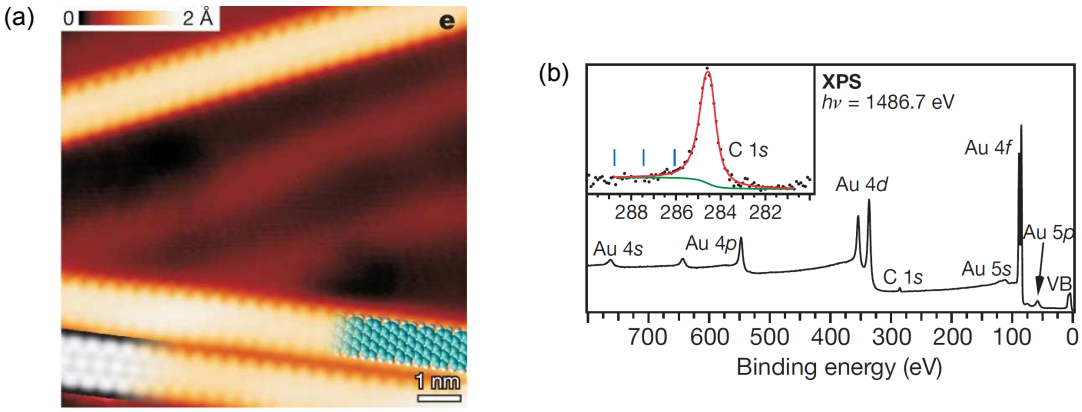

Figure 4.2: (a) - *In-situ* high resolution STM image of the on-surfaced synthesized GNRs. The white part at the bottom left is a DFT-based STM simulation. The very good agreement confirms their exact structure with hydrogen-terminated edges (the molecular model is shown at the bottom left). Adapted from [18]. (b) - XPS spectrum of the on-surface synthesized GNRs after exposure to air. The absence of the peaks corresponding to CO, C=O or COOH components (indicated by the blue lines in the inset) suggests the GNRs are inert under ambient conditions. Adapted from [18].

4.2 Characterization of electronic properties

Due to sever aggregation effects of in-solution synthesized GNRs and large size GQDs, the characterizations of electronic properties have been mainly performed on the on-surface synthesized GNRs. Their electronic structure and in particular the bandgap size (E_g) and the values of bands' effective mass (m_{VB} and m_{CB}), have been investigated locally with scanning tunneling spectroscopy (STS) and with averaging experimental techniques such as angle-resolved photoemission spectroscopy (ARPES) and high-resolution electron energy loss spectroscopy (HREELS).

The most widespread method used so far is STS. As illustrated by Fig. 4.3 - (a), a scanning tunneling spectrum is obtained by placing a tip above a particular place on the sample. With the height of the tip fixed, the electron tunneling current is then measured as a function of electron energy by varying the voltage between the tip and the sample (the tip to sample voltage sets the electron energy). The obtained curve is thus referred to as an $I - V$ curve. From the $I - V$ curve, the $\mathrm{d}I/\mathrm{d}V - V$ curve is finally obtained, which corresponds to the electron density of states at the local position of the tip, the LDOS. Two peaks at the sides of $V = 0$ can be resolved, corresponding to the valence

band and conduction band, respectively. From the onset of valence and conduction bands, an electronic band gap (E_g) is thus inferred. Bandgap values of $E_g = 2.37$ eV, $E_g = 1.38$ eV and $E_g = 1.40$ eV have been measured for the armchair edge 7-AGNR [86], 9-AGNR [28] and 13-AGNR [87] grown on Au(111), respectively. As shown in Fig. 4.3 - (b), these values (indicated by hollow triangles) have been compared with the predicted bandgap using many-body perturbation theory (GW) calculations with image charge (IC) corrections (indicated by solid signs), which are used to account for the polarization effect of the gold substrate [39,86,88]. The good agreement between the measured values and theoretical calculations thus demonstrates the tunability of the electronic properties of GNRs via the control of structure by the bottom-up chemistry.

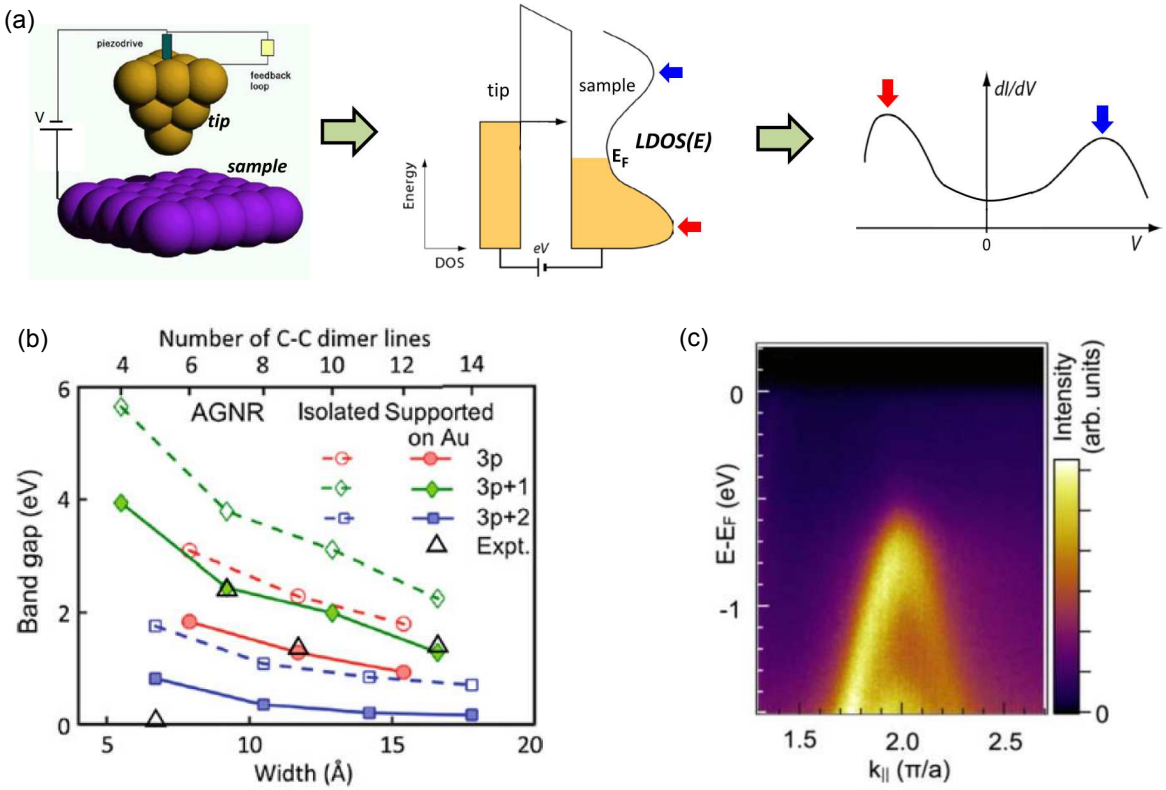

Figure 4.3: (a) - Schematic illustration of scanning tunneling spectroscopy (STS) for the measurements of local electron density of states (LDOS). Adapted from [56]. (b) - Experimental STS results and theoretical calculation prediction of the electronic bandgap (E_g) of armchair GNRs with different width. Colored hollow signs: GW calculation results predicting the bandgap of isolated GNRs. Solid signs: GW + image charge (IC) corrections results predicting the bandgap of GNRs supported on Au surface. Black hollow triangles: the experimental STS results of the GNRs on Au surface. Adapted from [88] together with the data in [28]. (c) - ARPES spectrum of 7-AGNRs grown on Au(788) substrate along the GNR axis. Adapted from [86].

Another common way to investigate the electronic properties of on-surface synthesized GNRs is angle resolved photoemission spectroscopy (ARPES), which gives access to the whole *energy versus parallel momentum* dispersion of occupied states (as shown in Fig. 4.3 - (c)) [86]. Being an ensemble averaging technique, domains of GNRs with the same orientation are required to obtain $k_{||}$-resolved ARPES spectrum. This has been realized by growing GNRs on vicinal Au surfaces that display a periodic array of steps. This type of surface can act as templates and drive the uniaxially oriented growth of the GNRs along the terraces direction (Fig. 4.8 - (a)). We will see in the next section that

such samples with aligned GNRs are also very useful to perform optical characterization.

4.3 Characterization of optical properties

Some theoretical calculations have been perform on the GQDs and GNRs to investigate their optical properties, such as the optical absorption spectra of different GQD [89–91] and GNR [92–94] structures, and scaling effect of exciton binding energy in GNRs [95]. In contrast, the intrinsic optical properties of GQDs and GNRs are almost unexplored experimentally. In this section, I will present the only few reports on the experimental study of their optical properties.

In-solution synthesized GQDs

Optical absorption spectroscopy is one of the most common way to characterize the optical properties of a material. To do this, the produced GQD powders are usually dispersed in organic solvents. However, when the size of GQD becomes larger, it is more insoluble and the aggregation effect is more sever. In consequence, with the increase of the size of GQD, the absorption spectra broaden and become structureless (Fig. 4.4 - (a)) [96]. Despite of this broadening, one can still distinguish that the larger GQDs have an absorption maximum at a lower energy. As shown in Fig. 4.4 - (a)) [97], from benzene to the GQD with 222 π conjugated electrons (thus $222/6 = 37$ aromatic sextets), E_{max} roughly has an inverse relation with the number of aromatic sextets[4], in agreement with lower quantum confinement for the larger GQDs.

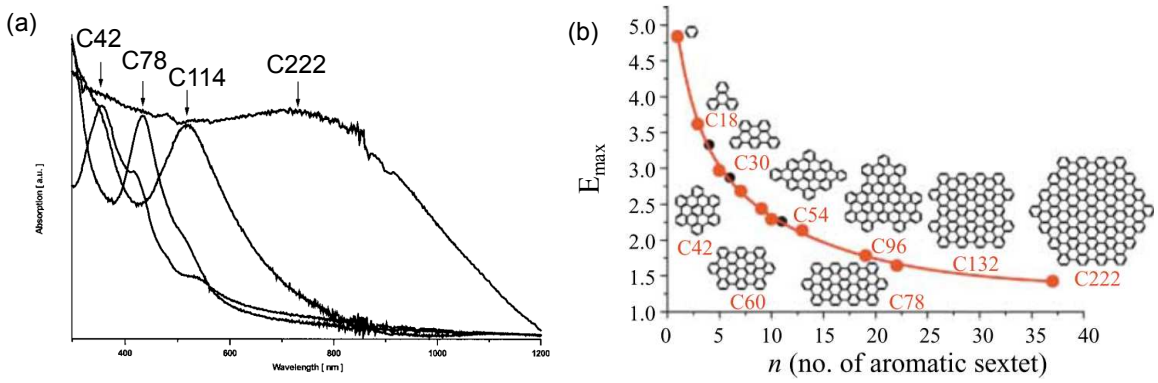

Figure 4.4: (a) - Optical absorption spectra of GQDs in different size. Adapted from [96]. (b) - The energy of maximum (E_{max}) in the optical absorption spectrum as a function of the GQD size (number of aromatic sextet). Adapted from [97].

Photoluminescence is another important optical properties for a semiconducting material. However, due to the aggregation effect, no pertinent photoluminescence results have been reported on the simple alkyl substituted GQDs with size larger than 60 π-electrons.

In 2010, the group of Dr. Liang-Li Shi at Indiana University developed a method to install 1,3,5-trialkyl phenyl groups at the edges of large C132 and C168 GQDs (Fig. 4.5 - (a)) [59]. These large substituted groups could wrap around the aromatic core of GQD forming a shell-like structure. In this way, the $\pi - \pi$ interactions between the

[4]All the GQDs shown here are armchair edge GQD.

GQD aromatic cores are reduced. Thus, such GQDs show enhanced solubility and lower aggregation compared to the GQDs with simple alkyl chains. They then performed a series of optical characterizations on dispersions of C132 GQD (Mueller *et al.*, 2010 [98]). In contrast to the simple alkyl chain substituted GQDs, the absorption spectrum of this "core-shell" GQD is more structured and the authors attributed the absorption lines to the transitions to the different singlet excited states (S_1, S_2, S_3, and S_4). The PL spectrum mainly consists of two lines, one at 670 nm the other at 740 nm. They also found that the time-resolved PL when detected at 670 nm is bi-exponential with two relative fast decay times of 1.7 ns and 5.4 ns, while the decay curve for the line at 740 nm is mono-exponential with a extreme long characteristic time of $\sim$4 µs. To explain these observations, the authors proposed that the spin-orbit coupling is very strong and singlet-triplet energy separation is very small in this large GQD. Thus the inter-system crossing (ISC) is very efficient and the emission at 670 nm corresponds to the fluorescence (relaxation from the singlet state S_1), while the emission at 740 nm corresponds to the phosphorescence (relaxation from the triplet state T_1) (as shown in Fig. 4.5 - (c)). Moreover, the authors performed photoluminescence excitation (PLE) measurements on these two PL lines (Fig. 4.5 - (d)). The PLE curve detected at 740 nm (red line) is in very good agreement with the absorption spectrum. However, the PLE detected at 670 nm (blue line) is broad and in resonance at higher energy (lower than 500 nm). The authors left an open question on this strange behavior. After that, the group of Dr. John A. McGuire at Michigan State University continued to investigate the optical properties of these large "core-shell" GQDs in collaboration with the group of Dr. Liang-Li Shi. By means of transient absorption spectroscopy, they observed efficient biexciton formation and fast biexciton Auger recombination rates, which implied strong carrier interactions in these large GQDs [99, 100].

In 2014, Riesen *et al.* [101] re-investigate the same C132 GQD by combining optical measurements and theoretical calculations. Using DFT based quantum chemical calculations, the measured absorption spectrum was well reproduced (Fig 4.6 -(a)). Moreover, as shown in Fig 4.6 -(b), the authors indicated that the two high energy transitions have strong oscillator strength, while the two low energy lines are nearly dark (very low oscillator strength). However, these two "dark " transitions could be brightened by the significant electron-vibrational intensity borrowing. Notably, in contradiction with the initial assignments by Mueller *et al.* [98], the authors in this paper proposed that the observed emission at 740 nm, which has long mono-exponential decay and the PLE similar to the absorption, arises from the lowest "dark" singlet transition instead of phosphorescence from the triplet state, while the emission at 670 nm, which has short multi-exponential decay and the PLE different to the absorption, arises from the impurities in the dispersion instead of the fluorescence of the C132 GQDs. This proposition was further supported by the experiment of adding external heavy atoms. It is known that by adding the heavy atoms in the solution, the inter-system crossing rate of molecules could be strongly enhanced [102]. Thus if the emission at 740 nm originated from the triplet state, an increase of the emission intensity would be expected when adding heavy atoms. However, after adding dibromoethane in the GQD dispersion, the intensity of emission at 740 nm was decreased a lot with even a much greater extent than the emission at 670 nm (Fig. 4.6 - (c)). This observation is in contradiction with the assignment of the emission at 740 nm as phosphorescence.

So we can see that to date, the photoluminescence properties of large bottom-up

synthesized GQDs are not clear (only one structure have been studied, and there are two totally different explanations on the observed results.). To this end, more systematic experimental studies and theoretical calculations on the GQDs with different structures are very needed.

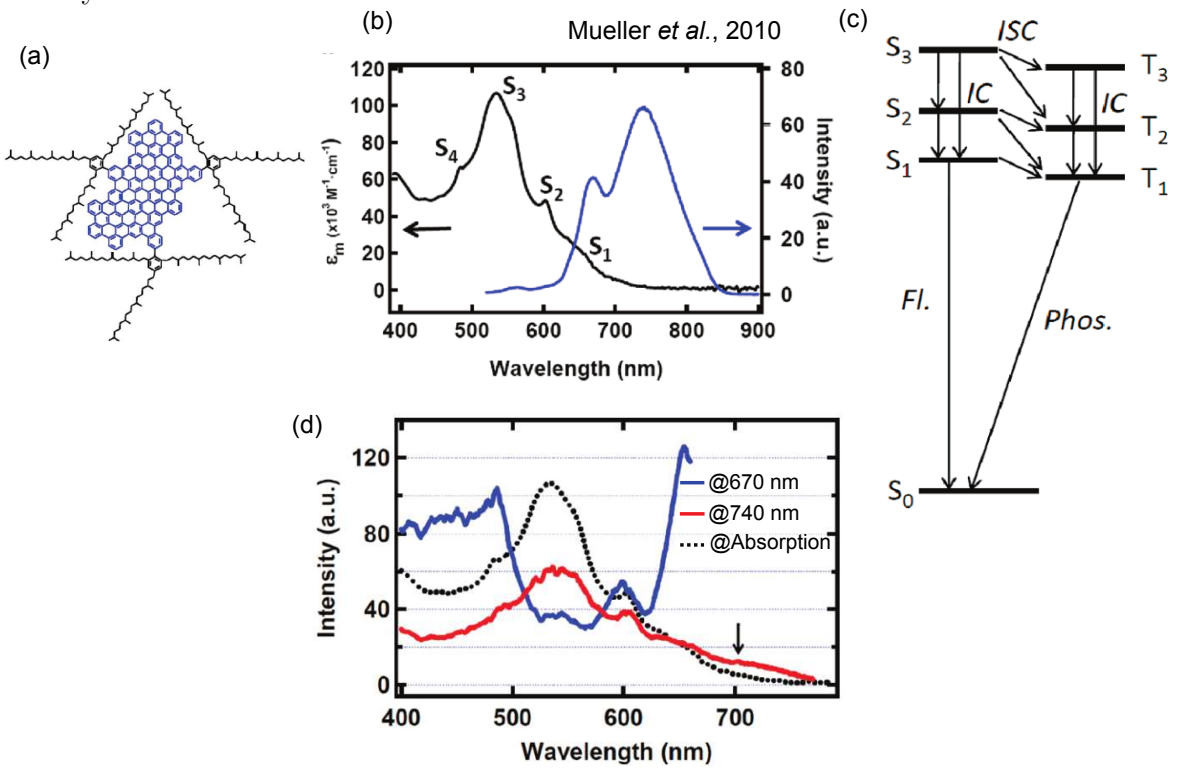

Figure 4.5: (a) - Chemical structure of C132 GQD. The three large chains could wrap around the aromatic core of GQD forming a "protective shell". (b - d) Optical characterizations of C132 GQD performed by Muelller *et al.* [98]. (b) - Optical absorption and PL spectra of C132 GQD dispersion. (c) - Schematic illustration of the proposed energy levels of C132 GQD. (d) - PLE curves of C132 GQD dispersion. Adapted from [98].

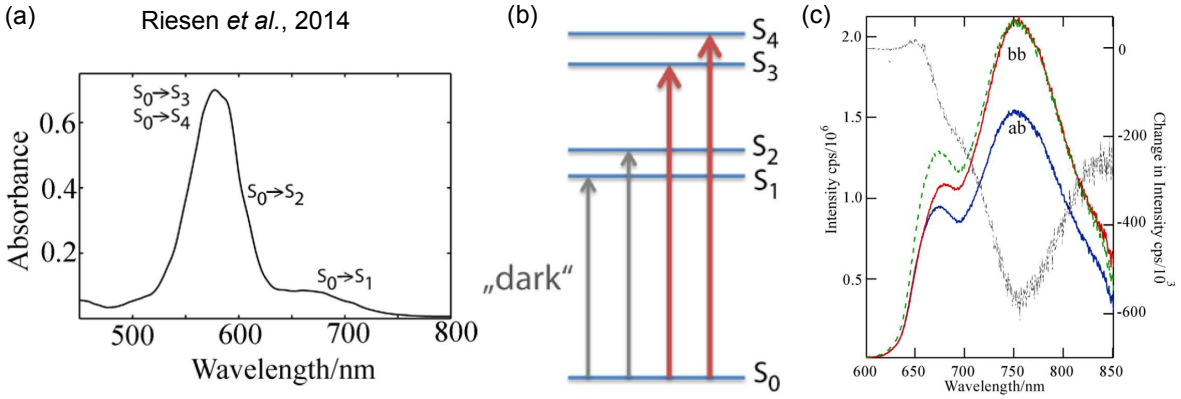

Figure 4.6: Optical investigations of C132 GQD performed by Riesen *et al.* [101]. (a) - Simulated absorption spectrum computed using the nuclear-ensemble approach, partly taking into account electron vibrational coupling. (b) - Schematic illustration of the four lowest optical singlet-singlet transitions. The two low energy transitions are "dark" (grey arrows), while the two high energy transitions are bright (red arrows). (c) - PL spectra of the C132 GQD dispersion before (bb) and after (ab) adding of dibromoethane. The grey curve is the difference spectrum. Adapted from [101].

In-solution synthesized GNRs

Similar to the case of GQDs, there are very few optical characterization results of in-solution synthesized GNRs that have been reported. The absorption spectra of cove-type edge GNRs with different width have been reported in [103, 104]. We can see in Fig. 4.7 -(a) that the absorption band of the wide cove-edge GNRs is red-shifted compared to the narrow ones, which is in agreement with the fact that the π electrons are more delocalized. However, these two papers just showed the absorption spectra without going into details. Apart from that, no results on the photoluminescence properties of such GNRs have been reported, which is presumably due to their very low insolubility. To date, there is only one paper that is dedicated to the optical characterizations of in-solution synthesized GNRs. In 2016, Soavi *et al.* [105] performed transient absorption spectroscopy on the suspension of four-atom-wide cove-edge GNRs (4-CGNRs). As shown in Fig. 4.7 - (b) left, they found positive differential transmission ($\Delta T/T$) signal around 650 nm when the GNR suspension was excited with a high fluence (indicated by the black arrow). Since it does not correspond to any resonant feature in the linear absorption spectrum and it is red-shifted compared to the lowest optical transition, the authors attributed this positive $\Delta T/T$ signal to the stimulated emission (SE). They proposed that at high excitation fluence, the excitons in GNRs undergo exciton-exciton annihilation effect and biexcitons could be efficiently formed (an Auger-like process, indicated by the green arrow in Fig. 4.7 - (b) right). Thus the observed SE signal is attributed to the radiative relaxation from the biexciton state to the one-exciton state of GNRs (the green waved line). From this point, the authors concluded that the GNRs is very promising in view of light-emission applications such as lasers and light-emitting diodes (LEDs). However, one should note that in this paper the authors did not show any steady-state photoluminescence spectra. Moreover, they also admitted that there might be GNR aggregates present in the suspension. Since the inter-molecular couplings could alter a lot the behavior of exciton, one can question on the influence of aggregation on these experimental results.

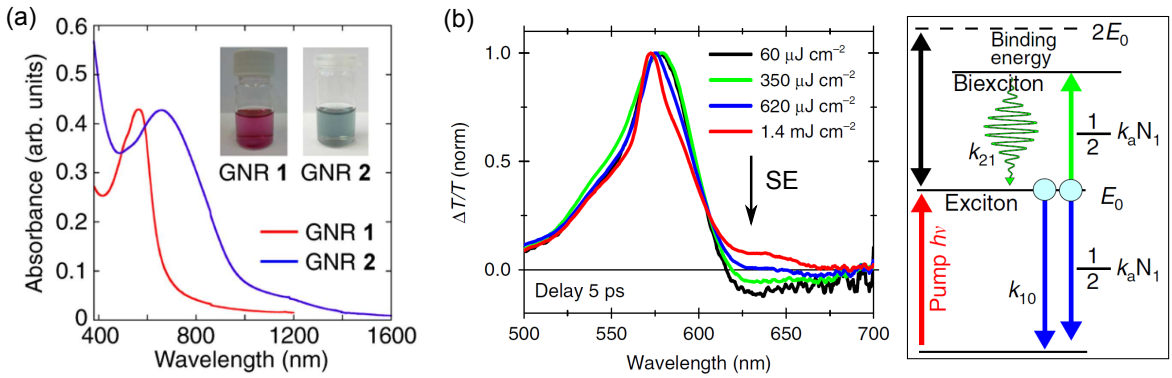

Figure 4.7: (a) - Optical absorption spectra of cove-edge GNRs with different width. Adapted from [103]. (b) - Left panel: Normalized $\Delta T/T$ spectra of four-atom-wide cove-edge GNR (4-CGNR) suspension for different excitation fluences at a fixed pump-probe delay of 5 ps. Right panel: Proposed exciton-biexciton model. Adapted from [105].

On-solution synthesized GNRs

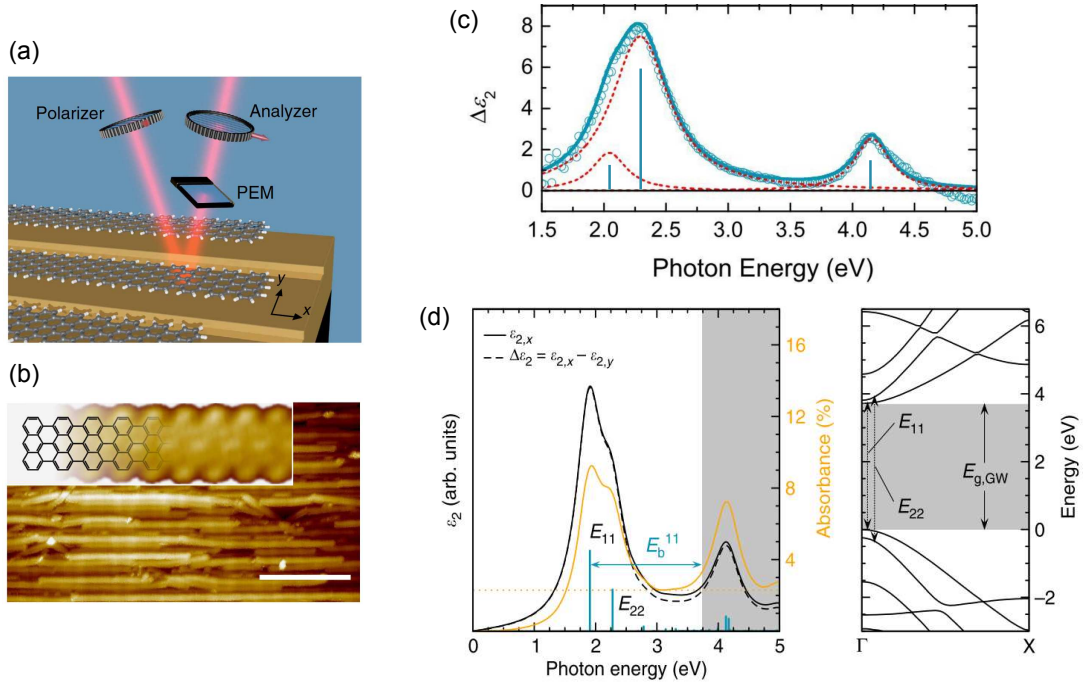

Figure 4.8: (a) - Schematic illustration of reflectance difference spectroscopy (RDS). PEM stands for photoelastic modulator that modulates polarization of light. One should note that in reality the laser beam size is far larger than a single nanoribbon. Thus RDS is an ensemble averaging technique. (b) - STM image of the aligned 7-AGNRs grown on Au(788). Scale bar: 20 nm. (c) - Dielectric response function $\Delta\varepsilon_2$ of 7-AGNRs on Au(788) obtained from the measured RD spectra. (d) - Left: GW + BSE calculated optical absorption spectrum of 7-AGNR (light is polarized along the ribbon axis). Right: Calculated electronic band structure of 7-AGNR within the GW approach. Adapted from [106].

As we have seen, the on-surface synthesis approach can grow isolated GNRs. However, due the metal (Au) substrate, it is impossible to directly perform optical absorption and photoluminescence spectroscopy[5]. The only reported method to characterize the optical property of GNRs on Au surface is reflectance difference spectroscopy (RDS) [106, 107]. RDS measures the sample's reflectance difference Δr for light polarized along two orthogonal directions x and y, which gives the anisotropic absorption information of the sample (Fig. 4.8 - (a)). Since it is an ensemble averaging technique, the measurement should be performed on the sample with GNRs grown in the same orientation (like the ARPES measurement that we previously discussed)(see Fig. 4.8 - (b)). In 2014, Denk *et al.* firstly performed RDS on seven-carbon-wide armchair GNRS (7AGNRs) [106]. As shown in Fig. 4.8 - (c), the obtained differential dielectric response $\Delta\varepsilon_2$ from the RDS measurement is dominated by three positive peaks at 2.1, 2.3 and 4.2 eV, respectively. The positive sign of $\Delta\varepsilon_2$ indicates that these transitions arise from the absorption of light polarized along the ribbon axis. Since there are no features relevant to the absorption of light polarized perpendicularly to the ribbon axis, such armchair edge GNRs show strong polarization anisotropy as observed in a similar quasi-1D system CNTs [108]. Moreover, the authors in this paper also performed GW + BSE

[5]The metal surface quenches the PL of GNRs

calculations to simulate the optical absorption spectrum of 7-AGNR, where the *GW* approximation was used to calculate the gas-phase bandgap, while the BSE equations was used to further including excitonic effects. As shown in Fig. 4.8 - (d) left, the simulated optical absorption spectrum shows three strong excitonic transitions located at 1.9, 2.3, 4.1 eV and they are both polarized along the ribbon axis, which are in excellent agreement with the experimental results. The computed data also indicate that the lowest two transitions around 2 eV arise from optical transitions between the last valence and first conduction bands (E_{11}), and the second valence and second conduction bands (E_{22}) (Fig. 4.8 - (d) right). Moreover, by comparing with the gas phase band gap value $E_{g,GW}$ (= 3.7 eV), the exciton binding energy for E_{11} and E_{22} is thus equal to 1.8 and 1.4 eV, respectively, which correspond to Wannier-like quasi-1D excitons fully delocalized along the nanoribbon width. This paper is the first demonstration that the intrinsic optical properties of GNRs predicted by the theory can be observed in the bottom-up synthesized GNRs.

In 2017, Senkovskiy *et al.* performed the transfer procedures of such Au-surface-grown 7-AGNRs in order to investigate their photoluminescence properties [109]. As shown in Fig. 4.9 - (a), by performing the electrochemical delamination process, the whole as-grown 7-AGNR film together with the spin-coated PMMA support layer were transferred onto a SiO_2/Si substrate. The PMMA was finally removed by acetic acid and methanol. However, as seen in Fig. 4.9 - (b), the PL spectrum of the transferred 7-AGNRs is dominated by the Raman peaks of GNRs and there is only a very weak and broad PL background instead of the expected strong emission from the lowest E_{11} excitonic transition as revealed by the RDS. The theoretical calculations predicted that there could be a dark state with energy very closed to the lowest E_{11} transition [92, 93]. The author thus proposed that the observed weak and broad PL is the signature of the existence of such dark states. However, we should note that the photoluminescence is usually very sensitive. Many factors could quench it. For example, the transfer procedure in this paper involved base solution NaOH and acetic acid. As people have observed in CNTs [110], such base and acid solutions could be a possible reason to quench the PL. Thus in view of a more detailed PL investigation, a transfer method in a clean and mild condition should be developed in the future. However, to date, the photoluminescence properties of the on-surface synthesized GNRs are still not clear.

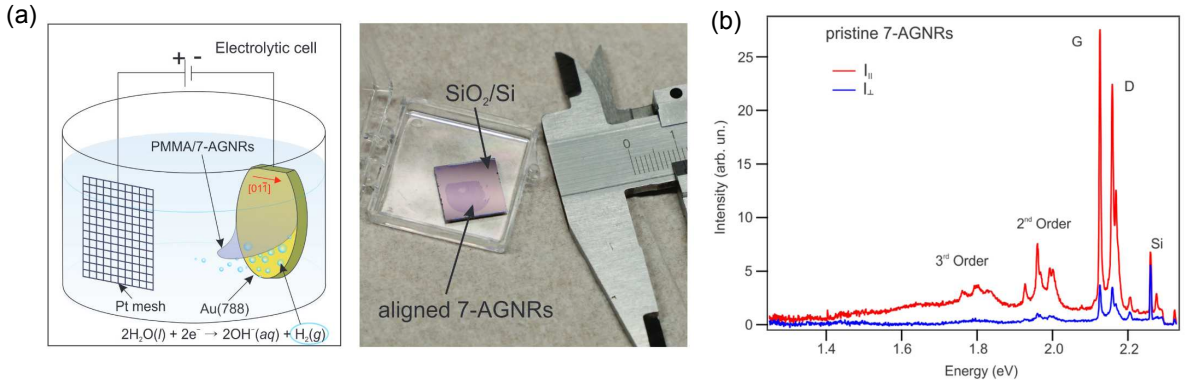

Figure 4.9: (a) - Schematic illustration of the electrochemical delamination transfer of 7-AGNR sample from a Au(788) substrate to a SiO_2/Si substrate. PMMA is used as the support layer for the transfer. (b) - PL spectra of the transferred 7-AGNRs on the SiO_2/Si substrate. Adapted from [109].

In addition to this PL measurement, we note that recently Chong *et al.* reported bright electroluminescence from the individual 7-AGNRs with specific edge structure [111]. In this paper, the authors first synthesized relatively short 7-AGNRs (∼10 nm) with zigzag shape terminus on Au surface. They then performed the dehydrogenation of the central carbon atom of the ribbon zigzag terminus (indicated by the red arrow in Fig. 4.10 - (a)). By lifting such an individual GNR with the gold-capped STM tip (see Fig. 4.10 - (b)) and applying voltage, they observed a bight and narrow band emission with energy lower than the optical bandgap of infinite 7-AGNRs (see Fig. 4.10 - (c)). Their *GW*-BSE calculations indicated that the emission is related to the electronic states localized at such specific GNR termini. This observation provides a novel way to investigate optical properties of on-surface synthesized GNRs.

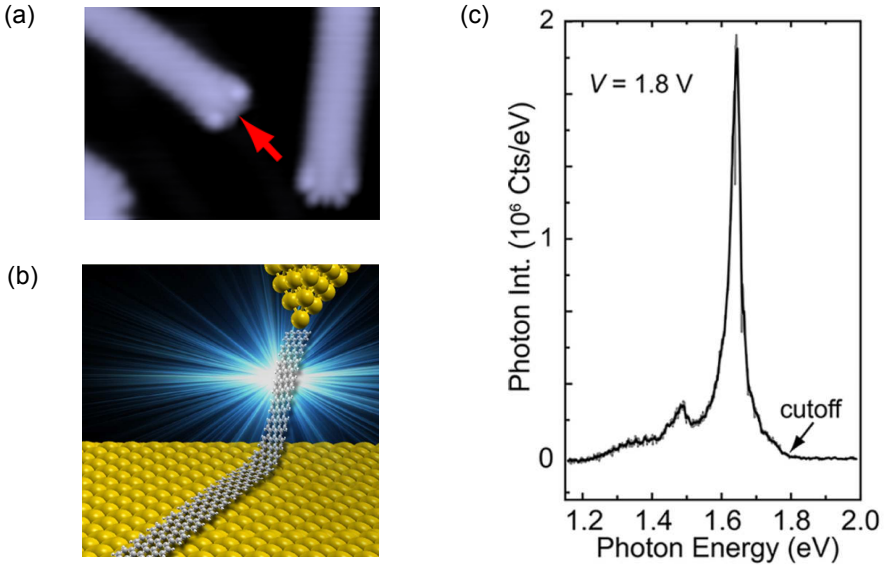

Figure 4.10: (a) - STM image of a 7-AGNR with the central carbon atom of the zigzag terminus dehydrogenated (indicated by the red arrow). The sample is on Au surface. (b) - Schematic illustration of the electroluminescence from a lifted 7-AGNR by a gold-capped STM tip. (c) - Corresponding emission spectrum. Adapted from [111].

5 Conclusion and objective of thesis

In this chapter, we have seen that by reducing the dimensionality of 2D graphene sheet in the form of 1D GNRs and 0D GQDs, it possible to open a bandgap. Moreover, theoretical calculations predicted that GNRs and GQDs display a large degree of tunability of their optoelectronic properties by controlling of the structure, e.g. a widely tunable bandgap (from semi-metallic to several eV) via the control of size and creation of spin polarized states via the control of edge structure. Now the bottom-up chemistry method could synthesize GNRs and GQDs with defined structure, making it possible to address the intrinsic properties predicted by theory. However, to date people have very little knowledge on their optical properties. In particular, as one of the key optical properties, the photoluminescence of individualized GQDs and GNRs is still not clear. If we look back on the research history of the very similar sp^2 carbon structure, carbon nanotubes (CNTs), we will find that during the first ten years after the discovery of CNTs in 1991 [112], there were very few optical characterizations of CNTs that had been reported, very similar to the present situation of GNRs and GQDs. In 2002, O'Connell *et al.* reported the efficient individualization of CNTs and the observation of the intrinsic photoluminescence from the individualized CNTs [113]. This observation can be regard as a millstone for the domain of the research of CNTs. After that, thousands of papers on the optical characterization of CNTs have been reported each year and now people have a very clear idea on the optical properties of CNTs. So, in analogy to the research progress of CNTs, in order to go deeper into the optical properties of GNRs and GQDs, it is essential to probe and study the intrinsic photoluminescence of single GNRs and GQDs, which is the main objective of this thesis. For this purpose, I present works on the solution preparation method used to dissolve and individualize in-solution synthesized GNRs and GQDs. Then I show results of optical spectroscopy measurements on their solutions, as well as the single-particle measurements by means of microphotoluminescence. In addition, the on-gold-surface synthesized GNRs are also investigated after transferring onto a dielectric substrate.

Part II

Experimental techniques

Summary

the probability of the optical transition at a given wavelength λ. Reversely, we can also calculate the concentration of the species by absorption spectroscopy, if we know its molar extinction coefficient.

When referring to an individual object, the equivalent of the molar extinction coefficient is the absorption cross-section σ. In a naïve picture, the absorption cross-section σ means that every photon passing the molecule within the area of σ would get absorbed by the molecule. The Beer-Lambert's law can then be written as [114]

$$I = I_0 \exp(-\frac{N}{V}\sigma L) \tag{1.3}$$

where N/V is the volume concentration of the absorbers (molecules). By convention, the absorption cross-section is in cm^2. Then it can be calculated from the extinction coefficient as

$$\sigma = 1000 \ln(10)\varepsilon/N_A = 3.82 \times 10^{-21}\varepsilon \tag{1.4}$$

with N_A being Avogadros constant.

1.2 Photoluminescence spectroscopy

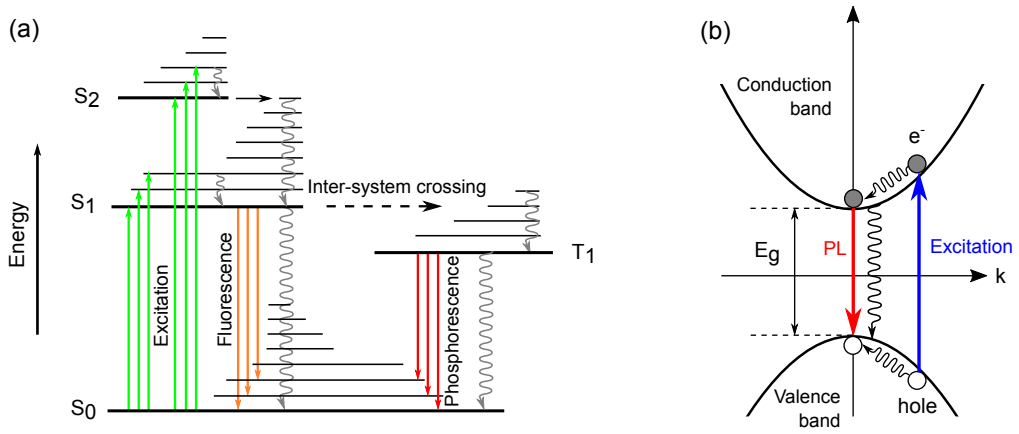

Figure 1.2: Schematic illustrations of the photoluminescence process in an organic molecule using a Jablonski diagram (a) and a bulk semiconductor using a simplified energy band diagram (b). Wavy arrows depict non-radiative processes.

The photoluminescence (PL) spectroscopy corresponds to the spectral study of the photons emitted by the sample after an optical excitation. A simplified energy level diagram (Jablonski diagram) explains the mechanism of photoluminescence in a molecule (see Fig. 1.2-(a)). The molecule is first excited, by absorbing a photon, from its singlet ground electronic state S_0 to one of the vibrational states in the excited electronic state S_1 or even higher excited states. Then it rapidly relaxes to the lowest vibrational level of S_1, which is called internal conversion. After that, the molecule drops down to one of the vibrational levels of the ground electronic state again by emitting a photon. We call this emission from the singlet state S_1 is fluorescence, in contrast to phosphorescence that is emission from the excited triplet state. For semiconductors, the process is similar, whereas their emission spectrum generally does not present vibronic structures

is fiber-coupled, we also have a good quality of the beam profile compared with the one filtered by the monochromators. When just performing simple PL measurements, several continuous-wave lasers can also be used as the excitation source: 405 nm (LBX, Oxxius), 532 nm (Sapphire, Coherent) and 635 nm (LDM, Thorlabs). The emission from the sample is dispersed by a monochromator (SP2300i, Princeton Instruments) and detected by a Peletier-cooled CCD camera (PIXIS100B, Princeton Instruments) operating at -75 °C.

1.3 Time-resolved photoluminescence

The time-resolved photoluminescence measurements can give us the dynamics of the light emission, which is not possible with the steady-state measurements. As shown in Fig. 1.2, from the excited state, molecules can generally decay either radiatively (straight lines) or non-radiatively (wavy lines) from the excited state, and decay rates are donated as k_r and k_{nr}, respectively. Suppose a sample of molecules is excited by a pulse of light with an infinitely sharp width (δ-function). This results in an initial population (n_0) of molecules in the excited state. The excited-state population will decay with a rate $k_r + k_{nr}$ according to

$$\frac{dn(t)}{dt} = -(k_r + k_{nr})n(t) \tag{1.5}$$

where $n(t)$ is the number of the excited molecules at time t following excitation. Thus, the excited-state population decay is exponential and expressed as

$$n(t) = n_0 \exp(-t/\tau) \tag{1.6}$$

In reality, we do not observe the number of excited molecules but rather the emission intensity, which is proportion to $n(t)$. Hence, the emission intensity $I(t)$ decays in the same way as $n(t)$:

$$I(t) = I_0 \exp(-t/\tau) \tag{1.7}$$

where I_0 is the intensity at zero time (upon excitation) and τ is the lifetime, which is given by

$$\tau = \frac{1}{k_r + k_{nr}} \tag{1.8}$$

Similarly, the emission quantum yield η_Q that is the ratio of the number of emitted photons to the number of absorbed photons, can be also expressed by the rate constants k_r and k_{nr} as

$$\eta_Q = \frac{k_r}{k_r + k_{nr}} \tag{1.9}$$

Thus, if the sample is mono-dispersed, we can deduced its radiative rate k_r from the measured intensity decay rate and the quantum yield, which can be independently determined by the steady-state spectroscopy [115].

For organic fluorescent molecules, the intensity decay often exhibits a mono-exponential behavior, with a lifetime between one and a few tens of nanoseconds [116]. However, in many cases, the intensity decay could be more complex. For example, the presence of aggregates may modify the relaxation pathways (either radiative or non-radiative). As a consequence, the quantum yield and the luminescent dynamics of the molecule will change [117]. Since the aggregation is inhomogeneous, the intensity decay

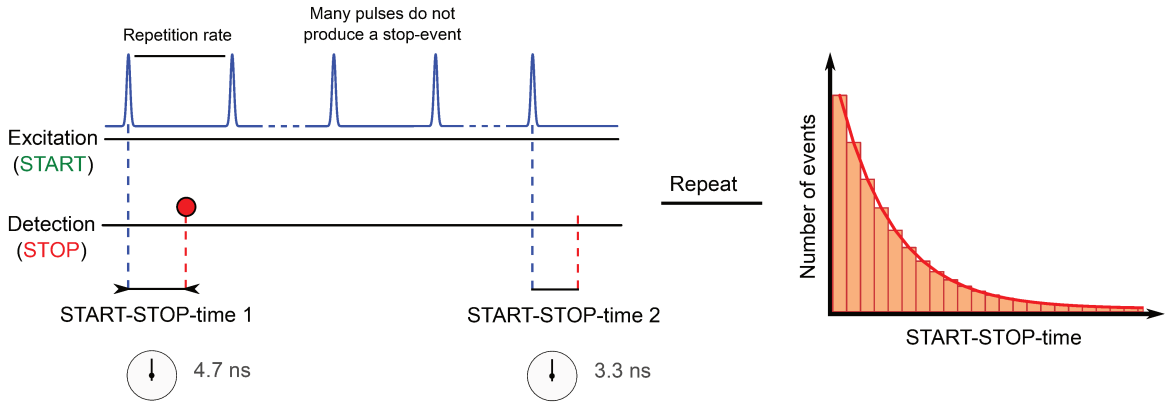

Figure 1.5: Schematic illustration for the principle of TCSPC.

In practice, we can directly determine the excited lifetime from the recorded decay curve if the lifetime τ is higher than the order of ns. However, the counter and the APD both have a timing resolution (12 ps and 40 ps, respectively), which results in a so-called time jitter and thus limits the global resolution of the measurement. If the decay curve exhibits a fast decay component, to precisely extract the dynamic information we should perform a deconvolution process between the recorded decay curve and the instrumental response function (IRF), which is the response of the instrument to a zero lifetime sample. To measure the IRF, attenuated laser pulses (scattered by an empty cuvette) are sent to the APD and then the corresponding histogram is built. Fig. 1.6 display the measured IRF of our setup at 700 nm, which possesses a very short component of 40 ps and a long component of 800 ps.

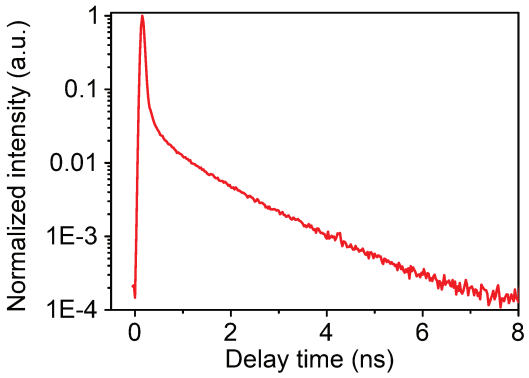

Figure 1.6: Instrument response function (IRF) of the time-resolved PL setup acquired at 700 nm.

Fig. 2.1 represents the scheme of our home-built microphotoluminescence setup based on a confocal microscope. We adapt an infinity-corrected optical system, for which we use an infinity-corrected objective. Since in this system the excitation beam and the emission beam are both collimated, it shows almost no distortion even when many different optical components or equipment are inserted onto the parallel light path. This inherent expandability gives us ample freedom to construct or modify the system in a way that meets our specific requirements.

Microscope objective In order to excite a small volume of the sample and to collect a maximum of photons, we use a high numerical aperture oil-immersion microscope objective (PLAPON 60XO, Olympus). Its numerical aperture (NA) is 1.42 with a working distance of 0.15 mm, an effective focal length of 3 mm and a magnification of ×60.

For an infinity-corrected microscope objective, the magnification of ×60 corresponds to the magnification of the object into an image formed at the focus of a tube lens of 180 mm focal length (180 mm is convention of Olympus). This means that the magnification $\mathrm{M} = 180\ \mathrm{mm}/f'_{\mathrm{obj}}$, hence an effective focal length f'_{obj} of 3 mm for this objective[7].

The focal excitation laser spot size is an important factor that determines the spatial resolution of confocal microscopy. Assuming the excitation laser beam is a Gaussian beam, which fully fills the pupil of the objective, the focal spot diameter can be expressed by the Rayleigh criteria:

$$\text{Spot diameter} = 1.22 \times \frac{\lambda_{\mathrm{exc}}}{\mathrm{NA}} \tag{2.1}$$

Thus, in our case, for NA = 1.42 and an excitation wavelength of 594 nm, we obtain a focused lase spot diameter of about 510 nm.[8]

To achieve the numerical apertures greater than unity, we use immersion oil whose refractive index is almost the same as the glass. The immersion oil must have a low level of fluorescence, because even if we do not focus directly in the oil, it is responsible for some of the parasitic fluorescence. The model of the immersion oil we used is 10976 (Fluka), which is designed to be UV-transparent and fluorescent-free. Its refractive index is 1.52. For an excitation beam of 1 mW at 405 nm that focused directly in the oil, only a few thousand photons are detected. Conversely, standard oil emits more than 10^6 photons per second under the same conditions.

Sometimes we study the samples on a non-transparent substrate (for example, silicium substrate) or a thick substrate. In this case, we use also a classical objective (MAPLON100X, Olympus). Its numerical aperture (NA) is 0.95 with a working distance of 0.35 mm, a magnification of ×100 and thus an effective focal length of 1.8 mm.

Confocal pinhole As we discussed above, the confocal pinhole can spatially reject out-of-focal-plane light, which defines the collection volume at the sample level. This volume is also called confocal volume and now we try to estimate it in our case. Fig. 2.2

[7]For more detail see https://www.microscopyu.com/microscopy-basics/infinity-optical-systems.

[8]This formula considers the beam with a homogeneous intensity distribution. Actually, the resulting size for a Gaussian beam should be slightly larger.

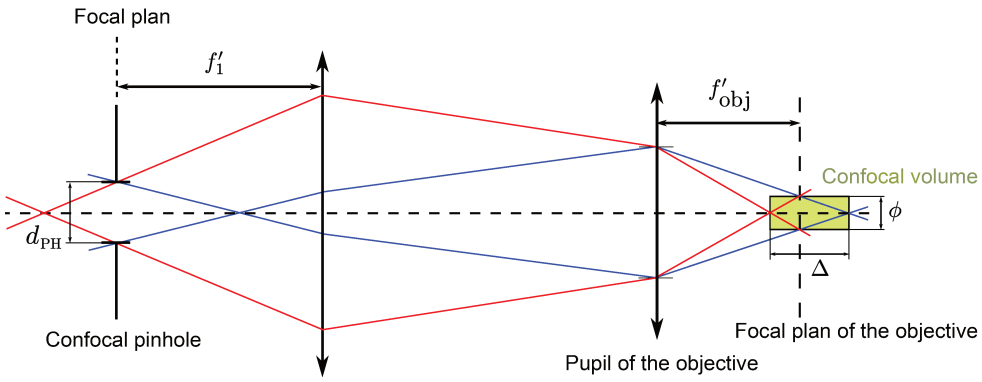

Figure 2.2: Schematic illustration of the principle of confocal pinhole using geometrical optics.

represents the relation between the confocal pinhole and the confocal volume using geometrical optics. For simplicity of the calculation, we can consider the confocal volume as a cylinder with a diameter ϕ and a height Δ (called depth of field). We can easily see that the diameter ϕ is given by

$$\phi = d_{\mathrm{PH}} \times \frac{f'_{\mathrm{obj}}}{f'_1} \tag{2.2}$$

with d_{PH} the diameter of the confocal pinhole, f'_{obj} the focal length of the objective and f'_1 the focal length of the lens in front of the confocal pinhole. Then, as a first approximation, the depth of field Δ can be expressed as

$$\Delta = \frac{\phi}{\mathrm{NA}} \tag{2.3}$$

In our setup, we use a pinhole of $d_{\mathrm{PH}} = 50$ µm and the focal length of the lens in front of the pinhole is 100 mm (AC-254-100 B, tholabs). Thus, we obtain the confocal volume V:

$$V = \frac{\pi\phi^2}{4} \times \Delta = \frac{\pi \times (1.5\ \mu\mathrm{m})^2}{4} \times \frac{1.5\ \mu\mathrm{m}}{1.42} \approx 2\ \mu\mathrm{m}^3 \tag{2.4}$$

when the oil immersion objective is used. This value is in the same order of the excitation laser spot size (diameter $2w_0 = 510$ nm and Rayleigh length $z_{\mathrm{R}} = \frac{\pi w_0^2}{\lambda} = 1.6$ µm). Therefore, we collect only the light coming exactly from the place that is excited by the laser.

Excitation 4 continuous-wave diode lasers operating at 405 nm, 532 nm, 594 nm and 635 nm, respectively can be used to excite the sample at different wavelengths. The supercontinuum coupled with the AOTF can also be used here for the pulsed excitation. Each laser line has a telescope system that collimates and expands the beam to cover the whole pupil of the objective[9]. A pinhole can be optionally added as the spatial filtering. In addition, we also put a clean-up filter on the optical path of each laser line to spectrally purify the excitation beam and thus eliminate the unwanted

[9]pupil diameter $\approx 2 \times \mathrm{NA} \times f = 2 \times 1.42 \times 3$ mm ≈ 8 mm.

laser background for detection. An optical polarizer/half-wave plate system controls the polarization of the excitation beam conserving a constant power. The polarizer used here is a Glan-Taylor prism (Thorlabs), which has high polarization purity (more than 100:1) and high damage threshold. Finally, a variable neutral density filter is put just in front of the dichroic mirrors to control the excitation power. The dichroic mirror for each laser line is mounted on a locking magnet base. We can thus easily switch the excitation source. Tab. 1 shows the model of the dichroic mirror and the emission filter[10] for each excitation laser line. The corresponding transmission curves are shown in Fig. 2.3. The data are measured using the optical absorption setup presented previously.

Laser	Dichroic mirror	Emission filter
LBX 405, Oxxius	DCLP436	BLP01-405R, Semrock
Sapphire 532, Coherent	LaserMUX552, Semrock	RazorEdge532, Semrock
Mambo 594, Cobolt	ZT594rdc, Chroma	FEHL600, Thorlabs
LDM 635, Thorlabs	ZT640rdc, Chroma	BLP01-635R, Semrock

Table 1: Laser sources and corresponding dichroic mirrors and emission filters

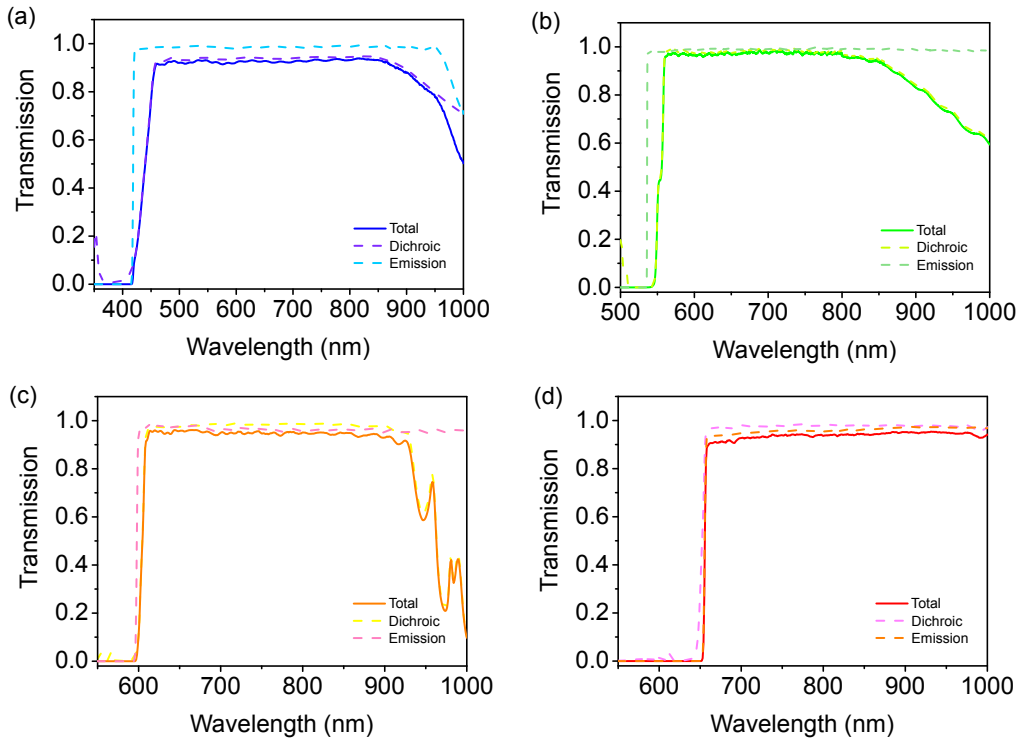

Figure 2.3: Transmission curves of filter sets for each laser line: (a) - 405 nm, (b) - 532 nm, (c) - 594 nm and (d) - 635 nm. Transmission curve for each dichroic mirror and emission filter is in dashed line and their total contribution is in solid line.

Collection We use two types of detectors: On the one hand, avalanche photodiodes allow us to measure photon fluxes to realize the optical scanning, and moreover to perform the photon correlation measurements. On the other hand, a CCD camera permits

[10]The emission filter in the detection path serves to block the residual excitation laser and transmit the emission from the sample.

us to measure the photoluminescence spectra. The switch between the two detection systems is realized by a flip mirror.

Avalanche photodiodes (APDs): the model of the two APDs that we used here is PerkinElmer SPCM-AQRH-13. It delivers a TTL pulse (0-5 V) when detecting a photon. This detector has a typical temporal resolution of 350 ps and a relatively low dark counts (about 200-300 counts/s). Its dead time after detection of a photon is typically 50 ns. The detection efficiency is defined as the overall probability to deliver a TTL pulse for one incident photon. For the photon at 650 nm, its detection efficiency is about 70 % and for the photon at 950 nm, it still has an efficiency of 25 %.

Charged-coupled device (CCD) camera: At the beginning of my thesis, the set-up was equipped with a PIXIS 100 (Princeton Instruments) coupled with a 150 mm focal length monochromator (SP2150i, Princeton Instrument). The aperture ratio (f-number) of the monochromator is 3.9 and the beam is focalized into the monochromator with a 50 mm achromatic lens[11]. The CCD camera is cooled down to -75 °C by Peltier effect. Concerning the sensibility, this CCD camera is able to resolve the spectrum of emission with a lower intensity limit of 5 000 counts/s on the APD. In this thesis, all the measurements on graphene nanoribbons are performed using this Peltier-cooled camera.

We received a new liquid-nitrogen-cooled CCD camera (PyLoN-100BRX, Princeton Instruments) at the end of the second year of my thesis. This CCD camera is operated at -120 °C and coupled with a 300 nm monochromator (SP2300i, Princeton Instruments) with silver coated optics. It has low electronics noise and high quantum efficiency over the range of 400–1000 nm. Compared to the Peltier-cooled camera, the quantum efficiency is enhanced about 5 times and we can resolve the spectrum of emission with a lower intensity limit of 1000–2000 counts/s on the APD. Moreover, since the focal length is longer, we have also less deformation of the spectrum on the edge CCD pixels.

To analyze the polarization of the emission beam, we use an achromatic half-wave plate/optical polarizer (Glan-Taylor prism) system. By fixing the polarizer and turning the half-wave plate, we can resolve the polarization of the emission beam. Since detectors always have their intrinsic polarization response, in this way, the response of detector does not affect the measured polarization diagram.

Scanning system In order to perform the optical mapping of the sample, we can scan the sample by moving the focal laser spot. To realize this, the microscope objective is mounted on a xyz piezoelectric scanner (Nano-PDQ, Mad City Labs). This scanner allows a motion range of 50 µm for all the xyz directions with a sub-nm resolution (0.1 nm). It is controlled by a Labview program via an acquisition card (PCIe-6323, National Instruments), which also serves as the counter of TTL impulsions from the APDs[12]. Thus, with the same Labview program, we can do the positioning of the laser spot, scan the sample and record the intensity trace with a minimum bin width of 1 ms. Moreover, when we want to do a long acquisition on a stable photoluminescent objet, a tracking subprogram can help us to overcome the mechanical and thermal drifts of the

[11] determined by the relation: f-number = focal length/beam size.

[12] The signal from the two APDs is firstly sent to an electronic box to do the sum. Then the output (sum of two APDs) is sent to the National Instruments module. This electronic box can also do the copy of the input signal, thus we can monitor the correlation measurement using the Labview scan program.

setup. It is a control loop of the photoluminescence intensity by random displacing the spot in xyz directions with a small step.

Estimation of the total collection efficiency In the previous paragraphs we have described our microphotoluminescence set-up. We can now give a rough estimate of its overall collection efficiency.

The collection angle of the objective (one-half angular aperture) θ is determined by the numerical aperture of the objective:

$$\mathrm{NA} = n \sin\theta \tag{2.5}$$

Thus the collection efficiency of the objective is the ratio between the solid angle corresponding to θ and 4π sr (entire sphere):

$$\eta_c = \frac{1}{4\pi} \int_0^\theta 2\pi \sin\alpha \; d\alpha = \frac{1-\cos\theta}{2} \tag{2.6}$$

For the oil immersion objective, NA=1.42 and n=1.52. We thus obtain the collection efficiency η_c=33%.

Once the light is collected, it is also necessary to take into account the propagation efficiency of the light through the different optical elements and also the detection efficiency of the APDs. For a beam at 650 nm, their contributions are listed as follows:

- transmission of the objective: 90%
- reflectance of the mirrors: 96% × 96%
- transmission of the dichroic mirror: 98%
- transmission of the beamsplitter of the HBT: 95%
- transmission of the optical filters (emission filter + IR filters (HBT)): 98% × 90%
- transmission of the lenses: 98% × 98% × 98%
- detection efficiency of the APD: 70%

Thus we obtain the upper limit of the overall collection efficiency of our microphotoluminescence setup $\eta_{tot} \approx 15\%$[13].

[13]The values listed here are theoretical designed values from constructor. In practice, we may have more losses and moreover, during the optical path there are also some aberrations. Thus the estimated collection efficiency should be the upper limit.

2.2 Second-order photon correlation measurements

In order to perform the second-order photon correlation measurements, a single detector is needed. However, every detector has a dead time - a time during which it cannot detect a second photon after the detection of the first one. As this dead time is much higher than the typical characteristic time of anti-bunching for most emitters, resolving the anti-bunching using one detection is impossible. To contour this problem, a two detectors configuration is commonly used. The Hanbury-Brown and Twiss (HBT) interferometer was designed by the two eponymous astronomers, in order to record intensity correlations between stars [120]. Even though it was not its primary goal, this configuration is now widely used to assess if a light emitter behaves as a single-photon source.

Principle of HBT interferometer and "start-stop" method

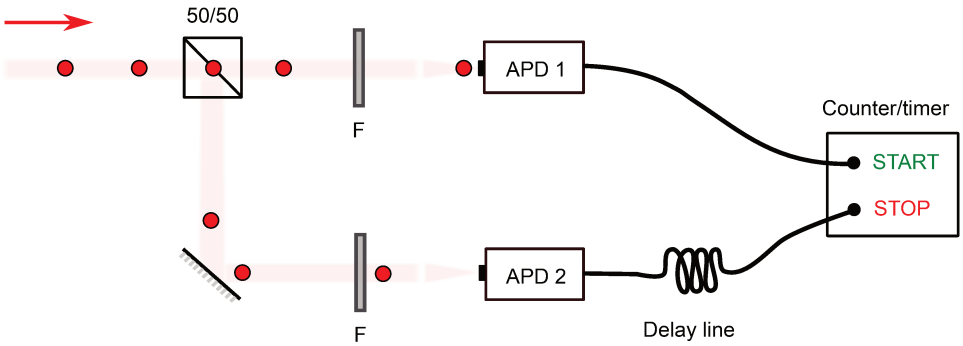

Figure 2.4: Schematic illustration of the HBT setup.

As shown in the Fig. 2.4, the setup of HBT interferometer is made of a 50/50 beamsplitter and two APDs in photon counting regime used to detect the light from our confocal microscope. The two APD detectors emit a TTL impulsion when they detect a photon. Then a so-called start-stop method is used to measure the second-order photon correlation function $g^{(2)}(\tau)$.

The start-stop method is based on the TCSPC, which is similar with the lifetime measurement (see Sec. 1.3). The signal from the two APDs is sent to the START channel and the STOP channel, respectively, of a counter/timer (Picoharp 300[14]). As shown in the Fig. 2.5 - (a), when a photon is detected by the APD 1, the START channel starts timing and then when a photon is detected by the APD 2, the STOP channel stops the timing. The time elapsed between the START and the STOP is then recorded: it is the time delay τ. In practice, a variable resistance is added between the APD 2 and the counter to introduce a time delay. This enables us to arbitrarily shift the position of the zero delay (in our case, the zero time delay between two photons is tuned at 260 ns on the counter). The experiment then runs during a time sufficiently long to build a histogram $K(\tau)$ of the delays (see Fig. 2.5 - (b)).

The $K(\tau)$ reflects the probability density that the next photon is recorded at time t provided that there was a photon at t_0. If the emitter is actually a single photon emitter,

[14] An inverter and an attenuator of 50 Ω should be connected with the module.

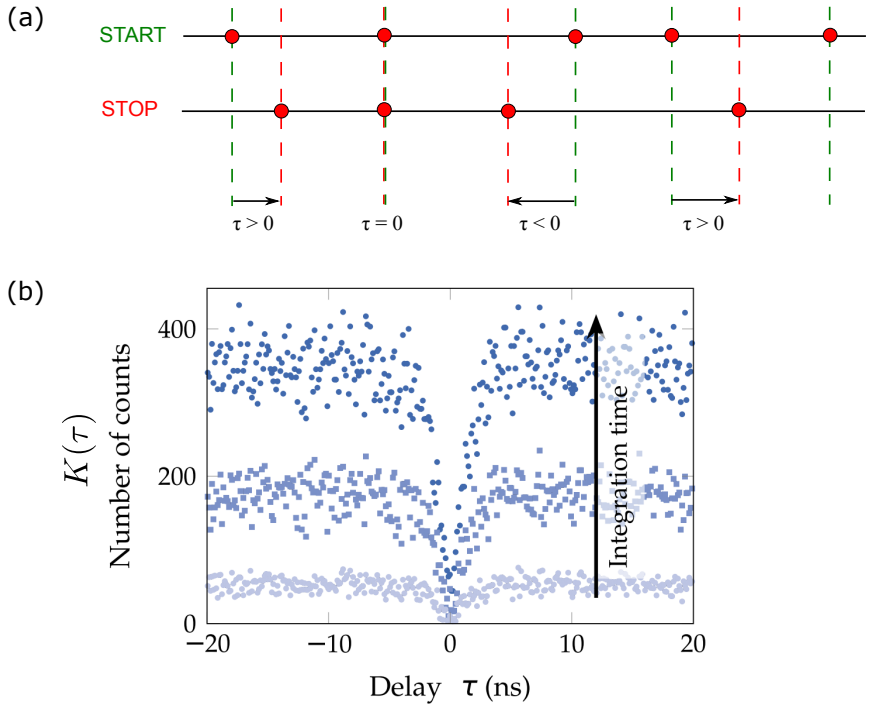

Figure 2.5: Principle the HBT setup.(a) - "start-stop" method enables to measure the delay between two consecutive single-photon detections. (b) - A histogram of $K(\tau)$ of the time delay τ is built. The figure here shows the evolution of this histogram when the integration time increases. The data are taken from [121].

it can emit only one photon at a time. We thus expect a dip at zero time delay of the histogram, reflecting the fact that two single photons emitted one after the other are at least separated temporally by duration of the order of its excited state lifetime.

By a first approximation [122], the $g^{(2)}(\tau)$ function can be obtained by a proper normalization of $K(\tau)$ histogram. As for a Poissonian source the value of $g^{(2)}$ is always equal to 1. The normalization process is thus to compare the studied light source with a Poissonian source of the same average intensity. Under continuous excitation, the relation between the $g^{(2)}(\tau)$ function and the recorded photon coincidence $K(\tau)$ is [122]

$$g^{(2)}(\tau) = \frac{K(\tau)}{R_1 R_2 T w} \tag{2.7}$$

with $R_{1,2}$ the count rates on each APD, T total integration time and w time bin width. Here the factor $R_1 R_2 T w$ corresponds to the coincidence rate for an equivalent Poissonian photon number distribution with the same count rate on the two detector. We note that this relation between $K(\tau)$ and $g^{(2)}(\tau)$ neglects any contribution from random background light emission.

In an ideal case, the value of $g^{(2)}(0)$ associated with N single-photon emitters is given by [123]

$$g^{(2)}(0) = 1 - \frac{1}{N} \tag{2.8}$$

Thus, in general, $g^{(2)}(0) < 0.5$ is the criteria for a single quantum emitter[15].

[15]In very rare cases, two emitters with different count rates could also lead to $g^{(2)}(0) < 0.5$.

Crosstalk phenomena

Here we use silicon avalanche photodiodes as single photon detectors because of their low dark count rate and high quantum efficiency. In order to detect efficiently single photons, the diode is reversely biased above breakdown voltage. When a photon arrives, it triggers a discharge and a current but also a luminescence signal called after-pulse. As shown in Fig. 2.6 [124], the emission of the APD ranges from 700 nm to 1000 nm, which falls in the same spectral range of most single-photon emitters.

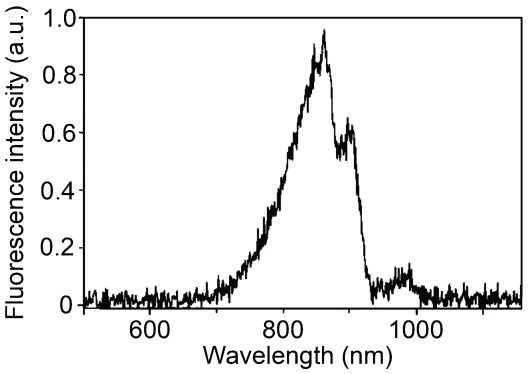

Figure 2.6: After-pulse emission spectrum of a typical avalanche photodiode, taken from [124].

This after-pulse emission is quite weak, but if the APDs are not carefully optically decoupled, this emission can be reflected by the beamsplitter and detected by the other APD. Thus the recorded histogram contains a number of detection events which are not related to the emission from the studied object. Fig. 2.7 presents a recorded coincidence histogram from a Poisonnian light (laser scattering by the substrate) with a 15 kcount/s count rate on each APD. We can clearly observe two non-negligible peaks on both sides of zero time delay with a characteristic time of about 10 ns due to the crosstalk phenomena.

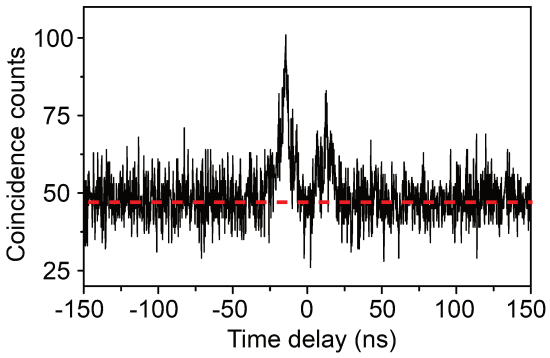

Figure 2.7: Influence of the after-pulse emission on the coincidence measurement of our setup.

The probability of getting a crosstalk count on one APD is proportional to the count rate in the other. As a consequence, the total crosstalk count rate is proportional to the sum of the count rates of both APDs. Since the coincidence rate is proportional to the

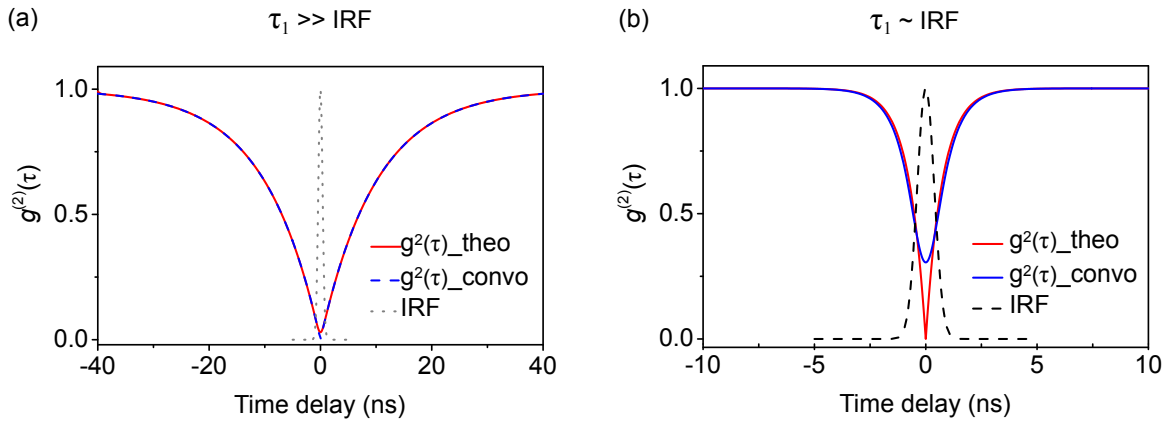

Figure 2.9: Influence of the instrument response function on the measured correlation function. (a) - The case when anti-bunching characteristic time τ_1 is significantly higher than the width of the IRF. (b) - The case when τ_1 and the width of the IRF are of the same order of magnitude.

As shown in the Fig. 2.9 - (b), the measured correlation function is deformed at the proximity of the zero time delay and the corresponding value of $g^{(2)}(0)$ becomes evidently higher than zero.

In practice, we measured the IRF by sending attenuated pulses of supercontinuum to our HBT setup. The resulting coincidence histogram is then fitted by a Gaussian function with FWHM = 0.9 ns (Fig. 2.10). A precise analysis of the measured correlation function can then be done by performing a deconvolution process.

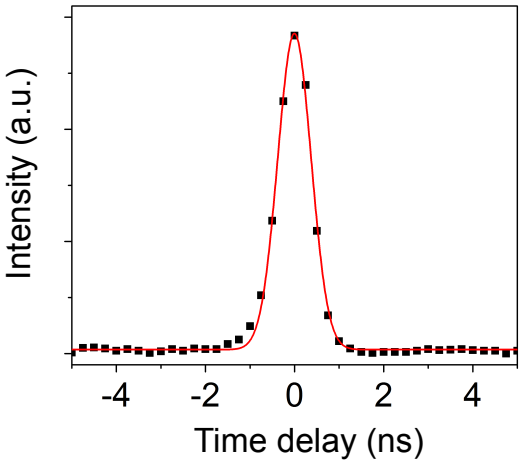

Figure 2.10: Measured instrument response function (IRF) of our HBT setup. Data is fitted by a Gaussian function with FWHM = 0.9 ns. Time bin width: 0.25 ns.

HBT under pulsed excitation

We can also perform the correlation measurement under pulsed excitation. In this way, the anti-bunching signature will not be affected by the time jitter of the detectors.

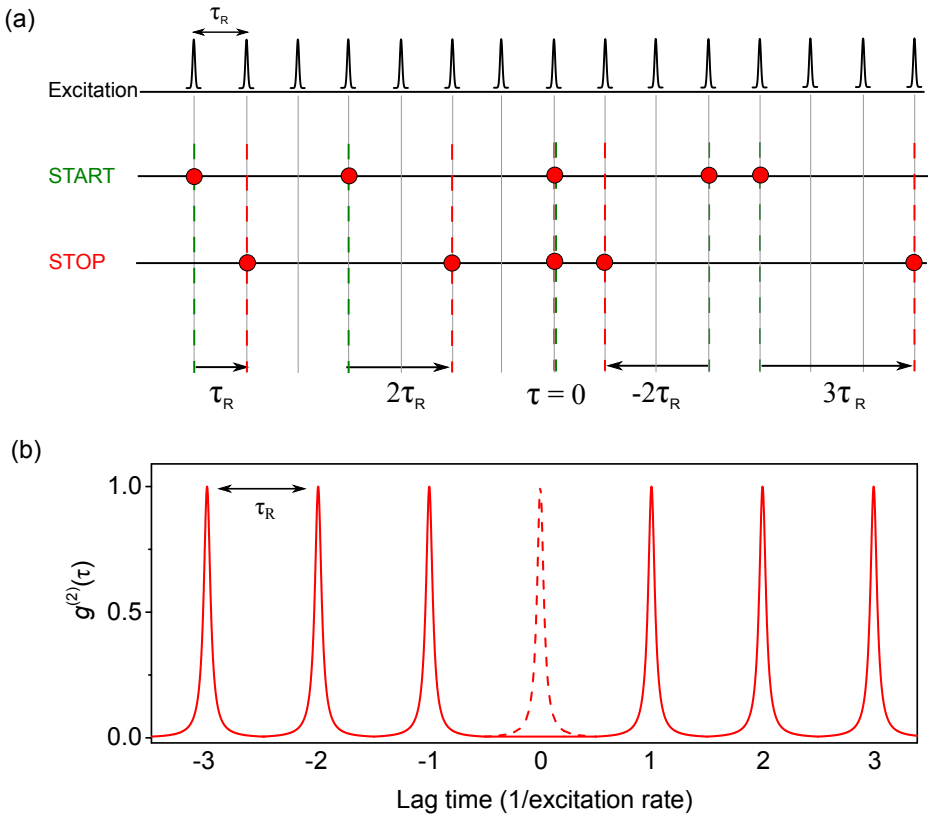

Figure 2.11: (a) - Schematic illustration for the principle of the "start-stop" method under pulsed excitation. (b) - Resulted auto-correlation function under pulsed excitation. A series of peaks are separated by the repetition period τ_R of the excitation laser (in our case, $\tau_R = 16.7$ ns for the supercontinuum). The central peak (dashed line) disappears for a single-photon source.

As shown in Fig 2.11 - (a), the principle is as follow: When the emitter is illuminated by a sufficiently intense excitation pulse, at least one photon is absorbed. It leads to the emission of either zero photon (non-radiative decay), one photon (anti-bunching) or several photons (no anti-bunching). Regarding the HBT setup, if a photon arrives on the START channel, either a photon arrives on the STOP channel from the same excitation pulse or the photon arrives with a later excitation pulse (the two photons are separated by m times the repetition rate of the laser, with m an integer). This means that the auto-correlation signal under pulsed excitation is composed of a series of peaks[16] and separated by the repetition period of the excitation source (see Fig. 2.11 - (b)). Anti-bunching is marked by the vanishing of the peak at zero delay, which means that it never happens that the same excitation pulse leads to the emission of more than one photon for a single-photon emitter. Thus, it does not depend on the resolution of the detectors and can drop down to zero for a perfect single-photon emitter.

In practice, to obtain the $g^{(2)}$ function and estimate the quality of a single-photon emitter, normalization on the peak area (total photon counts within the peak) should

[16]The peaks can be fitted by double-side exponential functions with a decay constant determined by the excited lifetime of the emitter and the timing resolution of the APDs.

be performed. The $g^{(2)}$ value associated with peak m is obtain as

$$g^{(2)}(m) = \frac{c(m)}{R_1 R_2 T \tau_R} \tag{2.11}$$

with $c(m)$ the total number of coincidence counts of the peak m, R_1 and R_2 the count rates of the two detectors, T the total acquisition time and τ_R excitation laser repetition period.

Similar to the case of using continuous excitation, if the normalized central peak area is less than 0.5, it implies that the measured signal originates from a single quantum emitter[17].

Correlation measurements with "start-record" method

A detailed photon statistics study using the second-order correlation measurement can give us insight into the photophysical properties of the emitter [126]. However, at longer time scales, the "start-stop" method, which measures the coincidence histogram $K(\tau)$, no longer delivers the second order correlation function $g^{(2)}(\tau)$. Indeed, if the time delay is too high, the counter will have a high probability of being stopped before this delay is reached. The coincidence histogram thus presents an exponential decaying envelop with a characteristic time R^{-1}, where R is the photon count rate on the detector [122,127]. As a consequence, the "start-stop" method is limited to correlation measurements at very short time scales compared with R^{-1}. Fig. 2.12 presents this significant deviation from the equivalence between the measured $K(\tau)$ of a Poissonnian light ($R = 25$ kcounts/s) and the corresponding $g^{(2)}(\tau)$ that should be equal to 1.

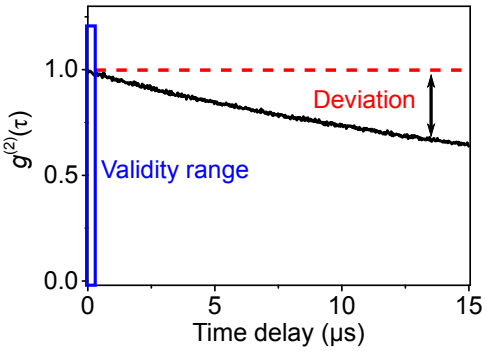

Figure 2.12: Inequivalence between the normalized coincidence histogram (black line) and its auto-correlation function (red dotted line) at long time scale.

In order to mesure the second-order correlation function $g^{(2)}(\tau)$ over a long time delay, here we use the HBT setup to rather measure $J(\tau)$ – the histogram of photons detected at time t provided that a photon is detected at time $t = 0$. To record $J(\tau)$, the two APDs are connected to a wide-range time digitizer (P7887, FastComtec). When a photon is detected on APD 1 (START channel), it triggers an acquisition on the APD 2 (RECORD channel) to record arrival time with respect to the START event of each

[17] Without considering the intensity fluctuation, the area of the central peak can be simply normalized to the area of a side peak.

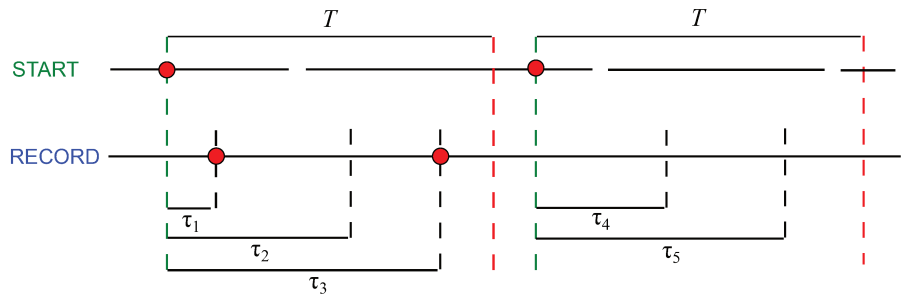

Figure 2.13: Schematic illustration of the "start-record" method to measure the correlation function. A detection event on the START channel triggers an acquisition sequence on the RECORD channel, which records the photon arrival times with respect to the START event of this sequence. The duration of the sequence T is adjustable.

detected photon over a time T. After time T, the RECORD channel stops record and waits for another detection event on START channel to trigger again the record. Over N repetitions of the measurement, the resulting histogram $J(\tau)$ is directly linked to the $g^{(2)}(\tau)$ function through [122]

$$g^{(2)}(\tau) = \frac{J(\tau)}{NwR_2} \tag{2.12}$$

where w is the time bin width and R_2 is the photon count rate on APD 2. Fig. 2.13 schematically illustrates the principle of this so called "start-record" method.

Using this method to mesure the photon correlation function is first proposed and experimentally validated by Huang *et al.* [127]. In this paper, the authors used this method to measure the correlation of a pseudo-thermal light source, which displays a long time scale bunching behavior. Moreover, this method has been also applied to study the single-photon emission from defects in h-BN crystal by Martinez *et al.* [128], suggesting that the "start-record" method can also be used without limitation at short time scale (< 50 ns).

2.3 Time tagged time-resolved (TTTR) measurements

Our PicoHarp 300 module possesses another measurement mode called time-tagged time-resolved (TTTR). The TTTR mode records the arrival time of all photons relative to the beginning of the experiment. A large "First In First Out" (FIFO) buffer is used in this mode to avoid data overflow when photon count rates are high. PicoHarp 300 actually supports two different time-tagging modes, T2 and T3 mode.

T2 mode In T2 mode both START and STOP channel of PicoHarp 300 are functionally identical. That means the detection events from the two channels are recorded independently and treated equally. A recorded event contains information about the channel it came from and the arrival time of the event with respect to the overall measurement start. Dead times exist only within each channel with a typical value of 90 ns,

but not across the channels. With T2 measurement mode, it allows us to analyze the photon statics of the emitter in a variety ways. we can plot the intensity time trace with time bin width down to microsecond. Furthermore, from the obtained time trace, we can also calculate the long-time scale $g^{(2)}(\tau)$ function for lag times τ larger than the dead time. The $g^{(2)}$ function is thus obtained by employing its classical definition (intensity auto-correlation function):

$$g^{(2)}(\tau) = \frac{\langle I(t)I(t+\tau)\rangle}{\langle I(t)\rangle^2} \tag{2.13}$$

with $I(t)$ the photon counts of the bin at time t in intensity time trace. In this way, we can also calculate the cross correlations. As the two channels are independent, for cross correlation functions the lag time can be down to zero.

Moreover, from the recorded time-tags we can build the histogram of the waiting time between successive photon detection events, which also allow us to analyze the photon statics. In fact, for a Poissonian light source the waiting time should obey exponential distribution with the characteristic parameter (time) equal to the inverse of count rate [122]. A multi-exponential behavior of the waiting time distribution implies the existence of intensity fluctuation for a quantum emitter [129](due to either energy transfer from the local environment or passage to the metastable state).

T3 mode In this mode one channel is the signal channel and the other one is the sync channel which is connected to a periodic excitation laser. The main objective of T3 mode is to allow high sync rates which could not be handled in T2 mode. As in conventional TCSPC, this mode performs a picosecond timing between START photon and STOP photon. In addition, it records the arrival time of the photon with respect to the overall experiment time. In contrast to T2 mode, this time-tag is not directly measured. It rather measures the start-stop timing difference between the photon event and the last sync event and it determines which sync period the photon event belongs to. Since the sync period is known precisely, the arrival time is then reconstructed. T3 mode is very useful in lifetime measurements. For instance, it allows us to record the intensity time trace and corresponding real-time fluorescence lifetime, which is very useful in single-molecule measurements. Furthermore, in this mode the measurement can be extended to contain markers for synchronization information derived from an imaging device (for example a piezo scanner). In this way, it allows us to perform lifetime imaging.

2.4 Atomic force microscope

Developed in the 1980s by the IBM researchers in Zurich, the atomic force microscopy (AFM) can be used to image nanoparticles with nanometric spatial resolution [101]. Since its birth, this technique has developed rapidly and today, high performance AFM microscopes are available commercially. The device used here is a commercial AFM system (MFP3D standalone, Asylum Research), which has been used to characterize non-linear crystals and nanodiamonds by the former PhD students [130, 131]. We use silicon tips (AC160TS, Olympus) to perform the imaging in tapping mode (also called intermittent contact or dynamic contact). During scanning, the cantilever of the tip is driven to oscillate up and down at its resonance frequency $f \approx 300$ kHz by a piezoelectric crystal. This oscillation is optically detected by recording the deflection of a laser beam

is 80 μm wide. The inverted configuration of the objective makes it possible to perform AFM and optical measurements simultaneously if we use a transparent substrate. To realize this, it is important to align precisely the AFM tip with the spot of the excitation laser. The imaging system of the AFM permits us to visualize the sample surface at the proximity of the tip and to do the alignment. As we can see in the 2.14 - (b), the sample surface is illuminated by a fiber white light. Turning the micrometric screws can move the AFM tip relative to the objective. It is also possible to move the objective relative to the AFM tip using the piezo mounted with the objective. When the AFM tip and the spot of the excitation laser are superimposed, the diffraction of the excitation laser beam by the AFM tip can be observed. This simple procedure provides AFM and optical system alignment with accuracy of a few hundred nanometers. Once this alignment has been achieved, the scan can be performed by moving the sample with the xy piezo stage of the AFM system and we obtain topographic and optical images on the same zone of the sample (Fig. 2.15).

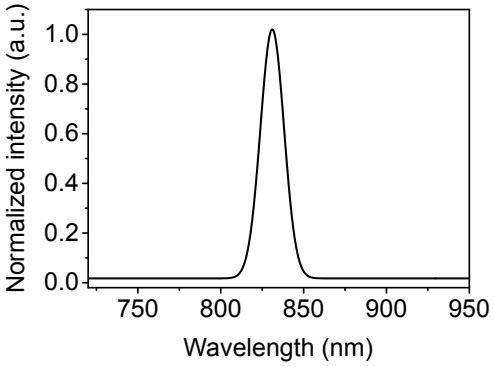

Figure 2.16: Emission spectrum of the diode laser used for AFM measurements.

Nevertheless, this AFM combined with optics system has two restrictions. The emission wavelength of the diode laser used to illuminate and detect the deflection of the cantilever is $\approx$ 800 nm (See Fig. 2.16). When we want to perform the optical measurement at the same time, it needs to eliminate this signal by adding an optical filter on the detection path. So we also lose a part of optical signal from the sample due to the additional filter. Another restriction in the present configuration is that when we use the oil immersion objective, the objective touches the sample. It is not a stable configuration for the AFM measurements. As a result, vibration patterns can be clearly observed on the AFM image. Thus, in practice, after the alignment of the two systems, we first performed the optical measurement with the diode laser off. Then we retract the objective and switch on the diode laser to perform the AFM measurement.

3 Sample preparation

3.1 Suspension preparation

The produced GNRs and GQDs via in-solution approach are under a powder form in which they stacks together due to strong π-π interactions. To perform optical measurements we need to break apart the aggregates and solubilize these nano pieces of graphene.

GQDs in organic solvents Previous optical spectroscopy studies on hexabenzocoronene [132] and STM measurements on unsubstituted $C_{132}H_{34}$ GQDs [80] have demonstrated that 1,2,4-trichlorobenzene (TCB) is a very efficient solvent to individualize molecular graphenes. Inspired by these results, we utilized TCB as the solvent for our GQDs. TCB has a relatively low polarity with a high density (1.46 g/cm^3), a high boiling point (214.4 °C) and low volatility. However, as ultrasonication can promote oxidative degradation of the organochlorine compound (termed sonochemical degradation) [133], TCB becomes yellow and intensely fluorescent (broad band in visible as seen in Fig. 3.1) just after several minutes of mild sonication using ultrasonic bath.

Considering the degradation of TCB, we adapted the following protocol to dissolve GQD particles: First, a small quantity of GQD powders is added into a vial of spectroscopy grade TCB solvent (256412, Sigma-Aldrich) to reach approximately a concentration of 0.1 mg/mL. The vial is sealed with parafilm. Then sonication using ultrasonic bath (Brancion) for 30 s is applied to break big particles. After that the solution is stirred (magnetic stirring at $\approx$ 600 rpm) for at least 24 h. The obtained stock solution is diluted by $\times$10 with stirring for another 24 h. In the same way, the dilution $\times$100 is obtained from the dilution $\times$10.

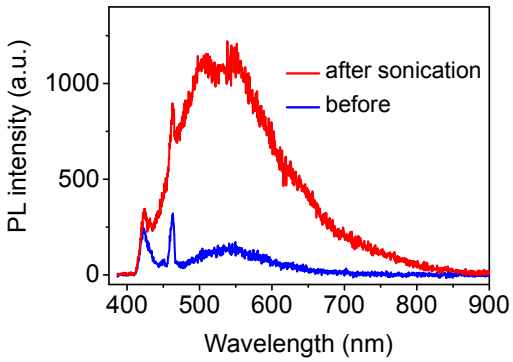

Figure 3.1: PL spectra of TCB solvent before (bleu line) and after 10 min of sonication using ultrasonic bath (red line). The peak at 463 nm present in both spectra is the Raman line of TCB. Excitation wavelength: 405 nm. Excitation Power: 300 µW. Acquisition time: 1s.

GNR micellar suspensions At first, we tried to disperse the GNRs into organic solvents such as TCB and NMP (the installement of side alkyl chains is for enhancing the solubility in organic solvents). However, as the solubility of GNRs decreases with

increasing of the length, it seems that the GNR dispersion might have been "fractionated", where only shorter and more soluble GNRs could be brought into the dispersion while longer and less soluble GNRs remained inside the particles. This "fraction" effect when using organic solvents has been put in evidence by our chemistry collaborators in Mainz: The average length of the produced GNRs has been estimated to be several hundreds of nm by measuring the length of polyphenylene precursors with laser light scattering experiments. In contrast, the STM measurements of GNRs by deposition from organic solvents show an average length of only several tens of nm [65,82]. The produced GNR powders could contains a very small quantity of shortest GNR dimers and trimers (as shown by the MALDI-TOF mass spectrum in Chap. I Fig. 4.1 - (d)), which have very high fluorescence quantum yield, high band gap and also good solubility in organic solvents. Due to the "fraction" effect, the contribution from these dimers and trimers is amplified and the observed PL signal of GNRs in organic solvent is dominated by a intense band in the blue region.

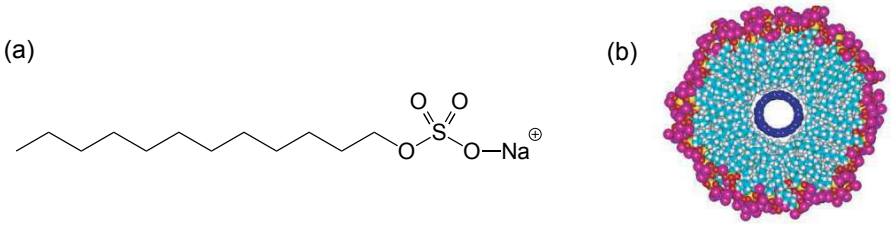

Figure 3.2: (a) - Chemical structure of sodium dodecyl sulfate (SDS). (b) - Schematic representation of SDS molecules around a carbon nanotube forming a micelle, taken from [113].

Besides organic solvents, another way to solubilize nanoparticles is using surfactants, for which we are not expected to show the preference to the lenght of GNRs. One mostly used surfactant is sodium dodecyl sulfate (SDS). As shown in Fig. 3.2 - (a), SDS molecules are amphilic, which means that they contains both hydrophobic groups (their tails) and hydrophilic groups (their heads). Indeed, the first true isolation of carbon nanotubes was achieved in aqueous suspension of this surfactant by O'Connell *et al.* in 2002 [113]. They performed ultrasonic agitation of raw nanotubes powders in presence of SDS. Upon strong sonication, SDS molecules forms a protective shell (micelle) around the nanotube with the hydrocarbon tails pointing toward the nanotube walls and the ionic heads connecting with water molecules (Fig. 3.2 - (b)). Thus, the SDS micelle prevents nanotube from re-aggregation and also eases the solubilization. As GNRs have the similar structure to carbon nanotubes, one would expect that SDS could also form micelles to solubilize GNRs. Moreover, as SDS do not degrade under sonication, we can perform strong tip sonication to mechanically break apart the aggregates. For these reasons above, we used SDS to prepare GNR suspensions.

The preparation protocol of GNRs in SDS micelles suspension is present as follows: We first prepare a 2 wt% suspension of SDS surfactant agents (L6025, Sigma-Aldrich) into a pH = 8 borate buffer (10^{-2} mol/L). We then add a small quantity of GNRs powders to reach a concentration of $\approx$ 0.1 mg/mL. Placing the sample into a 10 °C thermostatic water bath, a strong tip sonication (100% amplitude) is applied for 1h30. Finally, to remove larger aggregates and undispersed particles we perform a centrifugation of

2 min at 14 800 rpm and take the supernatant. The obtained GNR suspension is stable (without visible particles) from a few days or a few weeks depending on the type of GNR structures.

3.2 Spin coating

For the single-object level study using microPL set-up, the studied objects should be immobilized (avoid Brownian diffusion) and spatially individualized (single object per optical spot). A deposition technique called *spin coating* is thus used. As shown in Fig. 3.3 - (a), it consists in putting a drop of the solvent on a substrate and spin this substrate very quickly (usually $>$ 10 rotations per second = 600 rpm). The majority of the solution is flung off the side. The centripetal force combined with the surface tension of the solution pulls the liquid coating into an flat covering. During this time the solvent evaporates to leave the desired objects on the substrate in an homogeneous covering. The speed of the spinning and the concentration of the solution are the two parameters that one can adjust to tune the density of objects.

At first, we directly spin-coated our GQDs in TCB solution onto the glass coverslip. However, the photoluminescence was very weak and blinking a lot. There are two possible reasons that can affect the photoluminescence of GQDs: 1. Oxygen and atmospheric water could react with GQDs and open efficient channels for photobleaching. 2. Due to its planar and mono-layer structure, interactions with the substrate could be very strong and the GQDs could be very sensible to the local environment (i.e. local charge fluctuation). In order to reduce these perturbations (protect from oxygen and water, and disrupt the interaction with the substrate), one method is to embed GQDs in a polymer matrix (Fig. 3.3 - (b)). Indeed, this method has been demonstrated to be very effective in enhancing the photoluminescence properties of carbon nanotubes [134, 135].

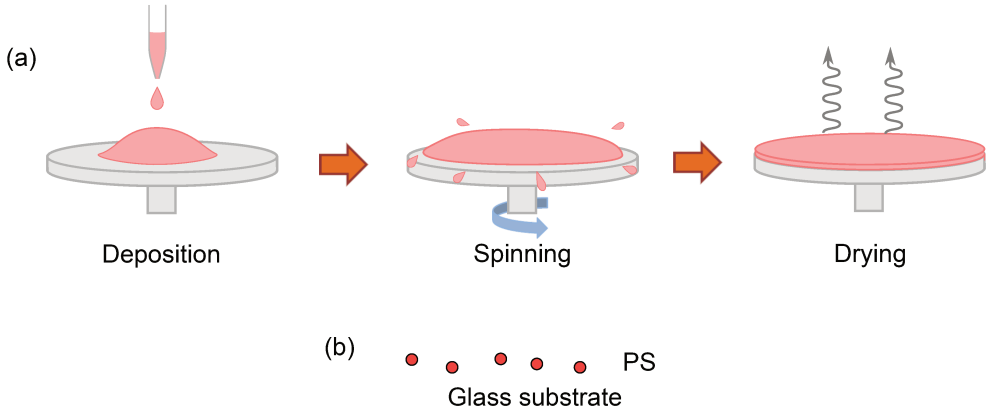

Figure 3.3: (a) - Schematic illustration of spin-coating. (b) - Schematic illustration of GQDs embedded in a polystyrene (PS) matrix.

Here we use the polystyrene (PS) (Sigma-Aldrich) as the host matrix. The procedure to prepare the sample for microPL measurements is as follow: Firstly, glass coverslips (Schott Nexterion) are treated by oxygen plasma for 5 min to remove organic contaminations on the surface, which could be fluorescent and disturb our optical measurements. PS grains are dissolved in TCB by heating at 40 °C for 1 h for a concentration of

5 wt% (0.075 mg/mL). 2 mL GQD solution is then mixed with 2 mL PS solution under ultrasonic bath for 10 s. Approximately 20 µL of the GQD-PS-TCB mixture is then spin-coated on the glass coverslip at 2000 rpm for 180 s.[18] The sample is dried by heating to 90 °C for 1 h on a hot plate. We thus obtain a film of PS with GQDs embedded in it. The PS film thickness has been measured by profilometry[19]. It turns to be in the order of 25 - 50 nm.

[18]To obtain good coverage we use dynamic dispense method. That means we dispense the solution after the substrate have reached its desired rotational speed. Moreover, when dropping the solution, we only use pipettors to the first stop in order to avoid additional drops or bubbles being cast onto the surface. As TCB has very high boiling point, we set a long spin coating duration to ensure that the sample is fully dried. A detailed guide on spin coating is in `https://www.ossila.com/pages/spin-coating#dynamic-dispense-spin-coating-technique`.

[19]This measurement is performed in the clean room of ENS Cachan

Part III

Optical study of bottom-up synthesized GNRs

Summary

Introduction

Graphene nanoribbons (GNRs) have attracted much attention as good candidates for the next-generation of semiconductor materials. As we have already seen in the first Chapter, GNRs have strong assets as we can engineering most of their properties (gap energy, electronic band structure, optical selection rules, magnetic order, etc...) via their structure [94,95,136,137]. In the past few years, solution-mediated [60,65,68] and surface-assisted [18, 77, 138] bottom-up chemical synthesis have been shown to produce GNRs that, unlike the one obtained via top-down fabrication [139, 140], possess a uniform width and a precise edge periphery. Moreover, since the structure of GNR produced by this approach is defined by the precursor monomers, it gives us access to a wide range of different graphene nanoribbon structures. The electronic and transport properties of bottom-up synthesized GNRs have been intensively studied, revealing finite band gaps that nicely confirm the theoretical predictions [83,86,141]. Nevertheless, the information on the optical properties especially the photoluminescence (PL) are still unexplored. For this reason, we decided to study the optical properties on the bottom-up synthesized GNRs in collaboration with the synthesis group at MPIP, Mainz led by Dr. Akimitsu Narita and Prof. Klaus Müllen and the group at EMPA, Dübendorf led by Dr. Pascal Ruffieux and Pr. Roman Fasel.

In the first section of this chapter, I will show the spectroscopy results on two different GNR structures synthesized via the solution-mediated method. I will then discuss the nature of the observed emission. Some possible approaches to individualize GNRs will be proposed. In the second section, I will present our studies on the effect of strain on the optical properties of GNRs. Combing experimental and theoretical results, modulation of the bandgap of GNRs by controlling over the structural distortion is demonstrated. In the third section, I will present our optical characterizations of GNRs synthesized by the on-surface approach. Since the grown metal surface is not suitable for the PL measurements, I will first describe the transfer procedure to an insulated substrate. Then I will present the microPL and AFM results on the transferred sample. We will discuss the nature of the unexpected broad emission at high-energy region. Finally, some distinct Raman features observed on GNRs will also be discussed.

1 Optical study of solution-mediated synthesized GNRs

1.1 General sample information

GNRs samples studied here were synthesized by the group of Dr. Akimitsu Narita and Prof. Klaus Müllen at Max Planck Institute for Polymer Research in Mainz. As we seen in Chap. I Sec. 3.2, the longitudinally extended GNRs were synthesized through the solution-mediated intramolecular oxidative cyclodehydrogenation of tailor-made polyphenylene precursors. The produced GNRs are in powder form with defined width and edge structure[20], in contrast to carbon nanotubes (CNTs), which are unavoidably

[20]The structure was supported by Fourier transform infrared (FTIR), Raman, solid-state nuclear magnetic resonance (NMR) spectroscopies.

obtained as a mixture of different diameters and chiralities [142].

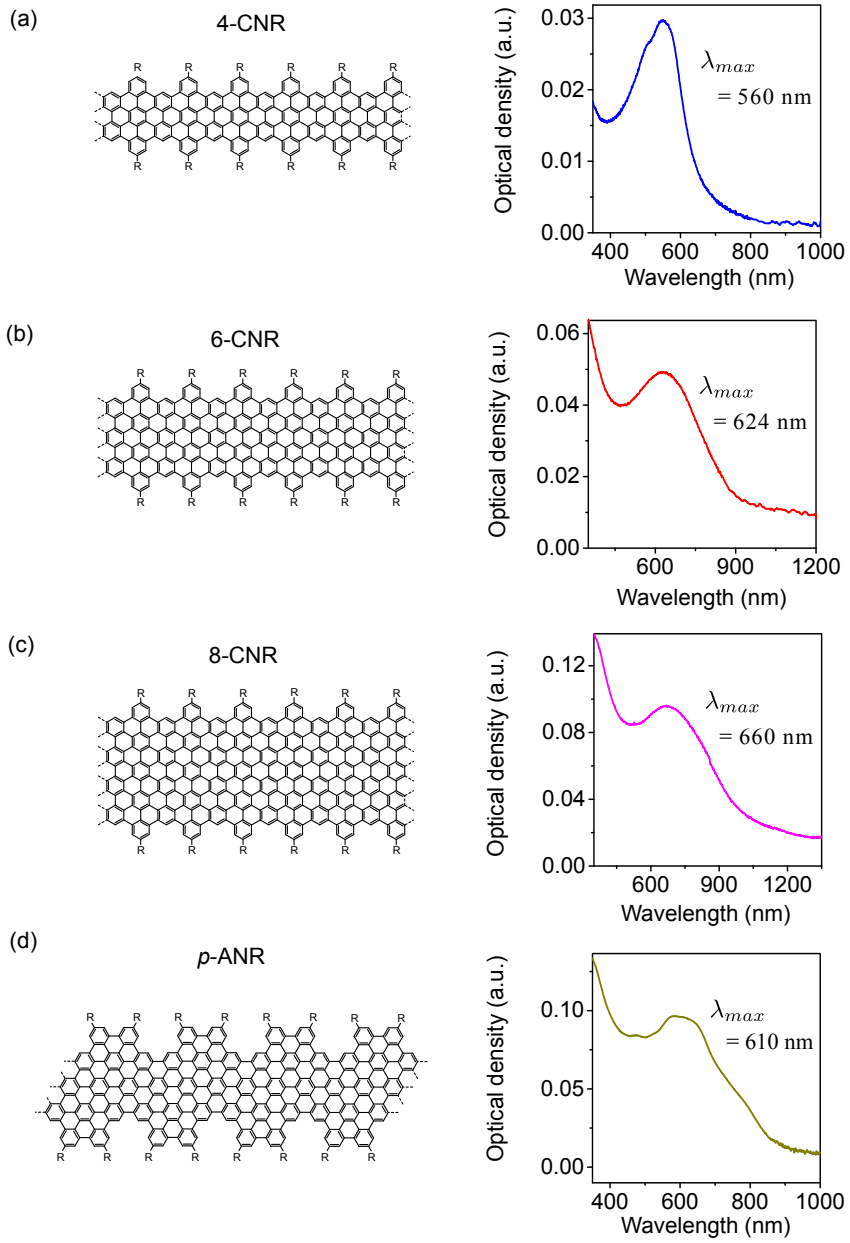

Figure 1.1: Chemical structure of different GNR structures and corresponding optical absorption spectra in SDS micelle. "R" stands for a -$C_{12}H_{25}$ (dodecyl) chain.

Fig. 1.1 shows the GNR structures that we possess and the corresponding optical absorption spectra. Unlike the GNRs synthesized via top-down method [140], here the bottom-up synthesized GNRs show distinct absorption lines, suggesting that the transition are intrinsic to the GNR structure. As the band gap of semiconducting GNRs originates from quantum confinement, the value of the gap generally decreases when the width of GNRs becomes larger [31]. Moreover, Yang *et al.* [143] predict that the value of quasi-particle band gap E_g of GNRs shows an inverse relation with the width w:

$$E_g = \frac{a}{w + w_0} \tag{1.1}$$

where a and w_0 are two constants[21]. This relation is very similar to the case of single-wall

[21]Depending on the family that GNRs belong to, the values of a and w_0 would be different

carbon nanotubes (SWNTs). For SWNTs, when drawing the optical transition energy as a function of their diameter d_t (the well-known Kataura plot), we can roughly find a $1/d_t$ relation which is predicted by the tight-binding model [144, 145]. Inspired by this, we plot the energy of the first optical transition of the GNR structures as a function of their width in order to compare with the predicted $E_g \propto \frac{1}{w+w_0}$ relation (Fig. 1.2). Here the energy of the first optical transition of each GNR structure is obtained from the wavelength at the maximum of the absorption spectrum. Since the width of GNR presented here are modulated, we employee rather the effective width defined as the weighted average of the different widths composing the unit cell of GNR [85]). The red curve in Fig. 1.2 is the fit using the inverse relation described by Eq. 1.1. We can see that the trend of optical transition energy obtained from absorption spectrum follows well the inverse relation.

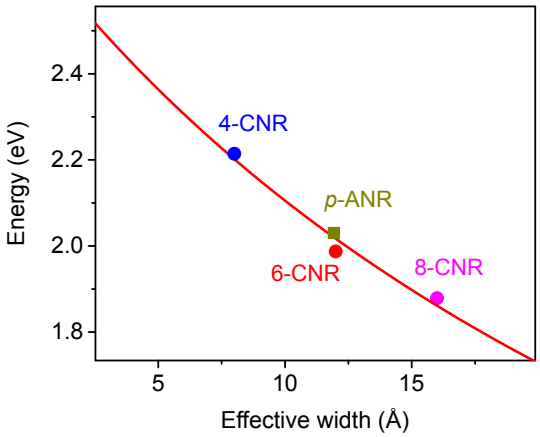

Figure 1.2: The first optical transition energy as a function of the effective width of GNRs. The optical transition energies are obtained from the wavelength of the maximum in absorption spectrum. The red curve is the fit using the inverse relation (Eq. 1.1).

1.2 Optical spectroscopy on 4-CNR and *p*-ANR suspensions

We now go into details of the optical properties of 4-CNR and *p*-ANR, which have different edge structures and widths. The 4-CNR, described on Fig. 1.3 - (a), has a structure based on $N = 4$ zigzag edge GNRs, where N stands for the number of carbon atoms across the nanoribbon. In addition, benzo-fused rings are regularly added on the edges to make all the elctrons paired [65]. It thus forms a "cove"-type edge configuration that leads to a semiconducting nanostructure with a visible optical band gap [94]. The *p*-ANR ("*p*" stands for "*para*") is based on a $N = 9$ armchair GNR with partially extended edges having the width a of $N = 15$ armchair GNR at the widest (see Fig. 1.3 - (b)) [69]. This GNR geometry is expected to have a near-infrared gap [94]. For both two GNR structures, alkyl groups (-$C_{12}H_{25}$) are regularly installed on the edges in order to improve the solubility.

In order to perform optical measurements, GNRs were dispersed in water with 2%wt of sodium dodecyl sulfate (SDS) by tip sonication (> 2 h, 100% amplitude) with a concentration of 0.1 mg/mL and followed by centrifugation (3 min at 14.4 krpm). The supernatant was then taken to perform the optical measurements. The experimental set-up used here is described in Chap. II Sec.II.

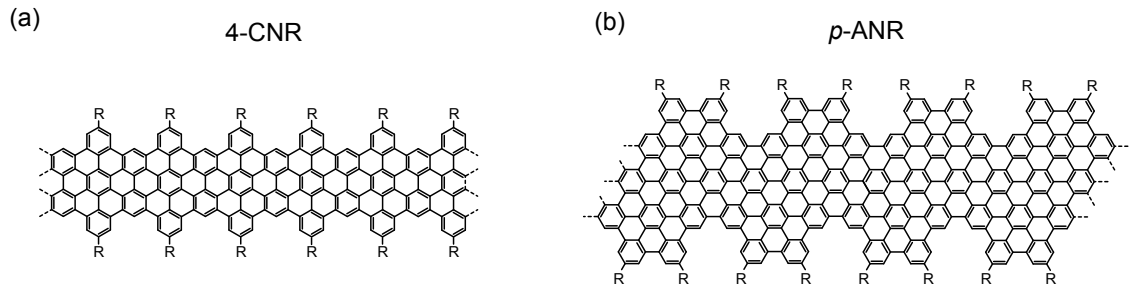

Figure 1.3: Chemical structure of 4-CNR (a) and *p*-ANR (b). "R" stands for a -$C_{12}H_{25}$ (dodecyl) chain.

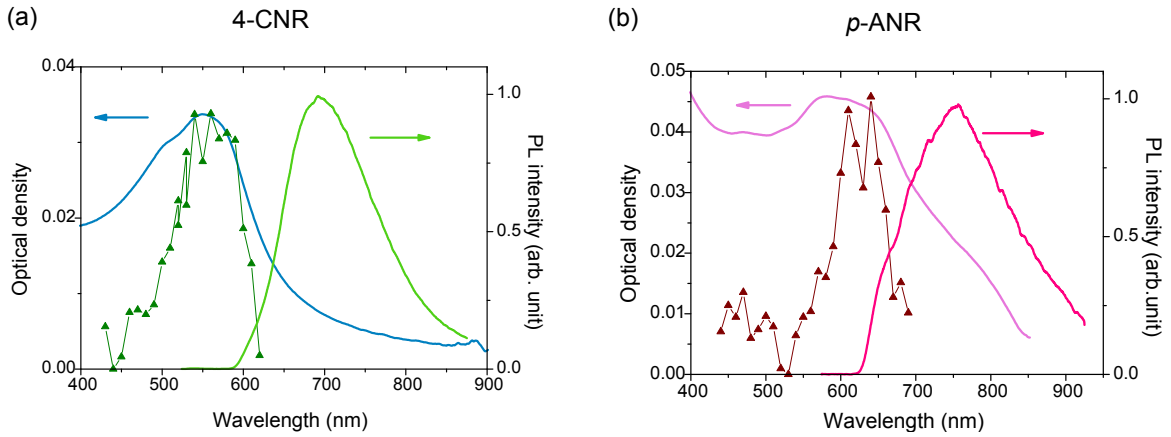

Figure 1.4: Optical absorption spectra, photoluminescence and photoluminescence excitation spectra (triangles) of 4-CNR (a) and *p*-ANR (b) in SDS suspensions. The PLE spectra are recorded at the maximum of each PL line.

The blue curve in Fig. 1.4 - (a) shows the absorption spectrum of the 4-CNR suspension in SDS micelles.[22] An absorption band centered at 560 nm (∼2.21 eV) with a small shoulder at 505 nm (∼2.45 eV) is observed, in good agreement with previous reported results in organic solvents [65, 105]. In Ref. [105], an *ab initio* calculation using GW approximation[23] plus Bethe-Salpeter equation (GW + BSE) approach were performed to calculate the optical response of free-standing 4-CNRs.[24] Such method could include both electron-electron and electron-hole interactions, which are known to dominate the electronic and optical properties in one-dimension systems [146]. From Fig. 1.5 - (a), we can see that the simulated optical response using GW-BSE approach (blue arrows) well reflects the measured absorption spectrum. As indicated in the band structure in Fig. 1.5 - (b), the first optical transition arises from the excitonic transition between

[22] We have also dispersed 4-CNR in sodium cholate (SC) micelle, N-Methyl-2-pyrrolidone (NMP) and 1,2,4-triclorobenzene (TCB). The optical spectra are generally the same form with slight peak position variance due to the solvatochromisme effect and also peak width variance, which is presumably attributed to different levels of GNRs aggregation.

[23] "G" and "W" stand for "Green's function" and "screened interaction", respectively.

[24] This theoretical study is conducted by Prof. Deborah Prezzi and Prof. Elisa Molinari's group at University of Modena and Reggio Emilia, Italy.

the last valence and second conduction band (E_{12}) and the second optical transition is between the next to last valence and first conduction bands (E_{21}). By comparing the oscillator strength of these two transitions, we can clearly see that the lowest optical transition of 4-CNRs is dominated by the E_{21} transition. Moreover, according to the calculations, the excitons in 4-CNR are tightly bound with a binding energy of ∼1.5 eV.

Besides the value of transition energies and the oscillator strength, another important optical property is the selection rules of 4-CNR to the polarization of light. The optical response simulated here is for the light polarized along the GNR length direction, while the light polarized perpendicular to the ribbons would not be efficiently absorbed.[25] This is due to the fact that for nearly-1D materials strong depolarization effects along the perpendicular direction could suppress the absorption [147, 148].

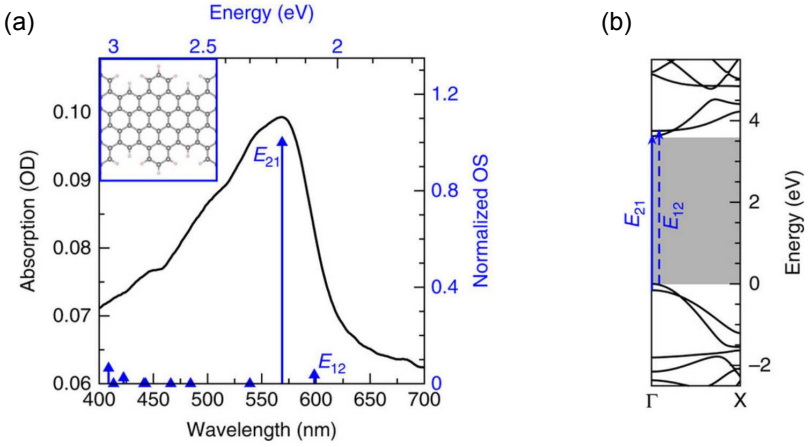

Figure 1.5: (a) - Calculated optical response of H-passivated 4-CNR using GW + BSE approach. The blue arrows indicate the calculated energy position and oscillator strength. The experimented absorption spectrum is shown in black line. Inset: chemical structure of 4-CNR. (b) - GW quasi-particle band structure of 4-CNR. Adapted from [105].

We now look at the emission properties of 4-CNR. The green curve in Fig. 1.4 - (a) shows the photoluminescence (PL) spectrum of 4-CNR suspension. We can see that its PL line is broad, structureless, and centered at 695 nm (∼1.78 eV). The difference between the maximum of the absorption and PL bands represents an apparent Stokes shift of ∼135 nm (∼470 meV). The full width at half maximum (FWHM) is ∼105 nm (∼330 meV). The values of the Stokes shift and of the FWHM will be discussed later in Sec. 1.3. Moreover, we also performed the photoluminescence excitation (PLE) measurement on 4-CNR. The PL spectrum does not change its form when varying the excitation wavelength (Fig. 1.6 - (a)). The green triangles in Fig. 1.4 - (a) display the PLE spectrum detected at the maximum of the emission. We can see that the PLE is in good agreement with the absorption band, confirming that the observed Stokes shifted luminescence arises from 4-CNRs.

Likewise, we also performed the measurements on p-ANR suspensions, which has a larger width and strongly curved edges compared to 4-CNR (see Fig. 1.3 - (b)). The

[25] This information on the selection rules of 4CNR was obtained via a private communication with Prof. Prezzi.

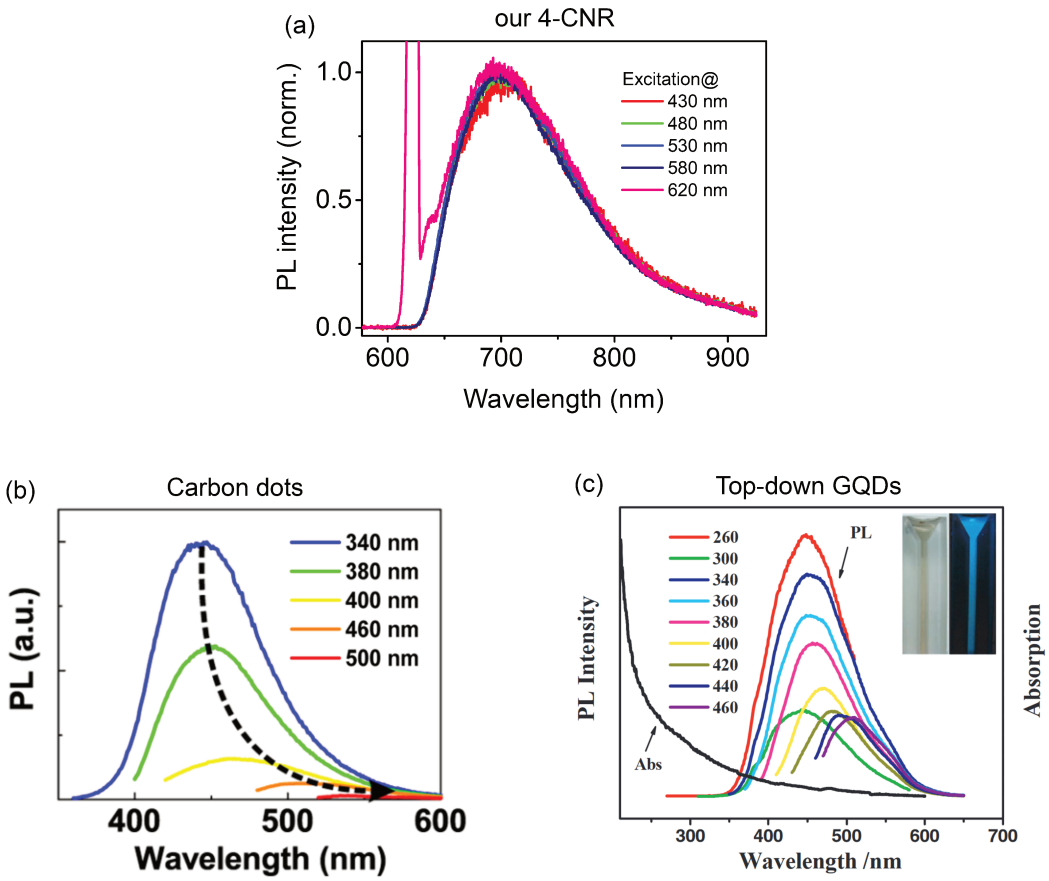

Figure 1.6: (a) - Normalized PL spectra of our 4-CNR suspension excited with different wavelengths. The peak at 620 nm originates from the excitation laser. (b) - PL spectra of a suspension of carbon dots with different excitation wavelengths. Adapted from [149]. (c) - PL spectra of a suspension of top-down fabricated graphene quantum dots (GQDs) with different excitation wavelengths. Adapted from [150]. We can clearly see a redshift when increasing excitation wavelength for carbon dots and top-down GQDs, while the PL spectrum of 4-CNRs remains unchanged, implying the intrinsic nature of the emission from 4-CNRs.

purple curve in Fig. 1.4 - (b) displays the optical absorption spectrum of the *p*-ANR suspension. The absorption band is red-shifted in comparison with the one of 4-CNR, with a maximum at ∼610 nm. This redshift is in agreement with the fact that *p*-ANR is larger than 4-CNR, which leads to the more delocalized π electrons. As for 4-CNR, the PL of *p*-ANR is broad (FWHM 170 nm (∼360 meV)) with a large Stokes Shift of 145 nm (∼400 meV). Likewise, the PLE spectrum shows that the maximum of PL efficiency is obtained for an excitation in resonance with the maximum of the absorption band.

Finally, time-resolved photoluminescence (TR-PL) measurements were performed on these two GNR structures. Results are displayed on Fig. 1.7 together with the impulse response function (IRF). For 4-CNR (Fig. 1.7 - (a)), the PL decay is slightly longer than the IRF of the setup (∼70 ps). The signal is fitted by the convolution of the measured IRF and a bi-exponential decay with a fast time component of the order of few ps and a long time component of ∼5 ns (blue curve). Similarly, for *p*-ANR (Fig. 1.7 - (b)), the TR-PL shows also a multi-exponential decay behavior with a more pronounced signal

at long time than on 4-CNR. The bi-exponential decay fit gives a short time of few ps and a long time of ∼5 ns (purple curve).

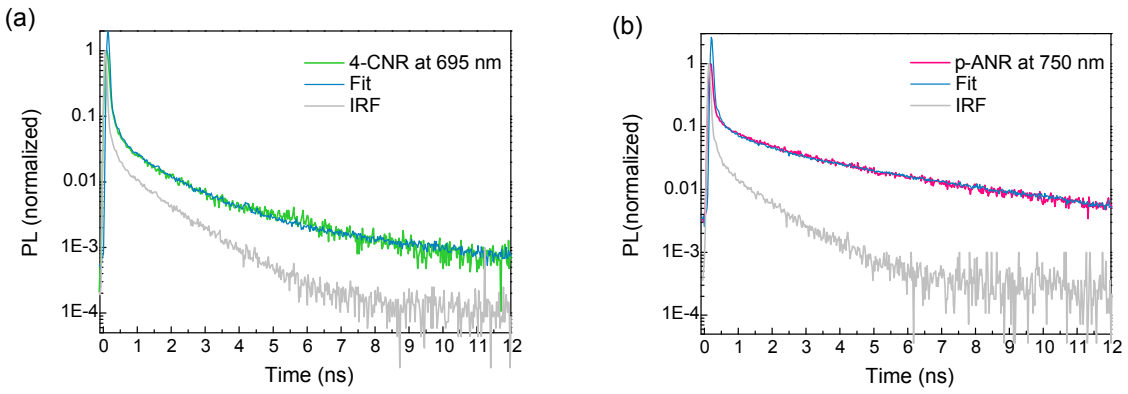

Figure 1.7: Time-resolved PL measurements on 4-CNR (a) and *p*-ANR (b) recorded at the maximum of each PL line. Both curves are fitted by the convolution between the corresponding IRF and a bi-exponential decay.

In order to get insight into the origin of theses multi-exponential decay, we performed the time-resoled PL measurements as a function of the excitation power. Indeed, it is known that some multi-exciton effects could occur when increasing the pumping intensity and these non-linear effects will alter the observed decay kinetics. For instance, a two-exciton interaction process named as exciton-exciton annihilation, in which one exciton recombines to the ground state and the other either dissociates into a free e-h pair or is promoted into a higher energy level, has been observed in some other confined systems such as 1D semiconducting SWNTs [151], conjugated polymers [152] and also 2D monolayer MoS_2 [153]. Indeed, Soavi *et al.* [105] have investigated this effect in 4-CNRs by means of femtosecond transient absorption spectroscopy. In this paper, the authors report that exciton-exciton annihilation occurs at fluences of the order of few hundreds of $\mu J.cm^{-2}$ and this process is ultrafast, dominating the time-resolved response in the first picoseconds. However, for our time-resolved PL setup, such short time scale is not accessible and the maximum pumping fluence is evaluated to be $\sim 1\ \mu J.cm^{-2}$ per pulse (in our case, the supercontinnum laser has 60 MHz repetition rate with a power of 3 mW and a large focused spot of $\sim 2.5\ mm^2$). This value is about two order of magnitudes lower than in the measurements by Soavi *et al.*. Thus, as shown in Fig. 1.8, we do not observe any variation of the photoluminescence decay on 4-CNR when varying the excitation power.[26] These results confirm that multi-excitonic processes do not influence the dynamics in our experimental conditions. Thus, we can say that the observed multi-exponential decay behavior does not originate from the multi-excitonic processes in 4-CNRS and one reasonable explanation is the contribution of different objects with different dynamics.

[26]Since the signal of the long decay component is very weak, the background could deform a lot the decay curve at long time scale. Thus, all the decay curves displayed here are subtracted from the background contribution (acquisition under the same experimental conditions but blocking the excitation laser or just taking off the sample).

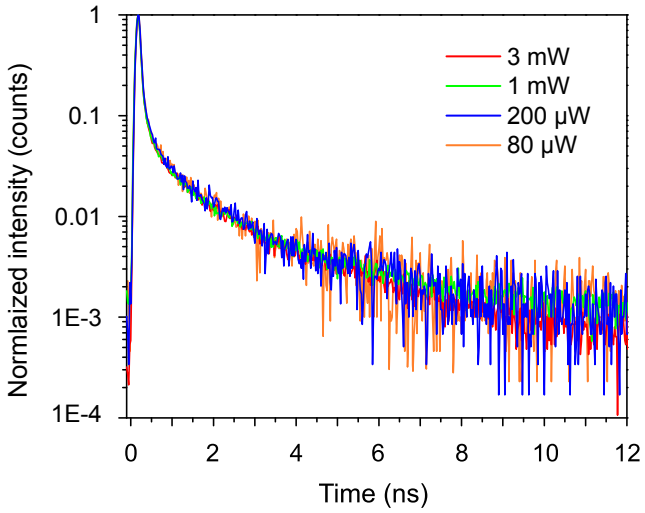

Figure 1.8: Time-resolved photoluminescence decay on a 4-CNR suspension with different excitation powers.

1.3 Discussion on the origin of emission

We now discuss the nature of the emission of these two GNR structures. First, the PL of 4-CNR and *p*-ANR share the similar behaviors: broad emission, large Stokes shift and multi-exponential decays. These observations differ significantly from what have been observed on other 1D carbon nanostructures. For instance, individual SWNTs emission shows almost no Stokes shift and the linewidth of a single chirality is of the order of 25 nm (∼25 meV) at room-temperature [113, 154, 155] (see Fig. 1.9 - (a)). Likewise, the "single chain" emission of conjugated polymers shows a small Stokes shift and a mono-exponential decay [156] (see Fig. 1.9 - (b) and (c)). It is unlikely that the observed luminescence also came from the intrinsic emission of individual GNRs, since we need to invoke (1) complicated vibronic structures to explain such broad and Stokes-shifted emission and (2) complex internal relaxation pathways for the multi-exponential decay.

One natural explanation would be then to attribute the emission to defect states in the GNRs structure. These defect states could arise from the presence of defects at the edges, from open-bonds or from the installed lateral alkyl chains (-$C_{12}H_{25}$, see figure 1.3). However, the precise control of the GNR structure by organic chemistry prevents the appearance of such major defects and moreover the structural integrity has also been confirmed by several spectroscopy measurements (FTIR, Raman and NMR). Besides, if we compare the emission behavior of our GNRs with another carbon structures like carbon dots and top-down fabricated graphene quantum dots (GQDs), whose emission originates from the sp^3 defects, for carbon dots and top-down GQDs we can clearly see a red-shift when increasing excitation wavelength (Fig. 1.6- (b) and (c)), while the form of the PL spectrum for GNRs remains unchanged (Fig. 1.6- (a)). Since the uncontrolled defects usually have a continuum of states as an inhomogeneous broadening, the excitation at lower energy selectively excite the defect states located at lower energy and the emission is then red-shifted. In contrast, as the emission of GNRs is independent to the excitation wavelength, it is unlikely that the emission arises from the defect states. It also implies that the transition of GNRs is based on a defined electronic structure.

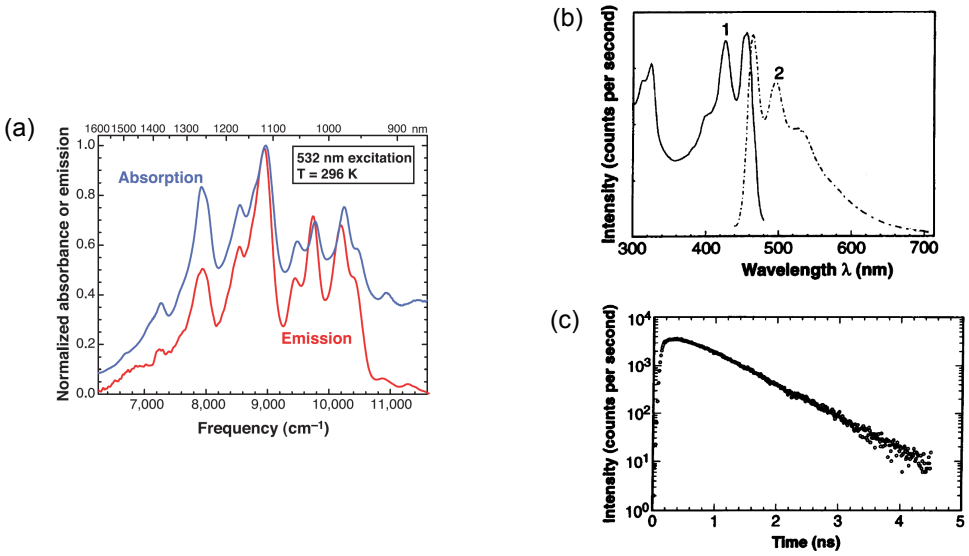

Figure 1.9: (a) - Absorption (blue) and emission (red) spectrum of SWNTs in SDS micelles, taken from [113]. (b) - PLE (curve 1) and PL (curve 2) spectrum of π-conjugated polybenzobisthiazole solution. (c) - Time resolved PL of π-conjugated polybenzobisthiazole solution, indicating a single exponential decay. (b) and (c) are taken from [156].

It is also very interesting to look at the effects of lateral alkyl chains on the electronical and optical properties of GNRs. Indeed, the theoretical and experimental studies on the Raman spectra of different bottom-up synthesized GNR structures, including 4-CNR, revealed significant effects of the alkyl chains on their vibrational properties [85]. For instance, the alkyl chains modify the radial-breathing-like mode (RBLM) frequency. Hence, it is rational to question on the influence of these chains on the electronic structure and it is possible that the replacement of hydrogen atoms of the edge by the alkyl chains could, for instance, create new states in the energy gap of GNRs. However, a recent theoretical work by C.E.P. Villegas *et al.* shows that side chains should have no influence on the optical properties of 4-CNR [157].[27] So, the presence of these alkyl chains cannot explain our observations.

On the other hand, despite the presence of the alkyl chains, the molecular solubilization of GNRs is still very challenging [69]. Here we used SDS micellar suspension since this it has been successful for the individualization of SWNTs and it allows us to use tip sonication [113]. Nevertheless, it is likely that aggregates are present in the GNR suspensions used in these experiments. Indeed, π-conjugated object are known to self-aggregate through $\pi - \pi$ interaction, even at moderate concentrations [158]. Moreover, in some cases the aggregation leads to a vibronic coupling between monomers (single isolated molecule) that results in strong modifications of their spectroscopic features. For instance, excimer emission has been reported on aggregates of small conjugated molecules such as pyrene, in conjugated polymers or in hexabenzocoronene [132, 158–160]. An excimer corresponds to the coupling between a monomer M_g in its ground state and a monomer M_{ex} in its excited states that form an excited dimer D_{ex}. The system returns back to equilibrium when D_{ex} dissociate in the ground state leading to a broad,

[27] In this paper, authors performed the calculations using GW + BSE approach.

structureless PL at much lower energy ($h\nu_D$) than the monomer absorption:

$$M_{ex} + M_g \leftrightharpoons D_{ex} \rightarrow M_g + M_g \ + \ h\nu_D \tag{1.2}$$

Since the formation of excimers takes place after the molecule goes into excited state and changes only the relaxation process, the electronic structure of the molecule at ground state is not affected. Hence, the absorption spectrum usually remains unchanged when excimer emission occurs [161].

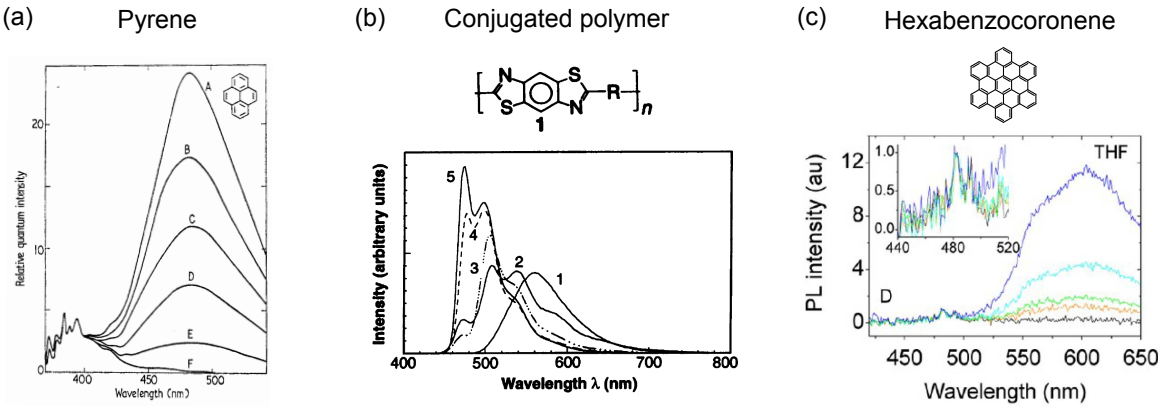

Figure 1.10: Photoluminescence spectra of pyrene (a), PBZTs conjugated polymer (b) and hexabenzocoronene (c) with different concentrations. For both three systems, a board and structureless (excimer) emission occurs when increasing the concentration. Adapted from [161], [156] and [132], respectively.

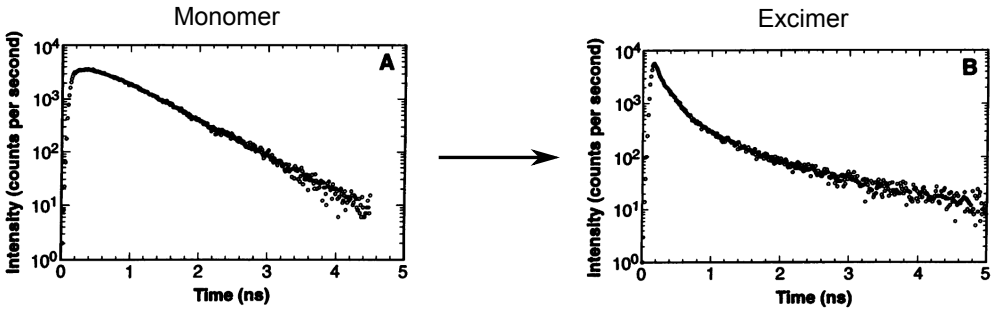

Figure 1.11: Time-resolved PL on PBZTs conjugated polymer. The emission from monomers shows mono-exponential decay (left), while the emission from excimer is multi-exponential (Right). Adapted from [156].

Studies of excimer in some molecular systems have shown that the basic supramolecular structures are cofacial sandwich-type configurations [156]. The most known system showing excimer emission is the pyrene molecule that emits excimer luminescence near ∼485 nm when the concentration is increased [161]. Its excimer emission is broad, structureless and red-shifted of ∼80 nm (∼490 meV) in comparison with that of the monomer (Fig. 1.10 - (a)). Similarly, excimer emission has been observed on stacks of π-conjugated polymers leading to a multi-exponential decay, with apparent Stokes-shift of ∼100 nm (∼500 meV) [156] (Fig. 1.10 - (b) and Fig. 1.11). Likewise, hexabenzocoronene (HBC) and its derivatives, which are studied as model systems for graphene, tend to form

aggregates in suspension though face to face $\pi - \pi$ interaction. Here again, this coupling results in a broad emission that is red-shifted in comparison with the one of the monomers, and that has been therefore attributed to an excimer-like emission [132,160] (Fig. 1.10 - (c)). Given their structure, GNRs are also likely to stack in the cofacial sandwich-type configuration. Since the PL of both GNR structures reported here share very similar characteristics with the one reported for those π-conjugated objects, it sounds reasonable to attribute it, at least partially, to the formation of excimers.

Nevertheless, despite their global similarities, some features of *p*-ANR's optical response differ from that of 4-CNR. First, an additional absorption band is observed on the red side of the main transition around 790 nm. This shoulder could be related to an intrinsic transition. Indeed, it has been predicted theoretically that *p*-ANR should exhibit a much complex peak structure than 4-CNR [94].[28] In that case, the PL line observed on *p*-ANR could be closed to that of single isolated GNR. This could also be in good agreement with the longer average lifetime of *p*-ANR in comparison with that of 4-CNR. On the contrary, the shoulder in the absorption spectrum of *p*-ANR could also be related to a much more pronounced aggregation than for 4-CNR.[29] Indeed, it has been demonstrated on hexabenzocoronene, that a high degree of aggregation could lead to such feature in absorption spectroscopy [132].

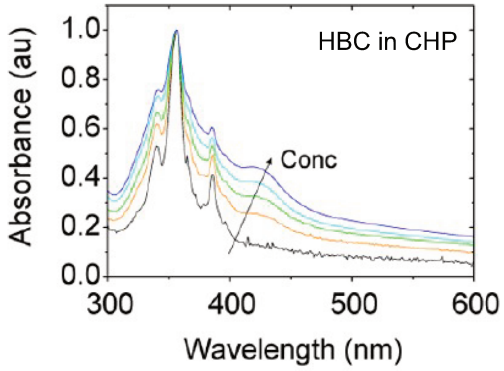

Figure 1.12: Optical absorption spectra of HBC in CHP solution with different concentrations. A broad peak at 425 nm appears when the concentration increases. Adapted from [132].

1.4 Single-particle measurements on *p*-ANRs

Since measurements on ensemble of objects are subject to averaging effects, experiments at the single-particle level have been performed in order to investigate close-to intrinsic properties of the GNRs. The SDS suspension of *p*-ANRs was drop-cast on the surface of a plasma-cleaned glass coverslip and rinsed several times to get rid of the excess

[28] In this paper, the authors used TD-DFT/HSE calculations ("TD-DFT" corresponds to time-dependent density functional theory and "HSE" corresponds to Heyd-Scuseria-Ernzerhof) to simulate the optical spectrum of finite oligomer (tetramer) rather than infinite GNR, because the periodic boundary condition cannot be applied in such quantum chemical calculation. In consequence, this method is not optimal for GNRs, compared with GW + BSE approach. The calculation is performed by Prof. David Beljonne's group at the University of Mons, Belgium

[29] The *p*-ANR suspension has broader optical density and lower PL intensity compared with the 4-CNR, which could be a indication of stronger aggregation effect in the *p*-ANR suspension.

of surfactant. The sample was then analyzed on a confocal microscopy setup that is coupled to an atomic force microscope (AFM) (see Chap. II Sec. 2.4 for more details).

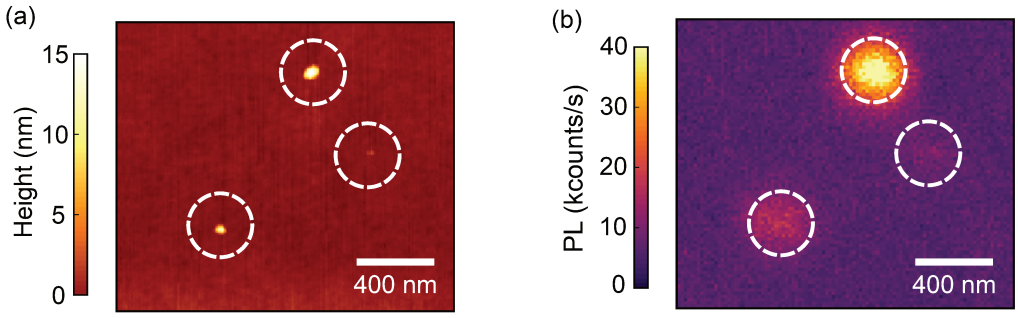

Figure 1.13: AFM image (a) and corresponding microphotoluminescence image (b) of *p*-ANR deposited on a glass coverslip. White dashed circles highlight three luminescent GNRs small aggregates, with heights of 2.5, 13 and 17 nm.

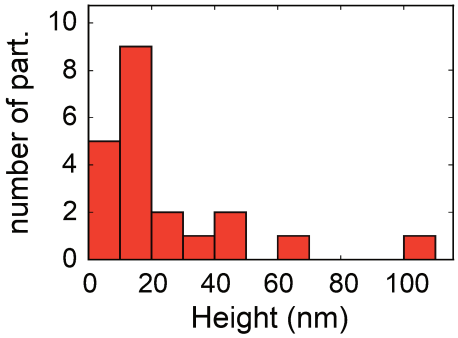

Figure 1.14: Height histogram of the luminescent GNR aggregates on the sample.

Fig. 1.13 - (a) shows a typical 1 × 1 μm^2 AFM image. Three small aggregates (white dashed circles) are present in this area with heights ranging from ∼17 nm to ∼2.5 nm. The very same location of the sample has been scanned by the microphotoluminescence setup using 594 nm laser. Fig. 1.13 - (b) displays this photoluminescence map demonstrating that the three small GNR aggregates emit light. This observation demonstrates the ability of GNRs to emit light in the solid state. Several scans were performed on the sample and the density of the GNR aggregates was found to be about 5 particles per 20 × 20 μm^2. A statistics on the GNR aggregate's height measured by AFM is displayed on Fig. 1.14. It shows that the height of most of the objects deposited from the SDS suspension is in the range of 10 to 20 nm. Here this observation implies that small GNR aggregates are present in the suspension or the aggregation takes place when the GNRs are deposited on the substrate.

Finally, Fig. 1.15 represents typical PL spectra recorded on these small aggregates. Notably, for all the spectra three sharp lines at the same position are observed (pointed by the stars (⋆)). Converting this lines into Raman shift from the excitation laser, we found that they correspond to the characteristic Raman modes of sp^2 carbon nanostructures at 2619 ± 20 cm^{-1} (2D mode), 2934 ± 20 cm^{-1} (D + G mode) and 3195 ± 20 cm^{-1} (2G mode), respectively [66, 85]. This observation strongly confirms that the emission spots observed by photoluminescence spectroscopy do correspond to the emission of

GNRs. Moreover, the spectra of those four aggregates show similar Stokes shift to the one observed in suspensions. Hence, this red-shifted emission from aggregates is consistent with the excimer emission. Furthermore, the shape of the PL line is varying from one spot to another. Sometimes a contribution centered at ∼795 nm dominates the spectrum (Fig. 1.15 - (a) and (b)). For another aggregates, the main line is centered at ∼725 nm (Fig. 1.15 - (c)), closer to the absorption edge. Finally, intermediate cases are also observed (Fig. 1.15 - (d)). This variety observed in the PL spectra of individual aggregates implies that the PL spectrum recorded in SDS suspension is inhomogeneously broadened. Finally, based on a statistic of about twenty aggregates, we did not find any correlation between the height of the particle and the shape of the spectrum, nor its intensity (see Fig. 1.16).

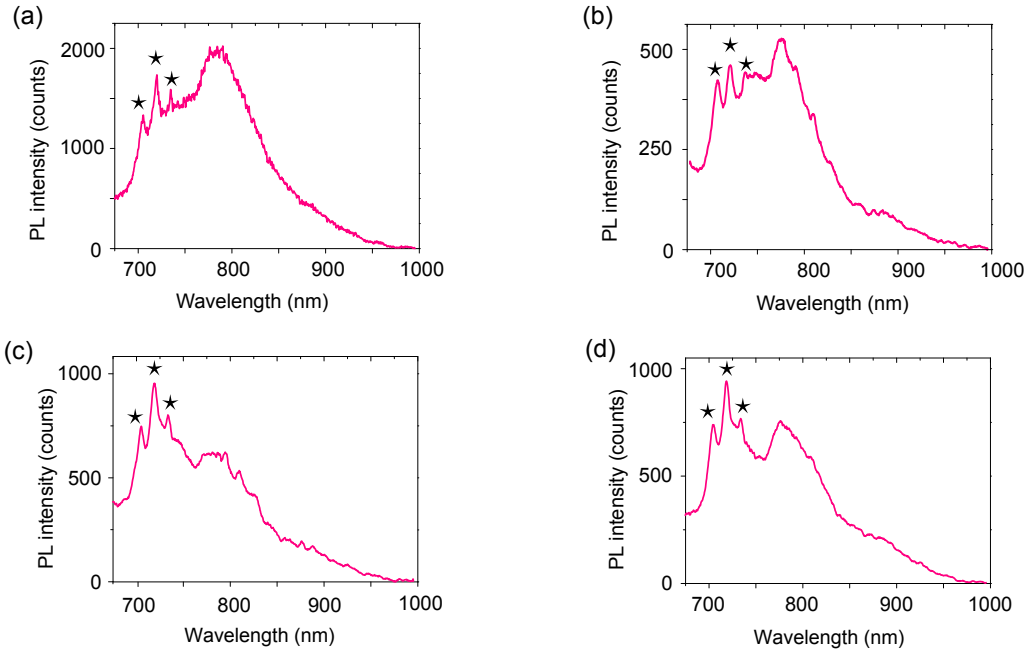

Figure 1.15: Typical PL spectra observed on four p-ANR aggregates with height of (a): 45 nm, (b): 20 nm, (c): 15 nm and (d): 25 nm. The excitation power is 5 µW at 594 nm. The acquisition time is 60 s. The stars ($\star$) refer to the second-order Raman lines of GNRs.

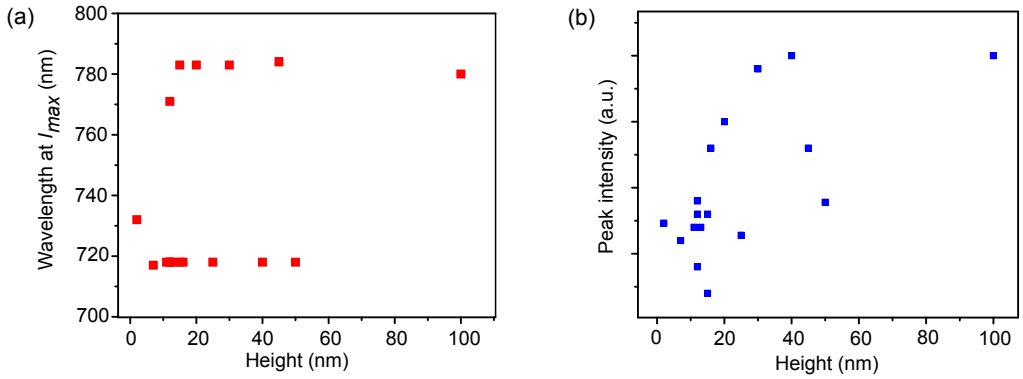

Figure 1.16: (a) - Wavelength of the emission maximum (y axis) and the corresponding height (x axis) of each p-ANR aggregate. (b) - Peak intensity (y axis) and the corresponding height (x axis) of each p-ANR aggregate.

1.5 Summary on the results of solution-mediated synthesized GNRs

Here we investigated the optical properties of two GNR structures: 4-CNR and *p*-ANR synthesized by in-solution bottom-up chemistry. They both display broad and highly Stokes shifted emission with multiexponential decay. After Comparing with other similar π-conjugated systems, we infer that this emission originates from excimer states in stacks of individual GNRs. Moreover, the broad emission of very small GNR aggregates at the solid state has been observed by means of AFM and microphotoluminescence. Raman lines are superimposed on the emission signal confirming the emission indeed from GNRs. We thus conclude that the suspension is mainly composed of small aggregates that blur the intrinsic properties of GNR. For further work, one major issue is how to individualize of GNRs. To reach this goal, several strategies are under development:

- Finding "good" solvents or surfactants and proper solubilization conditions for GNRs, which is the most straightforward strategy. For example, reports on individualization of hexabenzocoronenes in orgainc solvents [132] and micellar suspensions [160] could be a good guidance for this purpose.

- Edge functionalization to enhance the solubility of GNRs. As a first attempt, a high concentration GNR solution (up to 1 mg/L) has been obtained by grafting poly(ethylene oxide) (PEO) chains onto the GNR backbones [69].

- Since GNRs can be easily fold and/or bend, functionalization of the substrate surface may also be needed when performing the deposition. Several attempts have been also realized in order to obtain single "straight" GNRs at the solid state [83, 84].

On the other hand, as we have discussed in the introduction part, GNRs can also be synthesized via surface-assisted method. Unlike the solution-mediated method, single GNRs are grown directly on gold surface. Thus, we would not be limited by the low solubility of GNRs. In the Sec. 3.1, we will perform the optical characterizations on the on-surface synthesized GNRs, which have been transferred onto insulating substrates.

2 Bandgap engineering of GNRs by controlled structure distortion

2.1 Structural distortion induced by side chain installment

Strain-induced structural distortions of low dimensional materials have attracted increasing attention since it could act as an additional parameter to modulate physical and optical properties [162, 163]. As a example, by putting monolayer of WSe_2 onto an array of nanopillars, the induced localized strain leads to the trapping of excitons and thus creates single photon emitters [164, 165].

Some theoretical calculations have already been performed on GNRs to study the effects of non-planarity on their electronic properties. It is predicted that a bandgap

modulation of up to 1 eV could be reached, depending on the nature of structural distortions (e.g. bending [166], uniaxial strain (traction) [167], shear strain [168] and edge passivation induced strain [169]). Moreover, owing to the powerful bottom-up synthesis method, it could be possible to induce structural distortions on GNRs in a controlled manner and to systematically perform the experimental studies.

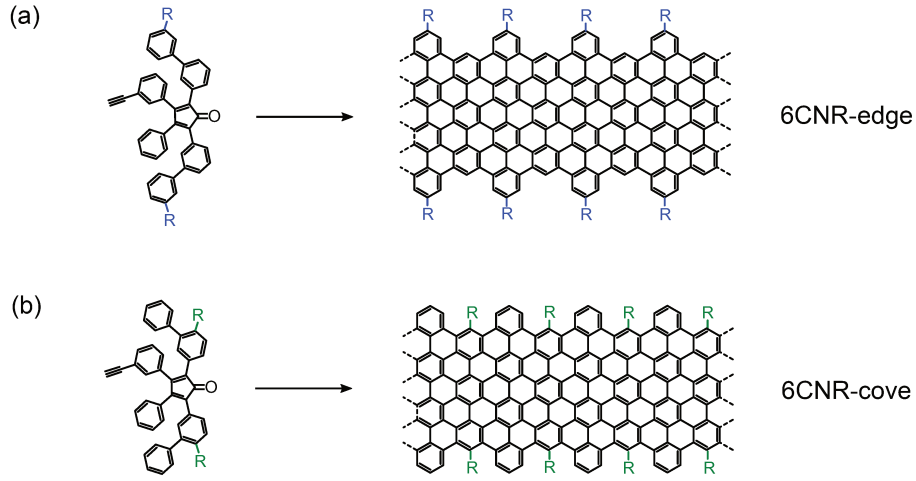

Figure 2.1: Chemical structure of 6CNR-edge (a) and 6CNR-cove (b) and corresponding starting monomers of chemical synthesis. "R" stands for a -$C_{12}H_{25}$ (dodecyl) chain.

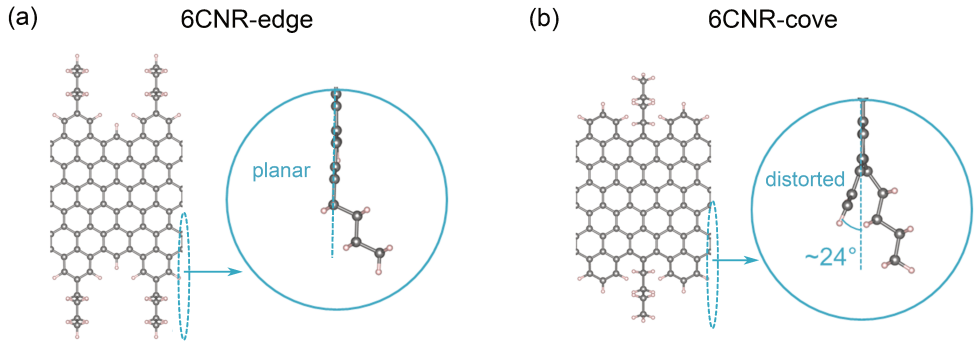

Figure 2.2: Simulated structures of 6CNR-edge (a) and 6CNR-cove (b) after the geometrical optimization. The dodecyl chains were replaced with butyl groups for the reason of reducing the calculation cost. Insets: Zoom of the side views of 6CNR-edge and -cove in the edge region reveal distinct geometrical structures. Adapted from [170].

For this motivation, our collaborators from MPIP in Mainz synthesized two GNR structures, having the identical 6-CNR aromatic core, but with alkyl side chains at different peripheral positions. As in Fig. 2.1, one has dodecyl chains (-$C_{12}H_{25}$) regularly installed at the outermost positions (named as 6CNR-edge), while the other one with -$C_{12}H_{25}$ chains installed at the innermost positions (named as 6CNR-cove). The two different GNR structures were obtained by changing the -$C_{12}H_{25}$ chains position on the starting monomers of the chemical synthesis as shown in Fig. 2.2. Due to the steric repulsion between the side chains and the aromatic protons, the planarity of the benzo-rings of 6CNR-cove is expected to be distorted, compared to the planar 6CNR-edge.

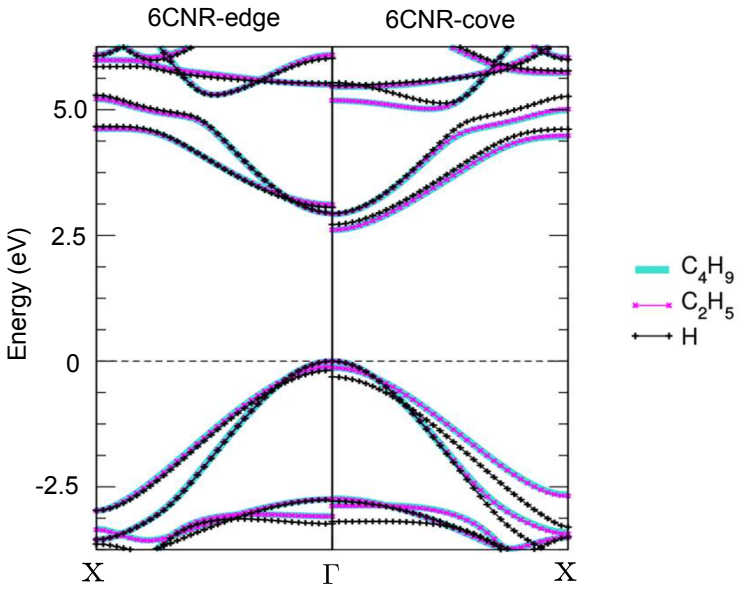

Figure 2.3: Simulated *GW* quasi-particle band structure of 6CNR-edge and -cove, as modelled by using alkyl chains of different length (i.e. -C_2H_5 and -C_4H_9), indicating that the chain length does not influence the electronic properties in the region of interest. The impact of the structural distortion is also evaluated by comparing the systems with H passivation only (black plus). Adapted from [170].

Theoretical calculations on these two GNR structures were also conducted by Prof. Deborah Prezzi and Prof. Elisa Molinari's group in Modena. The geometrical optimization by density functional theory (DFT) calculations reveals that the peripheral benzo-rings of 6CNR-cove are distorted by approximately 24° from the planarity, while 6CNR-edge is completely flat (see Fig. 2.2) [170]. They then performed the calculations of the quasi-particle band structure on these two 6-CNRs using the *ab initio* *GW* method. In order to reduce the calculation cost, after fixing the geometrical structure of backbones, the -$C_{12}H_{25}$ was replaced by shorter alkyl chains with two different length (-C_2H_5 and -C_4H_9) and also -H. From Fig. 2.3, we can see that for each 6-CNR structure, the obtained band structure are almost unchanged for these three edge substituents, which is in agreement with the result of similar calculations on 4-CNR [157]. This indicates that the band structure is determined by the backbone structure while the chain length does not influence the results of the calculations. Comparing between the two 6CNR structures, the lowest conduction band of 6CNR-cove is lowered by 0.27 eV than the corresponding band of 6CNR-edge while the highest valence bands are not significantly modulated, thus resulting in the overall decrease of the bandgap of 0.19 eV (bandgap for 6CNR-edge is 2.68 eV, while for 6CNR-cove is 2.49 eV).

2.2 Optical spectroscopy on distorted and non-distorted 6CNRs

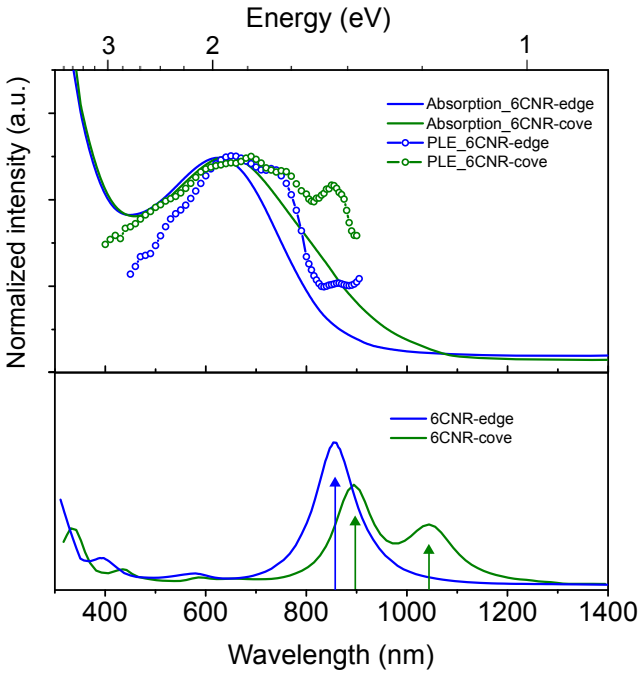

Figure 2.4: Upper panel: Experimental UV-vis-NIR absorption (solid lines) and photoluminescence excitation (solid lines with hollow circles) spectra of 6CNR-edge and -cove (recorded with suspensions in 1,2,4-trichlorobenzene). Lower panel: Simulated optical response of 6CNR-edge and -cove using GW + BSE approach. Arrows indicate the first optical transitions.

Inspired by the theoretical results, the Mainz group asked us for the optical spectroscopy experiments on the two 6-CNR structures. We dispersed the powders of these two structures in 1,2,4-triclorobenzene (TCB) by mild sonication for 30 min and followed by filtration with a membrane filter (pore size 5 μm) to remove larger aggregates and undispersed particles. We found that 6CNR-cove was more soluble than 6CNR-edge. It is presumably due to less efficient π-π interaction of the non-planar structure.

We then performed optical absorption and photoluminescence excitation (PLE) measurements on these two GNR suspensions. As we can see in the upper panel of Fig. 2.4, 6CNR-edge shows a broad absorption band with a maximum at 624 nm (1.98 eV) (blue solid line). In comparison, 6CNR-cove exhibited a red-shifted and broader absorption pattern with a long-wavelength absorption maximum at 649 nm (1.91 eV) (green solid line). This trend is consistent with the results of GW + BSE simulations that 6CNR-cove has a lower bandgap than 6CNR-edge due to the structural distortion (Fig. 2.3).

On the other hand, the photoluminescence spectra of 6CNR-edge and -cove are both broad and structure-less with a maximum at 800 nm (1.55 eV) and 925 nm (1.34 eV), respectively (Fig. 2.5 - (a)). Moreover, the PL decay of two GNR structures both show a bi-exponential behavior (Fig. 2.5 - (b)). These results are very similar to what we observed in 4-CNR and p-ANR (see Sec. 1.2), implying here again that the emission should arise from excimers.

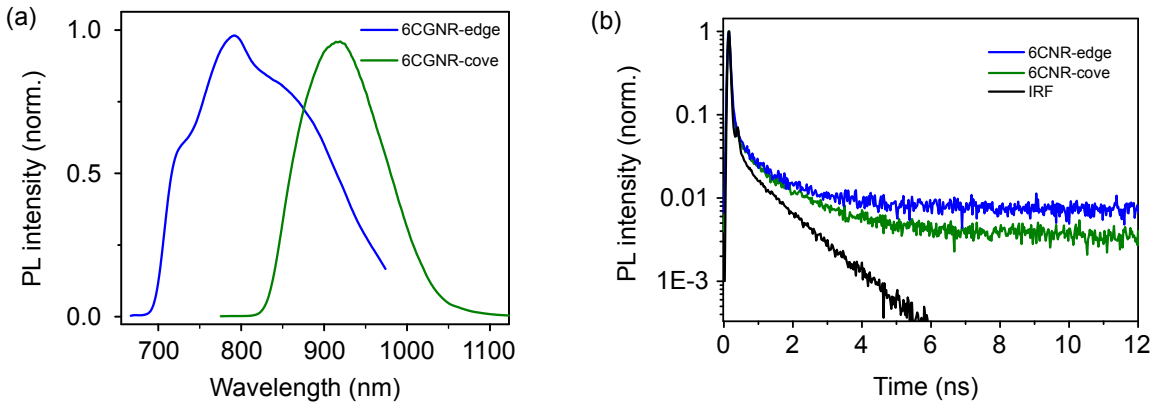

Figure 2.5: (a) - PL spectra of 6CNR-edge (blue) and 6CNR-cove (green) solutions. A long-pass filter cutting at 715 nm and 845 nm are put on the detection path for 6CNR-edge and -cove, respectively. (b) - Time-resolved PL measurements on 6CNR-edge and -cove solutions detected on the low energy tail of the PL signal, both showing a bi-exponential behavior.

The PLE spectra of 6CNR-edge and -cove are displayed by solid lines with hollow circles in the upper panel of Fig. 2.4.[30] We can see that they are both roughly in agreement with the corresponding optical absorption spectrum. Notably, for the PLE spectrum of 6CNR-cove, an additional peak at 850 nm (1.46 eV) is observed (indicated by the black arrow) and the optical absorption spectrum of 6CNR-cove also shows a should peak at approximately 850 nm. In contrast, for 6CNR-edge, both optical absorption and PLE spectrum show only one broad band centered at ∼630 nm. At 850 nm the intensity has already decreased a lot and become very weak. This implies again that 6CNR-cove has a lower (optical) band gap than 6CNR-edge. Moreover, simulated optical spectra based on the GW + BSE approach indicates only one optical transitions for 6CNR-edge while two separate optical transitions with lower energy for 6CNR-cove (see lower panel in Fig. 2.4), which is in agreement with the general trend of the PLE measurements.

The above agreement between the theoretical calculation and the optical measurement suggests that the observed difference when changing the side chain position, is intrinsic to GNRs. Thus, as a first attempt, the possibility of tailoring the optical and electronic properties of GNRs via a controlled structural distortion has been demonstrated. For further more systematical studies on this effect, one major issue is still how to enhance processability of GNRs or in another word, how to individualize GNRs.

The results of this collaborative work with the Mainz group is a part of the publication Hu *et al.*, *JACS* **140**, 7803 (2018).

[30]For excitation in the range 450-750 nm, the supercontinnum was coupled with monochromators, while for excitaiton from 700-950 nm, it was coupled with the AOTF. The data recorded with the two excitation sources have been glued at 750 nm. Since some GNR oligomers were present in the suspension, which has strong emission in the visible (see Chap. II. Sec. 3.1), to avoid this, the PL signal was monitored on the low energy tail of the PL spectrum.

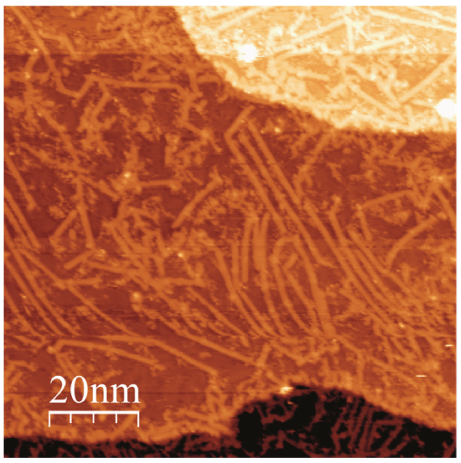

Figure 3.2: Representative room-temperature STM image of 9-ANRs on the Au/mica growth substrate.

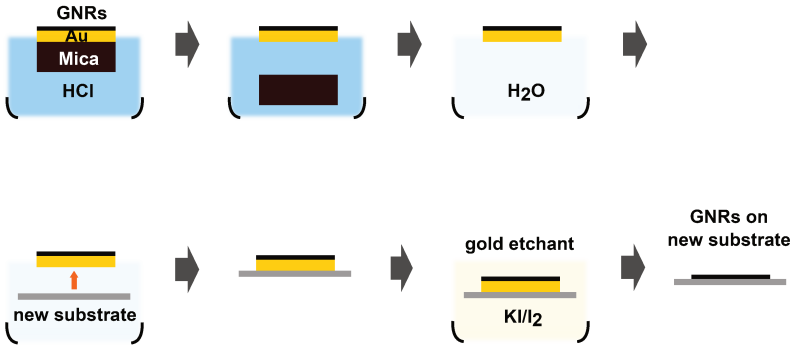

Figure 3.3: Transfer process of 9-AGNRs from the growth Au/Mica substrates onto the target glass substrates.

3.2 Structural quality analysis by Raman spectroscopy

The structural integrity of as-grown GNRs thin film after transfer was analyzed by Raman spectroscopy. This work was carried out at Pierre Aigrain Laboratory in collaboration with Christophe Raynaud, the PhD student in the group of Prof. Christophe Voisin. The measurements were performed using a Renishaw InVia Reflex Confocal Raman Microscope equipped with two different laser lines (532 nm, 633 nm). A 100× objective was used (leads to a spot size of $\sim$ 1 µm) and the power on the sample was kept below 0.5 mW to avoid damage.

Fig. 3.4 shows typical optical images of the transferred samples (white-light images from the Renishaw system). In the transferred area, it is easy to find uniform GNRs films with a extended size from tens of µm to one hundred µm. The optical contrast of these GNRs films is comparable to what is observed on a single layer graphene sample [172, 173], suggesting the preservation of the sub-monolayer coverage after transfer.. Moreover, at the edge of the films some wrinkles can be occasionally observed, which we assign to the folding of the GNR layer (white parts in Fig. 3.4 - (b)).

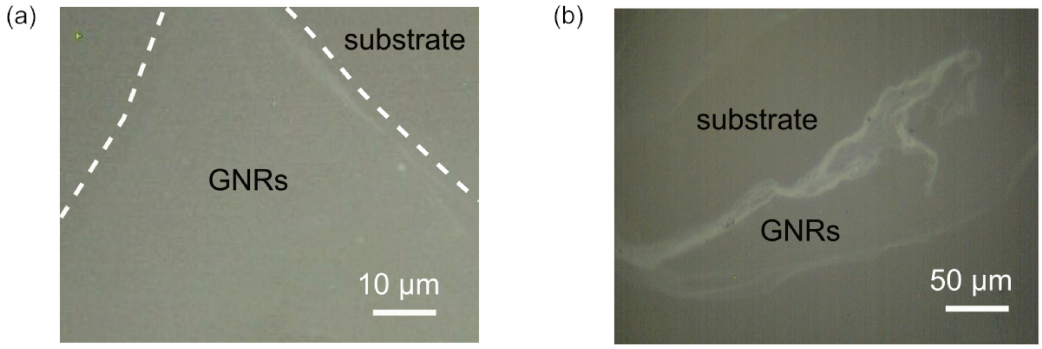

Figure 3.4: Optical microscope images of the 9-AGNR film transferred onto a glass substrate. Generally the film shows high uniformity with faint optical contrast (a). Sometimes a folding area could be found at the edge of the film (b).

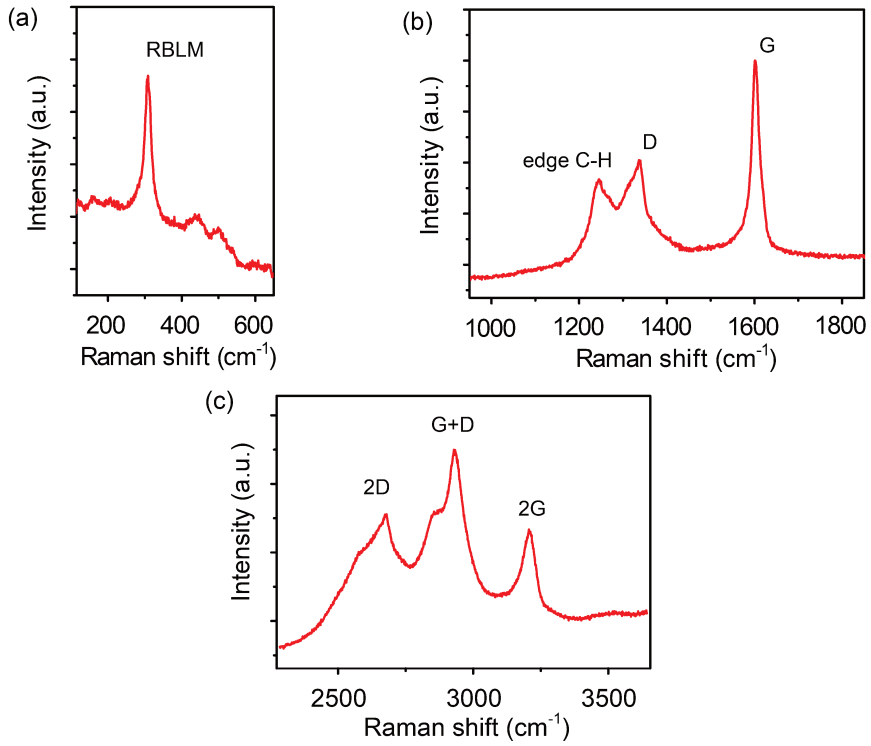

Figure 3.5: Raman spectra of the transferred 9-AGNR film in the low (a) and high-energy (b and c) spectral region, measured at 633 nm.

We then performed confocal Raman spectroscopy on these films to ensure the structural integrity of the transferred GNRs. Fig. 3.5 shows the typical Raman spectra with the 633 nm laser line. First, in the low-energy region (Fig. 3.5 - (a)), the spectrum shows the radial-breathing-like mode (RBLM) of 9-ANR at ∼310 cm^{-1}. Moreover, in the high-energy region (Fig. 3.5 - (b)), the G mode at ∼1600 cm^{-1}, the D mode at ∼1340 cm^{-1} and C-H bending mode at ∼1240 cm^{-1} are also observed with frequencies comparable to the ones measured on the gold substrate [28]. The presence of all characteristic Raman peaks, and in particular of the highly width sensitive RBLM, confirms that the structure of GNRs is preserved after the transfer procedures, in agreement with previous results on the *ex situ* measurements of the on-surface synthesized GNRs [174,175]. In addition, as we can see in Fig. 3.5 - (c), we also observed second-order 2D, G+D, 2G modes at

~2680, 2930, 3200 cm^{-1}, respectively. This observation is in contrast with the carbon nanotubes and defective graphene, where G+D mode are not observed in carbon nanotube [176] and G+D and 2G modes are not observed in defective graphene [177]. We will discuss this different Raman behavior of GNRs in Sec. 3.4.

Furthermore, we also performed Raman intensity mapping in order to obtain spatially resolved information on the transferred GNRs sample. Fig. 3.6 shows the peak intensity maps of RBLM (at 310 cm^{-1}), D mode (at 1340 cm^{-1}) and G mode (at 1600 cm^{-1}) superimposed onto the optical microscope image. The intensity of both all the three Raman modes on the faint part of the film is homogeneous, suggesting that the sample morphology in this area did not altered during the transfer. We also observed that the wrinkles at the edge of GNR films show stronger intensity, which can be attributed to the increasing amount of GNRs under the laser spot due to multi-layer folding.

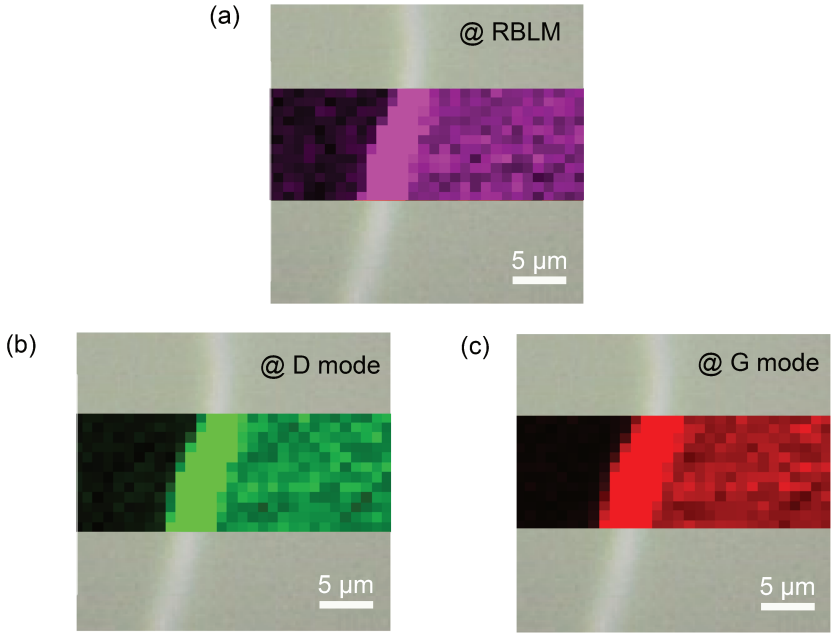

Figure 3.6: Raman maps superimposed onto a optical microscope image of 9-AGNR film. (a) - Raman peak intensity maps of RBLM (at 310 cm^{-1}), (b) - Raman peak intensity maps of D mode (at 1340 cm^{-1}). (c) - Raman peak intensity maps of G mode (at 1600 cm^{-1})

3.3 microphotoluminescence investigation

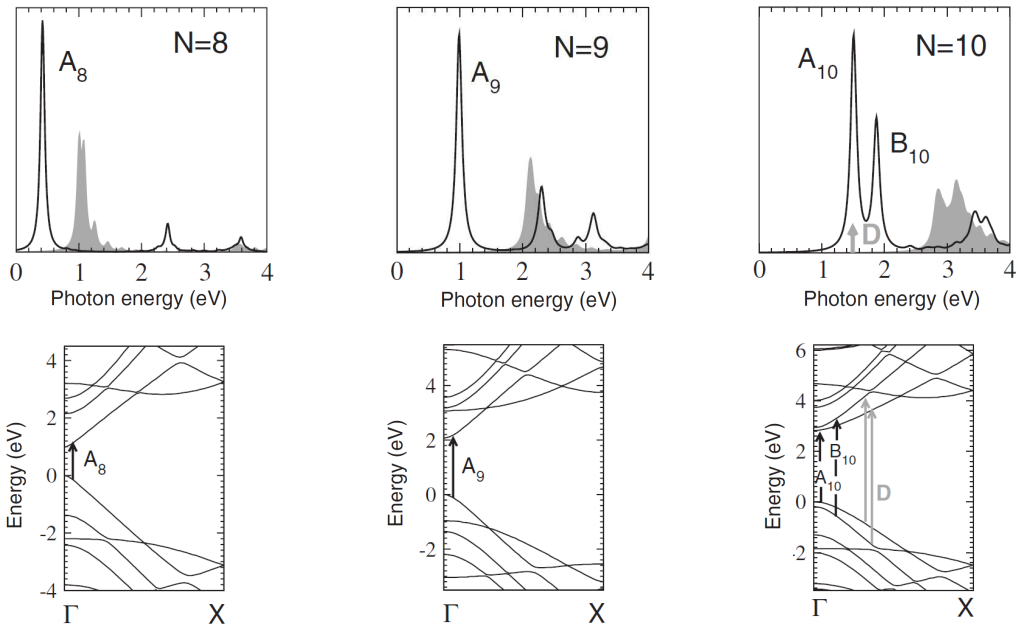

Figure 3.7: Upper panel: Calculated optical absorption spectra of hydrogen-passivated armchair GNRs in three different families (N = 8, 9 and 10). The solid line represents the spectrum with electron-hole interaction, while the spectrum in the single-particle picture is in gray. Lower panel: Corresponding quasi-particle band structures. Adapted from [93].

Having demonstrated the successful transfer of 9-AGNRs onto glass substrates, we then studied their PL properties.

Theoretical calculations indicate that graphene nanoribbons with armchair shaped edge (AGNRs) can be classified into three distinct families: $N = 3p, 3p+1$ and $3p+2$, with p an integer, where N indicates the number of carbon atoms across the width of ribbon. Depending on the family, AGNRs show different electronic behaviors [31,178,179]. Generally in each family the bandgap descreases when the ribbon width increases[32]. Moreover, Yang *et al.* [92] and Prezzi *et al.* [93] have performed the theoretical calculations using GW + BSE approach to investigate the optical properties of armchair graphene nanoribbons in all three families. As shown in lower panel of Fig. 3.7, the lowest-energy absorption peak of AGNRs arises from transitions between the last valence and first conduction bands (E_{11}). Similar to the cove edge shaped GNRs (Sec. 1.2), this transition has an excitonic nature with a large binding energy ∼1 eV. Notably, the authors pointed out that the excitonic structure also depends strongly on the family type. We can see from upper panel of Fig. 3.7, for the armchair GNRs belonging to the $3p+1$ family (N = 10 in the figure), a dark excitonic state (marked as D) is located almost at the same position of the lowest excitonic state.[33] Since the dark state provides

[32]Within each family, the bandgap E_g is inversely proportional to its width w ($E_g \sim 1/w$), as the bandgap originates from quantum confinement [31].

[33]The presence of low-energy dark excitons in GNRs is strongly dependent on the family, contrary to the case of SWNTs, where this is a common feature due to the mixing of K-K' transitions [180].

a competing path for nonradiative decay of optical excitations, the luminescence yield of the $3p+1$ ANRs would be reduced a lot. The 7-ANR, which is in the $3p+1$ family, have recently been experimentally explored by Senkovskiy *et al.* [109]. The authors interpret the weakness of the luminescence as the consequence of the existence of this dark exciton. On the contrary, AGNRs in the $3p$ family are not supposed to show such dark state. In this context, we expect to observe the intrinsic emission from 9-ANRs.

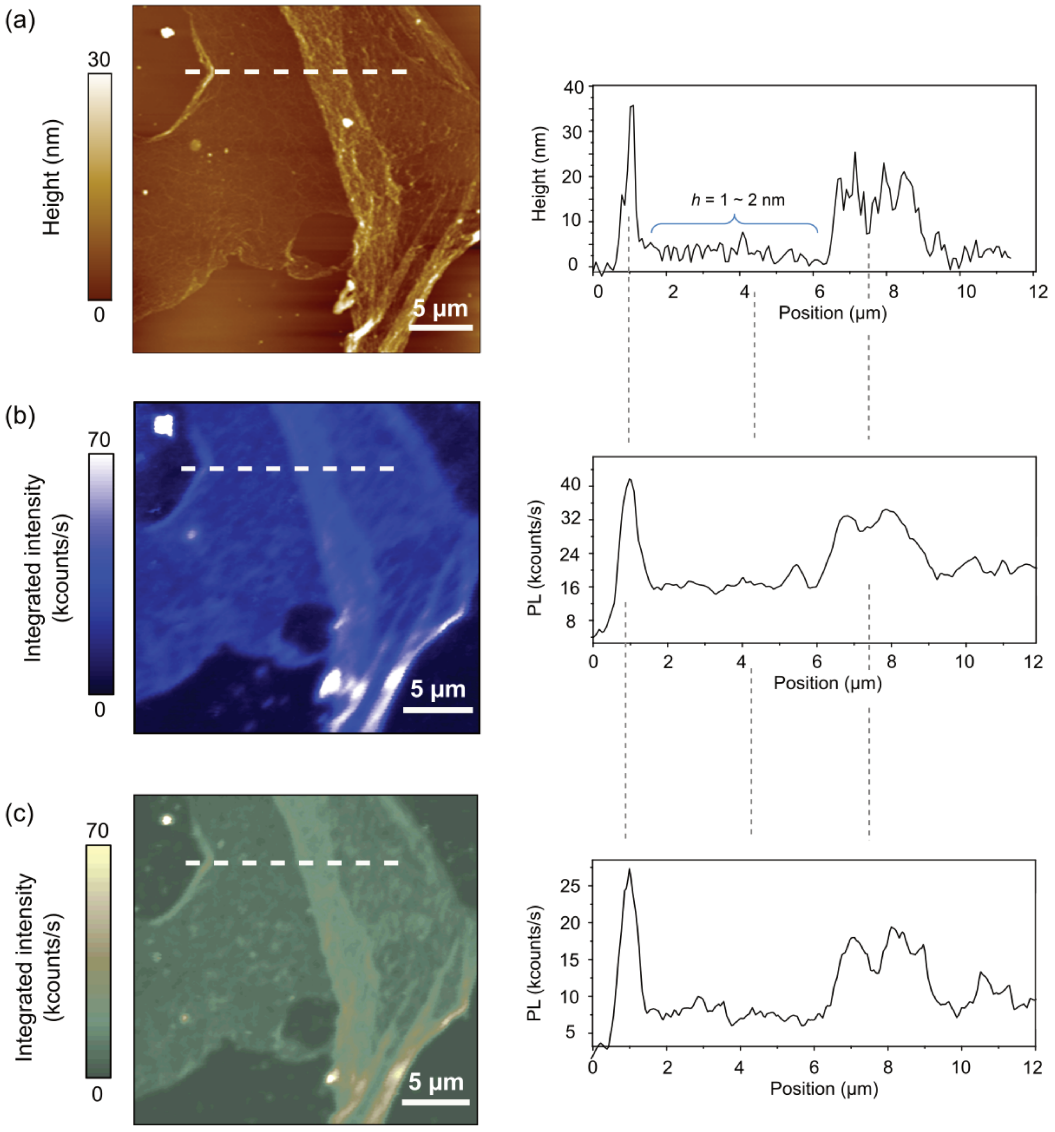

Figure 3.8: Correlation between AFM image and PL maps on a 9-AGNR film. (a) - AFM height image and corresponding cross sections profile taken along the dashed lines. (b and c) - Integrated PL intensity maps of the same sample area for laser excitation at 405 nm (b) and 594 nm (c) and corresponding cross section profile taken along the dashed white lines on the maps. The dash grey lines on the right are drawn to guide the eyes on the correlation between the AFM and PL maps.

Our transferred 9-ANRs sample was analyzed by confocal microscopy and atomic force microscope (AFM). Fig. 3.8 - (a) displays a typical 20×20 µm^2 AFM height image of the sample. It shows that the 9-ANRs film possesses large uniform areas. The cross-section profile reveals that the thickness of this uniform part is ∼1-2 nm. This value

is close to the one observed on monolayer graphene [19]. Therefore, this observation is compatible with the presence of a quasi-monolayer of GNRs on this sample, which proves the efficiency of the transfer. Meanwhile, at the edge of the film, rough wrinkles with a height ∼30-40 nm are also observed. This folding of multiple GNR layers is supposed to be introduced during the transfer process.

After the topography mapping by AFM, the same area of the 9-ANRs film was scanned by confocal PL microscopy. The value of the optical band gap (or the energy position of the first excitonic transition) of 9-ANR has not been known yet. However, it is recently reported that this value for 7-ANR is 2.1 eV (590 nm) by using reflectance difference spectroscopy [106]. This gives us a good reference for the optical band of 9-ANR. As 9-ANR is just two carbon atom wider than 7-ANR, it is reasonable that the value of optical band gap for 9-ANR would not decrease so much compared to 7-ANR, which could be around 700 nm (1.77 eV). For this reason, we decided to first perform the measurements using the confocal microscopy setup working in the visible.

Fig. 3.8 - (b) shows the corresponding integrated PL intensity map on this 9-ANR film using excitation laser at 405 nm. We observe that the whole film shows PL signal and that the thicker regions appear brighter. The correlation between thickness of the film and the PL intensity is further put in evidence by taking the same cross section profiles on the AFM height image and the PL maps (see the right part of Fig.3.8). This observation suggests that for the GNR film, the region with more quantity of GNRs shows more intense PL signal.

Fig. 3.9 - (a) displays a typical PL spectrum with excitation at 405 nm. The luminescence is very broad and extends from ∼450 nm up to 900 nm. Moreover, a series of relatively narrow peaks are superimposed on the luminescence spectrum. By converting the wavelengths of these lines into Raman shifts, we assigned them to high-order multi-phonon Raman modes of AGNRs (we will go into details on these Raman lines in the next section).

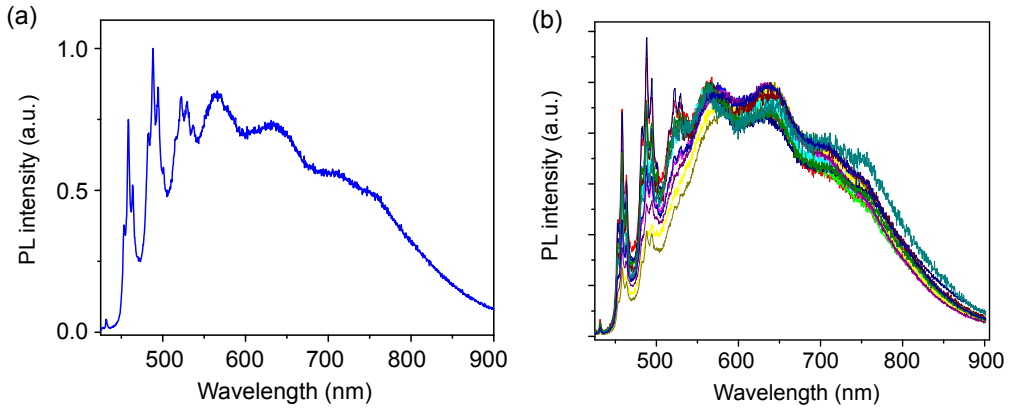

Figure 3.9: (a) - Representative PL spectrum on the 9-ANR film for excitation at 405 nm. (b) - PL spectra taken on the different positions of the film showing similar form.

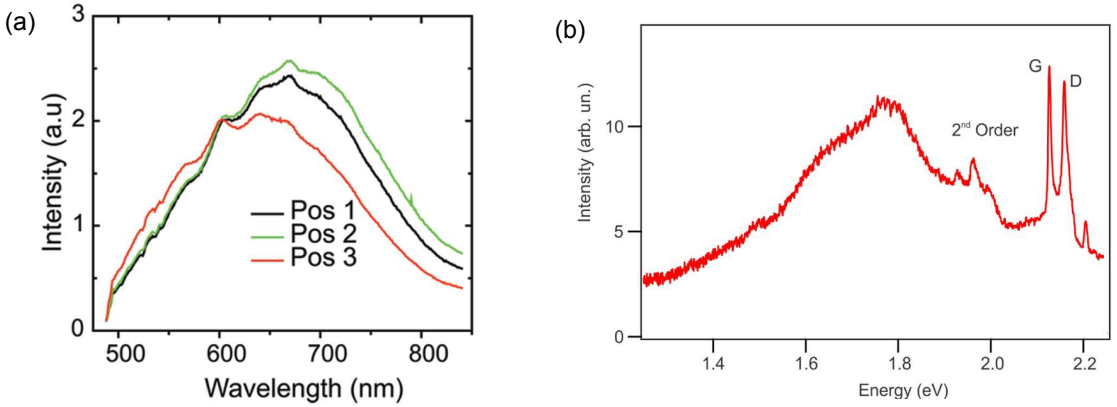

Figure 3.10: Defect emission from graphene (a) and 7-ANR (b). Adapted from [181] and [109], respectively.

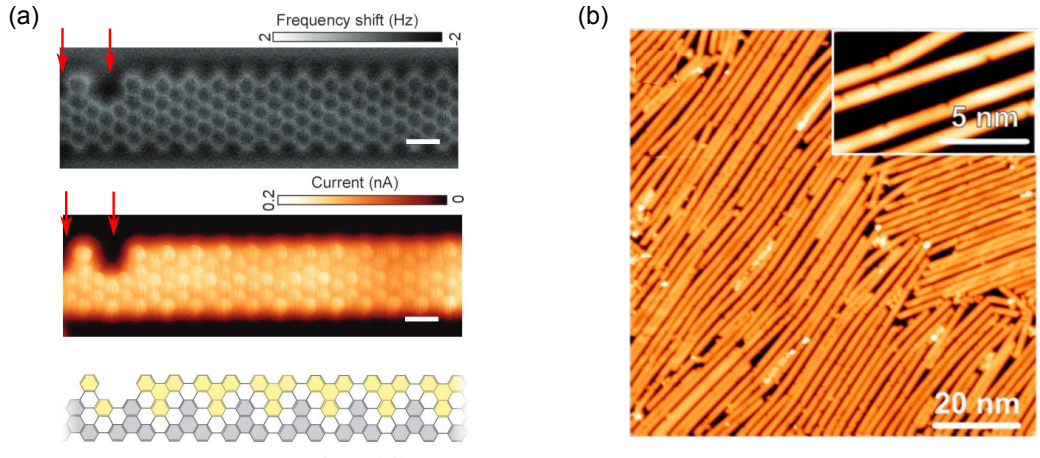

Figure 3.11: *In situ* observation of the phenyl ring missing defects in 9-ANRs. (a) - High-resolution nc-AFM frequency shift image (upper) and STM image (middle) showing two defects position of a 9-ANR (indicated by the red arrows). Scale bar: 0.5 nm. A structural model with two missing phenyl rings is proposed in the lower panel. The molecular building blocks are highlighted in gray/yellow. Adapted from the supporting information of [28]. (b) - A large zone STM image showing the relatively high density of the phenyl ring missing defect in 9-ANRs. Adapted from [171]. These measurements were performed at low temperature.

We now discuss the origin of the spectrally broad PL. As we mentioned before, 9-ANR should has a lower optical band gap than 7-ANR (for 7-ANR, it is 2.1 eV). Therefore, it is unlikely that the observed broad PL line, at short wavelength between 450 and 900 nm (1.38 - 2.76 eV), when excitation at 405 nm, comes from intrinsic excitonic emission. In contrast, all the features of this PL are quite close to the fluorescence led by defect sites in graphene [181] and also in the recently reported 7-ANRs [109] (see Fig. 3.10). Moreover, the *in situ* low-temperature STM and nc-AFM measurements [28, 171] have revealed that some phenyl rings is missing at the edge of produced 9-AGNRs (Fig. 3.11). As seen Fig. 3.11 - (b), the amount of this defects is non-negligible (about one out of ten edge phenyl rings are missing). Since no defects of the polymerized precursor are observed in STM, it suggests that C-C bond scission occurs during the cyclodehydrogenation

step, resulting the missing of phenyl rings. In consequence, these edge defects could be at the origin of the observed broad emission of 9-ANRs. We also acquired PL spectra on different positions of the film (both flat and rough parts). All the spectra look very similar (see Fig. 3.9 - (b)). This further indicates the homogeneity of the film. Moreover, when the film is continuously illuminated by the 405 nm laser, this broad PL signal becomes more and more intense (see Fig. 3.12). It is known that the high energy blue laser illumination can create defects in graphene structures [109]. Thus, we can say that the intensity increasing of the broad PL is due to more defects present in the 9-ANR film and this observation in turn suggests the defect nature of the broad PL.

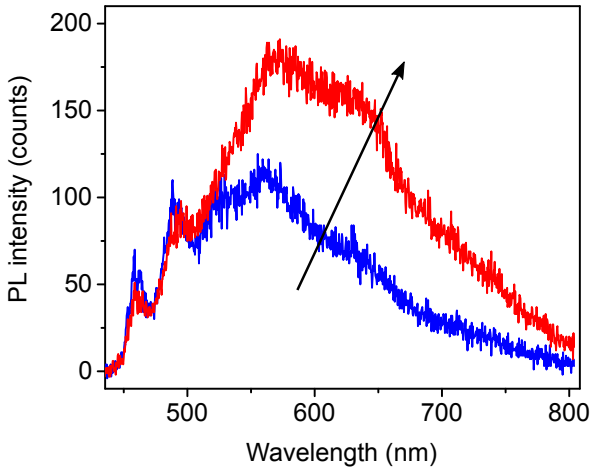

Figure 3.12: PL spectra of the 9-ANR film before (bleu) and after 5 min continuous illumination by 405 nm laser with a power of 100 μW(red). Both spectra are acquired with excitation wavelength of 405 nm for 10 s.

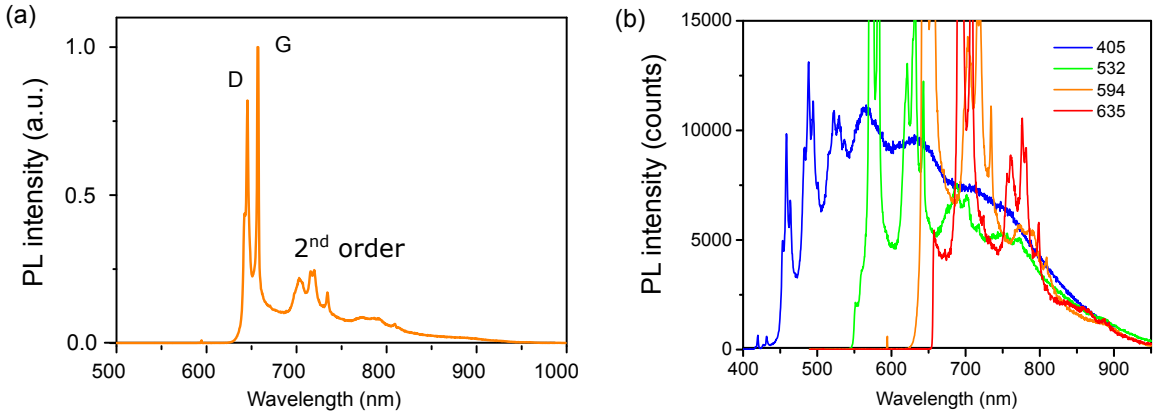

Figure 3.13: (a) - Representative PL spectrum of the 9-ANRs film with 594 nm excitation. (b) - PL spectra of the 9-ANRs film excited using different lasers with the same excitation power (150 μW) and acquisition time (10 s).

In order to work around these high energy defect states, we also performed experiments with excitation at lower energies. With a low energy excitation, only a subset of defect states could be excited. Since the contribution from defect states is reduced, one may expect the appearance of the intrinsic emission. Fig 3.8 - (c) displays the PL

map of the same area excited at 594 nm. The PL map looks quite similar with the one excited in the blue demonstrating one more time the homogeneity of the film. Fig. 3.13 - (a) shows the typical PL spectrum when excitation at 594 nm. The signal is clearly dominated by the G and D Raman lines. The fluorescence background is still broad and structure-less without any other features. Furthermore, we also tried to excite the film using 532 nm and 635 nm lasers. The form of the spectra is very similar. As in Fig. 3.13 - (b), when excitation with the same power and acquisition time, the intensity of this PL background does not change a lot for these four different excitation wavelengths. It turns out that the expected intrinsic emission still does not appear.

To conclude on this section, further studies are needed to explore the link between the observed broad PL at high energy and the nature and density of defects in the 9-AGNRs. Besides, several explanations could also explain the absence of the intrinsic excitonic emission. Firstly, the photoluminescence is usually very sensible. Many factors could open the non-radiative channel and result in the quenching of PL. For exemple, the PL could be quenched due to: interaction with the substrate; chemical doping during the transfer process; or non-radiative defects. In this perspective, performing dry transfer method and using h-BN substrate should be tested. Secondly, the exact energy position of the first excitonic transition of 9-AGNRs is not known to date. We have already seen in Fig. 3.7 that the theoretical calculations [93] predict that the lowest bright excition of 9-ANR is located in the infrared, about 1200 nm (1 eV). For this reason, we also performed infrared PL spectroscopy on the 9-ANR film[34]. However, the intrinsic emission is not observed either. To answer the questions that whether the 9-ANR sample has the defined optical transitions and where is the energy position of the optical transitions, we will perform micro absorption measurements because the absorption process directly reflects the optical transition.

3.4 Raman features in AGNRs

Although we did not observed the intrinsic emission from the 9-ANR sample, we found some distinct Raman features: the width dependent radial breathing like mode (RBLM), first order D mode and well-resolved high order Raman modes, which can be compared with graphene and carbon nanotube. We now try to get insight into these Raman features of 9-ANR.

Radial breathing like Mode (RBLM)

In the low energy region, specific vibrational modes have been observed for a variety of carbon allotropes. Most notably, carbon nanotubes (CNTs) display a characteristic peak associated to the radial breathing mode (RBM) of all the atoms of the structure. This RBM mode has been widely exploited to determine the tube diameter [182,183]. In analogy, GNRs also display a prominent peak in this region (see 3.5 - (a)) that is induced by the relative movements between the left and right parts of the GNRs. Fig. 3.14 - (a) illustrates the displacement pattern of this mode. In a unit cell of 9-ANR, the left eight atoms move to left, while the right eight atoms move to right. Since this mode is very similar to the RBM in CNTs, it is called RBLM, where "L" means "like".

[34]The measurement is carried out at Pierre Aigrain Laboratory.

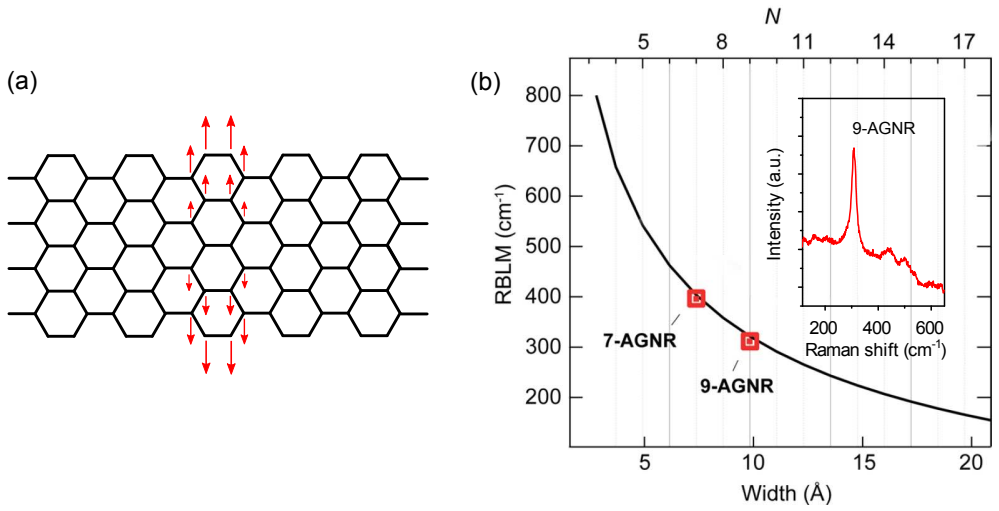

Figure 3.14: (a) - Illustration of the displacement pattern of the atoms in the nanoribbon unit cell due to the RBLM. The two halves of the unit cell oscillate in opposite phase. (b) - Wavenumber of the RBLM for 7-AGNRs (396 cm^{-1} [18]) and 9-AGNRs (310 cm^{-1}, shown in inset), together with the empirical model between the frequency of RBLM and ribbon width. Adapted from [28].

In fact, for the RBLM, the ribbon can be considered as a 1D oscillator (spring) along its width direction. As a consequence, the frequency of RBLM ω_{RBLM} can be written as [184]

$$\omega_{RBLM} = c\sqrt{k/M} \tag{3.1}$$

where k is the effective stiffness coefficient of the 1D oscillator and M is the mass of 1 unit cell of GNR. Based on the fact that the ribbon has a periodic structure and consists only of the carbon atoms, we can consider that M is proportional to its width w. Moreover, k is almost unchanged with w because of the same C-C bonds. Therefore, we expect to obtain a $\omega_{RBLM} \propto \sqrt{1/w}$ relation.

Vandescuren *et al.* [185] performed the DFT calculations on the RBLM frequency of a series of GNR with different width. They did the fit on the obtained values using

$$\omega_{RBLM} = a\sqrt{1/w} + b \tag{3.2}$$

where a and b are two constants. The fit gives the value of the two parameters: a = 1667.9 $cm^{-1}Å^{1/2}$ and b = -210.2 cm^{-1}. This empirical formula thus allows us to predict the frequencies of the RBLM. Indeed, as in Fig. 3.14 - (b), the experiment results of the 7-ANRs and our 9-ANRs are in good agreement with this model. Moreover, this also implies that the radial-breathing-like mode is indeed a sensitive probe of GNR width (one more carbon atom will results in 50 cm^{-1} difference of RBLM when the ribbon width is around 1 nm.)

D mode

As we have seen in Fig. 3.5 - (b), the 9-ANRs show a prominent first order D peak at about 1330 cm^{-1} with an intensity comparable to that of the G peak. This behavior is

in stark contrast to what is observed in graphene and CNTs. In general, the D mode comes from the in-plane breathing-like mode of the carbon rings (iTO phonon). It is activated by an intervalley double resonance process in the presence of defects [186] (see Fig. 3.15 - (a)). Thus, in pristine graphene and CNTs, the first order D peak is very weak while the 2D mode is relatively intense. The intensity ratio between D and G peak $I(D)/I(G)$ is used to evaluate the amount of defects. In contrast, as we can see from Fig. 3.15 - (b), the Brillouin zone (BZ) of armchair GNR covers only one half of the BZ of graphene. As a result, there is a single Dirac point (i.e. K and K′ point fold onto Γ) in the BZ of the armchair GNR [187]. Due to this BZ folding, we do not need a double-resonance process to activate the D mode but just a first-order process. For this reason, we are able to observe the first order D mode and also G+D mode (see Fig. 3.5 - (c)) in armchair GNRs without involving a defect.

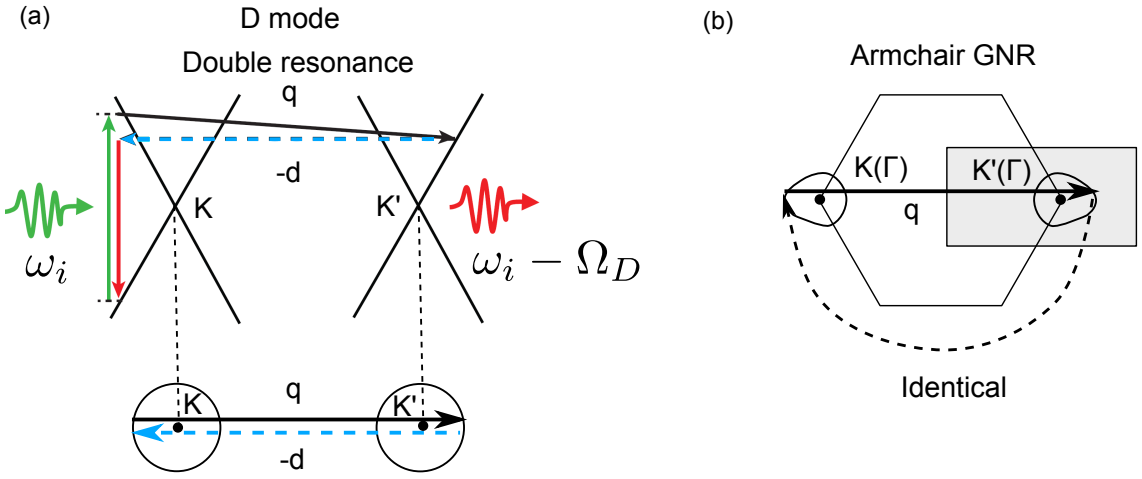

Figure 3.15: (a) - Upper panel: Schematic illustration of the double resonance process D mode in graphene. First, as indicated by the green arrow, an electron near the K point is excited into a real state by an incident photon with frequency ω_i, creating an electron-hole pair (the first resonance). Then the excited electron is inelastically scattered by a phonon of wavevector $\mathbf{q}$ with frequency Ω_D (D mode phonon, black arrow) to a second real state, near the K′ (the second resonance). Due to momentum conservation, the electron is elastically back-scattered into a virtual state near the K point by a defect (blue dashed arrow). Finally, the electron-hole pair in the K valley recombines with the emission of the scattered photon with frequency $\omega_s = \omega_i - \Omega_D$ for the energy conservation (indicated by the red arrow). Lower panel: the double resonance mechanism of D mode in graphene shown in top view. Adapted from [188]. (b) - The first order process D mode in armchair GNR shown in top view. Grey rectangle: Brillouin zone of armchair GNR. Hexagon: Brillouin zone of graphene. Black arrow denotes the phonon wavevector $\mathbf{q}$ contributing to the D mode in armchair GNR. In armchair GNR, because K and K′ point fold onto Γ, we do not need to involve an additional phonon to conserve the momentum. The D mode is thus a first order process. Adapted from [187].

In graphene, the phonon frequency varies abruptly near the K points (Kohn Anomaly), which leads to the result that the D peak in graphene is strongly dispersive with excitation energy (typically ∼50 cm^{-1}/eV) [189]. In contrast, due to the semiconducting nature of armchair GNRs, armchair GNRs no longer have linear electronic

dispersion and the formation of Kohn Anomaly is also prevented [190]. One would expect a nondispersive behavior for the D peak. Indeed, a smaller dispersion of the D peak in cove edge GNRs (10-30 cm^{-1}/eV for different widths) has been already observed by Verzhbitskiy *et al.* [85]. Similarly, we also plot the D mode position of the 9-ANR film as a function of the excitation energy[35] (see Fig. 3.16). A very small dispersion of the D peak is found (∼15 cm^{-1}/eV). This non-zero dispersion could be related to the some disorder-induced scattering (e.g. defects in the 9-ANR, see Fig. 3.11)

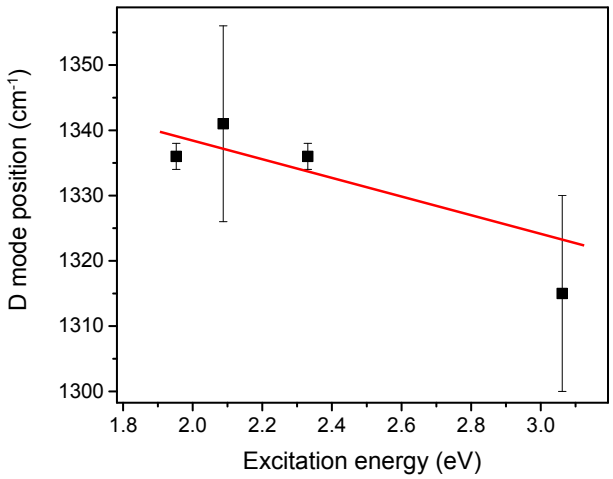

Figure 3.16: D mode dispersion of the 9-ANR film.

High order Raman mode

As we have already seen in the previous section, when the 9-ANRs film is excited at 405 nm, its emission spectrum shows a series of relatively narrow peaks. Interestingly, after converting the wavelengths of these lines onto Raman shifts, we can assigned them to high-order multi-phonon Raman modes from D (1335 cm^{-1}) and G (1600 cm^{-1}) overtones and combinations (see Fig. 3.17 and Tab. 2). We can clearly see that up to the 4^{th} order, the Raman modes are still narrow and clearly resolved. The further successive two broad peaks at 550-600 nm and 600-650 nm could be also tentatively attributed to the 5^{th} and 6^{th} order Raman modes, respectively.

The observation of well-resolved high-order Raman modes are in strong contrast to the fact that the Raman signal decreases dramatically with increasing the phonon order, as we can see in the case of graphene [191]. Moreover, since the multi-phonon Raman scattering can involve the phonons of different wavevectors as long as their total momentum is near to zero, the high-order Raman modes should become broad and cannot be resolved even after the second order [192].

[35]The values for the excitation energy equals 1.96 eV (633 nm) and 2.33 eV (532 nm) are taken using the micoRaman setup at LPA with high spectral resolution (∼5 cm^{-1}), while for the excitation energy equals 2.09 eV (594 nm) and 3.06 eV (405 nm) are taken using the confocal microscope setup in our lab with relatively low spectral resolution (∼15 cm^{-1})

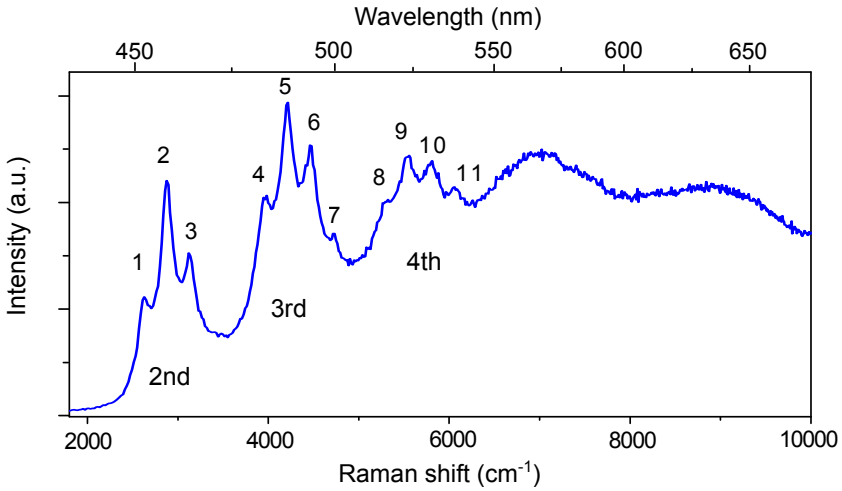

Figure 3.17: Raman spectrum of the 9-ANRs film. The high-order Raman modes are labeled in accordance with Tab. 2.

Number	Measured shift (cm^{-1})	Assigned mode	Expected shift (cm^{-1})
1	2629	2D	2670
2	2876	D + G	2935
3	3119	2G	3200
4	3983	3D	4015
5	4217	2D + G	4270
6	4478	D + 2G	4535
7	4732	3G	4800
8	5324	4D	5340
9	5556	3D + G	5605
10	5811	2D + 2G	5870
11	6059	D + 3G	6135

Table 2: Assignment of the Raman modes of Fig. 3.17 using combinations of G- and of D- phonon modes. The expected Raman shifts for these modes were calculated assuming frequencies of 1600 and 1335 cm^{-1} for G and D modes, respectively.

We now explain this distinct Raman feature of GNRs. We first draw a scheme to illustrate the process of n-th order Raman scattering. As shown in Fig. 3.18, an electron in the ground state $|0\rangle$ first absorbs a photon with energy $\hbar\omega_i$ and excited to the state $|i_0\rangle$. The electron is then scattered by the first phonon with energy $\hbar\omega_{q_1}$ and go to the state $|i_1\rangle$. Similarly, the electron is successively scattered by the second, third, ..., $(n-1)$th and nth phonon and in the $|i_n\rangle$ state. From this state, the electron go back to the ground state $|i_0\rangle$ by emission a stokes-shifted photon with energy $\hbar\omega_s$.

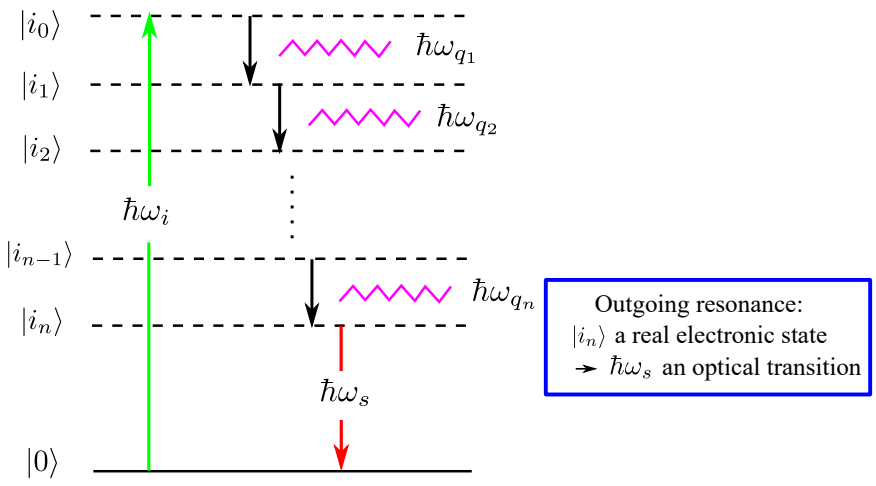

Figure 3.18: (a) - Schematic illustration of the n-th order Raman scattering process.

From the scheme described above, we can write the Fermi's golden rule of n-th order Raman scattering that directly reflects the intensity of the process [193]:

$$P_{\mathrm{ph}}(\omega_s) = \frac{2\pi}{\hbar}\left|\sum_{i_0,\ldots,i_n}\left(\frac{\langle 0|H_{eR}(\omega_S)|i_n\rangle\,\langle i_0|H_{eR}(\omega_i)|0\rangle}{\hbar\omega_i - E_{i_0}} \times \prod_{j=1,\ldots,n}\frac{\langle i_j|H_{e-ion}|i_{j-1}\rangle}{\hbar\omega_i - \sum_j \hbar\omega_{q_j} - E_{i_j}}\right)\right|^2 \times \delta(\hbar\omega_i - \sum_n \hbar\omega_{q_n} - \hbar\omega_s) \tag{3.3}$$

where H_{eR} is the electron-radiation coupling and H_{e-ion} is the electron-phonon coupling. ω_i is the incident photon frequency, ω_s is the stokes-shifted photon frequency and i_j describes a state with j phonons and E_{i_j} is its corresponding energy. The δ function $\delta(\hbar\omega_i - \sum_n \hbar\omega_{q_n} - \hbar\omega_s)$ describes the energy conservation.

Here two important components are involved in this formula: the electronic resonance factors (corresponds to the energy denominators $\hbar\omega_i - \sum_j \hbar\omega_{q_j} - E_{i_j}$) and the phonon density of states (DOS) (correspond to the Dirac function $\delta(\hbar\omega_i - \sum_n \hbar\omega_{q_n} - \hbar\omega_s)$). For 3D materials, the DOS close to the phonon band extrema typically vanishes [192]. In contrast, for one dimensional materials the DOS at such points remains finite, which makes it possible to observe the resonantly enhanced strong multi-phonon Raman modes. Indeed, the similar results have been reported on suspended individual single-wall nanotubes (SWNTs) by Wang *et al.* [194].[36] Moreover, after comparing the relative multi-phonon modes intensities between SWNTs and graphite, the authors also indicated

[36] As we have seen, D mode is a double resonance process in SWNTs. Thus for SWNTS only combinations including even number of the D mode phonons are allowed, whereas for our 9-ANRs we can observe both odd and even number D mode combinations due to the Brillouin zone folding.

that SWNTs exhibit appreciably stronger exciton-phonon coupling, which could also enhances the strength of the high-order Raman modes. Having observed this same feature as in SWNTs suggests the 1D nature of electronic structure of 9-ANRs.

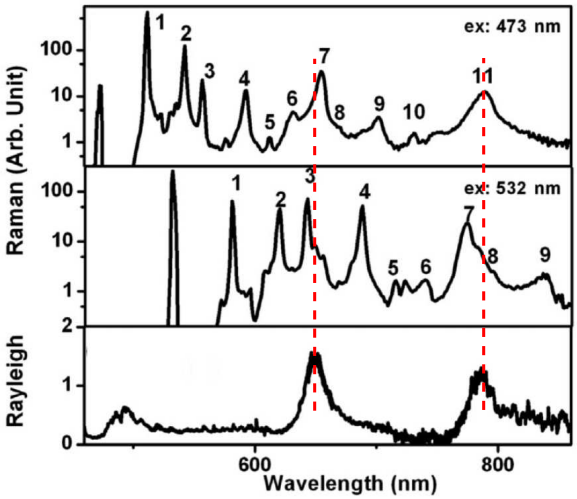

Figure 3.19: Illustration of the effect of resonant enhancement in the multi-phonon Raman process in SWNTs. By comparing of the Raman spectra (upper panel: excitation 473 nm and middle panel: excitation 532 nm) with the Rayleigh excitation spectrum (lower panel) for the same individual SWNT, the Raman modes with outgoing wavelengths close to the excitonic transitions (dashed red lines) exhibit a pronounced resonant enhancement. Adapted from [194].

Notably, the authors in this paper also observed that whereas the general decrease of the higher-order Raman intensity with increasing mode order, in specific cases higher-order modes in a SWNT can actually be stronger than the lower-order ones. As in Fig. 3.19, for two different excitation energies, strong enhancement was observed for Raman modes 7 and 11 in upper panel and modes 3 and 7 in middle panel (dashed red lines). Interestingly, the energy of these Stokes-shifted photons correspond to the excitonic transition of this SWNT, which was determined by Rayleigh scattering spectroscopy (lower panel). This behavior can be explained as a result of the electronic resonances in multiphonon Raman scattering related to the strongly peaked excitonic transitions in SWNTs. From Eq. 3.3, we can see that the multiphonon Raman process is resonantly enhanced whenever any intermediate step is close to an electronic resonance (that is a intermediate state i_j is a real electronic state and thus the energy denominators $\hbar\omega_i - \sum_j \hbar\omega_{q_j} - E_{i_j}$ vanishes.). Especially, there will be an outgoing (or the last step) resonance if i_n is a real electronic state. Due to the energy conservation condition $\hbar\omega_s = \hbar\omega_i - \sum_n \hbar\omega_{q_n}$, the outgoing resonance indeed corresponds to the emission of the Stokes-shifted photon ($\hbar\omega_s$) in resonance with an excitonic transition (see Fig. 3.18).

Similarly, for the 9-ANR film, we also observed that the 3rd and 4th order Raman modes are strongly enhanced with 405 nm excitation compared with other excitation lasers (532, 594 and 635 nm) (Fig. 3.20 - (a)). Morever, as shown in Fig. 3.20 - (b), this is further put into evidence by plotting the Raman intensities of different high-order Raman modes (normalized by the respective 2D mode intensity) for the 9-ANR film with different wavelengths and also for graphite and individual SWNT (data adapted from [195] and [194], respectively). We can see that similar to SWNT, the Raman signal intensity of the 9-ANR generally decreases with increasing phonon order more slowly than in graphite. Notably, compared to the other three excitation wavelengths, the intensity of the 3rd and 4th order Raman modes of 9-ANR is enhanced by a factor of 10 when excitation at 405 nm. This implies that the outgoing photon wavelength of these enhanced Raman modes (around 470-530 nm) could be in resonance with the excitonic transition of 9-ANR. Indeed, both the recently reported absorption spectrum of in-solution synthesized 9-ANRs [196] and the theoretical calculations on 9-ANRs [93, 197] indicated that an excitonic transition is located around this energy (see Fig. 3.21, indicated by the black solid arrow). Moreover, from the reported absorption spectrum, we can also find that these high order Raman modes are not in resonance when excitation with the other three wavelengths (indicated by the black dashed arrow).

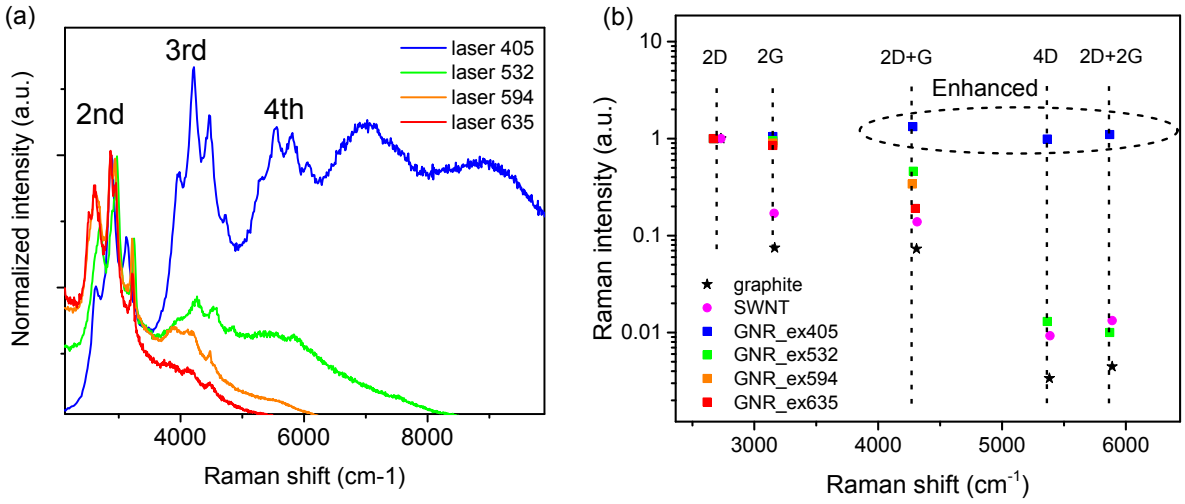

Figure 3.20: (a) - Raman spectra of the 9-ANRs film excited with different lasers. Using the 405 nm excitation, the 3rd and 4th order Raman mode are clearly enhanced, which correspond to the outgoing photons at $\sim$ 470-530 nm. All the spectra are normalized by the intensity of the 2nd order peak. (b) - Comparison of relative intensities of high order Raman modes in 9-ANR with different excitation wavelengths (405, 532, 594 and 635 nm) and also in graphite and individual SWNT (adapted from [195] and [194], respectively). All the mode intensities are normalized by the relative intensity of the 2D mode.

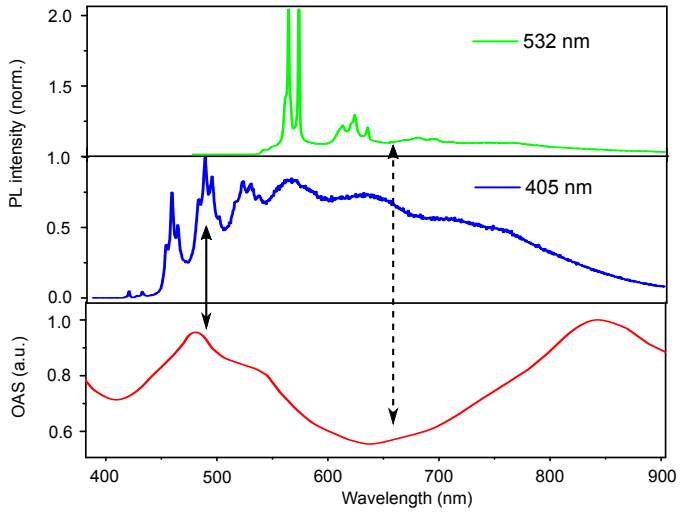

Figure 3.21: Upper panel: Raman spectrum of the 9-ANR film excited with 405 nm laser (blue line) and 532 nm laser (green line). Lower panel: Optical absorption spectrum of the solution of 9-ANRs which are synthesized by the solution-mediated method. Data adapted from [196]. When excitation at 405 nm, the outgoing photon wavelength of the 3th and 4th order Raman modes are in resonance with the excitonic transition shown in the absorption spectrum (indicated by the black solid arrow). In contrast, when excitation at 532 nm, the outgoing photon of these Raman modes are not in resonance (indicated by the dashed arrow).

Conclusion

This chapter has studied optical properties of GNRs of two different synthesis approach (solution-mediated and surface-catalyzed).

In the first section, we studied the emission properties of two GNR structures synthesized by solution-mediated approach. The samples were dispersed with SDS surfactants and the optical absorption and photoluminescence spectra as well as the life-time of the excited states have been shown. The possibility of the formation of excimer states in stacks of individual GNRs has been discussed in order to interpret the broad and highly red-shifted emission band observed on both structures. Besides, we have also shown the results of single-particle spectroscopic measurements using simultaneously confocal fluorescence microscopy and atomic force microscopy. The observation of emission of small aggregates confirms the ability of GNRs to emit light in the solid state. These results implies that in order to probe the intrinsic emission from single GNRs of this synthesis approach, one major issue is to individualize GNRs in dispersion. To realize this, we are trying to find a "good" solvent and perform the edge-functionalization.

In the second section, we have studied the effect of structural distortion on the optical properties of GNRs. Owing to the precise bottom-up chemical reactions, the Mainz group synthesized two GNR structures with the same aromatic core but one has planar geometry and the other is non-planar, which is bent by the steric repulsion with the side chains. We have performed the optical absorption and photoluminescence excitation (PLE) spectroscopy on the dispersions of these two GNRs. The results implies that the non-planar GNRs have a lower optical bandgap in agreement with the theoretical calculations, demonstrating the possibility of engineering GNR properties via controlled

structural distortion.

In the last section, we have shown our optical characterizations of the GNRs synthesized on gold surface. The sample has been transferred onto insulating substrates in order to perform the PL measurements. The microRaman results confirmed that the GNRs indeed have been transferred onto the target substrates. Spectrally broad high energy PL throughout the whole transferred GNR film has been observed, instead of bright bandgap emission. We have attributed this PL to the emission from the defects, which are created during the synthesis and could also be induced by the wet chemistry transfer method. So in the next step, the synthesis should be improved and we will also try to perform dry transfer method. At the end of this part, we have also discussed the origin of the distinct Raman features observed on this GNR sample: width specific RBLM mode, intrinsic D mode and well-resolved high order modes.

The results in this chapter shows the optical properties of bottom-up synthesized GNRs and these properties have not been observed in top-down fabricated GNRs due to the lack of structural control. Although the intrinsic emission from single GNRs has not been probed yet, our results provide a clear direction to realize it.

Part IV

Optical study of bottom-up synthesized GQDs

Summary

Introduction

Graphene quantum dots (GQDs), i.e. zero-dimensional graphene nanostructures, are attractive for potential applications such as opto-electronic devices and bioimaging markers. As seen in Chap. I, the electronic, optical and spin properties of GQDs can be in principle controlled by designing their size, shape and edges [36,59,61,198]. Similar to the situation of graphene nanoribbons, the bottom-up synthesis method makes it possible to precisely control its structure [57] and several sizes and shapes of GQDs have already been synthesized [199]. Also, due to the strong π-π stacking (aggregation effect), very few experimental studies are reported on the intrinsic optical properties of GQDs, especially in the solid state or at the single-emitter level. However, compared to graphene nanoribbons, the GQDs have a smaller aromatic core size (one to several nm, while GNRs have a length extending to tens or hundreds nm.). Thus, GQDs are expected to be more easily individualized. In this context, we performed optical spectroscopy on bottom-up synthesized GQDs to see whether we have individualized GQDs and to study their intrinsic properties. The GQDs studied in this chapter were synthesized by the group of Dr. Stéphane Campidelli at CEA Saclay.

In the first section of this chapter, I will show the steady-state and time-resolved photoluminescence spectroscopy studies on ensemble of GQDs. The results imply that the individual GQDs are indeed present in the solution. In the second section, I will go down to the single-particle level by performing microphotoluminescence spectroscopy. The nature of the observed emission from GQDs will be discussed, implying that the emission originates from their intrinsic quantum states. Then a detailed study of photophysical properties including second order photon correlation $g^{(2)}$ measurements of GQDs will be presented. Finally, edge-chlorinated GQDs will be investigated as a first example of controlled modification of the emission properties.

1 General sample information

Our GQD samples studied here were synthesized by Julien Lavie, PhD student in the group of Dr. Stéphane Campidelli at CEA Saclay. The GQDs were synthesized by the solution-mediated approach and generally consists in two steps: Diels-Alder reaction of the starting monomer precursors give the polyphenylene compounds and then the oxidative of cyclodehydrogenation polyphenylenes produces the corresponding GQDs (as we have seen in Chap. I Sec. 3.2). Moreover, the edge of GQDs can be precisely functionalized with the chlorine atoms by treatment with ICl. The intermediate polyphenylene compounds are fully characterized by ^{1}H NMR spectroscopy and the GQDs are characterized by MALDI-TOF mass spectroscopy to confirm the complete dehydrogenation and chlorination. Thus, the produced GQDs have a defined molecular structure, in contrast to the GQDs synthesized via top-down method [43, 44].

2 Optical spectroscopy on $C_{96}C_{12}$ dispersions

We now go into details of the optical properties of $C_{96}C_{12}$ GQD. As seen in Fig. 2.1 - (a), $C_{96}C_{12}$ consists of 96 sp^2 carbon atoms arranged in a triangular shape, which leads to a lateral size of ∼2 nm. Six alkyl chains ($C_{12}H_{25}$) are installed at the edge of the GQD to enhance its solubility. Its triangular shape makes it have a C_3 rotational symmetry. Moreover, according to Clar's aromatic π-sextet rule [200], C_{96} is fully benzenoid, i.e., the structure has $6n$ π-electrons, where n is an integer and thus, all the π-electrons are grouped into sextets.[37] As a consequence, the fully benzenoid structure usually has a high chemical stability. In view of the optical measurements, GQD powders were dispersed in 1,2,4-trichlorobenzene (TCB) with a concentration of ∼0.1 mg/mL (see Chap. II Sec. 3.1 for the sample preparation details). A further dilution of ×10 and ×100 was also prepared. The experimental set-up used here is described in Chap. II Sec.II.

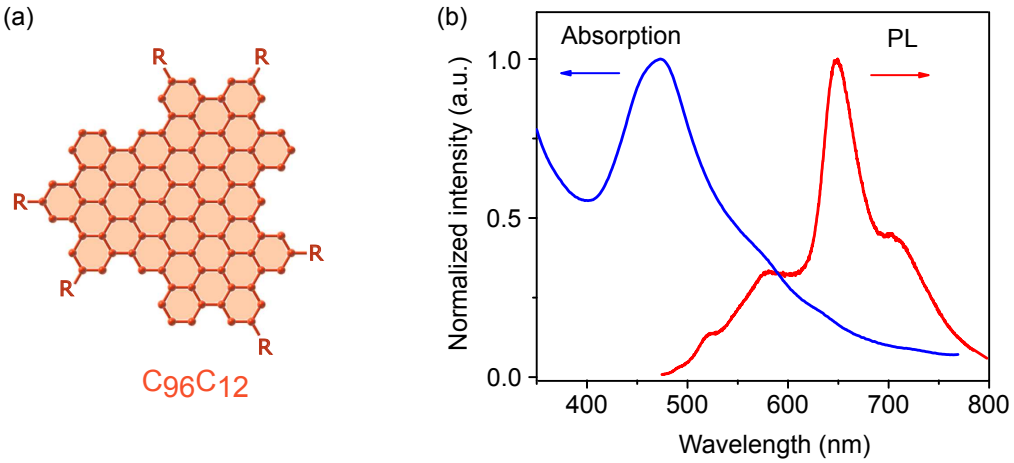

Figure 2.1: (a) - Chemical structure of $C_{96}C_{12}$ GQD. "R" stands for alkyl chain $C_{12}H_{25}$. (b) - Optical absorption spectrum (blue line) and photoluminescence spectrum (red line) of $C_{96}C_{12}$ dispersion in 1,2,4-trichlorobenzene (TCB).

2.1 Absorption, PL and time-resolved PL measurements

The blue curve in Fig. 2.1 - (b) shows the absorption spectrum of the $C_{96}C_{12}$ dispersion. An absorption line centered at 470 nm with a small shoulder at 450 nm is observed. Moreover, if we look at the low energy region, two weak lines at ∼575 nm and ∼630 nm can also be found. The red curve in Fig. 2.1 - (b) shows the corresponding PL spectrum of the $C_{96}C_{12}$ dispersion. In contrast to the PL spectra of GNR suspensions, which is structureless and very broad, the PL spectrum of $C_{96}C_{12}$ dispersion shows distinct lines. The main PL line is centered at 650 nm with a red-side shoulder at ∼705 nm. In the blue-side of the main line, there are also two weak PL lines centered at 520 nm and 575 nm.

We then performed time-resolved photoluminescence (TR-PL) measurements on the observed four PL lines. Results are displayed on Fig. 2.2 together with the impulse

[37] For our C_{96} GQD, there are 96 π-electrons so $n = 16$ sextets.

response function (IRF). The decay curves of the two low energy lines at 650 nm and 705 nm are mono-exponential with a time constant of ≈5 ns. The mono-exponential behavior reveals that the emission arises from species with the same relaxation decay. It is thus a strong indication that these two low energy PL lines originate from the emission of monomers (single GQDs). In contrast, the decay curves of the two high energy lines at 520 nm and 575 nm are multi-exponential. The multi-exponential behavior implies that the emission originates from the species with different decay dynamics. As between one aggregate and another the decay dynamics are usually not the same, multi-exponential decay is the characteristic of the emission of aggregates [116]. We thus suppose that there could be still some GQD aggregates present in the dispersion which emit between 500 nm and 600 nm.

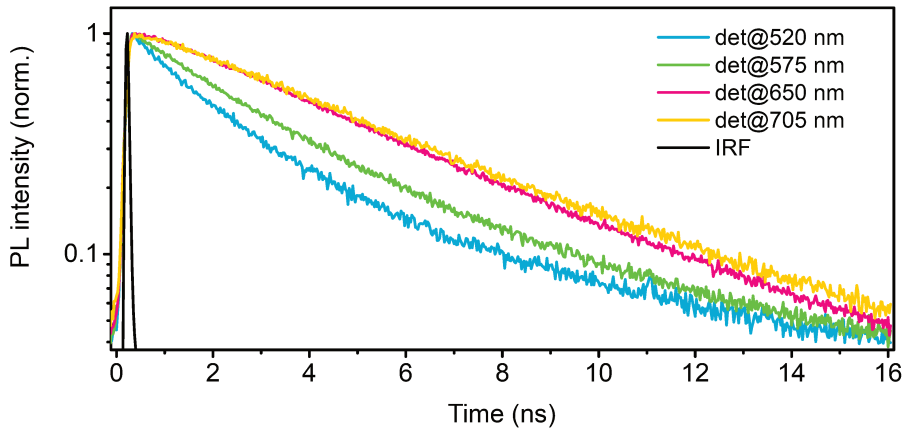

Figure 2.2: Time-resolved PL measurements on $C_{96}C_{12}$ dispersion recorded at the different PL lines (colored curves). The measured instrument response function (IRF) is also shown (black curve). We observe mono-exponential decay (≈ 5 ns) for the low energy lines (at 650 nm and 705 nm), while multi-exponential decay for the high energy lines (at 520 nm and 575 nm).

We have performed the measurements on GQD dispersions with different concentrations. The results are very similar (see Fig. 2.3)[38]. This implies that when preparing the GQD dispersion, the ultrasonication (first step) plays the major role in dissolving the GQD powders and breaking apart the aggregates, while the further dilutions have no obvious effect on the degree of aggregation. Moreover, we also observed that over the time the relative intensity of the two high energy lines increases compared to the two low energy lines (see Fig. 2.4 - (a)). 3 months after the preparation of the dispersion, the two low energy lines are totally immersed in the two high lines and become no longer resolved. It is reasonable that the emission at 650 nm now is dominated by the tail of the high energy line, which have a multi-exponential decay, in instead of the corresponding PL line with mono-exponential decay. Indeed, when we performed the time-resolved PL measurements detecting at 650 nm, the curve turns to be multi-exponential (see Fig. 2.4 - (b)). This evolution of PL and TR-PL spectra as a function of time suggests that the monomers of GQDs may gradually re-aggregate after the preparation of dispersion.

[38]The measurements are not performed on the same day: first the stock solution, then the solution of dilution × 10 and finally the solution of dilution × 100. The slight differences (i.e. the solution with lower concentration has broader absorption, more intense emission at high energy region and more obvious multi-decay behavior for the TR-PL) are thus presumably due to the re-aggregation effect. See the following discussion.

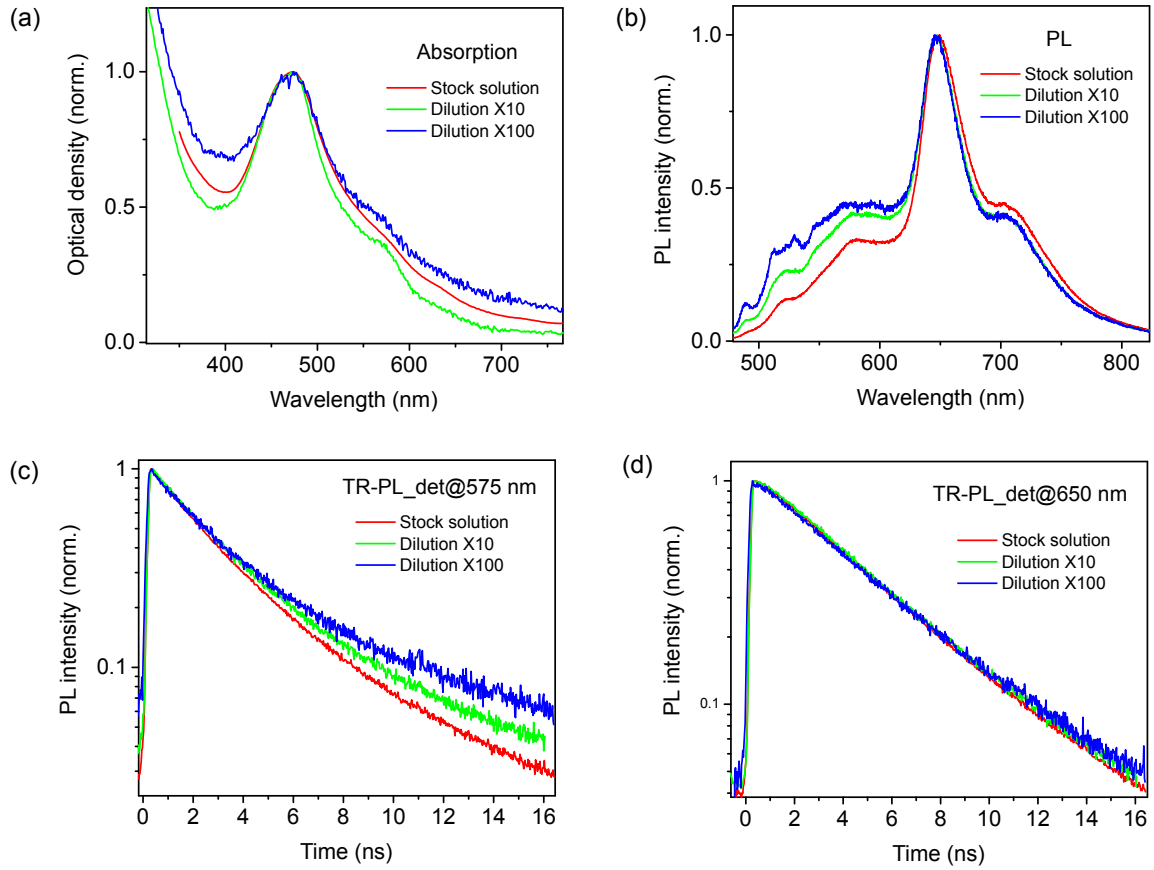

Figure 2.3: Optical absorption (a), PL (b) and TR-PL (c and d) spectra of the $C_{96}C_{12}$ dispersion of different concentrations (stock solution in red, solution of dilution $\times 10$ in green and solution of dilution $\times 100$ in blue). For the TR-PL spectra (a and b) the signal is detected at 575 nm and 650 nm, respectively.

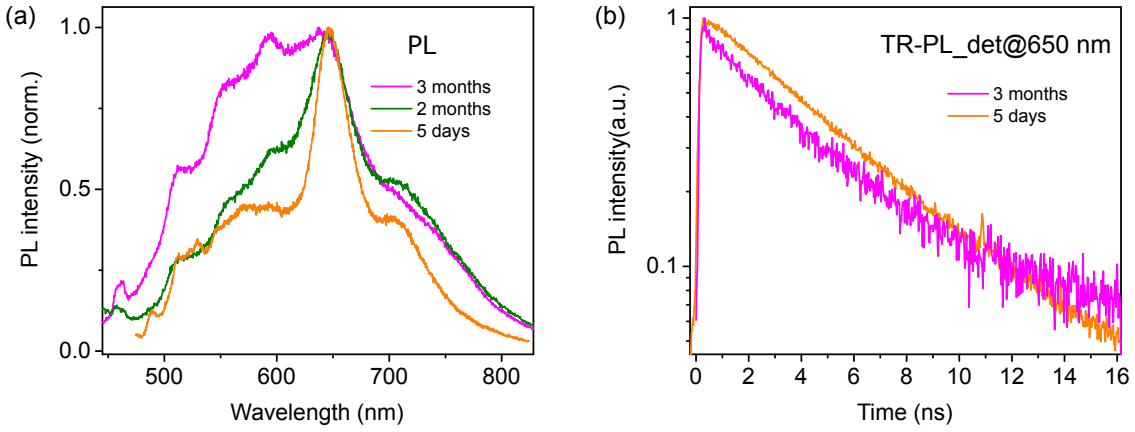

Figure 2.4: Time evolution of the PL spectrum (a) and TR-PL (b) of $C_{96}C_{12}$ dispersion. For the TR-PL spectra the signal is detected at 650 nm.

2.2 Photoluminescence excitation measurements

To get insight into the absorption behavior corresponding to each PL line, we performed photoluminescence excitation (PLE) measurements on $C_{96}C_{12}$ dispersion.

Before looking at the PLE spectra, we first plot the PL spectrum of $C_{96}C_{12}$ dispersion at different excitation wavelength (Fig. 2.5). We can see that the general shape of the PL spectra does not change with the excitation wavelength . This observation is in stark contrast with the top-down fabricated GQDs [150] or carbon dots [149], in which the emission wavelength red-shifts when increasing excitation wavelength (characteristic of the emission of defects). One should note that depending on the excitation wavelength there are some slight variations in the PL spectrum of $C_{96}C_{12}$ dispersions: when the excitation wavelength is between 500 and 600 nm, the whole PL spectrum becomes very broad (purple curve on Fig. 2.5). In contrast, when the excitation wavelength is longer than 600 nm, the two low energy PL lines become well-resolved (green curve). One possible explanation is that when the excitation wavelength is between 500 and 600 nm, the aggregates are more efficiently excited, while for longer excitation wavelengths, mostly monomers can be excited.

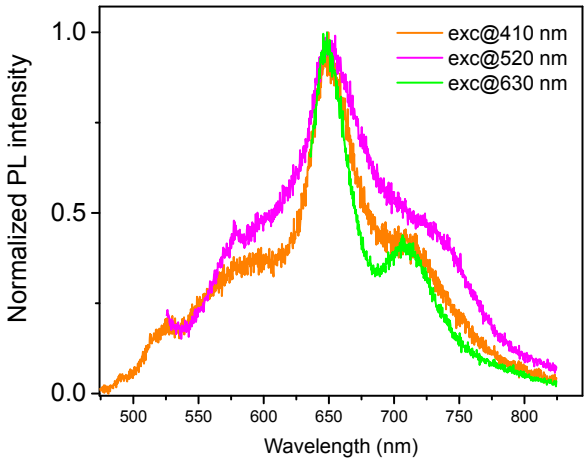

Figure 2.5: Normalized PL spectra of $C_{96}C_{12}$ dispersion excited at different wavelengths.

Fig. 2.6 - (a) displays the PLE spectra detected at the two low energy PL lines (650 nm and 705 nm) (green and purple respectively). We can see that the two PLE spectra show the very same behavior and they follow very well the trends of the absorption spectrum (blue). Moreover, these two PLE spectra are much more structured than the absorption spectrum. Even the very weak bands in absorption spectrum (bumps at 575 nm and 630 nm) are well-resolved in these PLE spectra. Meanwhile, Fig. 2.7 displays the PLE spectra detected at the two high energy PL lines (520 nm and 575 nm) (brown and orange respectively). We can see that these two PLE spectra are structure-less, in contrast to the PLE spectra detected at 650 nm and 705 nm. Moreover, these two PLE spectra are both blue-shifted compared to the absorption spectrum (blue) and the PLE spectrum detected at 520 nm is more blue-shifted than the one detected at 575 nm. In the next section, we will discuss these PLE results and the possible origin of the PL lines.

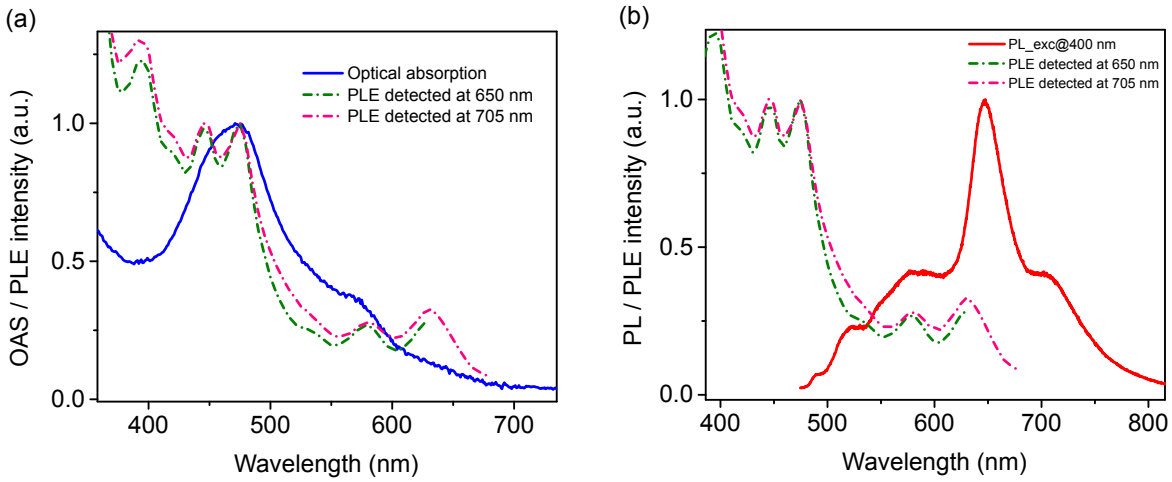

Figure 2.6: (a) - PLE spectra of $C_{96}C_{12}$ dispersion detected at the two low energy PL lines (green and purple), together with the optical absorption spectrum (blue). (b) - PLE spectra detected at the two low energy PL lines (green and purple), together with the PL spectrum (red).

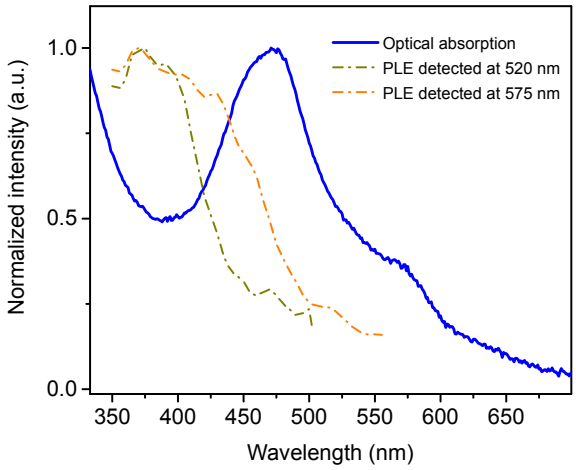

Figure 2.7: PLE spectra of $C_{96}C_{12}$ dispersion detected at the two high energy PL lines (brown and orange), together with the optical absorption spectrum (blue).

2.3 Discussion on the results of $C_{96}C_{12}$ dispersion

We now discuss the origin of the PL lines of $C_{96}C_{12}$ dispersion and the possible species present in $C_{96}C_{12}$ dispersion.

First, for the two PL lines at low energy region (650 nm and 705 nm), the corresponding PLE spectra shows the very same behavior and are in good agreement with the absorption spectrum, which implies that these two lines originate from the same species and these species are majority in the dispersion. Moreover, several resonances are clearly resolved in the PLE spectra and these two PL lines has mono-exponential decay dynamics with the same characteristic time (≈5 ns). All these results suggest that these two PL lines originate from the intrinsic emission of $C_{96}C_{12}$ monomers. We also compared these two PLE spectra with the PL spectrum (see Fig. 2.6 - (b)). We note

that the position of the first band in the PLE spectra is roughly the same as the main PL line (centered at 650 nm), which implies that the emission corresponds to the same electronic transition as this lowest absorption band. We will go into detail on the origin this transition and the electronic structure of $C_{96}C_{12}$ GQD in Sec. 3.1.

For the two high energy PL lines (520 nm and 575 nm), the PLE spectra have the different behavior with the absorption spectrum, which implies that the corresponding species of these two lines are minority in the dispersion. Moreover, the shape of the PLE spectra are relatively structure-less and these two PL lines show multi-exponential decay dynamics. One possible origin of these two high energy PL lines is the aggregates of $C_{96}C_{12}$ GQDs in the dispersion.

One possible reason for these two high energy PL lines is the presence of structurally imperfect GQDs. Since the MALDI-TOF mass spectroscopy does not have an enough resolution to exam the species with a very small quantity. We may have a question whether it is possible that the sample contains a minority of GQDs that are partially dehydrogenated in the last step of the synthesis. If this occurs, the partially dehydrogenated GQDs has the open-bond sp^3 defects and smaller π-conjugated size, which could lead to a blue-shifted transition. However, as we have seen, the intensity of two PL lines is very weak when just after the preparation and over the time their intensity increases. This behavior is more likely to be related to the aggregation effect rather than the partially dehydrogenated GQDs.

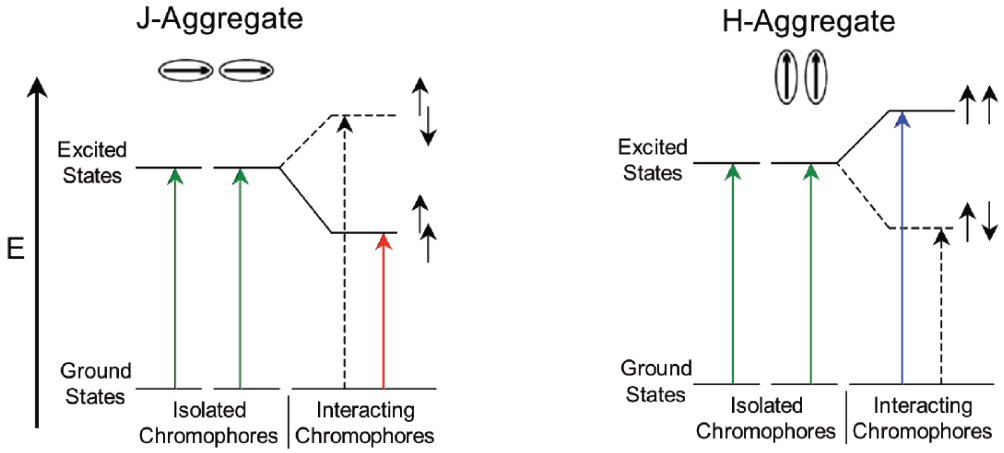

Figure 2.8: Schematic illustration of the energy diagram of J-aggregate that the transition dipoles are in-line (left) and H-aggregate that the transition dipoles are parallel (right). Adapted from [201]

It is interesting to discuss that which type of aggregates could lead to such blue shifted emission. Recalling the theory of coherent molecular aggregates, which was developed by Kasha in 1965 [201], the variation of the absorption transition when forming aggregates results from the coupling of the electromagnetic quantum dipole of each molecule. This dipole-dipole coupling give rise to a splitting of the initial energy level of the molecule monomers. As we can see in Fig. 2.8 left, when the molecules assemble in a top-bottom configuration (called J-aggregate), the dipoles are in-line. In this configuration, the low energy transition is allowed, while the high energy transition is forbidden, which results in the red-shift of the absorption and emission spectra. When the molecules assemble in a cofacial configuration (called H-aggregate, shown in the

right), the dipoles are parallel. In this configuration, the low energy transition is forbidden, while the high energy transition is allowed, which results in the blue-shift of the absorption and emission spectra. Considering the planar π-conjugated structure, $C_{96}C_{12}$ GQD favorably stack together forming H-aggregate. Therefore, the two high energy PL lines together with also blue-shifted PLE spectra are consistent with the behavior of H-aggregate. Thus, it is likely that these two PL lines originate from the densely stacked H-aggregates, which have efficient parallel dipole-dipole coupling. Moreover, the theory indicates that for H-aggregates the more molecules are coupled, the more blue-shift is [202]. So the PL line at 520 nm may originate from the larger aggregates than the line at 575 nm (e.g. the line at 575 nm may correspond to the emission of dimers, while the line at 520 nm corresponds to the emission of trimers or tetramers).

We also note that the absorption spectrum is broader and less resolved compared to the PLE spectra of the two low energy PL lines. Depending on the excitation wavelength, sometimes the PL spectrum is also relative broad. This implies that in the GQD dispersion there are some species that do not efficiently emit neither at the two low energy lines nor the two high energy lines but still contribute to the absorption. These species may be aggregates with a configuration where the orientation off dipoles are random and their electronic coupling is relatively weak, but such aggregates may have some mechanical coupling, which results in the broadening of the spectra.

Despite of the discussion above, it is very necessary to know the structure of the aggregates in the $C_{96}C_{12}$ GQD dispersion and build the theoretical model. These procedures are not only for explaining the optical results obtained here but also for understanding the mechanism of the interaction between such large nanographenes, which is an essential step for realizing their applications.

In this perspective, we have sent the $C_{96}C_{12}$ GQD dispersion to Dr. Hanako Okuno at CEA LETI, Grenoble, to perform high-resolution TEM experiments. The preliminary results are shown in Fig. 2.9. We found some well-organized "graphene-like" structures (highlighted by yellow circles), probably corresponding to the $C_{96}C_{12}$ monomers or the small H-aggregates (dimers or trimers). We also found some long columns with a relatively loose structure (highlighted by the red circle). These columns are presumably formed by an array of vertically standing GQDs and they could account for the broadening of the absorption spectrum. Indeed, the formation of such column packing has already been observed in a small triangle-shaped nanographene [203].

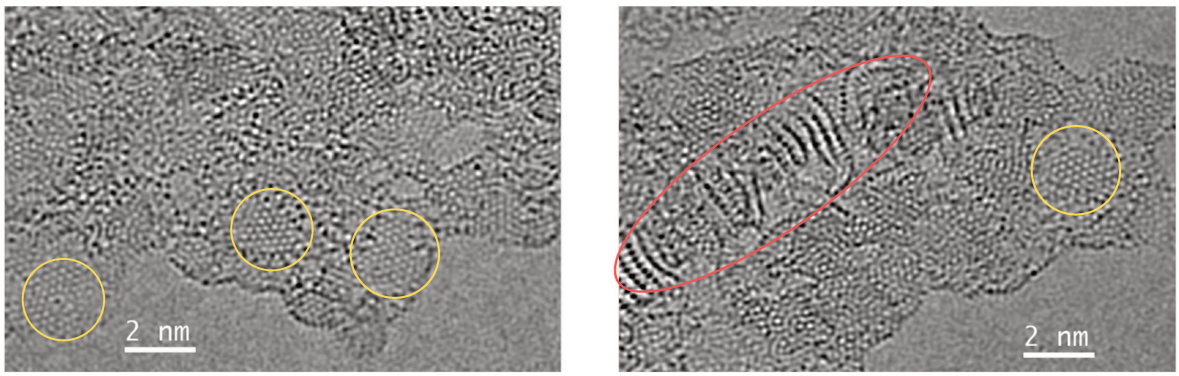

Figure 2.9: High-resolution TEM images of the sample prepared from the $C_{96}C_{12}$ dispersion with a $\times 100$ dilution. Substrate: graphene.

3 Optical study of single $C_{96}C_{12}$ GQDs

Having the strong indication that C_{96} GQDs are individualized in solution, we performed single-particle measurements, which allow us to overcome averaging effect inherent to the measurements on ensemble and to address the intrinsic properties of single GQDs. Here we performed a microphotoluminescence study using a home-built confocal microscopy under ambient conditions (for more details, see in Chap. II Sec. 2.1). The samples for this study were prepared following the procedures described in Chap.II Sec. 3.2. In general, we first mixed the C_{96} GQD solution with a solution of polystyrene (PS). The blend of GQD/PS was subsequently spin-coated onto a coverslip, leading to a thin film of polystyrene (thickness ∼25-50 nm) with C_{96} embedded in it. It is well-known that the surface charges of substrate could result in the degradation of the emission efficiency of quantum emitters [134,204]. Thus, embedding GQDs in a polystyrene matrix is expected to reduce these perturbations and also to isolate the GQDs from oxygen.

3.1 Microphotoluminescence spectroscopy of single $C_{96}C_{12}$ GQDs

PL maps

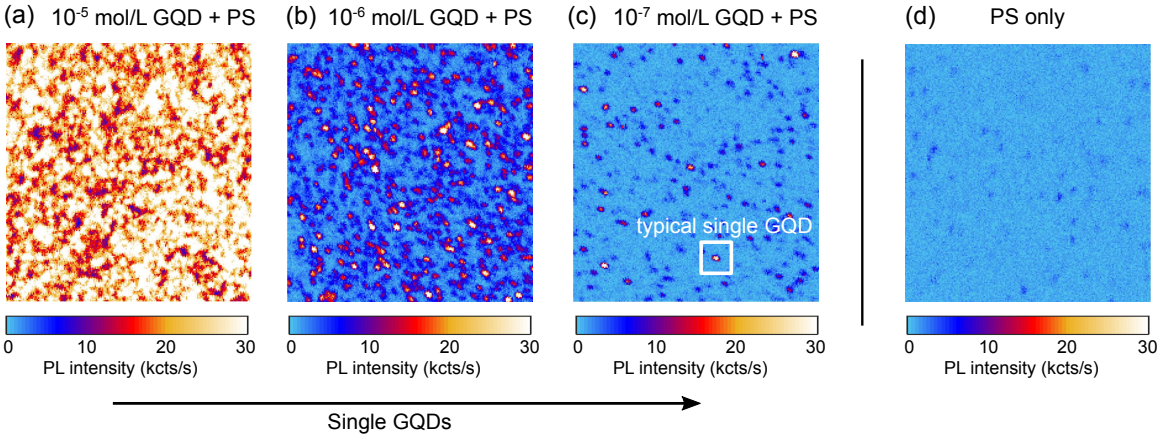

Figure 3.1: PL raster scan images of $C_{96}C_{12}$ GQDs embedded in a polystyrene matrix spin-coated from $C_{96}C_{12}$ solutions with different concentrations: (a): 10^{-5}mol.L^{-1}; (b): 10^{-6}mol.L^{-1}; (c): 10^{-7}mol.L^{-1} and (d): raw polystyrene film without GQDs. Size of all PL images: 20 × 20 μm^2. Excitation wavelength: 594 nm. Excitation power: 200 nW.

We first performed PL raster scan on the $C_{96}C_{12}$ samples. Since the solution PL results indicate that the sample may still have some aggregates emitting in the high energy region between 500 and 600 nm (see Fig. 2.1), we first used a continuous-wave laser diode at 594 nm as the excitation source in order to excite preferentially the monomers. The excitation power was set to 200 nW (∼ 120 W/cm^2). A long-pass filter with cut-off wavelength at 600 nm was put on the detection path to suppress the excitation laser signal (the transmission curves of the dichroic mirror and the long-pass filter for this excitation laser are shown in Chap. II Fig. 2.3) and the emission signal from the sample was detected by the APDs.

Fig. 3.1 shows typical PL intensity maps of the samples spin-coated from the solutions with different concentrations of $C_{96}C_{12}$ GQDs. We can see that when a highly concentrated solution (10^{-5}mol.L^{-1}) is used to make the sample, the whole PL image shows very strong luminescence signal (see Fig. 3.1 - (a)). When the concentration decreases, the spatial distribution of PL signal becomes more and more localized (Fig. 3.1 - (b)) and finally we observed mostly point-like spots (Fig. 3.1 - (c)). This correlation between the GQD concentration and the intensity of PL image ensures that the signal do arise from GQDs. For the highest dilution sample (Fig. 3.1 - (c)), we can easily find localized bright spots with intensity ∼30 kcounts/s (indicated by the white square). The density of such spots is about 2-5 per 100 μm^2. Moreover, we also performed PL scan on raw polystyrene films without GQDs as control experiment. Indeed, it is reported that organic solvents, polymer matrix and glass coverslips may contain quantum emitters [205–207]. This optical contamination could lead to the misinterpretation of the single-emitter spectroscopy results. As shown in Fig. 3.1 - (d), at the same experimental conditions, the polystyrene films shows very weak PL signal in contrast to the GQD samples. Although we can observe some PL spots with intensity less than 10 kcounts/s, they bleach quasi instantaneously in strong contrast with the bright GQD spots that are stable for hours. This result confirms again that the bright spots originate from GQDs.

Fig. 3.2 shows a magnified image around a typical localized and bright spot (each pixel corresponds to 20 nm). This image is fitted by a two-dimensional Gaussian function. The fit gives a $1/e^2$ spot diameter of ∼600 nm in good agreement with the diffraction limit of our set-up (see Chap. II Sect. 2.1). This implies that the emission arises from a point-like emitter, which could be a single C_{96} GQD. In the following parts, we will perform the optical characterization of these diffraction-limited bright spots.

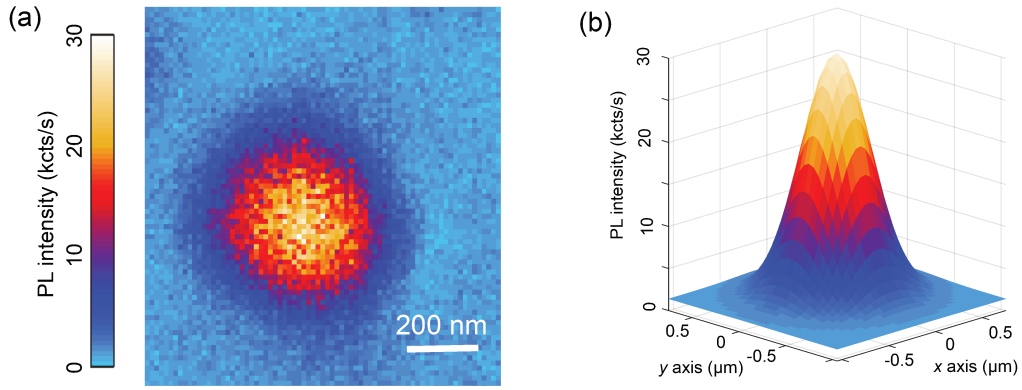

Figure 3.2: (a) - Magnified PL raster scan image around a typical localized and bright spot. (b) - Two-dimensional Gaussian fit of this image shown with a 3D representation. The fit gives a $1/e^2$ spot diameter of ∼600 nm, which is in good agreement with the diffraction limit of our set-up (see Chap. II Sect. 2.1 for more information).

PL spectra

A typical PL spectrum acquired on such a spot is displayed on Fig. 3.3 - (a). For this particular $C_{96}C_{12}$ GQD, the spectrum is composed of three lines, noted 1, 2 and 3, centered at 653 nm (1.90 eV), 719 nm (1.73 eV) and 797 nm (1.56 eV), respectively. The full width at half maximum of the main line is of the order of 27 nm (80 meV). Note that this line shape is very similar to the low energy part of the PL spectrum of $C_{96}C_{12}$ solution (Fig. 2.1). We have acquired the PL spectrum on more than 25 GQDs. The shape of PL spectra are generally very same with slight variations of the relative intensity between three PL lines. We thus tentatively fitted all the spectra by using three Lorentzian peaks (Fig. 3.4 - (a)). We observe that the highest energy line (line 1) always has an asymmetric profile. Nevertheless, the fitting procedures well give the position of each line. Fig. 3.3 - (b) shows line 1 wavelength distribution. We can see that for this set of 25 GQDs, line 1 is mostly located between 615 nm and 660 nm and no GQDs with line 1 longer than 670 nm are observed.[39] Such variation of emission wavelength might result from the differences in the local environments of GQDs.

Moreover, from the fits we also find an average energy splitting of 170±5 meV between lines 1 and 2 (ΔE_{1-2}) and 165±10 meV between line 2 and 3 (ΔE_{2-3}) (Fig. 3.4 - (b) and (c), respectively). Moreover, for each spectrum the value of ΔE_{1-2} and ΔE_{1-2} are almost the same (the difference usually less than 5 meV)(Fig. 3.4 - (d)).

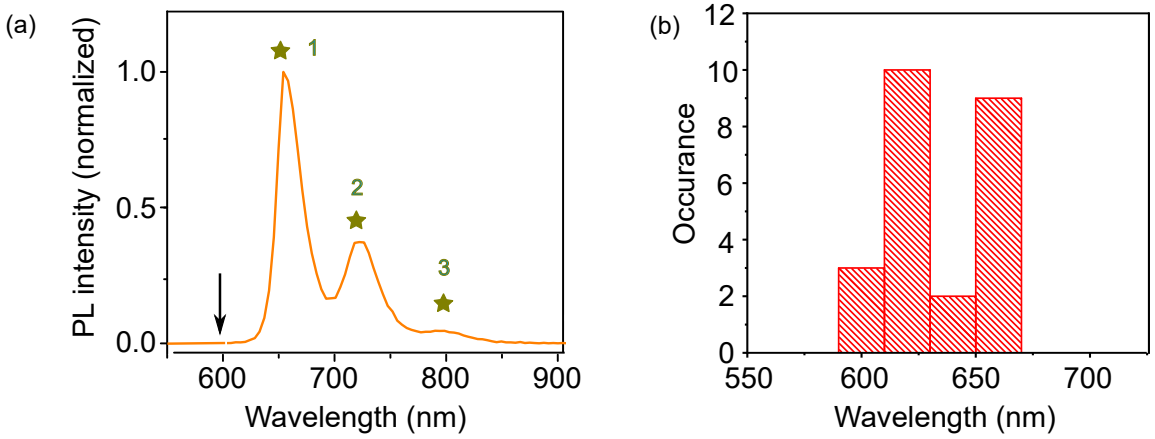

Figure 3.3: (a) - Typical Room-temperature PL spectrum of single $C_{96}C_{12}$ GQD. Arrow indicates the excitation laser wavelength (594 nm). (b) - Histogram of the line 1 wavelength position for a set of 25 single $C_{96}C_{12}$ GQD.

[39]Note that the wavelength of line 1 can tentatively be categorized into two families: one is around 620 nm (2.00 eV) and the other is around 655 nm (1.89 eV). It is known that some single defects in wide-band-gap materials could have different charges states that have very different optical properties like the emission wavelength, e.g. nitrogen-vacancy (NV) in diamond could have NV^-, NV^0 and optical inactive NV^+ states [208–210]. Thus, for the works in the future, it is worth to acquire more PL spectra to confirm whether GQD could have different emission families and to further investigate the origin of such differences.

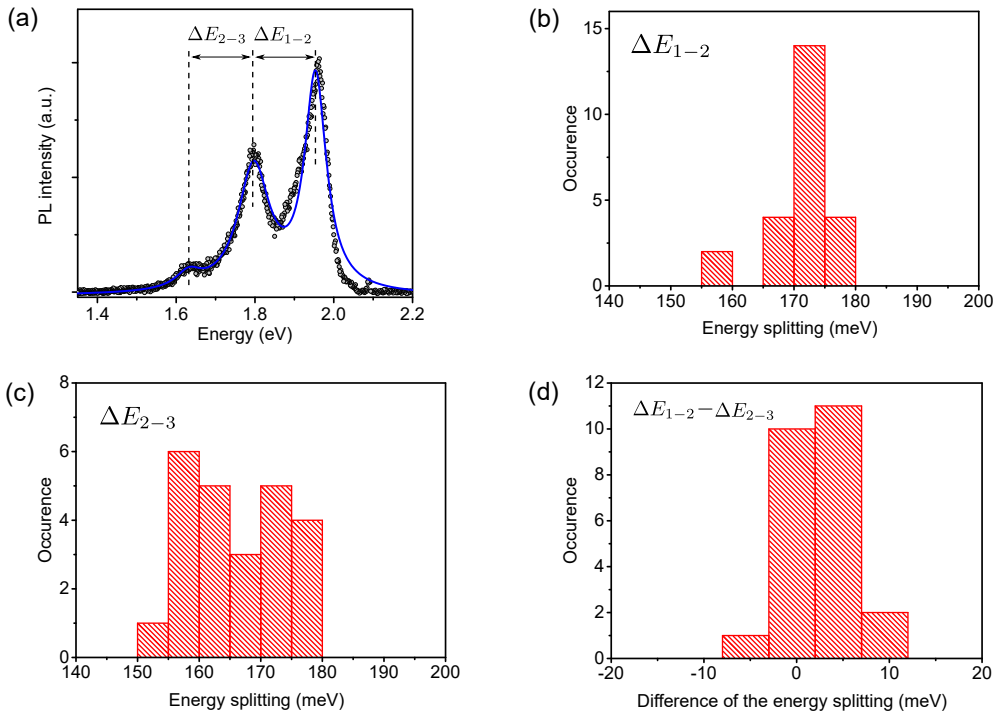

Figure 3.4: (a) - PL spectrum of a GQD displayed in photon energy. Blue line is the fit using Lorenzian functions. ΔE_{1-2} and ΔE_{2-3} denote the energy splitting between line 1 and 2 and line 2 and 3, respectively. (b) and (c) - Histograms of the values of ΔE_{1-2} and ΔE_{2-3}, respectively. (d) - Histogram of the difference between ΔE_{1-2} and ΔE_{2-3}.

To confirm that the two high energy lines (between 500 - 600 nm) observed in solution originate from aggregates rather than single GQDs (monomers). We have also performed PL spectroscopy on $C_{96}C_{12}$ GQD spots using a green laser at 532 nm (2.33 eV) with the corresponding dichroic mirror and long-pass filter cutting off at 550 nm (see in Chap. II Fig. 2.3 for the transmission curves). In such way, if this two high energy PL lines observed in solution were intrinsic to $C_{96}C_{12}$ GQDs, we would expect to observe them when we excited at 532 nm. Fig. 3.5 - (a) shows the PL spectra acquired on the same $C_{96}C_{12}$ spot with the two different excitation wavelength (532 nm and 594 nm)[40]. We can see that the obtained spectrum is almost the same[41] and nothing appears at the high energy part when the excitation is at 532 nm. This confirms again that the two high energy lines observed in solution stems from the aggregates. We should note that here we excited the spots with only two different excitation wavelengths. In the future, a detailed photoluminescence excitation (PLE) measurements, e.g. using the supercontinuum coupled to the AOTF filter as a variable source, should be performed in order to investigate the electronic structure of $C_{96}C_{12}$ GQDs at single-object level.

Moreover, in the domain of semiconductor optics, it is well know that in high excitation regime, two or more excitons can be present and their interaction can lead to some new features appearing in the PL spectrum. For example, people have detected biexciton emission in CdSe/ZnSe quantum dots [211] and charged exciton (trion) emission peaks

[40]To do this, we first acquired the PL spectrum using 594 nm laser. We then switched to 532 nm laser together with the corresponding dichroic mirror and long-pass filter. We performed the PL scan to find the spot and acquired the PL spectrum on it.

[41]The slight difference is presumably due to the change of the grating angle of spectrometer.

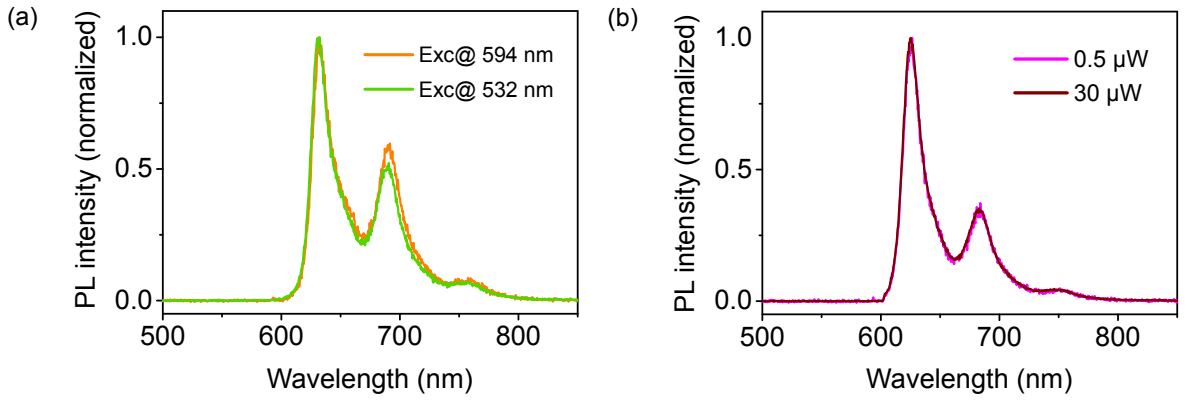

Figure 3.5: (a) - PL spectra of a single GQD at different excitation wavelength. Orange line: 594 nm. Green line: 532 nm. (b) - PL spectra of a single GQD at different excitation powers using 594 nm laser. Purple line: 0.5 μW. Dark red line: 30 μW.

have also been observed in single-walled carbon nanotubes (SWNTs) when excitation higher than 1 kW/cm^2 [212]. Moreover, people have recently reported observation of a biexciton state in GQDs with a similar structure to our C_{96} by pump-probe measurements [100]. In this context, we performed PL spectroscopy at high excitation power in order to search such multi-exciton process in our $C_{96}C_{12}$ GQDs. Fig. 3.5 - (b) shows the PL spectrum with a high excitation power of 30 μW(∼18 kW/cm^2). We can see that the spectrum does not change compared to that with low excitation power (0.5 μW). For future investigations, it is worth to perform the measurements under pulsed regime with a high peak power. Moreover, since the PL spectrum is relatively broad at room temperature, performing the PL measurements at low temperature would be very valuable and will be an axis of research in our group.

Discussion on the nature of photoluminescence

Having detected the photoluminescence from single $C_{96}C_{12}$ GQDs, we now discuss the nature of the quantum states at the origin of the observed three PL lines. From a structural point of view, our GQDs can be considered as polycyclic aromatic hydrocarbons (PAHs) with large aromatic core size. As the "unit cell" of PAHs, the electronic structure of benzene is well understood (see Fig. 3.6 - (a) left). One would expect four possible HOMO-LUMO transitions, i.e. from the $\pi_{2,3}$ into $\pi^*_{4,5}$. By including configuration interactions (CI)[42], the degenerate configuration states are split. Finally, as shown in Fig. 3.6 - (a) right, benzene is found to have two dark transitions which arises from the ground state $^1A_{1g}$ to two symmetry-forbidden $^1B_{1u}$ and $^1B_{2u}$ states and a bright transition to higher energy $^1E_{1u}$ state, characterized by a twofold degeneracy and a large oscillator strength. From the nomenclatures derived from group theory, these two low energy symmetry-forbidden transitions are called α and p bands and the high energy bright transition is called β band [213]. By analogy with benzene, the absorption spectra of PAHs also display similar dark low energy α, p and bright high energy β bands (Fig. 3.6 - (b)). Moreover, the lowering of symmetry in PAHs will make the degeneracy of β band lifted, leading to the appearance of a β' band. Besides, due to the coupling with the vibrations of the lattice or symmetry breaking[43], the two dark transitions α and p band can be brightened by borrowing oscillator strength from the β band [214].

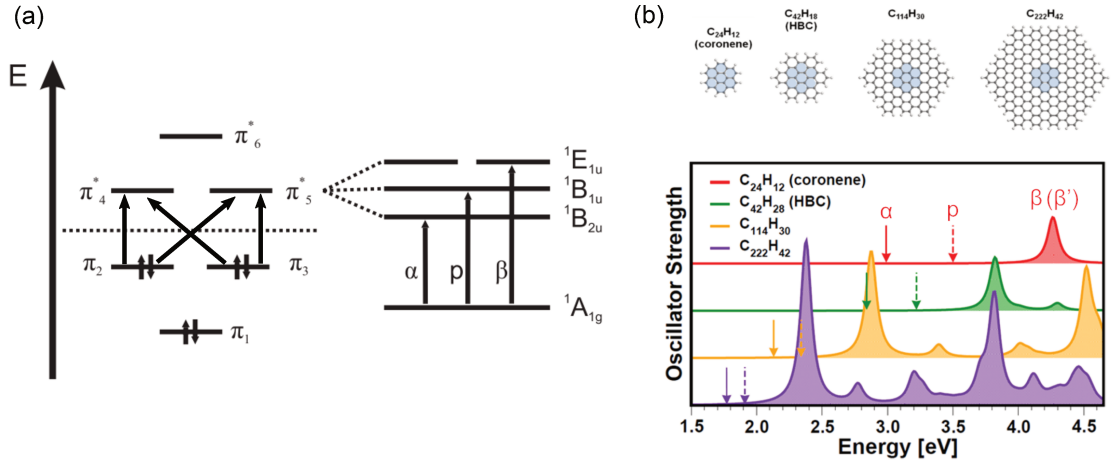

Figure 3.6: (a) - Energy levels and configurations of benzene (left) and the electronic transitions obtained from configuration interaction (CI) correction (right). Adapted from [215]. (b) - Calculated optical absorption spectra of a series of hexagonal PAHs (D_{6h} point group symmetry) of different sizes. Similar to benzene, they have two low energy dipole-forbidden transitions (α and p bands, indicated in the spectra by solid and dashed arrows, respectively) and a high energy intense absorption peak (β band), which is given by a doubly degenerate transition. For the lower symmetry PAHs, the degeneracy will be lifted, leading to the appearance of a β' band. Adapted from [90].

With this picture in mind, looking back on the optical absorption and PLE spectra of $C_{96}C_{12}$ GQD solution, the two intense lines at 445 nm and 470 nm together with

[42]This approach accounts for the electron correlation effects, i.e. the motion of one electron can influences other electrons. In contrast, the basic HartreeFock method considers that the the electrons move in the average potential field of all the other electrons.

[43]The symmetry breaking can be due to, e.g., structural distortion and charge fluctuations induced by the local environment.

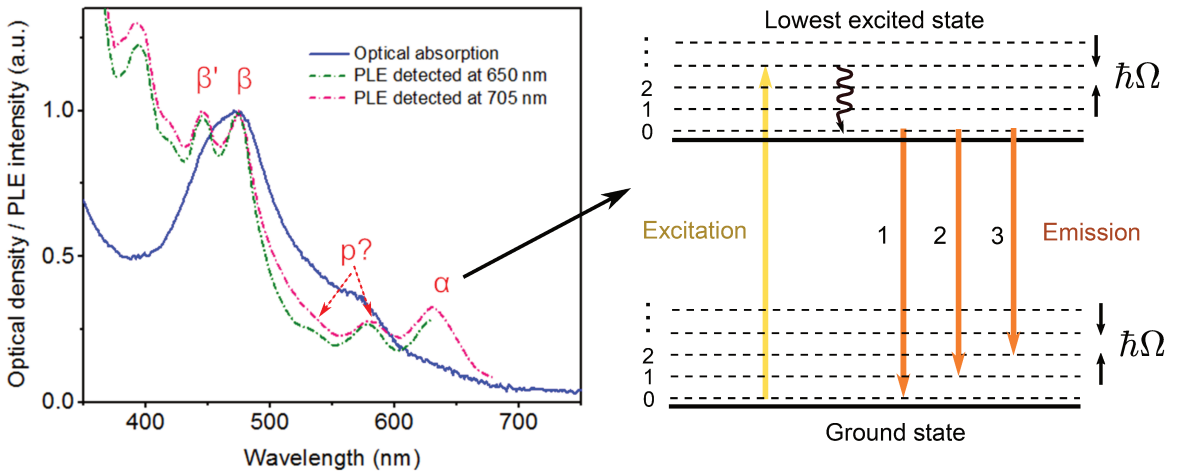

Figure 3.7: Left: optical absorption spectrum of $C_{96}C_{12}$ GQD in solution (blue solid line) and PLE spectra (green and red dash-dot lines). The observed peaks can be assigned to α, p, β and β' bands, according to Clar's notations [215]. One should note that there are two possibilities for the assignment of the p band. One is the peak at 580 nm. Another is the bump at ~530 nm. In this case, the peak at 580 nm would be the 1-0 vibronic transition of α band, since the splitting between the peak at 580 nm and 630 nm is also 170 meV. Right: schematic illustration of the proposed nature of the photoluminescence of $C_{96}C_{12}$ GQD by a simplified Jablonski diagram. The two solid lines represent the electronic states and the dashed lines represent vibrational states. The observed PL corresponds to the lowest transition (α band) and the its three lines correspond to the 0-0, 0-1 and 0-2 vibronic (i.e. vibrational-electronic) transitions, respectively, with energy splitting $\hbar\Omega = 170$ meV.

the two relatively weak lines at 580 nm and 630 nm are in very good agreement with the four characteristic transitions α, p, β and β' (see Fig. 3.7 left). Thus, the main PL line at ~650 nm, which is very closed to the lowest line of PLE spectrum (630 nm), could correspond to the emission line of α band. Moreover, as we have seen in Fig. 3.4, the energy splitting between the successive PL lines is almost equal with a value of ~170 meV. Since this value is very close to the C=C stretching vibration mode, we tentatively attribute the first PL line to the 0-0 transition of α band followed up with two vibronic replicas, with a quantum of vibration $\hbar\Omega = 170$ meV (as illustrated by a simplified Jablonski diagram in Fig. 3.7 right).

One should note that the energy splitting of between the two PLE lines at 580 nm and 630 nm is also 170 meV. It is possible that the line at 580 nm is the 1-0 vibronic transition of α band rather than the higher electronic transition p band. It can be seen here that further studies, including calculations and the PLE measurements on single $C_{96}C_{12}$ spots, are necessary for a full understanding of the electronic structure.

Polarization response

Finally, to investigate the polarization response of $C_{96}C_{12}$ GQD, we performed the polarization-resolved PL measurements on single GQD spots. For these measurements, we acquired the PL spectrum as a function of the excitation (detection) polarization angle. Fig. 3.8 - (a) shows the results of excitation angle dependence of a typical single

GQD spot. From the 2D PL intensity map (upper panel), we plot the intensities of the three PL lines as a function of the excitation polarization angle (lower panel). For all the three PL lines, the polarization response are fitted with a $\cos^2(\theta)$ function. The fits gives that the three PL lines have the same response to the excitation polarization. The polarization direction is at 105°(indicated by the black dashed line). Moreover, the polarization visibility $(I_{max} - I_{min})/(I_{max} + I_{min})$ are more than 95% (line 1: 97%, line 2: 98% and line 3: 98%). These results show undoubtedly that the GQD has a defined single linearly polarized absorption transition dipole. Similarly, as shown in Fig. 3.8 - (b), we performed the emission polarization measurements by varying the detection polarization angle. We can see that the main PL line (line 1) is polarized in the same direction as the excitation one at 15°(indicated by the black dashed line) with a polarization visibility of 75%. Meanwhile, for the line 2 and line 3, which we tentatively attribute to the vibronic replicas, the detection polarization angle is slightly shifted by 5° (both at 100°) with a polarization visibility of 78% and 86%.

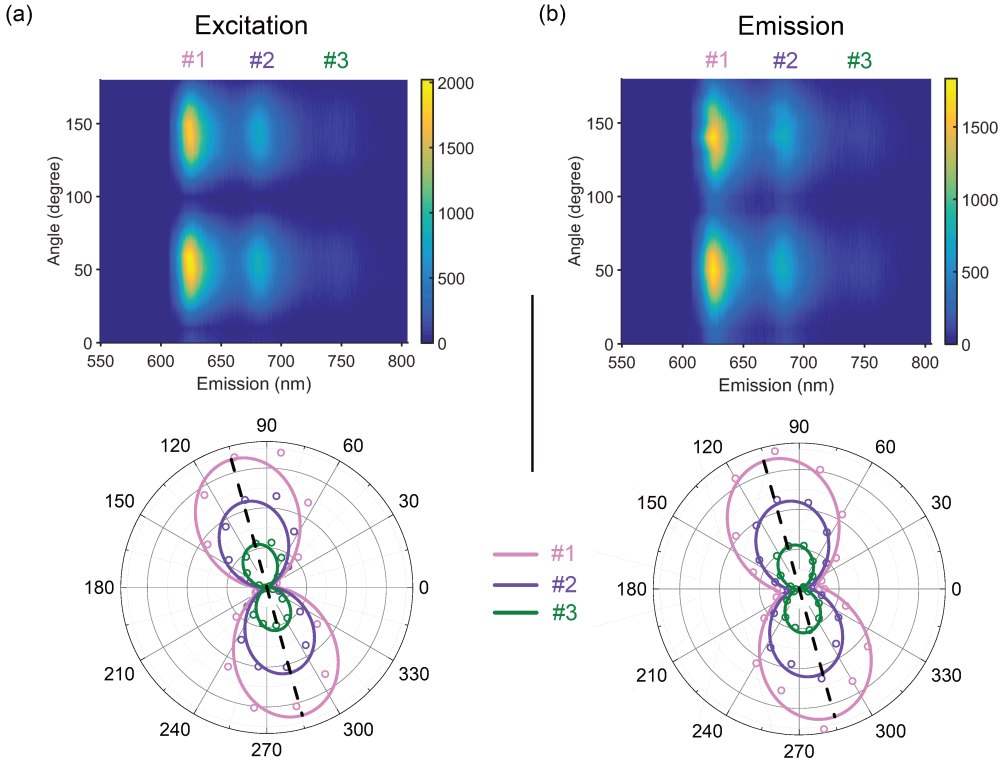

Figure 3.8: (a)- Polarization measurements of a single GQD in excitation. Upper panel in (a): PL intensity plot as a function of the polarization excitation angle. Lower panel in (a): The corresponding excitation polarization diagram of the three PL lines. (b)- Polarization measurements of the same GQD in detection. Upper panel in (b): PL intensity plot as a function of the polarization detection angle. Lower panel in (b): The corresponding detection polarization diagram of the three PL lines. Solid lines in polarization diagrams are the fits using a $\cos^2(\theta)$ function. The black dashed lines indicates the polarization direction. Excitation wavelength: 594 nm.

We have performed such polarization measurements on 10 single GQDs. The excitation diagram of the three PL lines and the emission diagram of the main PL line are always polarized in the same direction with a high polarization visibility. In contrast, for line 2 and 3, their emission polarization diagrams always show more or less difference with the main line and between these two lines the diagram can also be very different.

Fig. 3.9 shows the emission polarization measurements on an another GQD, in which the emission diagram of the three lines are clearly very different. The emission polarization of the main line is still parallel to the excitation polarization at an angle of 165° (polarization visibility 62%). Line 2 is polarized at 209° with a polarization visibility of 31%. Line 3 is polarized at 226° with a polarization visibility of 65%. From the results shown above, we can conclude that for $C_{96}C_{12}$ GQD, the main emission transition dipole is parallel to the absorption transition dipole in a defined direction[44], while the emission dipoles of the two satellite PL lines show different behaviors.

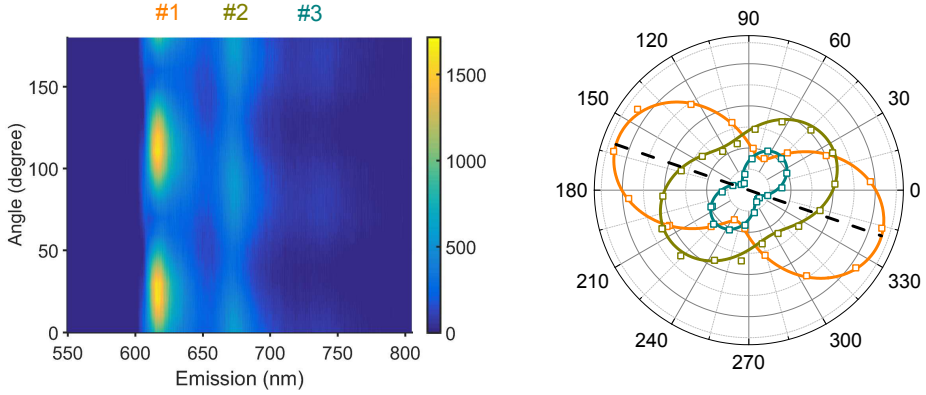

Figure 3.9: Emission polarization measurement results for a single GQD showing different behavior. The response of the main PL line is still parallel to the direction of the absorption dipole (indicated by the dashed line). In contrast, the two satellite lines are polarized differently.

We now discuss these results of polarization measurements on $C_{96}C_{12}$ GQD. In [89], the authors performed theoretical calculations on C_{168} GQD that has the same C_3 rotational symmetry as $C_{96}C_{12}$ GQD (see Fig. 3.10 - (b)). Their results may help us to understand the polarization behavior of $C_{96}C_{12}$ GQD. They first calculated the eigenstates and eigenvalues of C_{168} using a tight-binding approach and fill them with spin-up and spin-down 168 π-electrons. Due to the 3-fold symmetry, the eigenstates can be characterized according to their angular momenta projections, m, with $m = \{0, 1, 2\}$. The highest valence band (VB) state and the lowest conduction band (CB) state are both double-degenerate with $m = 1$ and 2 (see Fig. 3.10 - (a) left). Therefore, there are four degenerate lowest singlet transitions (singlet means no flip of spin): two crossed transitions that $\Delta m = +1$ and -1 (Fig. 3.10 - (a) middle); two vertical transitions that $\Delta m = 0$ (Fig. 3.10 - (a) right). The selection rules indicates that the vertical transitions ($\Delta m = 0$) are dark, while the crossed transitions ($\Delta m = \pm 1$) are optically active. The transitions with $\Delta m = \pm 1$ correspond to circularly polarized light with σ^+ and σ^- polarization[45], in analogy to semiconductor quantum dots [217]. Furthermore, by including electron-electron screened Coulomb direct, exchange, and scattering interactions, the degeneracy of the four transitions are finally moved and the authors found the very same results as we discussed in the previous section: The two bright transitions

[44] One should note that when changing the excitation angle, the obtained emission diagram do not change.

[45] The authors also indicated that the degeneracy in the 3-fold rotational GQDs is somewhat similar to the valley degeneracy of graphene or TMDs [216]. It is due to the fact that the first Brillouin zone of a hexagonal lattice is also hexagonal and has a 3-fold rotational symmetry. This symmetry links K points with a phase of $2\pi/3$, as well as the K' points with a phase of $2\pi/3$, which generates two distinct but degenerate subspaces, just like the $m = +1$ and -1 subspaces in GQD a with C_3 symmetry.

with $m = \pm 1$ have higher energies (indicated in red in Fig. 3.10 - (c)), which thus correspond to the β and β' bands. The two dark transitions with $m = 0$ have lower energies (indicated in red in Fig. 3.10 - (c)), which correspond to the p and α bands. Applying this picture on our $C_{96}C_{12}$ GQD, the excitation (at 594 nm) and emission thus both corresponds to the lowest "dark" transition (α band) with total angular momentum $\Delta m = 0$. The authors in this paper did not discuss the exact polarization of the $\Delta m = 0$ transitions, as they considered that they were dark. However, it is known that in a disordered matrix, such as a polymer (in our case the polystyrene), the molecules undergo local strains. It is thus possible that the strains could lower the symmetry and brighten the dark transition, and this transition could have a linearly polarized dipole depending on the orientation of the strain. For further investigations, it is very valuable to do the experiments with higher excitation energy, i.e. around 475 nm, which corresponds to the "bright" transition, to see whether we can find a polarization response on the circularly polarized light as predicted by this theory.

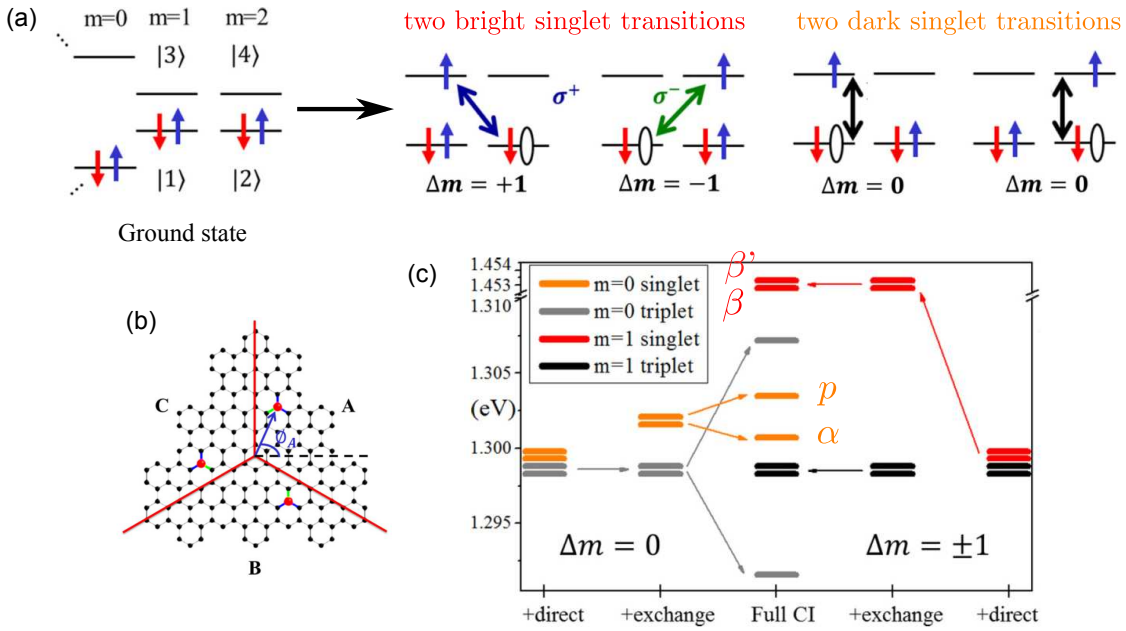

Figure 3.10: (a) - Left panel: ground state at band edge of the C_{168} GQD. Middle and right panel: Four lowest singlet transitions: two with total angular momentum $\Delta m = \pm 1$ (middle) and two with $\Delta m = 0$ (right). (b) - Structure of the C_{168} GQD showing C_3 rotational symmetry. (c) - Evolution of energy of the lowest transitions with the inclusion of different interactions. Adapted from [89].

We now look at the possible reason for the mismatch between the emission dipoles of the two satellite PL lines and the main PL line. It is most possible that the three emission dipoles are all in the plan of GQD. Moreover, considering the C_3 symmetry, it is possible that the emission dipole turns 60° from one line to another. However, since the GQDs orientate randomly in matrix, we observe the angle between each PL line is random. But if this assumption is true, when the plan of GQD is more parallel to the sample plan we should observe higher emission intensity and more clear difference between the emission dipole angles. In contrast, when the plan of GQD is more perpendicular to the sample plan we should observe lower emission intensity and the emission dipole angles should be more parallel. To verify this, we are accumulating more data to see whether there is a correlation between the emission intensity and the angle between each emission dipole.

Besides, theoretical modeling is very required to explain this experimental observation.

3.2 Photophysical properties of single $C_{96}C_{12}$ GQDs

Second order photon correlation measurements

In order to identify the number of emitters associated with such diffraction limited spot and spectrum, we measured the second order correlation function ($g^{(2)}(\tau)$) at room temperature on photons from the entire spectrum. To do this, a standard Hanbury-Brown and Twiss (HBT) setup in a "start-stop" mode is used (for the principle of this measurement, see Chap. II Sec. 2.2).

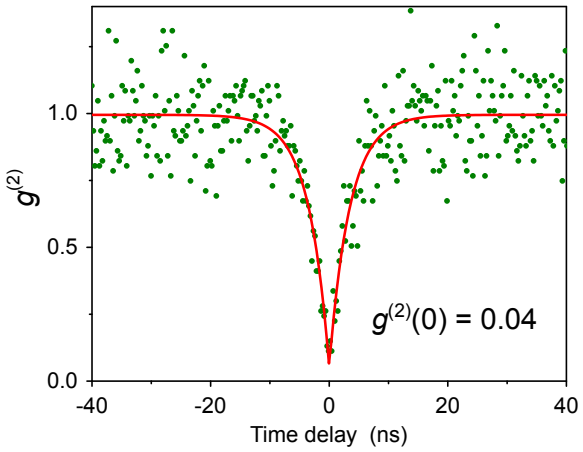

Figure 3.11: Typical $g^{(2)}(\tau)$ trace on a single $C_{96}C_{12}$ GQD. Excitation power: 200 nW. The red line is the fit to a double-side exponential with a characteristic time of ∼4.1 ns.

Fig. 3.11 shows a typical $g^{(2)}(\tau)$ curve on a spot of $C_{96}C_{12}$ GQD under a moderate excitation power of 200 nW. Strong anti-bunching at zero delay is clearly observed. We fit this curve using a double-side exponential[46]:

$$1 - (1 - b)e^{-|\tau|/\tau_1} \tag{3.1}$$

with τ_1 the anti-bunching characteristic time and b the bunching residual at zero delay. The fit gives $\tau_1 = 4.1$ ns and $g^{(2)}(0) = 0.04$. This very small $g^{(2)}(0)$ value undoubtedly proves that a single emitter is detected (criteria for a single photon emitter: $g^{(2)}(0) < 0.5$). This is in strong contrast with the results of such experiments performed on "top-down" GQDs where no anti-bunching is observed [218]. The authors in this paper interpret the absence of anti-bunching as a consequence of the extrinsic nature (i.e. the defects) of the emission from "top-down" GQDs. Moreover, we have performed measurements on more than 40 GQDs, all of them leading to $g^{(2)}(0) < 0.1$ (see Fig. 3.12 and 3.13). As these $g^{(2)}$ measurements were performed by integrating all the wavelengths on the detector, it implies that the spectrum described in the previous section indeed arises from a single GQDs and not from several objects. Considering the good agreement between PL/PLE measurements and the theoretical predictions (discussed in the

[46]Under such low excitation power, the $g^{(2)}$ measurements are not affected by the time jitter of detectors and eventual inter-system crossing. Thus the obtained $g^{(2)}$ curves can be accurately fitted by this sample formula. We will see in Sec. 3.3 how the $g^{(2)}$ evolves as a function of the excitation power.

precedent section), we can further confirm that the emission indeed arises from intrinsic quantum states of $C_{96}C_{12}$ GQD. Moreover, the more the $g^{(2)}(0)$ value tends to zero, the better purity of single photons emission is and the purity of single photon emission is crucial for quantum information processing [219]. The weak value of $g^{(2)}(0)$ observed for GQDs enforces it as an interesting alternative to other single sources in 2D materials, such as defects in WSe_2 [220–224] or in h-BN [128, 225, 226].

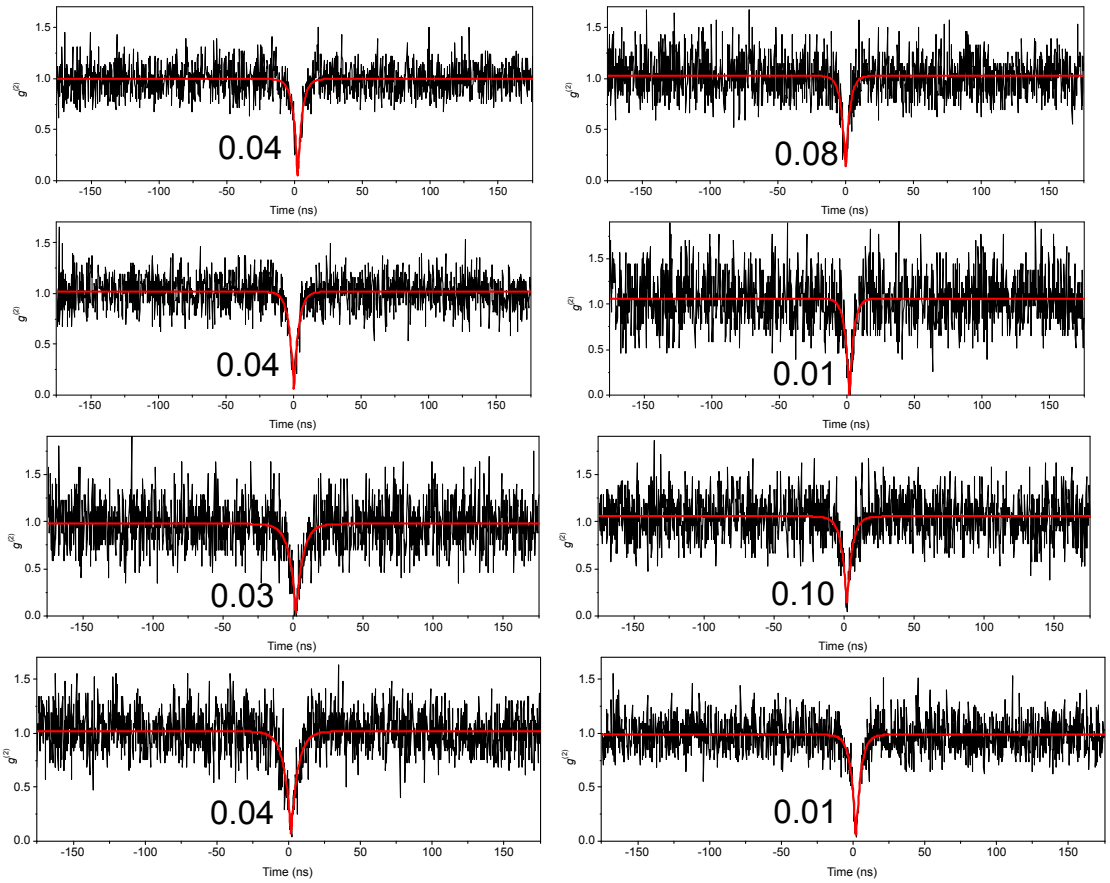

Figure 3.12: Examples of $g^{(2)}(\tau)$ traces on different GQDs recorded at a moderate excitation power (≈200 nW) without any background correction. The red lines represent a fit to a double-sided exponential function $1-(1-b)e^{-|\tau|/\tau_1}$. The obtained $g^{(2)}(0)$ values from the fits are shown in the graphs.

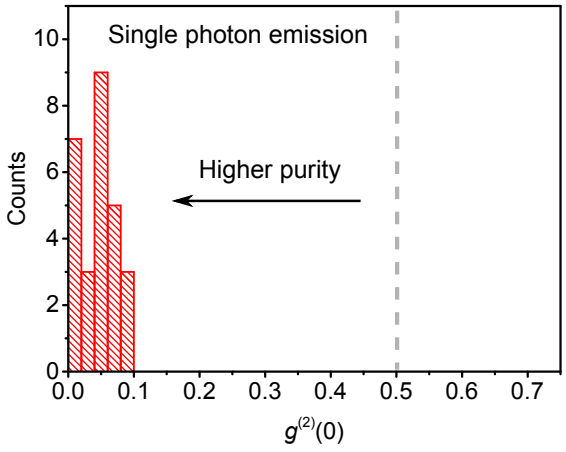

Figure 3.13: Histogram of the $g^{(2)}(0)$ values from 40 single $C_{96}C_{12}$ GQDs.

Lifetime measurements

Having confirmed that the sample contains single GQDs, we performed time-resolved photoluminescence (TRPL) experiments to measure their excited lifetime. Here the supercontinuum laser tuned at 580 nm is used as the pulsed excitation source. Before the lifetime measurements, we performed the $g^{(2)}$ measurements on the GQD spots to ensure that a single GQD is studied. Fig. 3.14 - (a) shows a typical coincidence histogram of a GQD spot under the pulsed excitation. The total absence of the central peak demonstrates single photon emission, thus ensuring that the spot corresponds to a single GQD. The PL decay curve of this single GQD (recorded over the entire emission spectrum) is shown in Fig. 3.14 - (b). The data is well fitted by a mono-exponential with a decay time constant of ∼5.4 ns. We have performed lifetime measurements on 7 single GQDs. The obtained time-resolved PL curves are always mono-exponential with decay time constants ranging from 3.1 to 5.5 ns in agreement with the result of GQD solution (5 ns).

As indicated by the dashed circle in Fig. 3.15 - (a), sometimes a spot with size larger than the diffraction limit can also be found in the PL scan image. Such a spot shows a broad and structure less PL spectrum (Fig. 3.15 - (b)) and is not as stable as the single GQD spot (intensity fluctuations and decreasing). Moreover, the $g^{(2)}$ measurements of these delocalized spots do not show anti-bunching (Fig. 3.15 - (c)), which implies that the spot contains more than one emitters. We thus attribute such spots to GQD aggregates. Fig. 3.15 - (d) display the time-resolved PL on such GQD aggregate, which clearly shows a multi-exponential decay behavior. These aggregates could already exist in the GQD solution as we discussed in the previous section. They could also be formed during the spin-coating process.

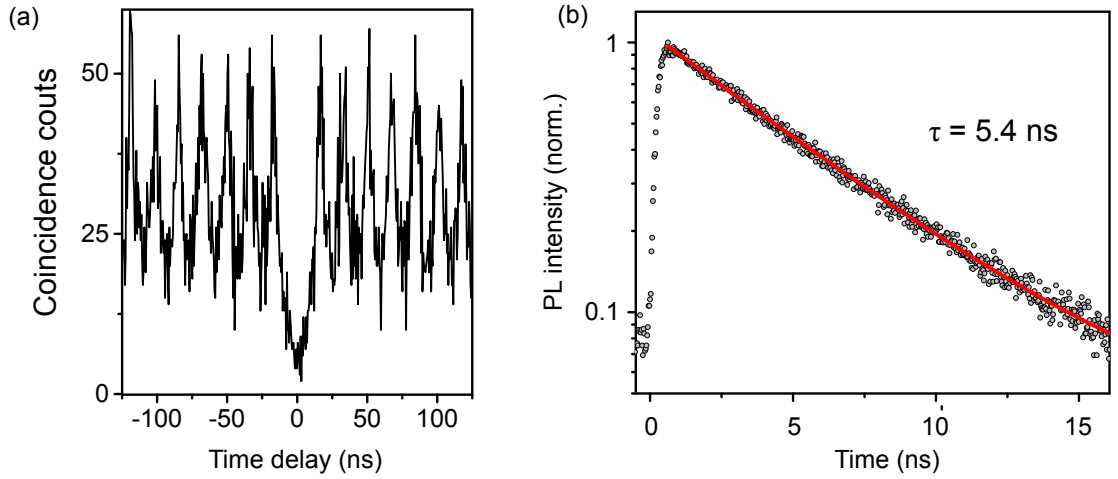

Figure 3.14: (a) - Typical coincidence histogram of a GQD spot under a pulsed excitation (supercontinuum). A series of peaks separated by the repetition period of the supercontinuum laser (16.7 ns) are observed. The absence of the central peak indicates single photon emission (thus, single GQD). (b) - Corresponding time-resolved PL of the same GQD spot (recorded over the entire emission spectrum). The red line is the fit using a single exponential, which gives a decay time of 5.4 ns.

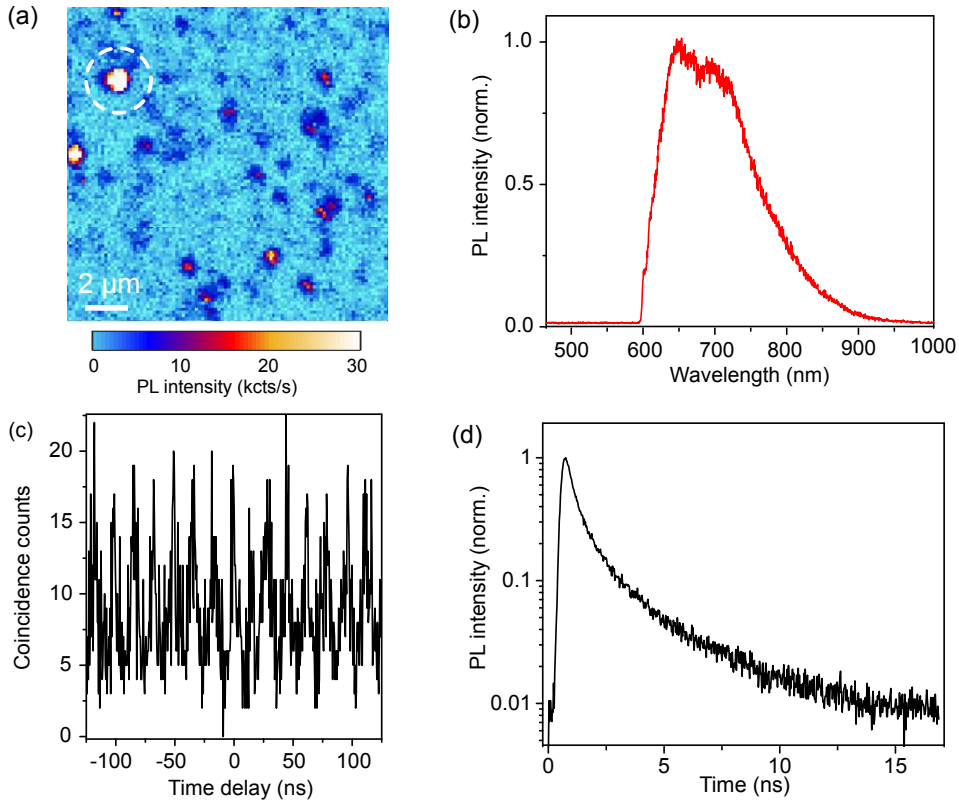

Figure 3.15: (a) - PL raster scan image showing large spot with a size ∼1.5 µm (indicated by the dashed circle). (b-d) Corresponding PL spectrum (b), coincidence histogram (c) and time-resolved PL (d) of this GQD spot.

Saturation curve

Having revealed the single photon emission from $C_{96}C_{12}$ GQDs, we are now going to characterize some emission properties of $C_{96}C_{12}$ which are very important for a single photon emitter. One figure of merit of a single quantum emitter is its brightness. To characterize the brightness, we measured the emission intensity of a single GQD as a function of the excitation power density to obtain a saturation curve (see Fig. 3.16 - (a)).[47] It is fitted by

$$R = R_\infty/(1 + I_{\text{sat}}/I_{\text{exc}}) \tag{3.2}$$

with R_∞ the count rate at saturation, I_{sat} the excitation power density at saturation and I_{exc} the excitation power density. From this fit, we obtain $R_\infty \approx 9.7$ Mcounts/s, and $I_{\text{sat}} \approx 28$ kW/cm^2.

We now try to compare this value of count rate at saturation with other quantum emitters. To date, one of the brightest single photon emitters at room-temperature is defects in h-BN [128, 225, 226]. In Ref. [128], the authors performed the saturation measurements on a single defect in h-BN crystal, which gave a sautration rate $R_\infty \approx$ 3.9 Mcounts/s (see inset of Fig. 3.16). Moreover, they performed the same measurements on a NV center in 100-diamond using the same experimental set-up and they found

[47] For each excitation power, we performed a PL scan around the spot. The obtained PL intensity image was then fitted by a 2D Gaussian function, which allows exactly determining the emission intensity without the contribution from background.

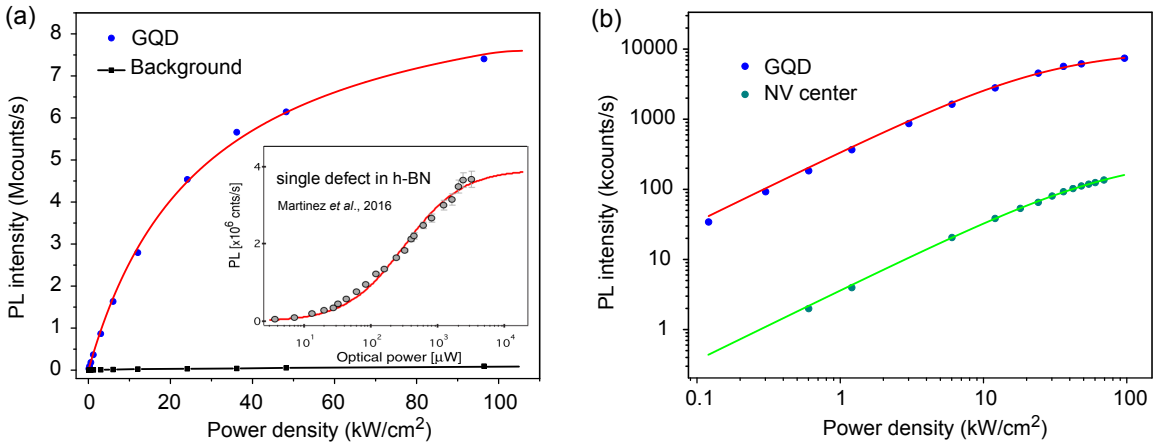

Figure 3.16: (a) - Saturation curve of a single GQD (blue dots) as a function of the excitation power density. The red line is the fit according to Eq. 3.2 giving a saturation rate $R_\infty \approx 9.7$ Mcounts/s. Black dots show the contribution of background emission, which is more than 100 times lower than the emission of GQD. Inset: Saturation curve of a single defect in h-BN crystal, adapted from [128]. The authors also used Eq. 3.2 to fit the curve, which gives a $R_\infty \approx 3.9$ Mcounts/s for the single defect in h-BN crystal. (b) - Saturation curves of a GQD (blue dots) and a single NV center in bulk (111) diamond (green dots). We recorded these two curves using the same set-up. The solid lines are the fit according to Eq. 3.2.

the saturation count rate of the defect in h-BN is about 20 times higher than the NV center. As we know, NV centers in bulk diamond are one widely used quantum emitter. Its brightness is well-documented and almost unchanged between one sample to another [227]. This makes NV centers as a connection for the comparison of brightness between different quantum emitters. Similarly, we performed the experiments on a single NV center in a 111-diamond[48] on the same experimental setup as the one used for GQDs. A saturation count rate of 0.3 Mcounts/s was measured (see Fig. 3.16 - (b)) in good agreement with literature [227]. The count rate at saturation of GQDs is thus about 30 times higher than NV centers. Since we found very similar ratio of count rate between our GQD and NV center as the authors found between defect in h-BN and NV center in [128], and these two experimental set-ups are also very similar (confocal microscopy with the objective of similar numerical aperture and similar model of APDs as detector), it turns that the GQDs are, at least, as bright as defects in h-BN. Thus, it puts GQDs in the highest values of brightness among other quantum emitters.

Photostability

Now we address the question of the photostability of GQDs. In this perspective, GQDs have also good properties. We can easily find single GQDs with stable emission up to hours under a moderate excitation power, as shown in Fig. 3.17 - (a) (the small intensity fluctuations indicated by the stars are due to the instability of set-up.). This observation is in strong contrast to the case of fluorescent molecules. Although many efforts have been made to improve the photostability of fluorescent molecules [228, 229], under ambient

[48] One should note that since the emission dipole is parallel to the surface plan for NV centers in 111-diamond, they generally have ∼20% more count than NV centers in 100-dimond.

condition a single molecule can only emit up to 10^7 photon before photobleaching, i.e. the irreversibly transform the molecule into a non-fluorescent specie. Here, from Fig. 3.17 - (a) we can see that a single GQD can emit more than 10^9 photons[49] without photobleaching. This encouraging result could even be improved by engineering the surrounding matrix. Moreover, Fig. 3.17 - (b) shows that no blinking is observed on the PL time trace with a short time bin of 10 ms. The corresponding histogram of counts per bin is well fitted to a Poissonian distribution (see Fig. 3.17 - (c)), which further suggests that there is no intensity fluctuation of the GQD. This observation is in strong contrast with numerous single emitters that undergo quantum jumps between bright and dark states (e.g. CdSe nanocrystals [230], as shown in Fig. 3.18). We will perform a more detailed analysis on the photo-dynamics of single GQDs in Sec. 3.3 and 3.4.

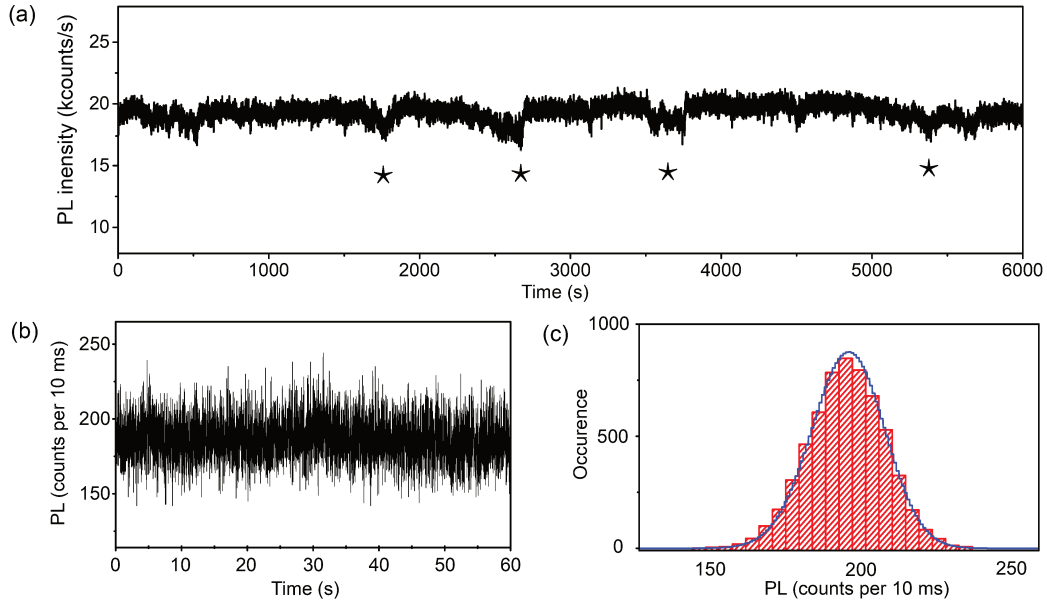

Figure 3.17: (a) - PL time trace of a stable GQD over 100 minutes. Bin width: 200 ms. Intensity fluctuations around 1800 s, 2600 s, 3600 s and 5400 s (indicated by the stars) are due to the instability of set-up. (b) - Zoom of the PL time trace on a timescale of 60 s. Bin width: 10 ms. (c) - Corresponding count per bin histogram of the PL time trace in (b). The histogram was fitted using a Poissonian distribution (blue line), implying the absence of intensity fluctuations. Excitation power for the measurements: 200 nW.

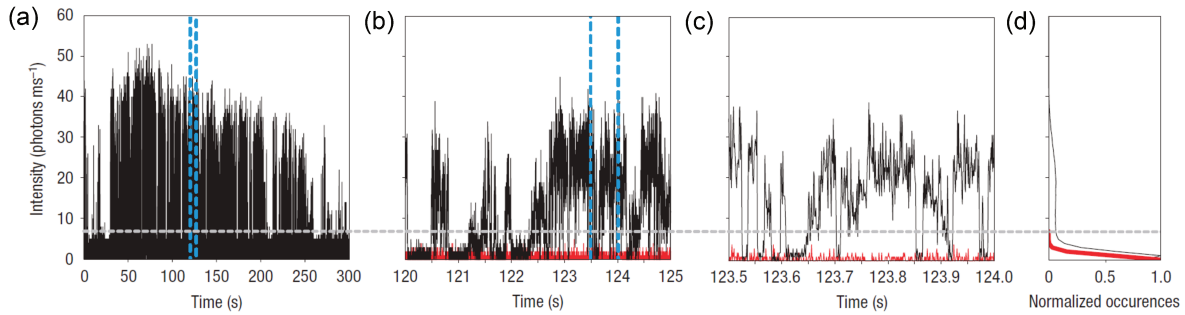

Figure 3.18: PL time trace of a single CdSe-ZnS nanocrystal over different timescales: 5 min (a), 5 s (b) and 0.5 s (c), showing sever intensity fluctuations. (d) - Normalized count per bin distribution, indicating that the dark state is visited more than half of the time. Adapted from [230].

[49]This value is obtained by taking into account of the general detection efficiency of ∼15%.

Despite of the high stability, the emission of GQDs ends up disappearing. The emission intensity always drops discretely, which is also the characteristic of single emitters. Fig. 3.19 - (a) shows two different PL time traces around the time of disappearance of the emission. We can see that in the first one the emission intensity drops down to zero sharply. On the contrary, the second one goes through an intermediate "grey" state before ending up to zero. These two behaviors are representative of what we observed on all the GQDs. Moreover, it is known that for some quantum emitters they could re-emit after a long dark period. For example, people have observed that when a CdSe nanocrystal is under excitation, charges could be occasionally trapped on its surface, which bleaches the emission of nanocrystal. This trapping of the charge could last for several minutes. However, once the charge moves away, the nanocrystal lights up again [231]. It is thus necessary to see whether the emission of GQD is irreversibly quenched or if they are able to re-emit light after a certain time. We have checked c.a. 10 single GQDs. In most of the cases, the emission of GQDs is not recovered. We found one situation where the GQD re-emit light after ≈1 minute of dark period. We note that after the recovery of emission, its PL spectrum is blue-shifted of ∼20 nm with a slight increase of the count rate Fig. 3.19 - (b).[50] Nevertheless, a detailed work is needed in order to understand the mechanisms behind such behaviors. First of all, more data should be acquired in order to perform a statistical study on the proportion of the GQDs with each bleaching behavior and also the proportion of the GQDs which can re-emit light. Besides, it is also valuable to see whether there is a correlation between the emission wavelength and emission intensity states.

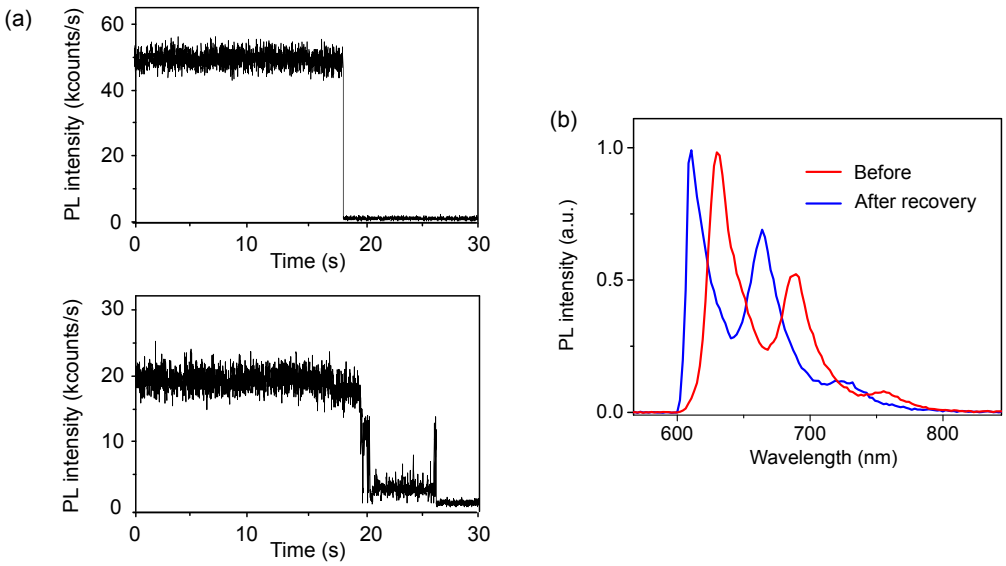

Figure 3.19: (a) - Two different behaviors of PL time trace of single GQDs around the time when disappearing of emission occurs. Top panel: Intensity drops down to zero sharply. Bottom panel: intensity goes through an intermediate "grey" state before ending up to zero. Bin width: 10 ms. (b) - PL spectra of a single GQD before photobleaching (red line) and after recovery from photobleaching (blue line). The sharp shape at 600 nm is due to the cut-off edge of the long-pass filter.

[50] Many possible processes could result in such modification of the emission spectrum: the conformational rearrangement as in molecules [232], the quantum confinement Stark effect as in SWNTs [233] and semiconductor quantum dots [234], or the chemical structure change.

3.3 Analysis of photo-dynamics on a single $C_{96}C_{12}$ GQD

In this section, we will perform a detailed analysis of photo-dynamics of $C_{96}C_{12}$ GQD to get insights into its quantum states. We will first propose a three-level model to explain the behavior of $C_{96}C_{12}$ GQD. A study on the evolution of $g^{(2)}(\tau)$ function as a function of the excitation power will help us to understand the population dynamics of $C_{96}C_{12}$ GQD. The results shown in this section are obtained from a stable single GQD.

Three-level system

As we can see in Fig. 3.20, for a large majority of fluorescent molecules, the ground state is a singlet state as its electrons are paired off in bonds with their spins anti-parallel (total electronic spin S is equal to 0). This ground state is called S_0. After absorption of a photon the first excited state is also a singlet state called S_1. The reason for this is that a photon cannot flip the spin of the electron because the magnetic field of a light wave is too weak. However, due to non-negligible spin-orbit effect, there is finite torque acting on the spin of the electron in the excited state. This results in a small probability that the spin of the excited electron is reversed. This process is known as inter-system crossing (ISC) and usually its rate is much smaller than the excited state decay rate. If a spin flip happens, the total electronic spin of the molecule S changes from 0 to 1. As we know, the multiplicity of the spin state is equal to $(2S+1)$, because there are $(2S+1)$ degenerate M_s sublevels. Thus the $S=1$ state is called triplet state, in contrast to a singlet state for $S=0$. This triplet state lies at a lower energy than the singlet S_1 state, because the exchange interaction between the electrons in parallel spin increases their average distance in accordance with Hund's rule. The increased average distance thus leads to the reduction of Coulomb repulsion between the electrons. Once a molecule undergoes an inter-system crossing into the triplet state it could decay into the singlet ground state. However, since this is a spin-forbidden transition that needs re-flip of the spin, the triplet state has an extremely long lifetime (often microseconds to seconds).

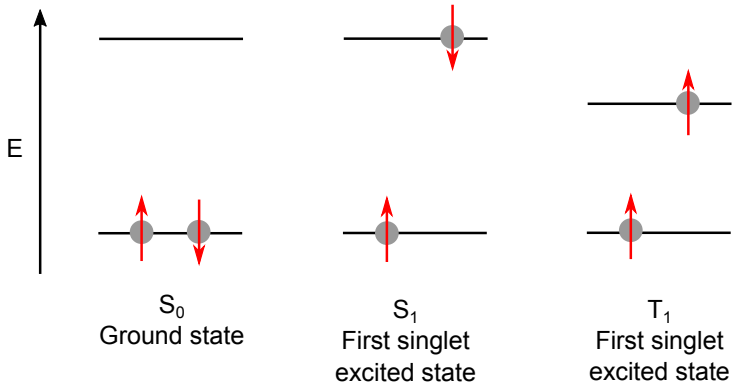

Figure 3.20: Spin picture of a typical fluorescent molecule.

By examining the structure using Clar's sextet rule [200], the $C_{96}C_{12}$ GQD is fully benzeniod which means that all the π-electrons of are grouped into sextets without unpaired electron left (the structure can be regarded as a set of benzene rings connected

by six single bonds to neighboring rings or hydrogen atoms.) Moreover, the theoretical calculations indicate that for the family of fully benzeniod GQDs, there is at least one triplet state lying tens to few hundreds of meV below the first excited singlet state [89, 91, 235]. Hence it is reasonable to apply the same spin picture on the $C_{96}C_{12}$ GQD.

In analogy to the experiments performed on single molecules [126, 236], we performed long time scale $g^{(2)}$ measurements on a single GQD with high excitation powers. As shown in Fig. 3.21, we observed the bunching phenomena ($g^{(2)} > 1$) which is a signature of the existence of a metastable state where the system is trapped with no photon emission. It is possible that this metastable state corresponds to the low lying triplet state of GQD.

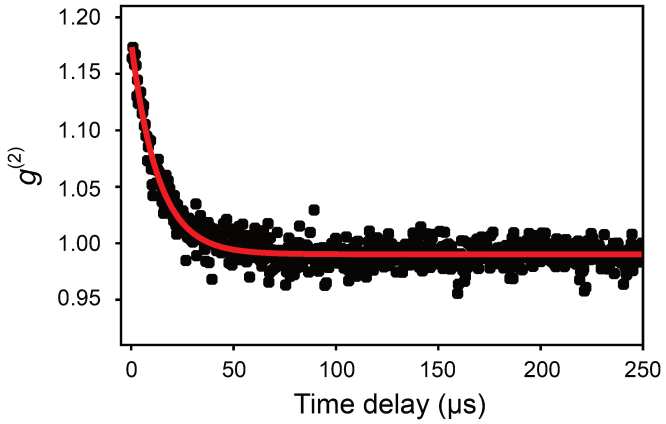

Figure 3.21: Second order correlation function of a $C_{96}C_{12}$ GQD recorded over a long time scale (250 μs) with high excitation power (30 μW). The bunching phenomena ($g^{(2)} > 1$) is clearly observed.

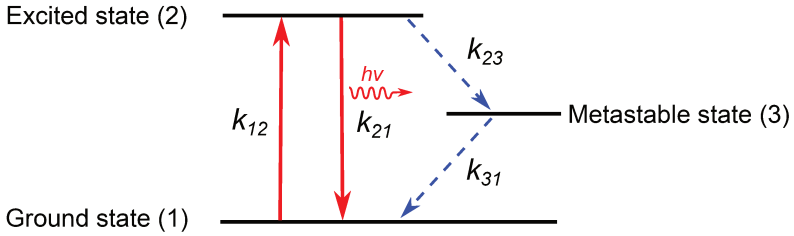

Figure 3.22: Schematic illustration of the proposed three-level model to interpret the photo-dynamics of $C_{96}C_{12}$ GQD.

We model the $C_{96}C_{12}$ GQD as a three-level system[51] (see Fig. 3.22) to study the photo-dynamics. The state (1) and (2) correspond respectively to the ground state and excited state of the radiative transition. The state (3) is the metastable state (triplet state), which is populated by the inter-system crossing. The state (3) is considered as a dark state with long lifetime. Using the transition rates that interconnect these states, the evolution of the population of each state is governed by a coupled system of differential equations:

$$\frac{\mathrm{d}}{\mathrm{d}t}\begin{pmatrix} p_1 \\ p_2 \\ p_3 \end{pmatrix} = \begin{pmatrix} -k_{12} & k_{21} & k_{31} \\ k_{12} & -(k_{21}+k_{23}) & 0 \\ 0 & k_{23} & -k_{31} \end{pmatrix} \begin{pmatrix} p_1 \\ p_2 \\ p_3 \end{pmatrix} \tag{3.3}$$

[51] We neglect the very fast relaxation within the vibrational manifold.

where p_i is the population of the state (i) and k_{ij} is the transition rate from the state (i) to the state (j). As the GQD should be in one of the three states at any time, we have

$$p_1 + p_2 + p_3 = 1 \tag{3.4}$$

One should note that by writing these rate equations we assume that the coherence is lost as our experiment is performed at room-temperature and the laser is non-resonant with the emission. For further investigations at cryogenic temperatures, it is very interesting to perform the experiments with resonant excitation to see whether our GQD shows Fourier-limited photons. If it is the case, we should apply the full quantum Master equation to include the stimulated emission by laser and some coherent effects such as Rabi oscillation could appear [237, 238].

We now express the time evolution of the second order photon correlation function $g^{(2)}(\tau)$ using the transition rates of the three-level system. In the quantum picture of light, $g^{(2)}(\tau)$ can be written as [125]

$$g^{(2)}(\tau) = \frac{P(t, t+\tau)}{P^2(t)} \tag{3.5}$$

where $P(t)$ is the probability to detect at any time t and $P(t, t+\tau)$ is the joint probability to detect a photon at time t and a photon at time $t+\tau$. As the normalized jointed probability is the conditional probability, we obtain

$$g^{(2)}(\tau) = \frac{P(t+\tau|t)}{P(t)} \tag{3.6}$$

with $P(t+\tau|t)$ the conditional probability to detect a photon at time $t+\tau$ knowing that a photon have been detected at t.

For a single emitter, the detection of a photon at time t prepares the system in the ground state. Thus, $P(t+\tau|t)$ can be rewritten as $P(\tau|p_2(0) = 0)$. Moreover, the probability of detection a photon is proportional to the population of the excited state p_2. $P(\tau|p_2(0) = 0)$ is then expressed by the evolution of the population of the excited state $p_2(\tau)$ on starting from the conditions that $p_1(0) = 1$, $p_2(0) = 0$ and $p_3(0) = 0$:

$$P(t+\tau|t) = P(\tau|p_2(0) = 0) = \eta_{det}\ \eta_Q\ k_{21}\ p_2(\tau) \tag{3.7}$$

with η_{det} and η_Q the overall detection efficiency and quantum yield of the emitter, respectively. In the same manner, the simple probability $P(t)$ that is the probability of detection a photon at any time, can be written as

$$P(t) = \eta_{det}\ \eta_Q\ k_{21}\ p_2(\infty) \tag{3.8}$$

with $p_2(\infty)$ the stationary population of the excited state (2). Therefore, the $g^{(2)}(\tau)$ is expressed as

$$g^{(2)}(\tau) = \frac{p_2(\tau)}{p_2(\infty)} \tag{3.9}$$

So now, it just need to resolve the coupled differential equations Eq. 3.3 to express $p_2(\tau)$ and $p_2(\infty)$ using the transition rates. First, the analytical solution form of Eq. 3.3 is

$$\begin{pmatrix} p_1 \\ p_2 \\ p_3 \end{pmatrix} = \begin{pmatrix} a_{11} & a_{12} & a_{13} \\ a_{21} & a_{22} & a_{23} \\ a_{31} & a_{32} & a_{33} \end{pmatrix} \begin{pmatrix} \exp(-\lambda_1 t) \\ \exp(-\lambda_2 t) \\ \exp(-\lambda_3 t) \end{pmatrix} \tag{3.10}$$

with λ_i the eigenvalues of the matrix in Eq. 3.3 and a_{ij} the multiples of eigenvectors, which depends on the initial conditions. We then express the coefficients a_{ij} and λ_i using the transition rates.

By diagonalizing the matrix in Eq. 3.3, we obtain

$$\begin{aligned}
\lambda_1 &= \frac{1}{2}\left[k_{12}+k_{21}+k_{23}+k_{31}+\sqrt{(k_{12}+k_{21}+k_{23}-k_{31})^2-4k_{21}k_{23}}\right] \\
\lambda_1 &= \frac{1}{2}\left[k_{12}+k_{21}+k_{23}+k_{31}-\sqrt{(k_{12}+k_{21}+k_{23}-k_{31})^2-4k_{21}k_{23}}\right] \\
\lambda_3 &= 0
\end{aligned} \tag{3.11}$$

As we discussed above, the inter-system crossing is spin-forbidden. We assume that the transition rates to and from the triplet state are very small compared to the decay rate from the excited state to the ground state: $(k_{23},\ k_{31}) \ll k_{21}$. Thus, the following approximate expression of λ_1 and λ_2 is derived:

$$\begin{aligned}
\lambda_1 &= k_{12}+k_{21} \\
\lambda_2 &= k_{31}+k_{23}k_{12}/(k_{12}+k_{21})
\end{aligned} \tag{3.12}$$

We now turn to express the coefficients a_{ij}. When $t \to \infty$, we deduce the stationary population of each state from Eq. 3.10:

$$p_1(\infty) = a_{13},\ p_2(\infty) = a_{23} \text{ and } p_3(\infty) = a_{33}. \tag{3.13}$$

and thus:

$$a_{13}+a_{23}+a_{33} = 1 \tag{3.14}$$

We assume the fact that $\mathrm{d}p_i/\mathrm{d}t = 0$ at $t \to \infty$, Eq. 3.3 can be written as

$$\begin{pmatrix} 0 \\ 0 \\ 0 \end{pmatrix} = \begin{pmatrix} -k_{12} & k_{21} & k_{31} \\ k_{12} & -(k_{21}+k_{23}) & 0 \\ 0 & k_{23} & -k_{31} \end{pmatrix} \begin{pmatrix} a_{13} \\ a_{23} \\ a_{33} \end{pmatrix} \tag{3.15}$$

Together with Eq. 3.14 and making use of the approximation $(k_{23},\ k_{31} \ll k_{21})$, we obtain

$$\begin{aligned}
a_{13} &= k_{21}k_{31}/(k_{21}k_{31}+k_{12}k_{31}+k_{12}k_{23}) \\
a_{23} &= k_{12}k_{31}/(k_{21}k_{31}+k_{12}k_{31}+k_{12}k_{23}) \\
a_{33} &= k_{12}k_{23}/(k_{21}k_{31}+k_{12}k_{31}+k_{12}k_{23})
\end{aligned} \tag{3.16}$$

At $t = 0$, we assume that the population is all in the ground state and so we have the initial conditions $p_1 = 1$, $p_2 = 0$ and $p_3 = 0$. Together with the expression of p_2 and $\mathrm{d}p_2/\mathrm{d}t$ (Eq. 3.3 and 3.10, respectively), we obtain the following set of relations:

$$\begin{aligned}
a_{21}+a_{22}+a_{23} &= 0 \\
\lambda_1 a_{21}+\lambda_2 a_{22} &= -k_{12}
\end{aligned} \tag{3.17}$$

Then we obtain the expression of a_{21} and a_{22}:

$$\begin{aligned} a_{21} &= -k_{12}/(k_{12}+k_{21}) \\ a_{22} &= k_{12}^2 k_{23}/[(k_{12}+k_{21})(k_{21}k_{31}+k_{12}k_{31}+k_{12}k_{23})] \end{aligned} \tag{3.18}$$

Finally, by replacing the coefficients in Eq. 3.10 with the transition rates, we obtain

$$g^{(2)}(\tau) = \frac{p_2(\tau)}{p_2(\infty)} = 1 - (1+a)\,\exp(-\lambda_1\tau) + a\,\exp(-\lambda_2\tau) \tag{3.19}$$

with the parameters λ_1, λ_2 and a given by

$$\lambda_1 = k_{12} + k_{21} \tag{3.20}$$

$$\lambda_2 = k_{31} + k_{23}k_{12}/(k_{12}+k_{21}) \tag{3.21}$$

$$a = k_{23}k_{12}/[k_{31}(k_{12}+k_{21})] \tag{3.22}$$

We now look at the shape of this deduced second correlation function $g^{(2)}(\tau)$. As k_{23} and $k_{31} \ll k_{21}$, we have ${\lambda_1}^{-1} \ll {\lambda_2}^{-1}$. Thus, at short delay time the $g^{(2)}(\tau)$ function exhibits anti-bunching effect ($g^{(2)}(0) = 0$) with characteristic time ${\lambda_1}^{-1}$. Anti-bunching is a clear indication for non-classical light. Its physical reason is that the quantum system modeled above cannot emit more than one photon at the same time. At longer time scale the anti-bunching disappears and the $g^{(2)}(\tau)$ function is characterized by photon bunching ($g^{(2)}(\tau) > 1$). This bunching originates from transitions to the triplet state which stops the system from emission and results in the fluctuation of intensity. Moreover, for time delay $\tau \to \infty$, bunching effect also disappears and we reach the classical limit of a Poissonian source for which $g^{(2)}(\tau) \to 1$.

Transition rates

The population rate k_{12} of excited state (2) is given by

$$k_{12} = \sigma(\lambda_{ex}) \times \frac{\lambda_{ex}}{hc} \times I_{ex} \tag{3.23}$$

where $\sigma(\lambda_{ex})$ is the absorption cross-section at excitation wavelength λ_{ex}, I_{ex} is the excitation power density[52], h is the Planck constant and c is the speed of light in vacuum.

From this relation we can see that k_{12} is directly determined by the excitation power. Thus, $g^{(2)}(\tau)$ function varies also with the excitation power. In the following part, we will study the variation of $g^{(2)}(\tau)$ as a function of the excitation power to deduce the values of the transition rates.

A series of $g^{(2)}(\tau)$ functions with different excitation powers were recorded on a stable $C_{96}C_{12}$ GQD. As the bunching characteristic time λ_2 is very long (typically $\sim\mu$s), we used a wide-range time digitizer (P7887, FastComtec) to perform the full time range acquisition. The technical details have been discussed in Chap. II Sec. 2.2.

[52] As the laser spot has a 2D Gaussian profile, the area S is calculated for its $1/e^2$ diameter which is about 1 μm^2. I_{ex} is thus the excitation power density at the center of the Gaussian spot, which is given by $2P_{ex}/S$ with P_{ex} the excitation power. For our set-up, an excitation power of 1 μWcorresponds to a power density of about 0.6 kW/cm^2.

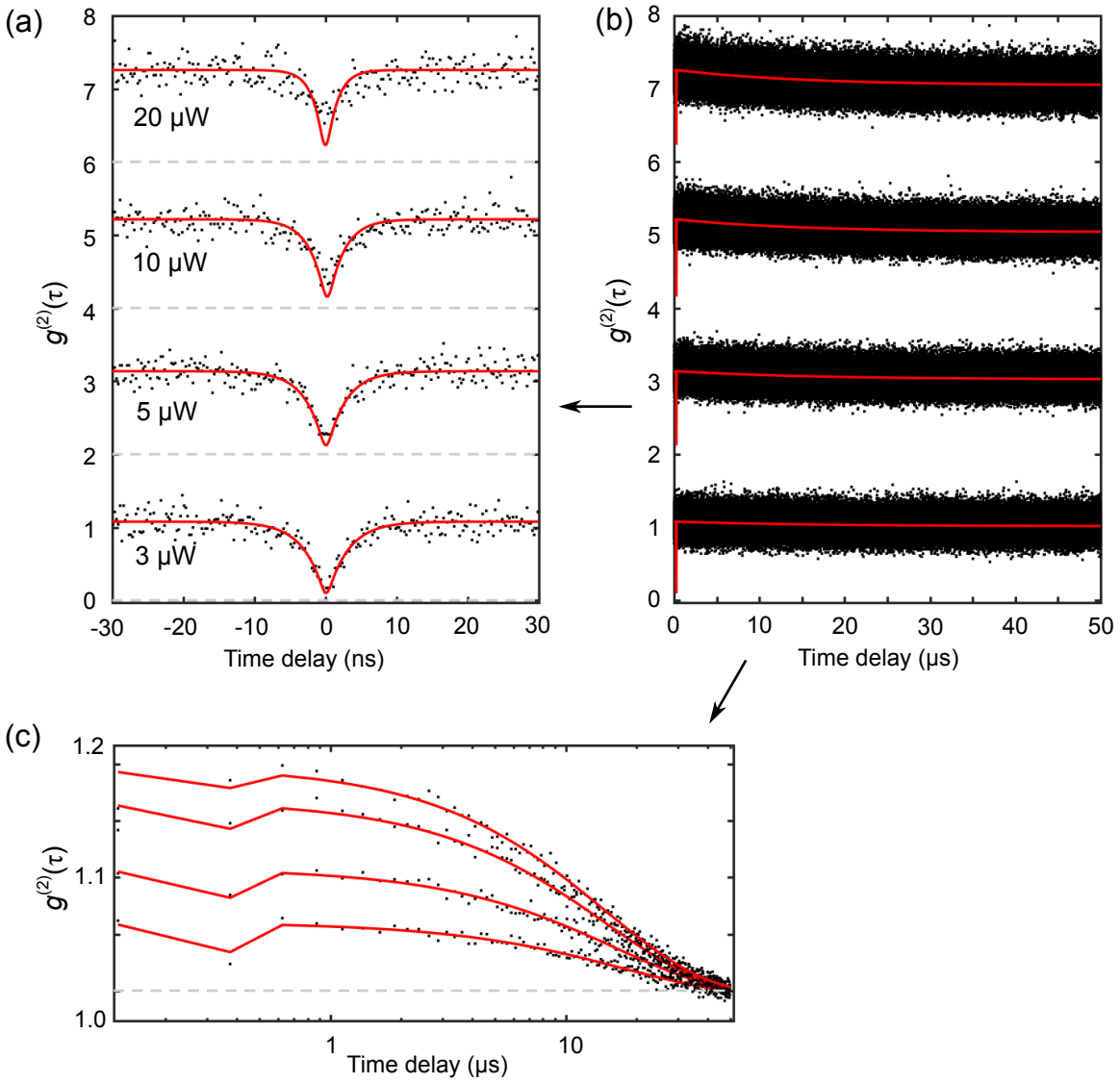

Figure 3.23: $g^{(2)}(\tau)$ functions recorded on a stable $C_{96}C_{12}$ GQD with different excitation powers. (a) - Zoom on short time delay of the full time scale $g^{(2)}(\tau)$ functions which are displayed in (b). Time bin width is 0.25 ns. At short time delay, we can observe shortening of the anti-bunching characteristic time when the excitation power increases. (c) - Long time scale part of of the $g^{(2)}(\tau)$ functions in (b). For clarity, the data are binned over 250 ns. We can observe the bunching phenomena ($g^{(2)} > 1$) with a characteristic time ∼10 µs and the bunching phenomena becomes stronger when the excitation power increases. The red lines are the fits using Eq. 3.19 convoluted by the instrument response function (IRF).

The obtained $g^{(2)}(\tau)$ functions are shown in Fig. 3.23 - (b). They are fitted using Eq. 3.19 convoluted with the instrument response function (IRF). The IRF was independently measured as a 1.5 ns FWHM Gaussian function (see Sec. 2.2). From these fits, we obtain the values of parameter λ_1, λ_2 and a for different excitation power densities I_{ex}.

First, we plot λ_1 as a function of I_{ex} (Fig. 3.24 - (a)). Combining Eq. 3.20 and Eq. 3.23, we obtain

$$\lambda_1 = \sigma(\lambda_{ex}) \times \frac{\lambda_{ex}}{hc} \times I_{ex} + k_{21} \tag{3.24}$$

By fitting the plot of λ_1 with this linear equation, for excitation wavelength λ_{ex} = 594 nm, we obtain the absorption cross-section and the relaxation rate of the excited state (2):

$$\sigma \simeq 1.0 \times 10^{-14} \text{ cm}^2 \tag{3.25}$$

$$k_{21} = 0.28 \pm 0.02 \text{ ns}^{-1} \tag{3.26}$$

Thus, the lifetime of excited state ${k_{21}}^{-1}$ is calculated to be 3.55 ± 0.24 ns. This value is compatible with the time-resolved PL measurements leading to lifetime ranging from 3.1 to 5.5 ns depending on the single GQDs (see the previous section).

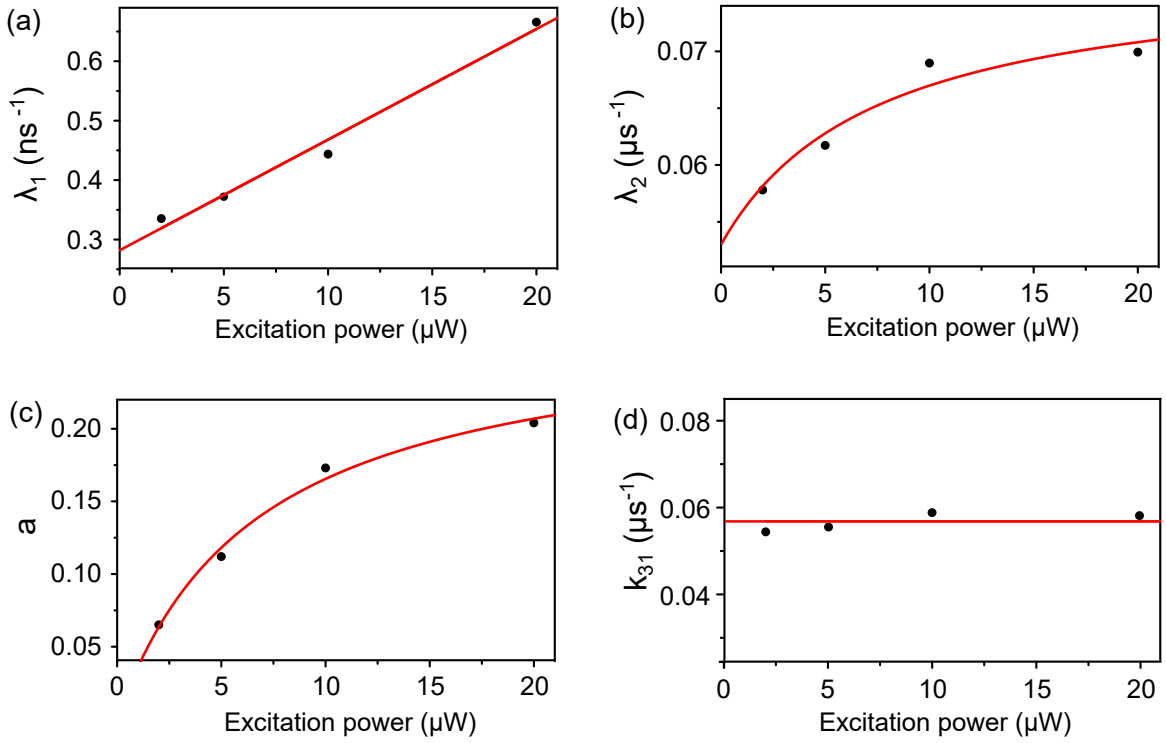

Figure 3.24: (a-c) - Excitation power dependence of the parameters λ_1 (a), λ_2 (b) and a (c) in $g^{(2)}$ function. Red lines are fits according to Eq. 3.20 - 3.22. (d) - Excitation power dependence of the relaxation rate k_{31} of metastable state. The value of k_{31} is unchanged within the excitation power range from 0 to 20 μW(constant, indicated by the red line).

Then the values of λ_2 and a as a function of I_{ex} are plotted on Fig. 3.24 - (b) and (c), respectively. Using Eq. 3.21 and 3.22, the values of relaxation rate k_{31} of metastable state is given by

$$k_{31} = \frac{\lambda_2}{1+a} \tag{3.27}$$

From Fig. 3.24 - (d), we can see that k_{31} is unchanged within the excitation power range from 0 to 20 μWand the fit (red line) gives $k_{31} = 0.053 \pm 0.001$ μs^{-1}, which corresponds to a triplet state lifetime k_{31}^{-1} of 18 μs.[53]

[53]The previous photophysics studies on individual emitters like single molecules [126] and point defects [128, 239] reveal that the deshelving rate (k_{31}^{-1}) often has a linear power dependence. In our case, the value of k_{31}^{-1} of this GQD is roughly unchanged till 20 μW and when we tried to excite with a higher power, the GQD is photobleached.

Finally, using Eq. 3.21, 3.22 and 3.23 we fit the evolution of λ_2 and a as a function excitation power. Since the value of σ and k_{21} have been already deduced previously, here the only fit parameter is inter-system crossing rate k_{23}. Treating k_{23} as a constant, we obtain

$$k_{23} = 0.025 \pm 0.005 \ \mu s^{-1} \tag{3.28}$$

Estimation of quantum efficiency

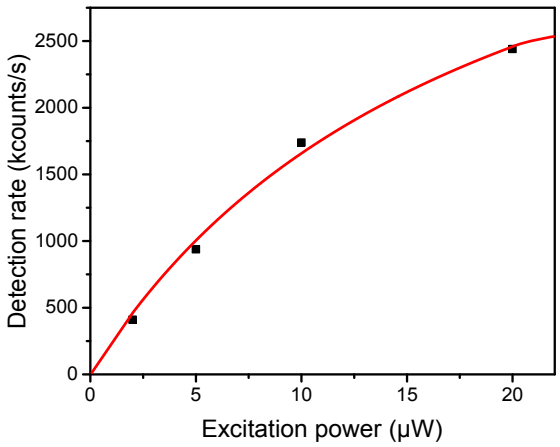

Figure 3.25: Saturation curve recorded on the same single $C_{96}C_{12}$ GQD as previous $g^{(2)}$ measurements. The red line is the fit according to Eq. 3.30.

We now estimate the quantum efficiency this single $C_{96}C_{12}$ GQD. The detected photoluminescence intensity R is linked to the stationary population of the excited state (2) $p_2(\infty)$ with the following expression:

$$R = \eta_{det} \ \eta_Q \ k_{21} \ p_2(\infty) \tag{3.29}$$

where η_{det} and η_Q is the overall detection efficiency and the fluorescence quantum efficiency, respectively. By replacing $p_2(\infty)$ with the already deduced expression Eq. 3.13 and 3.16, we obtain

$$R = \eta_{det}\eta_Q \frac{k_{21}}{(k_{21}/k_{12} + k_{23}/k_{31} + 1))} \tag{3.30}$$

Assuming that

$$R_\infty = \eta_{det}\eta_Q \frac{k_{31}k_{21}}{k_{23} + k_{31}} \tag{3.31}$$

$$I_\infty = \frac{k_{31}k_{21}}{(\sigma\lambda_{ex}/hc)(k_{23} + k_{31})} \tag{3.32}$$

we end up with the following relation:

$$R = R_\infty \ \frac{I}{I + I_\infty} \tag{3.33}$$

where I is excitation power density, entering via the relation in Eq. 3.23. We can see that for a three-level system modeled above, the detection rate R as a function of excitation power density I also represents a saturation behavior, which is similar to the case of

two-level system. This saturation behavior is characterized by the two parameters R_∞ and I_∞. R_∞ describes the detection rate at infinitely strong excitation power and I_∞ is the power density at which the detection rate is equal to $R_\infty/2$.

Therefore, we plot the detection rate of the GQD as a function of the excitation power (Fig. 3.25). By fitting this curve using Eq. 3.33, we obtain $\eta_{det} \times \eta_Q = 0.054$. The overall detection efficiency of our setup is expected to be lower than 15% (see Chap. II Sec. 2.1). We thus obtain a lower bound of the photoluminescence quantum efficiency:

$$\eta_Q \approx 35\% \tag{3.34}$$

Discussion on the deduced photophysical parameters

We now make some comments on the deduced values of the photophysical parameters of $C_{96}C_{12}$ GQD. The model of three-level system indicates that the metastable (triplet) state play a central role in the photodynamics of the emitter. Since the triplet state is considered as a dark state, the emission intensity trace presents dark periods lasting for the triplet lifetime on average. As a result, the dye molecules often exhibit obvious blinking due to the long triplet state lifetime (∼millisecond) [240]. In contrast, for $C_{96}C_{12}$ GQD, the triplet state lifetime $1/k_{31}$ is very short (∼18 µs). Moreover, the ratio k_{21}/k_{23} is also very low ($\sim 10^{-4}$). This means that for each 10^4 excitation-emission cycle there is only one time the system goes into the triplet state. So we can conclude that the effect of triplet state on the emission efficiency of $C_{96}C_{12}$ GQD is very limited. This also explains the absence of observable blinking in the emission intensity trace.

Besides, the photostability of fluorescent molecule can be also correlated to its triplet state. It is well-known that under ambient conditions the presence of oxygen can make the molecule photobleach [241]. O_2 has a triplet ground state and it is relatively inert. However, electron or energy transfer can occur between oxygen and the fluorescent molecule in triplet state, yielding excited singlet oxygen. The singlet oxygen is very reactive and can react with the fluorescent molecule and leads to its chemical degradation to non-fluorescent products (photobleaching). If we look at $C_{96}C_{12}$ GQD, its low inter-system crossing yield and short triplet lifetime make it less possible to interact with oxygen. Thus, it could be a reason for its high photostability.

As we can see from Eq. 3.30, the excited state decay rate k_{21} is one of the major factors that determine the emission rate (or brightness) of a quantum emitter. The shorter excited lifetim k_{21}^{-1} is, the higer emission rate we may have. Here, in a bare photonic configuration, we found a lifetime k_{21}^{-1} of $C_{96}C_{12}$ GQD ∼5 ns. For comparison, the two common quantum emitters: NV centers in nanodiamond and CdSe nanocrystals usually have a excited life time more than 10 ns [242,243]. The relative short value of k_{21}^{-1} together with the low inter-system crossing yield thus gives rise to the high brightness of $C_{96}C_{12}$ GQD. Moreover, the brightness can be further increased by coupling GQDs to a optical cavity.

We compare the obtained absorption cross-section value of $C_{96}C_{12}$ GQD with other conjugated carbon structures. Considering that our GQD consists of 96 conjugated carbon atoms, its absorption cross-section per carbon atom is $\approx 1.0 \times 10^{-16}$ cm^2. A single terrylene diimide (TDI, one typical dye molecule) is reporteed to have a absorption cross-section of 1.8×10^{-15} cm^2 [244], which corresponds to 0.6×10^{-16} cm^2/C atom. For

single wall carbon nanotubes (SWCNTs) with chirality of (6,5), the absorption cross-section for the S_{22} transition is reported to be 0.4×10^{-16} cm^2/C atom [245]. Thus the absorption cross-section per carbon atom for our GQD is in the same order as other conjugated carbon structures.

One should note that these values of the photophysical parameters are obtained from one specific GQD. Depending on the local environments, the values could be different from one GQD to another. It is thus very necessary to perform such photo-dynamic measurements on more GQDs to see how the values of the parameters will change [246]. We may eventually perform a statistical analysis in order to have a general image on the photophysical properties of $C_{96}C_{12}$ GQD.

3.4 Analysis photon statistics by waiting time distribution

In addition to the measurement of second order correlation function $g^{(2)}$ with a HBT configuration, photon statistics could be studied in other ways. Here we record individual photon detection events of the two APDs[54] with their arrival time in respect with the start of the experiment (see Fig. 3.26).

From the data, we can build a histogram of the inter-photon waiting time. Although the waiting time distribution cannot give access to the anti-bunching phenomena due to the finite instrument dead time, it gives us a clear image on the blinking with a time scale down to µs. For a Poissonian source, waiting time distribution is a single exponential with decay time τ equal to the inverse of the count rate. If the source exhibits blinking with off-time on a time scale $\tau_{\text{blink}} > \tau$, the distribution should have an additional component with characteristic decay time determined by τ_{blink}. This method have been applied to characterize the emission statistic of single photon emitters, e.g. single defects in WSe_2 [222] and dibenzoterrylene (DBT) molecules [247].

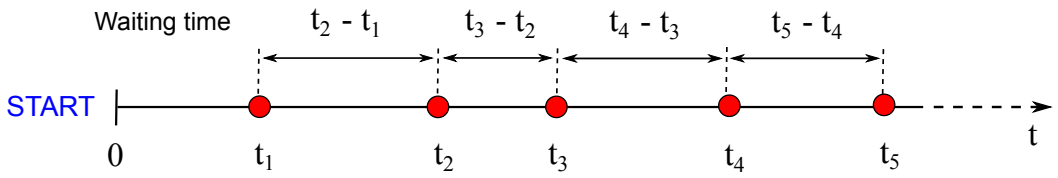

Figure 3.26: Schematic illustration of the waiting time distribution measurement.

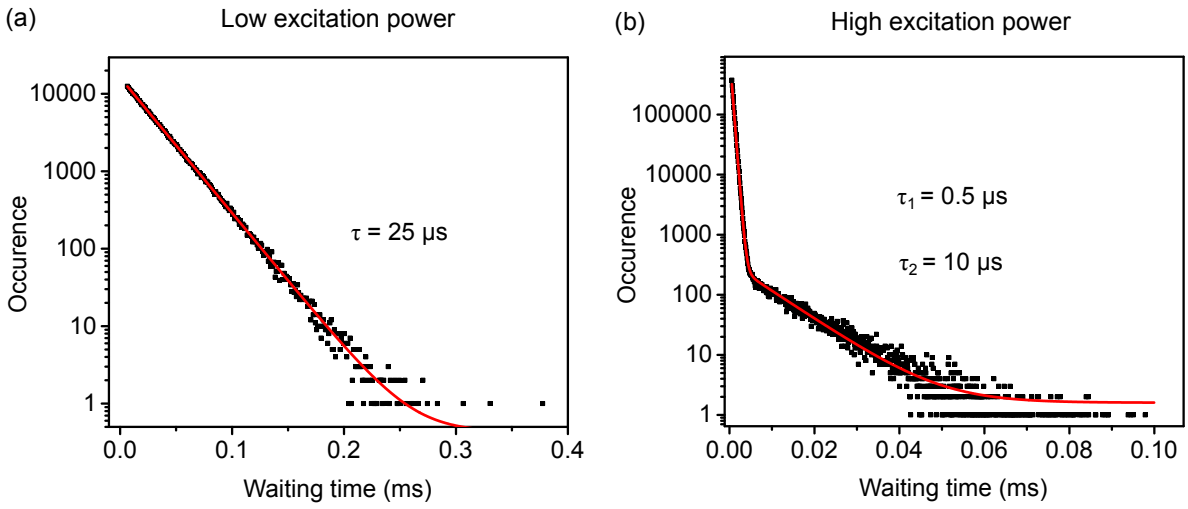

Figure 3.27: Inter-photon waiting time histograms of a single $C_{96}C_{12}$ GQD for two excitation powers. (a) - At low excitation power (200 nW), the histogram displays a mono-exponential decay. (b) - At high excitation power (30 µW), the histogram displays a bi-exponential decay.

Fig. 3.27 shows the inter-photon waiting time histograms of a single $C_{96}C_{12}$ GQD for two excitation powers. At low excitation power, the waiting time can be fitted with a single exponential with decay time τ of 25 µs, in good agreement with the detection

[54] In contrast to the $g^{(2)}$ measurement by "start-stop" method, here the two APDs operate identically. They are connected to the PicoHarp aquisition card in time-tagged time-resolved (TTTR) mode.

count rate of 40 kcounts/s. It implies that there is no blinking on a time scale longer than 25 µs. Note that this observation is in strong contrast with what is observed on several nanoobjects where long off-times are measured (up to tens of seconds for some semiconductor nanocrystals [248]). At higher excitation power, the histogram exhibits a fast decay $\tau_1 = 0.5$ µs, directly linked to the detection count rate (2 Mcounts/s), and a slow decay $\tau_2 = 10$ µs that we attribute to the dark time due to inter-system crossing. This slow decay time is indeed in good agreement with the triplet lifetime $k_{31}^{-1} \sim 18$ µs. Likewise, the weight ratio between the slow and fast component is about 10^{-4} again in good agreement with the inter-system crossing yield $k_{23}/k_{21} \sim 10^{-4}$. The two waiting time histograms confirm that the intensity fluctuations only originate from the passage to the triplet state and that its effect on the emission efficiency of GQD is very limited.

Moreover, the acquired photon arrival time can also be used to calculate the $g^{(2)}$ function by using the classical definition of intensity auto-correlation function: $g^{(2)}(\tau) = \langle I(t)I(t+\tau)\rangle / \langle I(t)\rangle^2$. Fig. 3.28 shows the long timescale $g^{(2)}$ function obtained from this method and the photon arrival time data used here was the same as the waiting time distribution shown in Fig. 3.27 - (b). The fit (red line) gives a bunching characteristic time of 11 µs and an bunching amplitude of 0.1 with excitation power of 30 µW. These values are consistent with the results in Fig. 3.24.

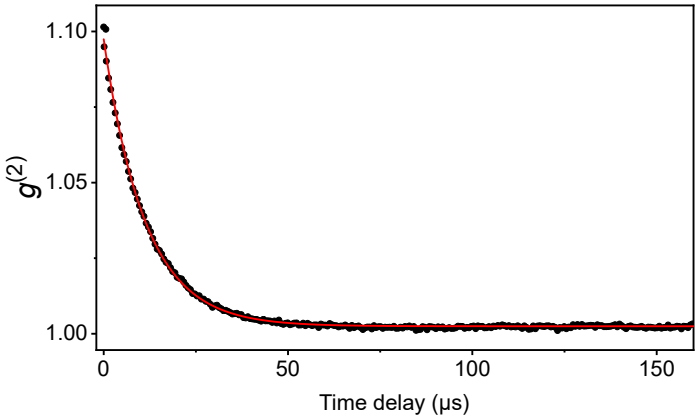

Figure 3.28: $g^{(2)}$ function obtained from the photon arrival time data (same as the Fig. 3.27 - (b)). The red curve is the fit using a mono-exponential decay function.

4 Optical study on $C_{96}Cl$ GQD

Having the very encouraging results of $C_{96}C_{12}$, we now perform the measurements on $C_{96}Cl$ that has the same aromatic core as $C_{96}C_{12}$ but with the chlorinated edges (Fig. 4.1 - (a)), to see how the structure would influence the properties of GQD.

4.1 Optical spectroscopy on $C_{96}Cl$ dispersions

First, we performed the optical spectroscopy of $C_{96}Cl$ dispersions. The $C_{96}Cl$ were also dispersed in TCB. Theoretical calculations indicate that due to the strong steric hindrance induced by the chlorine atoms $C_{96}Cl$ has a non-planar geometry compared to $C_{96}C_{12}$ [60]. Thus, $C_{96}Cl$ is expected to have an enhanced solubility (less aggregation) since the π-π stacking is reduced.

The blue curve in Fig. 4.1 - (b) shows the optical absorption spectrum of $C_{96}Cl$. The spectrum is more structured, suggesting less aggregation. The main absorption line is centered at 505 nm with a blue side shoulder at 476 nm and two red-side shoulders at 530 nm and 545 nm. Compared to $C_{96}C_{12}$, we can see that the absorption spectrum is generally red-shifted. One should note that besides these sharp lines around 500-550 nm, the spectrum does not show the weak lower energy lines, in contrast to what we have observed in $C_{96}C_{12}$. The pink curve in Fig. 4.1 - (b) shows the PL spectrum. The shape of the spectrum is very similar to $C_{96}C_{12}$, it consists of two low energy lines (main line at 780 nm and a shoulder at ≈875 nm) and some high energy lines between 600-700 nm. So we can see that the PL spectrum is also red-shifted compared to $C_{96}C_{12}$ (the main line is re-shifted by ∼130 nm). Theoretical calculations indicate that since chlorine atom has strong electronegativity, the edge chlorination could lead to a asymmetric stabilization of the frontier molecular orbital of GQD [60]. As a result, it is expected to have a lower optical band gap for the edge chlorinated GQDs than the unsubstituted ones. The fact that the emission of $C_{96}Cl$ is red-shifted by 130 nm compared to $C_{96}C_{12}$ is in agreement with the theoretical predictions.

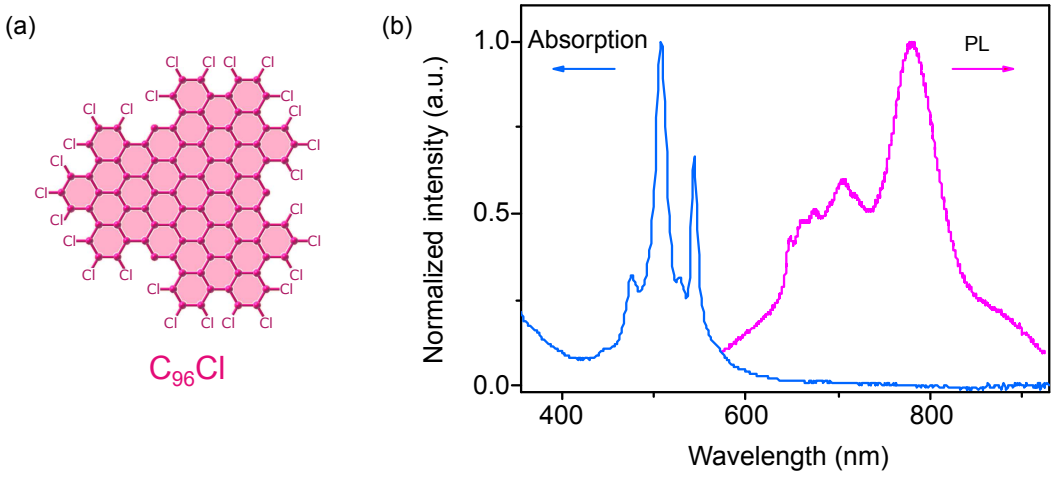

Figure 4.1: (a) - Chemical structure of $C_{96}Cl$ GQD. (b) - Optical absorption spectrum (blue line) and photoluminescence spectrum (pink line) of $C_{96}Cl$ dispersion in 1,2,4-trichlorobenzene (TCB). To acquire photoluminescence spectrum, we used the super-continuum laser tuned at 450 nm.

We then performed time-resolved PL on these lines (see Fig. 4.2). Similar to the results of $C_{96}C_{12}$, the two low energy lines at 780 nm and 875 nm roughly have a mono-exponential decay with a time constant of $\approx$ 5 ns[55], while the high energy lines between 600-700 nm decay multi-exponentially. We thus attribute the two low energy lines to the emission of $C_{96}Cl$ monomers and the high energy lines to the emission from the aggregates.

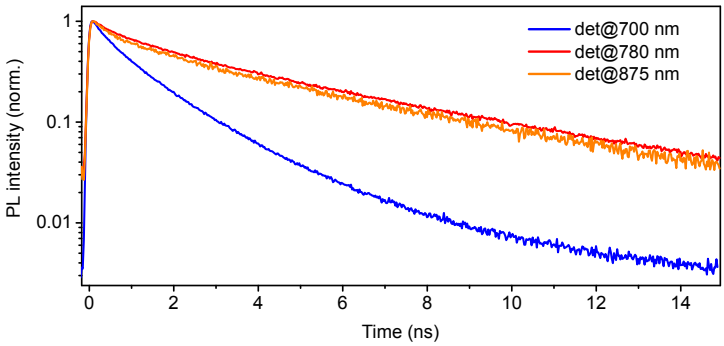

Figure 4.2: Time-resolved PL measurements on C96Cl dispersion recorded at the different PL lines.

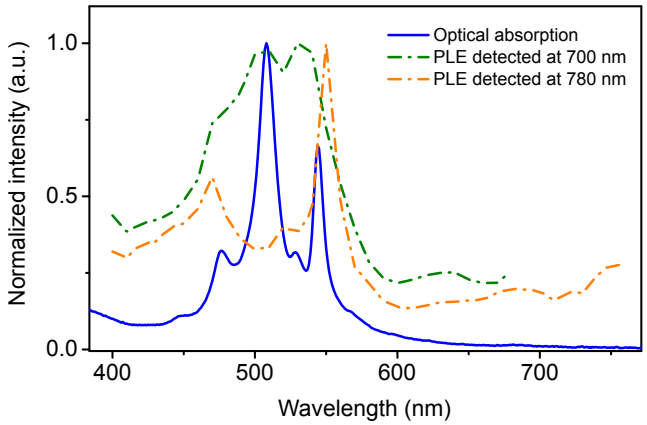

Figure 4.3: PLE spectra of C96Cl dispersion detected at the different PL lines.

Finally, we performed PLE measurements (see Fig. 4.3)[56]. The orange line displays the PLE curve when recorded on the main PL line at 780 nm. We can see that it is in good agreement with the absoption spectrum (blue line): the absorption peaks at 476 nm, 530 nm and 545 nm can be found in this PLE curve. We also note that the main absorption peak at 505 nm is missing in the PLE curve. The green curve displays the PLE curve when recorded on the high energy PL line at 700 nm. It is broad and centered at ~505 nm same as the absorption spectrum.

In analogy to the results on $C_{96}C_{12}$ GQD, the PLE curve detected at 780 nm should reflects the intrinsic absorption behavior of $C_{96}Cl$ monomers. Assuming that the edge chlorination just reduce the energy of quantum states in $C_{96}Cl$ compared to $C_{96}C_{12}$, we can tentatively attribute the line at 530 nm and 545 nm to the β and β' band as we discussed in Sec. 3.1. However, the lower energy lines which correspond to α and p bands are not well-resolved (which could correspond to the bump at 680 nm and

[55]We observed that the curves have a small contribution from a very fast decay component with a time constant of 800 ps.

[56]The PLE measurements are performed at PPSM laboratory, ENS Cachan using a fluorometer. Above 730 nm, its detection efficiency becomes very low.

750 nm in the PLE curve, but the signal is too weak.). This observation is in contrast to the results of $C_{96}C_{12}$, which suggests that the two lowest transitions in $C_{96}Cl$ have a lower oscillator strength than in $C_{96}C_{12}$. This implies that $C_{96}Cl$ may have a more symmetric conformation than $C_{96}C_{12}$. Moreover, the intense peak at 505 nm observed in absorption spectrum is missing in this PLE curve. One possible explanation is that the peak originates from the aggregates. Theoretical calculations indicates that the major intermolecular interactions between $C_{96}Cl$ GQDs is Cl-Cl and Cl-π short contacts rather than π-π interactions [60]. These two interactions may result in a new stacking structure and lead to such absorption peak. Nevertheless, further investigations, for example, TEM measurements and theoretical modeling, are very necessary to explain theses distinct features of $C_{96}Cl$ GQD.

4.2 Microphotoluminescence spectroscopy of $C_{96}Cl$

We also performed the microphotoluminescence spectroscopy on the samples containing $C_{96}Cl$, which are prepared by the same procedures as $C_{96}C_{12}$. Similarly, we found diffraction-limited spots when we performed PL scan on the sample with the highest dilution (10^{-7} mol/L). We note that the emission intensity of $C_{96}Cl$ spots in the PL scan images is usually 5 times weaker than the spots of $C_{96}C_{12}$.[57] This could be due to the fact that the lowest transition in $C_{96}Cl$ is relatively "dark" (as we have seen in the absorption and PLE spectra of $C_{96}Cl$ solution, the line that corresponds to this transition is almost non-resolved (Fig. 4.3)). Moreover, as we mentioned, $C_{96}Cl$ has a non-planar geometry. This non-planar geometry could lead to more vibrational dissipation and thus a lower quantum yield.

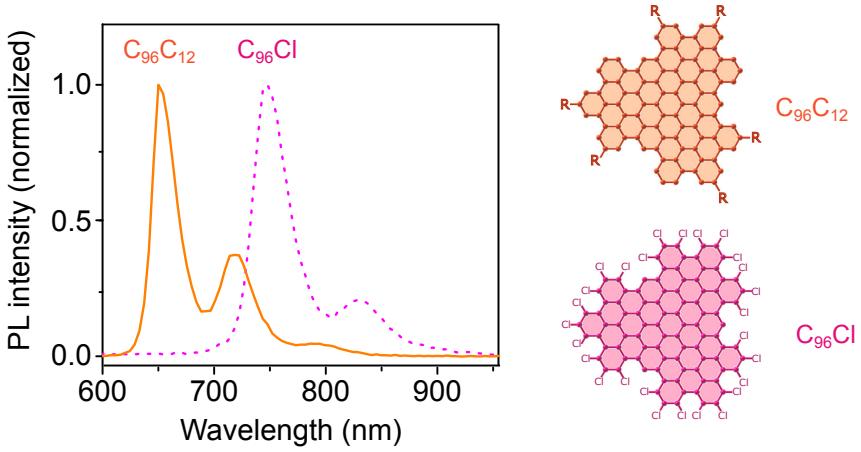

Figure 4.4: Left panel: Typical room temperature PL spectra of a single $C_{96}C_{12}$ GQD (solid orange line) and a single $C_{96}Cl$ GQD (dashed purple line). The main line of $C_{96}Cl$ is rigidly red-shifted by 100 nm ($\sim$ 250 meV) compared to $C_{96}C_{12}$. Excitation wavelength: 594 nm. Right panel: chemical structures of $C_{96}C_{12}$ and $C_{96}Cl$.

Although the emission is not as strong as $C_{96}C_{12}$, it is enough to perform PL spectroscopy. A typical PL spectrum of such a spot of $C_{96}Cl$ is displayed by the pink dotted line in Fig. 4.4. We can see that the emission wavelength is rigidly red-shifted by 100 nm

[57] To obtain a count rate of $\sim$30 kcounts/s, we should increase the excitation power to 1 μW, while for $C_{96}C_{12}$ we need only 200 nW.

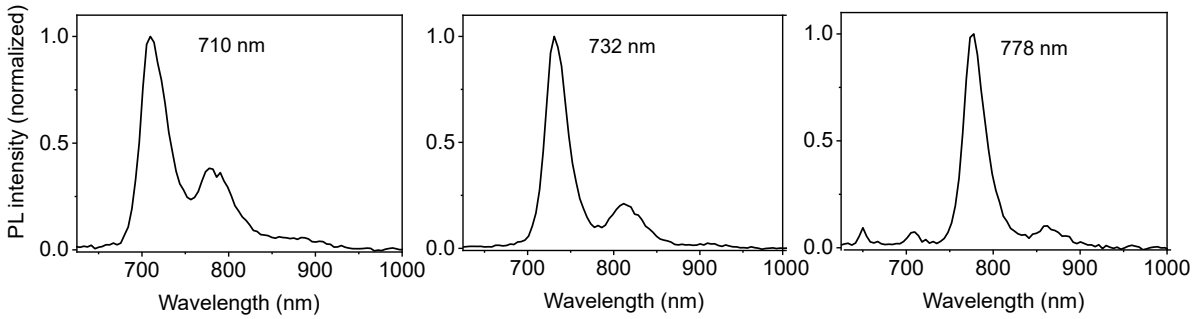

Figure 4.5: Additional three PL spectra of singe $C_{96}Cl$ GQDs. The position of line 1 is located at 710 nm, 732 nm and 778 nm, respectively.

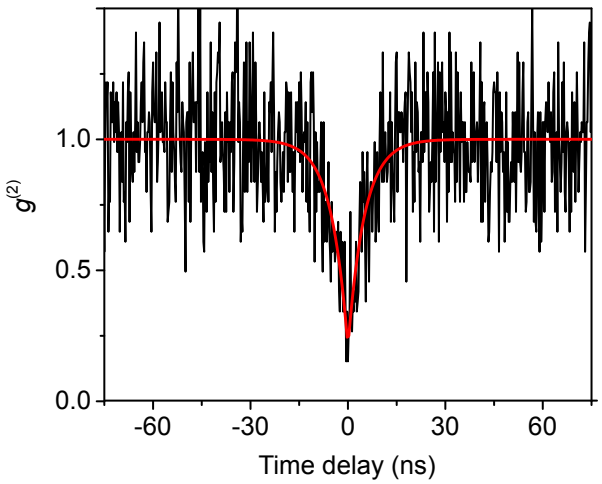

Figure 4.6: $g^{(2)}$ curve of a single $C_{96}Cl$ GQD (black line) with a double exponential fit (red line). Excitation wavelength: 594 nm. Excitation power: 1 μW. Here the non-zero value of $g^{(2)}(0)$ is presumably due to the background emission, as the count rate of $C_{96}Cl$ is relatively low.

($\sim$ 250 meV) while the shape of the PL of $C_{96}Cl$ is very similar to $C_{96}C_{12}$. The main PL line of $C_{96}Cl$ is at 750 nm (1.65 eV). Note that this PL spectrum is also in good agreement with the results in $C_{96}Cl$ solution (Fig. 4.1). We have performed PL spectroscopy on four single $C_{96}Cl$ GQDs and the position of line 1 are all longer than 700 nm (Fig. 4.4 and 4.5). By comparing with the wavelength distribution of line 1 of $C_{96}C_{12}$ GQD (Fig. 3.3), these statistical results further confirm the emission wavelength of $C_{96}Cl$ GQD is red-shifted.

Moreover, we also performed the second order photon correlation $g^{(2)}(\tau)$ measurements on such spots of single $C_{96}Cl$ GQD. A typical $g^{(2)}$ curve is shown in Fig. 4.6. The strong anti-bunching demonstrates that the edge chlorinated GQDs maintain single photon emission at room temperature.

As we have mentioned in the introduction, one of the great potential of GQDs lies in the precise engineering of their electronic properties through the control of their structure. Indeed, this result shows a example that the intrinsic properties, here is the emission wavelength, of GQDs can be controlled by the bottom-up synthesis.

Conclusion

In this chapter, I showed a detailed study on the optical properties of bottom-up synthesized graphene quantum dots (GQDs). I first performed the steady-state and time-resolved photoluminescence spectroscopy measurements on the solution of GQDs. The results imply that the GQDs are indeed individualized. I then performed a microphotoluminescence to directly address the intrinsic properties of single GQDs. The intrinsic emission of GQDs at the single object level was observed. Second-order photon correlation measurements revealed that GQDs exhibit single-photon emission at room temperature with a high purity, high brightness and good stability. Moreover, a photo-dynamic analysis on a single GQD was performed to understand its population dynamics. This measurement also provided a strong indication of the existence low lying triplet state in GQD. Finally, I showed that by precise edge-chlorination, the emission wavelength of a single GQD can be red-shifted by 100 nm. It is the first example of the optical tunability of GQDs through the control of their structure. The results shown in this chapter demonstrate that the high potential of GQDs revealed by theory is now accessible experimentally.

Conclusion and perspectives

This manuscript has been dedicated to the optical study, especially the photoluminescence studies of bottom-up synthesized GNRs and GQDs. This work has demonstrated the remarkable properties of such GNRs and GQDs.

In the first section, we studied the GNRs synthesized by two different bottom-up approaches: solution-mediated and surface-assisted. For the solution-mediated approach, it is necessary to disperse the produced GNR powders into suspension. Our optical spectroscopy results of such GNR suspensions displayed broad and highly Stokes shifted emission with multiexponential decay, which is possible to be related to the formation of excimer states due to the π-π stacking of GNRs. Besides, we have also shown the results of single-particle spectroscopic measurements using simultaneously confocal fluorescence microscopy and atomic force microscopy. The observation of emission of small aggregates confirms the ability of GNRs to emit light in the solid state. These results imply that the suspension are mainly composed of small aggregates that blur the intrinsic optical properties of GNR. For further work, one major issue is how to individualize such in-solution synthesized GNRs. To this end, several strategies are under development:

- Find efficient solvents or surfactants and proper solubilization conditions.
- Edge functionalization to enhance the solubility and reduce the aggregation effect.
- Since GNRs can be easily fold and/or bend, functionalization of the substrate surface may also be needed when performing the deposition.

For the on-surface approach, individualized GNRs are grown on the gold surface. Due to the coupling between gold substrate and GNRs, the sample has been transferred onto insulating substrates. The microRaman results confirmed that the GNRs indeed have been transferred onto the target substrates. Moreover, some remarkable Raman features have been observed, implying the distinct vibrational properties of GNRs compared to graphene and carbon nanotubes. We observed spectrally broad high energy PL throughout the whole transferred GNR film, instead of bright bandgap emission. This emission has been attributed to the emission of defects, which could be created during the synthesis and also be induced by the wet chemistry transfer method. So in the next step, the synthesis should be improved and we will try to perform a dry transfer method. In addition, the microabsorption measurement are planned in order to know the exact optical transition positions of the on-surface synthesized GNRs.

This section show the optical properties of bottom-up synthesized GNRs and these properties have not been observed in top-down fabricated GNRs due to the lack of structural control. Although the intrinsic emission from single GNRs has not been probed yet, our results provide a clear direction to realize it.

In the second section, we studied optical properties of bottom-up synthesized GQDs. The steady-state and time-resolved photoluminescence spectroscopy results indicated that the GQDs are indeed individualized in their dispersion. A microphotoluminescence study was then performed to directly address the intrinsic properties of single GQDs. The intrinsic emission of GQDs at the single object level was observed. Second-order photon correlation measurements revealed that GQDs exhibit single-photon emission at

room temperature with a high purity, high brightness and good stability. Moreover, a photo-dynamic analysis on a single GQD was performed to understand its population dynamics. These measurements provided a strong indication of the existence of a low lying triplet state in GQD. Finally, by precise edge-chlorination, the emission wavelength of a single GQD can be red-shifted by 100 nm. It is first example of the optical tunability of GQDs through the control of their structure. The results shown in this chapter demonstrate that the high potential of GQDs revealed by theory is now accessible experimentally. For further investigations, the microphotoluminescence measurements at low temperature are very necessary. Such measurements could allow us to go deeper into the electronic structure of GQDs and to reveal the potential rich physics of GQDs (e.g., charge state emission, multi-exciton formation, fine structure splitting, etc.). Moreover, since our results implies the existence of low lying triplet state in GQDs, to highlight the potential of GQDs for spin physics, it is interesting to perform optically detected magnetic resonance (ODMR) measurements as people have been done on N-V centers in diamond [249,250]. In addition, as GQDs with different size and shape can be synthesized by bottom-up chemistry, a systematical study on the link between the properties and the structure of GQDs should be performed.

References

[1] Novoselov, K. S. *et al.* Electric field effect in atomically thin carbon films. *Science* **306**, 666–669 (2004). (cited page 8)

[2] Zhang, Y., Tan, Y.-W., Stormer, H. L. & Kim, P. Experimental observation of the quantum hall effect and berry's phase in graphene. *Nature* **438**, 201 (2005). (cited page 8)

[3] Novoselov, K. S. *et al.* Room-temperature quantum hall effect in graphene. *Science* **315**, 1379–1379 (2007). (cited pages 8, 15)

[4] Bolotin, K. *et al.* Ultrahigh electron mobility in suspended graphene. *Solid State Communications* **146**, 351 – 355 (2008). (cited pages 8, 15)

[5] Liao, L. *et al.* High-speed graphene transistors with a self-aligned nanowire gate. *Nature* **467**, 305 (2010). (cited page 8)

[6] Novoselov, K. *et al.* A roadmap for graphene. *Nature* **490**, 192–200 (2012). (cited page 8)

[7] Balandin, A. A. *et al.* Superior thermal conductivity of single-layer graphene. *Nano Letters* **8**, 902–907 (2008). (cited page 8)

[8] Ghosh, S. *et al.* Extremely high thermal conductivity of graphene: Prospects for thermal management applications in nanoelectronic circuits. *Applied Physics Letters* **92**, 151911 (2008). (cited page 8)

[9] Lee, C., Wei, X., Kysar, J. W. & Hone, J. Measurement of the elastic properties and intrinsic strength of monolayer graphene. *Science* **321**, 385–388 (2008). (cited page 8)

[10] Nair, R. R. *et al.* Fine structure constant defines visual transparency of graphene. *Science* **320**, 1308–1308 (2008). (cited page 8)

[11] Bae, S. *et al.* Roll-to-roll production of 30-inch graphene films for transparent electrodes. *Nature Nanotechnology* **5**, 574 (2010). (cited page 8)

[12] Zhang, Y. *et al.* Direct observation of a widely tunable bandgap in bilayer graphene. *Nature* **459**, 820 (2009). (cited page 8)

[13] Schwierz, F. Graphene transistors. *Nature Nanotechnology* **5**, 487 (2010). (cited page 8)

[14] Ohta, T., Bostwick, A., Seyller, T., Horn, K. & Rotenberg, E. Controlling the electronic structure of bilayer graphene. *Science* **313**, 951–954 (2006). (cited page 8)

[15] Elias, D. C. *et al.* Control of graphene's properties by reversible hydrogenation: Evidence for graphane. *Science* **323**, 610–613 (2009). (cited page 8)

[16] Nair, R. R. *et al.* Fluorographene: A two-dimensional counterpart of teflon. *Small* **6**, 2877–2884 (2010). (cited page 8)

[17] Pereira, V. M., Castro Neto, A. H. & Peres, N. M. R. Tight-binding approach to uniaxial strain in graphene. *Phys. Rev. B* **80**, 045401 (2009). (cited page 8)

[18] Cai, J. *et al.* Atomically precise bottom-up fabrication of graphene nanoribbons. *Nature* **466**, 470–473 (2010). (cited pages 9, 23, 24, 27, 66, 94)

[19] Novoselov, K. S. *et al.* Two-dimensional atomic crystals. *PNAS* **102**, 10451–10453 (2005). (cited pages 9, 90)

[20] Reich, S., Thomsen, C. & Maultzsch, J. *Carbon Nanotubes: Basic Concepts and Physical Properties* (Wiley, 2004). (cited pages 12, 15)

[21] Ando, T. Theory of electronic states and transport in carbon nanotubes. *Journal of the Physical Society of Japan* **74**, 777–817 (2005). (cited pages 13, 15)

[22] Charlier, J.-C., Blase, X. & Roche, S. Electronic and transport properties of nanotubes. *Rev. Mod. Phys.* **79**, 677–732 (2007). (cited page 13)

[23] Wallace, P. R. The band theory of graphite. *Phys. Rev.* **71**, 622–634 (1947). (cited page 13)

[24] Reich, S., Maultzsch, J., Thomsen, C. & Ordejón, P. Tight-binding description of graphene. *Phys. Rev. B* **66**, 035412 (2002). (cited page 13)

[25] Du, X., Skachko, I., Barker, A. & Andrei, E. Y. Approaching ballistic transport in suspended graphene. *Nature Nanotechnology* **3**, 491 (2008). (cited page 15)

[26] Novoselov, K. S. *et al.* Two-dimensional gas of massless dirac fermions in graphene. *Nature* **438**, 197 (2005). (cited page 15)

[27] Wakabayashi, K., Sasaki, K.-i., Nakanishi, T. & Enoki, T. Electronic states of graphene nanoribbons and analytical solutions. *Science and Technology of Advanced Materials* **11**, 054504 (2010). (cited page 16)

[28] Talirz, L. *et al.* On-surface synthesis and characterization of 9-atom wide armchair graphene nanoribbons. *ACS Nano* **11**, 1380–1388 (2017). (cited pages 16, 28, 84, 86, 91, 94)

[29] Rozhkov, A. V. & Nori, F. Exact wave functions for an electron on a graphene triangular quantum dot. *Phys. Rev. B* **81**, 155401 (2010). (cited pages 16, 17)

[30] McGuire, J. A. Growth and optical properties of colloidal graphene quantum dots. *physica status solidi (RRL)* **10**, 91–101 (2016). (cited page 17)

[31] Son, Y.-W., Cohen, M. L. & Louie, S. G. Energy gaps in graphene nanoribbons. *Phys. Rev. Lett.* **97**, 216803 (2006). (cited pages 17, 18, 67, 88)

[32] Güçlü, A. D., Potasz, P. & Hawrylak, P. Excitonic absorption in gate-controlled graphene quantum dots. *Phys. Rev. B* **82**, 155445 (2010). (cited page 18)

[33] Nakada, K., Fujita, M., Dresselhaus, G. & Dresselhaus, M. S. Edge state in graphene ribbons: Nanometer size effect and edge shape dependence. *Phys. Rev. B* **54**, 17954–17961 (1996). (cited page 18)

[34] Hod, O., Barone, V. & Scuseria, G. E. Half-metallic graphene nanodots: A comprehensive first-principles theoretical study. *Phys. Rev. B* **77**, 035411 (2008). (cited page 18)

[35] Fujita, M., Wakabayashi, K., Nakada, K. & Kusakabe, K. Peculiar localized state at zigzag graphite edge. *Journal of the Physical Society of Japan* **65**, 1920–1923 (1996). (cited page 18)

[36] Wang, W. L., Meng, S. & Kaxiras, E. Graphene nanoflakes with large spin. *Nano Letters* **8**, 241–245 (2008). (cited pages 18, 104)

[37] Martin-Martinez, F. J., Fias, S., Van Lier, G., De Proft, F. & Geerlings, P. Tuning aromaticity patterns and electronic properties of armchair graphene nanoribbons with chemical edge functionalisation. *Phys. Chem. Chem. Phys.* **15**, 12637–12647 (2013). (cited page 19)

[38] Kawai, S. *et al.* Atomically controlled substitutional boron-doping of graphene nanoribbons. *Nature Communications* **6**, 8098 (2015). (cited pages 19, 23, 24)

[39] Corso, M., Carbonell-Sanromà, E. & de Oteyza, D. G. Bottom-up fabrication of atomically precise graphene nanoribbons. In de Oteyza, D. G. & Rogero, C. (eds.) *On-Surface Synthesis II*, 113–152 (Springer International Publishing, Cham, 2018). (cited pages 19, 28)

[40] Sevinçli, H., Topsakal, M. & Ciraci, S. Superlattice structures of graphene-based armchair nanoribbons. *Phys. Rev. B* **78**, 245402 (2008). (cited page 19)

[41] Han, W., Kawakami, R. K., Gmitra, M. & Fabian, J. Graphene spintronics. *Nature Nanotechnology* **9**, 794 (2014). (cited page 19)

[42] Ponomarenko, L. A. *et al.* Chaotic dirac billiard in graphene quantum dots. *Science* **320**, 356–358 (2008). (cited page 19)

[43] Peng, J. *et al.* Graphene quantum dots derived from carbon fibers. *Nano Letters* **12**, 844–849 (2012). (cited pages 19, 20, 104)

[44] Pan, D., Zhang, J., Li, Z. & Wu, M. Hydrothermal route for cutting graphene sheets into blue-luminescent graphene quantum dots. *Advanced Materials* **22**, 734–738 (2010). (cited pages 19, 104)

[45] Li, F., Kou, L., Chen, W., Wu, C. & Guo, T. Enhancing the short-circuit current and power conversion efficiency of polymer solar cells with graphene quantum dots derived from double-walled carbon nanotubes. *Npg Asia Materials* **5**, e60 (2013). (cited page 19)

[46] Chua, C. K. *et al.* Synthesis of strongly fluorescent graphene quantum dots by cage-opening buckminsterfullerene. *ACS Nano* **9**, 2548–2555 (2015). (cited page 19)

[47] Guanxiong, C. *et al.* Rupturing c60 molecules into graphene-oxide-like quantum dots: Structure, photoluminescence, and catalytic application. *Small* **11**, 5296–5304 (2015). (cited page 19)

[48] Kwon, W. *et al.* Electroluminescence from graphene quantum dots prepared by amidative cutting of tattered graphite. *Nano Letters* **14**, 1306–1311 (2014). (cited page 19)

[49] Li, X., Wang, X., Zhang, L., Lee, S. & Dai, H. Chemically derived, ultrasmooth graphene nanoribbon semiconductors. *Science* **319**, 1229 (2009). (cited pages 20, 26)

[50] Tapaszt, L., Dobrik, G., Lambin, P. & Bir, L. P. Tailoring the atomic structure of graphene nanoribbons by scanning tunnelling microscope lithography. *Nature Nanotechnology* **3**, 397 (2008). (cited page 20)

[51] Bai, J., Duan, X. & Huang, Y. Rational fabrication of graphene nanoribbons using a nanowire etch mask. *Nano Letters* **9**, 2083–2087 (2009). (cited page 20)

[52] Jiao, L., Wang, X., Diankov, G., Wang, H. & Dai, H. Facile synthesis of high-quality graphene nanoribbons. *Nature Nanotechnology* **5**, 321 (2010). (cited page 20)

[53] Jiao, L., Zhang, L., Wang, X., Diankov, G. & Dai, H. Narrow graphene nanoribbons from carbon nanotubes. *Nature* **458**, 877 (2009). (cited page 20)

[54] Wang, X.-Y., Narita, A. & Müllen, K. Precision synthesis versus bulk-scale fabrication of graphenes. *Nature Reviews Chemistry* **2**, 0100 (2017). (cited page 20)

[55] Kosynkin, D. V. *et al.* Longitudinal unzipping of carbon nanotubes to form graphene nanoribbons. *Nature* **458**, 872 (2009). (cited page 20)

[56] Crommie, M. Graphene nanoribbons: A route to atomically precise nanoelectronics (2015). `https://www.onr.navy.mil/en/Conference-Event-ONR/Future-Force-Expo/~/media/Files/Conferences/EXPO-2015/Proceedings/VR-31-Nano-Science-Crommie.ashx`. (cited pages 21, 28)

[57] Wu, J., Pisula, W. & Müllen, K. Graphenes as Potential Material for Electronics. *Chem. Rev.* **107**, 718–747 (2007). (cited pages 21, 104)

[58] Simpson, C. D. *et al.* Nanosized molecular propellers by cyclodehydrogenation of polyphenylene dendrimers. *Journal of the American Chemical Society* **126**, 3139–3147 (2004). (cited page 21)

[59] Yan, X., Cui, X. & Li, L.-s. Synthesis of Large, Stable Colloidal Graphene Quantum Dots with Tunable Size. *J. Am. Chem. Soc.* **132**, 5944–5945 (2010). (cited pages 21, 22, 29, 104)

[60] Tan, Y.-Z. *et al.* Atomically precise edge chlorination of nanographenes and its application in graphene nanoribbons. *Nature Communications* **4**, 2646 (2013). (cited pages 21, 23, 66, 141, 143)

[61] Konishi, A. *et al.* Synthesis and characterization of teranthene: A singlet biradical polycyclic aromatic hydrocarbon having kekul structures. *J. Am. Chem. Soc.* **132**, 11021–11023 (2010). (cited pages 21, 22, 104)

[62] Patern Giuseppe, M. *et al.* Synthesis of dibenzo[hi,st]ovalene and its amplified spontaneous emission in a polystyrene matrix. *Angew. Chem. Int. Ed.* **56**, 6753–6757 (2017). (cited page 22)

[63] Tomović, Ž., Watson, M. D. & Müllen, K. Superphenalene-Based Columnar Liquid Crystals. *Angew. Chem. Int. Ed.* **43**, 755–758 (2004). (cited page 22)

[64] Chen, L., Hernandez, Y., Feng, X. & Müllen, K. From nanographene and graphene nanoribbons to graphene sheets: Chemical synthesis. *Angewandte Chemie - International Edition* **51**, 7640–7654 (2012). (cited page 22)

[65] Narita, A. *et al.* Synthesis of structurally well-defined and liquid-phase-processable graphene nanoribbons. *Nat Chem* **6**, 126–132 (2014). (cited pages 22, 23, 25, 26, 62, 66, 68, 69)

[66] Schwab, M. G. *et al.* Structurally Defined Graphene Nanoribbons with High Lateral Extension. *Journal of the American Chemical Society* **134**, 18169–18172 (2012). (cited pages 22, 25, 77)

[67] Yang, X. *et al.* Two-dimensional graphene nanoribbons. *Journal of the American Chemical Society* **130**, 4216–4217 (2008). (cited page 22)

[68] Vo, T. H. *et al.* Large-scale solution synthesis of narrow graphene nanoribbons. *Nature Communications* **5**, 3189 (2014). (cited pages 23, 66)

[69] Huang, Y. *et al.* Poly(elthylene oxide) Functionalized Graphene Nanoribbons with Excellent Solution Processability. *Journal of the American Chemical Society* **138**, 10136–10139 (2016). (cited pages 23, 68, 74, 79)

[70] Keerthi, A. *et al.* Edge functionalization of structurally defined graphene nanoribbons for modulating the self-assembled structures. *Journal of the American Chemical Society* **139**, 16454–16457 (2017). (cited page 23)

[71] Perkins, W. & Fisher, F. R. Inserting porphyrin quantum dots in bottom-up synthesized graphene nanoribbons. *Chem. Eur. J.* **23**, 17687–17691 (2017). (cited page 23)

[72] Slota, M. *et al.* Magnetic edge states and coherent manipulation of graphene nanoribbons. *Nature* **557**, 691–695 (2018). (cited page 23)

[73] Ruffieux, P. *et al.* On-surface synthesis of graphene nanoribbons with zigzag edge topology. *Nature* **531**, 489–492 (2016). (cited pages 23, 24)

[74] Cloke, R. R. *et al.* Site-specific substitutional boron doping of semiconducting armchair graphene nanoribbons. *Journal of the American Chemical Society* **137**, 8872–8875 (2015). (cited page 24)

[75] Zhang, Y. *et al.* Direct visualization of atomically precise nitrogen-doped graphene nanoribbons. *Applied Physics Letters* **105**, 023101 (2014). (cited page 24)

[76] Nguyen, G. D. *et al.* Bottom-up synthesis of n = 13 sulfur-doped graphene nanoribbons. *The Journal of Physical Chemistry C* **120**, 2684–2687 (2016). (cited page 24)

[77] Cai, J. *et al.* Graphene nanoribbon heterojunctions. *Nat Nano* **9**, 896–900 (2014). (cited pages 24, 66)

[78] Chen, Y.-C. *et al.* Molecular bandgap engineering of bottom-up synthesized graphene nanoribbon heterojunctions. *Nature Nanotechnology* **10**, 156 (2015). (cited page 24)

[79] Bastard, G. *Wave mechanics applied to semiconductor heterostructures*. Monographies de physique (Les Éditions de Physique, 1988). (cited page 24)

[80] Samorí, P., Severin, N., Simpson, C. D., Müllen, K. & Rabe, J. P. Epitaxial composite layers of electron donors and acceptors from very large polycyclic aromatic hydrocarbons. *Journal of the American Chemical Society* **124**, 9454–9457 (2002). (cited pages 25, 61)

[81] Rder, H. J. *et al.* Processing of giant graphene molecules by soft-landing mass spectrometry. *Nature Materials* **5**, 276 (2006). (cited page 25)

[82] Narita, A. *Bottom-up Solution Synthesis of Structurally Defined Graphene Nanoribbons*. Ph.D. thesis, Johannes Gutenberg University Mainz (2014). (cited pages 25, 62)

[83] Abbas, A. N. *et al.* Deposition, characterization, and thin-film-based chemical sensing of ultra-long chemically synthesized graphene nanoribbons. *J. Am. Chem. Soc.* **136**, 7555–7558 (2014). (cited pages 26, 66, 79)

[84] Konnerth, R. *et al.* Tuning the deposition of molecular graphene nanoribbons by surface functionalization. *Nanoscale* **7**, 12807–12811 (2015). (cited pages 26, 79)

[85] Verzhbitskiy, I. *et al.* Raman fingerprints of atomically precise graphene nanoribbons. *Nano Letters* **16**, 3442–3447 (2016). (cited pages 27, 68, 74, 77, 96)

[86] Ruffieux, P. *et al.* Electronic structure of atomically precise graphene nanoribbons. *ACS Nano* **6**, 6930–6935 (2012). (cited pages 28, 66)

[87] Chen, Y.-C. *et al.* Tuning the band gap of graphene nanoribbons synthesized from molecular precursors. *ACS Nano* **7**, 6123–6128 (2013). (cited page 28)

[88] Kharche, N. & Meunier, V. Width and crystal orientation dependent band gap renormalization in substrate-supported graphene nanoribbons. *The Journal of Physical Chemistry Letters* **7**, 1526–1533 (2016). (cited page 28)

[89] Ozfidan, I., Korkusinski, M., Güçlü, A. D., McGuire, J. A. & Hawrylak, P. Microscopic theory of the optical properties of colloidal graphene quantum dots. *Phys. Rev. B* **89**, 085310 (2014). (cited pages 29, 120, 121, 130)

[90] Cocchi, C., Prezzi, D., Ruini, A., Caldas, M. J. & Molinari, E. Anisotropy and Size Effects on the Optical Spectra of Polycyclic Aromatic Hydrocarbons. *J. Phys. Chem. A* **118**, 6507–6513 (2014). (cited pages 29, 117)

[91] Li, Y., Shu, H., Wang, S. & Wang, J. Electronic and Optical Properties of Graphene Quantum Dots: The Role of Many-Body Effects. *J. Phys. Chem. C* **119**, 4983–4989 (2015). (cited pages 29, 130)

[92] Yang, L., Cohen, M. L. & Louie, S. G. Excitonic effects in the optical spectra of graphene nanoribbons. *Nano Lett.* **7**, 3112–3115 (2007). (cited pages 29, 34, 88)

[93] Prezzi, D., Varsano, D., Ruini, A., Marini, A. & Molinari, E. Optical properties of graphene nanoribbons: The role of many-body effects. *Phys. Rev. B* **77**, 041404 (2008). (cited pages 29, 34, 88, 93, 100)

[94] Osella, S. *et al.* Graphene nanoribbons as low band gap donor materials for organic photovoltaics: Quantum chemical aided design. *ACS Nano* **6**, 5539–5548 (2012). (cited pages 29, 66, 68, 76)

[95] Zhu, X. & Su, H. Scaling of Excitons in Graphene Nanoribbons with Armchair Shaped Edges. *J. Phys. Chem. A* **115**, 11998–12003 (2011). (cited pages 29, 66)

[96] Watson, M. D., Fechtenktter, A. & Müllen, K. Big is beautifularomaticity revisited from the viewpoint of macromolecular and supramolecular benzene chemistry. *Chemical Reviews* **101**, 1267–1300 (2001). (cited page 29)

[97] Müller, S. & Müllen, K. Expanding benzene to giant graphenes: towards molecular devices. *Philos Transact A Math Phys Eng Sci* **365**, 1453 (2007). (cited page 29)

[98] Mueller, M. L., Yan, X., McGuire, J. A. & Li, L.-s. Triplet States and Electronic Relaxation in Photoexcited Graphene Quantum Dots. *Nano Lett.* **10**, 2679–2682 (2010). (cited pages 30, 31)

[99] Sun, C., Figge, F., McGuire, J. A., Li, Q. & Li, L.-s. Biexciton Auger Recombination in Colloidal Graphene Quantum Dots. *Phys. Rev. Lett.* **113**, 107401 (2014). (cited page 30)

[100] Sun, C. *et al.* Biexciton binding of dirac fermions confined in colloidal graphene quantum dots. *Nano Letters* **15**, 5472–5476 (2015). (cited pages 30, 116)

[101] Riesen, H., Wiebeler, C. & Schumacher, S. Optical Spectroscopy of Graphene Quantum Dots: The Case of C132. *J. Phys. Chem. A* **118**, 5189–5195 (2014). (cited pages 30, 31)

[102] McGlynn, S., Azumi, T. & Kinoshita, M. *Molecular spectroscopy of the triplet state*. Prentice-Hall international series in chemistry (Prentice-Hall, 1969). (cited page 30)

[103] Narita, A. *et al.* Bottom-up synthesis of liquid-phase-processable graphene nanoribbons with near-infrared absorption. *ACS Nano* **8**, 11622–11630 (2014). (cited page 32)

[104] Ivanov, I. *et al.* Role of edge engineering in photoconductivity of graphene nanoribbons. *Journal of the American Chemical Society* **139**, 7982–7988 (2017). (cited page 32)

[105] Soavi, G. *et al.* Exciton-exciton annihilation and biexciton stimulated emission in graphene nanoribbons. *Nature Communications* **7**, 11010 (2016). (cited pages 32, 69, 70, 72)

[106] Denk, R. *et al.* Exciton-dominated optical response of ultra-narrow graphene nanoribbons. *Nat. Commun.* **5**, 4253 (2014). (cited pages 33, 90)

[107] Denk, R. *et al.* Probing optical excitations in chevron-like armchair graphene nanoribbons. *Nanoscale* **9**, 18326–18333 (2017). (cited page 33)

[108] Sfeir, M. Y. *et al.* Probing electronic transitions in individual carbon nanotubes by rayleigh scattering. *Science* **306**, 1540–1543 (2004). (cited page 33)

[109] Senkovskiy, B. V. *et al.* Making graphene nanoribbons photoluminescent. *Nano Lett.* (2017). (cited pages 34, 89, 91, 92)

[110] Strano, M. S. *et al.* Reversible, band-gap-selective protonation of single-walled carbon nanotubes in solution. *The Journal of Physical Chemistry B* **107**, 6979–6985 (2003). (cited page 34)

[111] Chong, M. C. *et al.* Bright electroluminescence from single graphene nanoribbon junctions. *Nano Letters* **18**, 175–181 (2018). (cited page 35)

[112] Iijima, S. Helical microtubules of graphitic carbon. *Nature* **354**, 56 (1991). (cited page 36)

[113] O'Connell, M. J. *et al.* Band gap fluorescence from individual single-walled carbon nanotubes. *Science* **297**, 593–596 (2002). (cited pages 36, 62, 73, 74)

[114] Lakowicz, J. *Principles of Fluorescence Spectroscopy* (Springer US, 2007). (cited page 39)

[115] Wang, F., Dukovic, G., Brus, L. E. & Heinz, T. F. Time-resolved fluorescence of carbon nanotubes and its implication for radiative lifetimes. *Phys. Rev. Lett.* **92**, 177401 (2004). (cited page 41)

[116] Lakowicz, J. R., Szmacinski, H., Nowaczyk, K., Berndt, K. W. & Johnson, M. Fluorescence lifetime imaging. *Analytical Biochemistry* **202**, 316 – 330 (1992). (cited pages 41, 106)

[117] Yuan, W. Z. *et al.* Changing the behavior of chromophores from aggregation-caused quenching to aggregation-induced emission: Development of highly efficient light emitters in the solid state. *Adv. Mater.* **22**, 2159–2163 (2010). (cited page 41)

[118] Wilson, T. & Masters, B. R. Confocal microscopy. *Appl. Opt.* **33**, 565–566 (1994). (cited page 44)

[119] Moerner, W. E. & Fromm, D. P. Methods of single-molecule fluorescence spectroscopy and microscopy. *Review of Scientific Instruments* **74**, 3597–3619 (2003). (cited page 44)

[120] Hanbury Brown, R. & Twiss, R. Q. A test of a new type of stellar interferometer on sirius. *Nature* **178**, 1046 (1956). (cited page 50)

[121] Proux, R. *Indistinguishability of the photons emitted by a semiconductor quantum dot under continuous-wave resonant excitation.* Theses, École Normale Suprieure (Paris) (2015). (cited page 51)

[122] Reynaud, Serge. La fluorescence de résonance : Etude par la méthode de l'atome habillé. *Ann. Phys.* **8**, 315–370 (1983). (cited pages 51, 56, 57, 58)

[123] Beveratos, A. *Experimental realisation of a single photon source by fluorescence of individual color centers in diamond. Application to quantum cryptography.* Theses, Université Paris Sud - Paris XI (2002). (cited page 51)

[124] Kurtsiefer, C., Zarda, P., Mayer, S. & Weinfurter, H. The breakdown flash of silicon avalanche photodiodes-back door for eavesdropper attacks? *Journal of Modern Optics* **48**, 2039–2047 (2001). (cited page 52)

[125] Fox, M. *Quantum Optics: An Introduction.* Oxford Master Series in Physics (OUP Oxford, 2006). (cited pages 53, 131)

[126] Fleury, L., Segura, J.-M., Zumofen, G., Hecht, B. & Wild, U. P. Nonclassical photon statistics in single-molecule fluorescence at room temperature. *Phys. Rev. Lett.* **84**, 1148–1151 (2000). (cited pages 56, 130, 135)

[127] Huang, C.-H., Wen, Y.-H. & Liu, Y.-W. Measuring the second order correlation function and the coherence time using random phase modulation. *Opt. Express* **24**, 4278–4288 (2016). (cited pages 56, 57)

[128] Martínez, L. J. *et al.* Efficient single photon emission from a high-purity hexagonal boron nitride crystal. *Phys. Rev. B* **94**, 121405 (2016). (cited pages 57, 123, 125, 126, 135)

[129] Delteil, A., Gao, W.-b., Fallahi, P., Miguel-Sanchez, J. & Imamoğlu, A. Observation of quantum jumps of a single quantum dot spin using submicrosecond single-shot optical readout. *Phys. Rev. Lett.* **112**, 116802 (2014). (cited page 58)

[130] Slablab, A. *Study of the generation of second harmonic optical radiation in nanoscale systems and manufacture of optical probes for near field.* Theses, École normale supérieure de Cachan - ENS Cachan (2010). (cited page 58)

[131] Rondin, L. *Realisation of a NV coulour centre based magnetometer.* Theses, École normale supérieure de Cachan - ENS Cachan (2012). (cited pages 58, 59)

[132] Hughes, J. M. *et al.* High Quality Dispersions of Hexabenzocoronene in Organic Solvents. *Journal of the American Chemical Society* **134**, 12168 (2012). (cited pages 61, 74, 75, 76, 79)

[133] Goel, M., Hongqiang, H., Mujumdar, A. S. & Ray, M. B. Sonochemical decomposition of volatile and non-volatile organic compoundsa comparative study. *Water Research* **38**, 4247 – 4261 (2004). (cited page 61)

[134] Ai, N., Walden-Newman, W., Song, Q., Kalliakos, S. & Strauf, S. Suppression of blinking and enhanced exciton emission from individual carbon nanotubes. *ACS Nano* **5**, 2664–2670 (2011). (cited pages 63, 112)

[135] Schweiger, M., Zakharko, Y., Gannott, F., Grimm, S. B. & Zaumseil, J. Photoluminescence enhancement of aligned arrays of single-walled carbon nanotubes by polymer transfer. *Nanoscale* **7**, 16715–16720 (2015). (cited page 63)

[136] Zheng, H., Wang, Z. F., Luo, T., Shi, Q. W. & Chen, J. Analytical study of electronic structure in armchair graphene nanoribbons. *Phys. Rev. B* **75**, 165414 (2007). (cited page 66)

[137] Magda, G. Z. *et al.* Room-temperature magnetic order on zigzag edges of narrow graphene nanoribbons. *Nature* **514**, 608–611 (2014). (cited page 66)

[138] Chen, Y.-C. *et al.* Molecular bandgap engineering of bottom-up synthesized graphene nanoribbon heterojunctions. *Nat Nano* **10**, 156–160 (2015). (cited page 66)

[139] Han, M. Y., Özyilmaz, B., Zhang, Y. & Kim, P. Energy band-gap engineering of graphene nanoribbons. *Phys. Rev. Lett.* **98**, 206805 (2007). (cited page 66)

[140] Kosynkin, D. V. *et al.* Longitudinal unzipping of carbon nanotubes to form graphene nanoribbons. *Nature* **458**, 872–6 (2009). (cited pages 66, 67)

[141] Koch, M., Ample, F., Joachim, C. & Grill, L. Voltage-dependent conductance of a single graphene nanoribbon. *Nat Nano* **7**, 713–717 (2012). (cited page 66)

[142] Yang, F. *et al.* Chirality-specific growth of single-walled carbon nanotubes on solid alloy catalysts. *Nature* **510**, 522 (2014). (cited page 67)

[143] Yang, L., Park, C.-H., Son, Y.-W., Cohen, M. & Louie, S. Quasiparticle Energies and Band Gaps in Graphene Nanoribbons. *Physical Review Letters* **99**, 186801 (2007). (cited page 67)

[144] Kataura, H. *et al.* Optical properties of single-wall carbon nanotubes. *Synthetic Metals* **103**, 2555 – 2558 (1999). International Conference on Science and Technology of Synthetic Metals. (cited page 68)

[145] Weisman, R. B. & Bachilo, S. M. Dependence of optical transition energies on structure for single-walled carbon nanotubes in aqueous suspension: an empirical kataura plot. *Nano Letters* **3**, 1235–1238 (2003). (cited page 68)

[146] Prezzi, D. & Molinari, E. Optical excitations of quasionedimensional systems: carbon nanotubes versus polymers and semiconductor wires. *phys. stat. sol. (a)* **203**, 3602–3610 (2006). (cited page 69)

[147] Marinopoulos, A. G., Reining, L., Rubio, A. & Vast, N. Optical and loss spectra of carbon nanotubes: Depolarization effects and intertube interactions. *Phys. Rev. Lett.* **91**, 046402 (2003). (cited page 70)

[148] Chang, E., Bussi, G., Ruini, A. & Molinari, E. Excitons in carbon nanotubes: An ab initio symmetry-based approach. *Phys. Rev. Lett.* **92**, 196401 (2004). (cited page 70)

[149] Fu, M. *et al.* Carbon dots: A unique fluorescent cocktail of polycyclic aromatic hydrocarbons. *Nano Letters* **15**, 6030–6035 (2015). (cited pages 71, 108)

[150] Li, L.-L. *et al.* A facile microwave avenue to electrochemiluminescent twocolor graphene quantum dots. *Adv. Funct. Mater.* **22**, 2971–2979 (2012). (cited pages 71, 108)

[151] Ma, Y.-Z., Valkunas, L., Dexheimer, S. L., Bachilo, S. M. & Fleming, G. R. Femtosecond spectroscopy of optical excitations in single-walled carbon nanotubes: Evidence for exciton-exciton annihilation. *Phys. Rev. Lett.* **94**, 157402 (2005). (cited page 72)

[152] Stevens, M. A., Silva, C., Russell, D. M. & Friend, R. H. Exciton dissociation mechanisms in the polymeric semiconductors poly(9,9-dioctylfluorene) and poly(9,9-dioctylfluorene-co-benzothiadiazole). *Phys. Rev. B* **63**, 165213 (2001). (cited page 72)

[153] Sun, D. *et al.* Observation of rapid excitonexciton annihilation in monolayer molybdenum disulfide. *Nano Letters* **14**, 5625–5629 (2014). (cited page 72)

[154] Lauret, J. S. *et al.* Bandgap photoluminescence of semiconducting single-wall carbon nanotubes. *Physica E: Low-dimensional Systems and Nanostructures* **21**, 1057–1060 (2004). (cited page 73)

[155] Berger, S. *et al.* Temperature dependence of exciton recombination in semiconducting single-wall carbon nanotubes. *Nano Letters* **7**, 398–402 (2007). (cited page 73)

[156] Jenekhe, S. A. & Osaheni, J. A. Excimers and exciplexes of conjugated polymers. *Science* **265**, 765–768 (1994). (cited pages 73, 74, 75)

[157] Villegas, C. E. P., Mendonça, P. B. & Rocha, A. R. Optical spectrum of bottom-up graphene nanoribbons: towards efficient atom-thick excitonic solar cells. *Scientific Reports* **4**, 6579 (2014). (cited pages 74, 81)

[158] Kastler, M., Pisula, W., Wasserfallen, D., Pakula, T. & Müllen, K. Influence of alkyl substituents on the solution- and surface-organization of hexa-peri-hexabenzocoronenes. *Journal of the American Chemical Society* **127**, 4286–4296 (2005). (cited page 74)

[159] Fleming, A. J., Coleman, J. N., Fechtenkotter, A., Müllen, K. & Blau, W. J. Intermolecular vibronic coupling in self-assembling molecular nanowires of hexabenzocoronene derivatives. *Organic Photonic Materials and Devices V* **4991**, 460–466 (2003). (cited page 74)

[160] Englert, J. M., Hauke, F., Feng, X., Müllen, K. & Hirsch, A. Exfoliation of hexa-peri-hexabenzocoronene in water. *Chemical communications (Cambridge, England)* **46**, 9194–9196 (2010). (cited pages 74, 76, 79)

[161] Birks, J. B. Excimers. *Rep. Prog. Phys.* **38**, 903 (1975). (cited page 75)

[162] Si, C., Sun, Z. & Liu, F. Strain engineering of graphene: a review. *Nanoscale* **8**, 3207–3217 (2016). (cited page 79)

[163] Roldán, R., Castellanos-Gomez, A., Cappelluti, E. & Guinea, F. Strain engineering in semiconducting two-dimensional crystals. *Journal of Physics: Condensed Matter* **27**, 313201 (2015). (cited page 79)

[164] Branny, A., Kumar, S., Proux, R. & Gerardot, B. D. Deterministic strain-induced arrays of quantum emitters in a two-dimensional semiconductor. *Nature Communications* **8**, 15053 (2017). (cited page 79)

[165] Palacios-Berraquero, C. *et al.* Large-scale quantum-emitter arrays in atomically thin semiconductors. *Nature Communications* **8**, 15093 (2017). (cited page 79)

[166] Koskinen, P. Graphene nanoribbons subject to gentle bends. *Phys. Rev. B* **85**, 205429 (2012). (cited page 80)

[167] Sun, L. *et al.* Strain effect on electronic structures of graphene nanoribbons: A first-principles study. *The Journal of Chemical Physics* **129**, 074704 (2008). (cited page 80)

[168] Lu, Y. & Guo, J. Band gap of strained graphene nanoribbons. *Nano Research* **3**, 189–199 (2010). (cited page 80)

[169] Peng, X. & Velasquez, S. Strain modulated band gap of edge passivated armchair graphene nanoribbons. *Applied Physics Letters* **98**, 023112 (2011). (cited page 80)

[170] Hu, Y. *et al.* Bandgap engineering of graphene nanoribbons by control over structural distortion. *Journal of the American Chemical Society* **140**, 7803–7809 (2018). (cited pages 80, 81)

[171] Di Giovannantonio, M. *et al.* On-surface growth dynamics of graphene nanoribbons: The role of halogen functionalization. *ACS Nano* **12**, 74–81 (2018). (cited pages 84, 91)

[172] Geim, A. K. & Novoselov, K. S. The rise of graphene. *Nature Materials* **6**, 183–191 (2007). (cited page 85)

[173] Blake, P. *et al.* Making graphene visible. *Appl. Phys. Lett.* **91**, 063124 (2007). (cited page 85)

[174] Llinas, J. P. *et al.* Short-channel field-effect transistors with 9-atom and 13-atom wide graphene nanoribbons. *Nat. Commun* **8**, 633 (2017). (cited page 86)

[175] Fairbrother, A. *et al.* High vacuum synthesis and ambient stability of bottom-up graphene nanoribbons. *Nanoscale* **9**, 2785–2792 (2017). (cited page 86)

[176] Thomsen, C. & Reich, S. *Raman Scattering in Carbon Nanotubes*, 115–234 (Springer Berlin Heidelberg, Berlin, Heidelberg, 2007). (cited page 87)

[177] Canado, L. G. *et al.* Quantifying defects in graphene via raman spectroscopy at different excitation energies. *Nano Letters* **11**, 3190–3196 (2011). (cited page 87)

[178] Ezawa, M. Peculiar width dependence of the electronic properties of carbon nanoribbons. *Phys. Rev. B* **73**, 045432 (2006). (cited page 88)

[179] Barone, V., Hod, O. & Scuseria, G. E. Electronic structure and stability of semiconducting graphene nanoribbons. *Nano Letters* **6**, 2748–2754 (2006). (cited page 88)

[180] Zhao, H. & Mazumdar, S. Electron-electron interaction effects on the optical excitations of semiconducting single-walled carbon nanotubes. *Phys. Rev. Lett.* **93**, 157402 (2004). (cited page 88)

[181] Gokus, T. *et al.* Making graphene luminescent by oxygen plasma treatment. *ACS Nano* **3**, 3963–3968 (2009). (cited page 91)

[182] Maultzsch, J., Telg, H., Reich, S. & Thomsen, C. Radial breathing mode of single-walled carbon nanotubes: Optical transition energies and chiral-index assignment. *Phys. Rev. B* **72**, 205438 (2005). (cited page 93)

[183] Rao, A. M. *et al.* Diameter-selective raman scattering from vibrational modes in carbon nanotubes. *Science* **275**, 187–191 (1997). (cited page 93)

[184] Zhou, J. & Dong, J. Vibrational property and raman spectrum of carbon nanoribbon. *Applied Physics Letters* **91**, 173108 (2007). (cited page 94)

[185] Vandescuren, M., Hermet, P., Meunier, V., Henrard, L. & Lambin, P. Theoretical study of the vibrational edge modes in graphene nanoribbons. *Phys. Rev. B* **78**, 195401 (2008). (cited page 94)

[186] Thomsen, C. & Reich, S. Double resonant raman scattering in graphite. *Phys. Rev. Lett.* **85**, 5214–5217 (2000). (cited page 95)

[187] Sasaki, K.-i., Kato, K., Tokura, Y., Suzuki, S. & Sogawa, T. Pseudospin for raman *d* band in armchair graphene nanoribbons. *Phys. Rev. B* **85**, 075437 (2012). (cited page 95)

[188] Beams, R., Canado, L. G. & Novotny, L. Raman characterization of defects and dopants in graphene. *Journal of Physics: Condensed Matter* **27**, 083002 (2015). (cited page 95)

[189] Ferrari, A. C. *et al.* Raman spectrum of graphene and graphene layers. *Phys. Rev. Lett.* **97**, 187401 (2006). (cited page 95)

[190] Gillen, R., Mohr, M., Maultzsch, J. & Thomsen, C. Lattice vibrations in graphene nanoribbons from density functional theory. *physica status solidi (b)* **246**, 2577–2580 (2009). (cited page 96)

[191] Rao, R., Tishler, D., Katoch, J. & Ishigami, M. Multiphonon raman scattering in graphene. *Phys. Rev. B* **84**, 113406 (2011). (cited page 96)

[192] Weinstein, B. A. & Cardona, M. Second-order raman spectrum of germanium. *Phys. Rev. B* **7**, 2545–2551 (1973). (cited pages 96, 98)

[193] Yu, P. & Cardona, M. *Fundamentals of Semiconductors: Physics and Materials Properties*. Graduate Texts in Physics (Springer Berlin Heidelberg, 2010). (cited page 98)

[194] Wang, F. *et al.* Multiphonon raman scattering from individual single-walled carbon nanotubes. *Phys. Rev. Lett.* **98**, 047402 (2007). (cited pages 98, 99, 100)

[195] Kawashima, Y. & Katagiri, G. Fundamentals, overtones, and combinations in the raman spectrum of graphite. *Phys. Rev. B* **52**, 10053–10059 (1995). (cited page 100)

[196] Li, G., Yoon, K.-Y., Zhong, X., Zhu, X. & Dong, G. Efficient bottom-up preparation of graphene nanoribbons by mild suzukimiyaura polymerization of simple triaryl monomers. *Chemistry - A European Journal* **22**, 9116–9120 (2016). (cited pages 100, 101)

[197] Wang, S. & Wang, J. Quasiparticle energies and optical excitations in chevron-type graphene nanoribbon. *The Journal of Physical Chemistry C* **116**, 10193–10197 (2012). (cited page 100)

[198] Debije, M. G. *et al.* The optical and charge transport properties of discotic materials with large aromatic hydrocarbon cores. *J. Am. Chem. Soc.* **126**, 4641–4645 (2004). (cited page 104)

[199] Müllen, K. Evolution of graphene molecules: Structural and functional complexity as driving forces behind nanoscience. *ACS Nano* **8**, 6531–6541 (2014). (cited page 104)

[200] Clar, E. *The Aromatic Sextet*, vol. 13 (Wiley, London, 1972). (cited pages 105, 129)

[201] Kasha, M., Rawls, H. R. & El-bayoumi, M. A. The exciton model in molecular spectroscopy. *Pure Appl. Chem.* 371–592 (1965). (cited page 110)

[202] Delport, G. *Non-convalent functionalization of carbon nanotubes : From the organization of surfactants to the self-assembly ofporphyrins.* Ph.D. thesis, École normale supérieure de Cachan - ENS Cachan (2016). (cited page 111)

[203] Feng, X. *et al.* Towards high charge-carrier mobilities by rational design of the shape and periphery of discotics. *Nature Materials* **8**, 421 (2009). (cited page 111)

[204] Noé, J. C. *et al.* Environmental electrometry with luminescent carbon nanotubes. *Nano Letters* **18**, 4136–4140 (2018). (cited page 112)

[205] Rabouw, F. T. *et al.* Non-blinking single-photon emitters in silica. *Scientific Reports* **6**, 21187 (2016). (cited page 113)

[206] Wang, X. *et al.* Retraction: Non-blinking semiconductor nanocrystals. *Nature* **527**, 544 (2015). (cited page 113)

[207] Neumann, A., Lindlau, J. & Högele, A. Contamination of polymethylmethacrylate by organic quantum emitters. *ArXiv e-prints* (2017). `1706.08341`. (cited page 113)

[208] Rondin, L. *et al.* Surface-induced charge state conversion of nitrogen-vacancy defects in nanodiamonds. *Phys. Rev. B* **82**, 115449 (2010). (cited page 114)

[209] Hauf, M. V. *et al.* Chemical control of the charge state of nitrogen-vacancy centers in diamond. *Phys. Rev. B* **83**, 081304 (2011). (cited page 114)

[210] Grotz, B. *et al.* Charge state manipulation of qubits in diamond. *Nature Communications* **3**, 729 (2012). (cited page 114)

[211] Kulakovskii, V. D. *et al.* Fine structure of biexciton emission in symmetric and asymmetric cdse/znse single quantum dots. *Phys. Rev. Lett.* **82**, 1780–1783 (1999). (cited page 115)

[212] Santos, S. M. *et al.* All-optical trion generation in single-walled carbon nanotubes. *Phys. Rev. Lett.* **107**, 187401 (2011). (cited page 116)

[213] Klevens, H. B. & Platt, J. R. Spectral resemblances of cata-condensed hydrocarbons. *The Journal of Chemical Physics* **17**, 470–481 (1949). (cited page 117)

[214] Sprafke, J. K. *et al.* Belt-shaped -systems: Relating geometry to electronic structure in a six-porphyrin nanoring. *Journal of the American Chemical Society* **133**, 17262–17273 (2011). (cited page 117)

[215] Rieger, R. & Müllen, K. Forever young: Polycyclic aromatic hydrocarbons as model cases for structural and optical studies. *J. Phys. Org. Chem.* **23**, 315–325 (2010). (cited pages 117, 118)

[216] Xu, X., Yao, W., Xiao, D. & Heinz, T. F. Spin and pseudospins in layered transition metal dichalcogenides. *Nature Physics* **10**, 343 (2014). (cited page 120)

[217] Trojnar, A. H., Kadantsev, E. S., Korkusiński, M. & Hawrylak, P. Theory of fine structure of correlated exciton states in self-assembled semiconductor quantum dots in a magnetic field. *Phys. Rev. B* **84**, 245314 (2011). (cited page 120)

[218] Xu, Q. *et al.* Single-Particle Spectroscopic Measurements of Fluorescent Graphene Quantum Dots. *ACS Nano* **7**, 10654–10661 (2013). (cited page 122)

[219] Lounis, B. & Orrit, M. Single-photon sources. *Reports on Progress in Physics* **68**, 1129 (2005). (cited page 123)

[220] He, Y.-M. *et al.* Single quantum emitters in monolayer semiconductors. *Nat. Nanotechnol.* **10**, 497–502 (2015). (cited page 123)

[221] Koperski, M. *et al.* Single photon emitters in exfoliated WSe2 structures. *Nat. Nanotechnol.* **10**, 503–506 (2015). (cited page 123)

[222] Srivastava, A. *et al.* Optically active quantum dots in monolayer WSe2. *Nat. Nanotechnol.* **10**, 491–496 (2015). (cited pages 123, 139)

[223] Chakraborty, C., Kinnischtzke, L., Goodfellow, K. M., Beams, R. & Vamivakas, A. N. Voltage-controlled quantum light from an atomically thin semiconductor. *Nat. Nanotechnol.* **10**, 507–511 (2015). (cited page 123)

[224] Tonndorf, P. *et al.* Single-photon emission from localized excitons in an atomically thin semiconductor. *Optica* **2**, 347–352 (2015). (cited page 123)

[225] Tran, T. T., Bray, K., Ford, M. J., Toth, M. & Aharonovich, I. Quantum emission from hexagonal boron nitride monolayers. *Nat. Nanotechnol.* **11**, 37 (2016). (cited pages 123, 125)

[226] Grosso, G. *et al.* Tunable and high-purity room temperature single-photon emission from atomic defects in hexagonal boron nitride. *Nat. Commun.* **8**, 705 (2017). (cited pages 123, 125)

[227] Lesik, M. *et al.* Perfect preferential orientation of nitrogen-vacancy defects in a synthetic diamond sample. *Applied Physics Letters* **104**, 113107 (2014). (cited page 126)

[228] Jacques, V. *et al.* Enhancing single-molecule photostability by optical feedback from quantum jump detection. *Applied Physics Letters* **93**, 203307 (2008). (cited page 126)

[229] Vogelsang, J. *et al.* A reducing and oxidizing system minimizes photobleaching and blinking of fluorescent dyes. *Angewandte Chemie International Edition* **47**, 5465–5469 (2008). (cited page 126)

[230] Mahler, B. *et al.* Towards non-blinking colloidal quantumdots. *Nature Materials* **7**, 659 (2008). (cited page 127)

[231] Nirmal, M. *et al.* Fluorescence intermittency in single cadmium selenide nanocrystals. *Nature* **383**, 802 (1996). (cited page 128)

[232] Hofkens, J. *et al.* Conformational rearrangements in and twisting of a single molecule. *Chemical Physics Letters* **333**, 255 – 263 (2001). (cited page 128)

[233] Ma, X. *et al.* Influence of exciton dimensionality on spectral diffusion of single-walled carbon nanotubes. *ACS Nano* **8**, 10613–10620 (2014). (cited page 128)

[234] Empedocles, S. A. & Bawendi, M. G. Quantum-Confined Stark Effect in Single CdSe Nanocrystallite Quantum Dots. *Science* **278**, 2114–2117 (1997). (cited page 128)

[235] Schumacher, S. Photophysics of graphene quantum dots: Insights from electronic structure calculations. *Phys. Rev. B* **83**, 081417 (2011). (cited page 130)

[236] Bernard, J., Fleury, L., Talon, H. & Orrit, M. Photon bunching in the fluorescence from single molecules: A probe for intersystem crossing. *J. Chem Phys.* **98**, 850–859 (1993). (cited page 130)

[237] Batalov, A. *et al.* Temporal coherence of photons emitted by single nitrogen-vacancy defect centers in diamond using optical rabi-oscillations. *Phys. Rev. Lett.* **100**, 077401 (2008). (cited page 131)

[238] Proux, R. *et al.* Measuring the photon coalescence time window in the continuous-wave regime for resonantly driven semiconductor quantum dots. *Phys. Rev. Lett.* **114**, 067401 (2015). (cited page 131)

[239] Wu, E. *et al.* Narrow-band single-photon emission in the near infrared for quantum key distribution. *Opt. Express* **14**, 1296–1303 (2006). (cited page 135)

[240] Basch, T., Kummer, S. & Bruchle, C. Direct spectroscopic observation of quantum jumps of a single molecule. *Nature* **373**, 132 (1995). (cited page 137)

[241] Kozankiewicz, B. & Orrit, M. Single-molecule photophysics, from cryogenic to ambient conditions. *Chem. Soc. Rev.* **43**, 1029–1043 (2014). (cited page 137)

[242] Tisler, J. *et al.* Fluorescence and spin properties of defects in single digit nanodiamonds. *ACS Nano* **3**, 1959–1965 (2009). (cited page 137)

[243] de Mello Donegá, C., Bode, M. & Meijerink, A. Size- and temperature-dependence of exciton lifetimes in cdse quantum dots. *Phys. Rev. B* **74**, 085320 (2006). (cited page 137)

[244] Celebrano, M., Kukura, P., Renn, A. & Sandoghdar, V. Single-molecule imaging by optical absorption. *Nature Photonics* **5**, 95 (2011). (cited page 137)

[245] Vialla, F. *et al.* Chirality dependence of the absorption cross section of carbon nanotubes. *Phys. Rev. Lett.* **111**, 137402 (2013). (cited page 138)

[246] Veerman, J. A., Garcia-Parajo, M. F., Kuipers, L. & van Hulst, N. F. Time-varying triplet state lifetimes of single molecules. *Phys. Rev. Lett.* **83**, 2155–2158 (1999). (cited page 138)

[247] Toninelli, C. *et al.* Near-infrared single-photons from aligned molecules in ultrathin crystalline films at room temperature. *Opt. Express* **18**, 6577–6582 (2010). (cited page 139)

[248] Frantsuzov, P., Kuno, M., Jank, B. & Marcus, R. A. Universal emission intermittency in quantum dots, nanorods and nanowires. *Nature Physics* **4**, 519 (2008). (cited page 140)

[249] Gruber, A. *et al.* Scanning confocal optical microscopy and magnetic resonance on single defect centers. *Science* **276**, 2012–2014 (1997). (cited page 148)

[250] Rondin, L. *et al.* Magnetometry with nitrogen-vacancy defects in diamond. *Reports on Progress in Physics* **77**, 056503 (2014). (cited page 148)

Résumé de la thèse

Des nanorubans de graphène (acronyme anglais : GNRs) et des boites quantiques de graphène (acronyme anglais : GQDs), qui présentent d'une bande interdite finie en raison de la réduction de la dimensionnalité du graphène, sont intéressants à la fois pour les études fondamentales et les applications pratiques en optoélectronique. Les calculs théoriques indiquent que leurs propriétés électroniques, optiques et de spin peuvent en principe être contrôlées par leur taille, leur forme et leurs bords. Au cours des deux dernières décennies, la synthèse chimique dite '*bottom-up*' a été développée, ouvrant la voie à un contrôle précis de la structure des GNRs et des GQDs. Cependant, à ce jour, très peu d'études expérimentales ont été rapportées sur leurs propriétés optiques intrinsèques. En particulier, les propriétés de photoluminescence (PL) restent largement sous-explorées. Dans ce contexte, ce manuscrit présente une étude de spectroscopie optique sur les GNRs et GQDs synthétisés par la méthode chimique de '*bottom-up*'.

Dans la première partie, les GNRs synthétisés par deux approches différentes (en solution et catalysée en surface) ont été étudiés. Pour les GNRs synthétisés en solution, les échantillons ont été dispersés avec des surfactants SDS. Les spectres d'absorption et de photoluminescence ainsi que la durée de vie des états excités sont présentés. La possibilité de former des états excimères en raison de l'agrégation des GNRs a été discutée afin d'interpréter l'émission qui a une bande spectrale large et fortement décalée vers le rouge. Par ailleurs, nous avons également montré les résultats de mesures spectroscopiques sur des objets uniques en utilisant simultanément la microscopie confocale et la microscopie à force atomique. L'observation de l'émission de petits agrégats confirme la capacité des GNRs à émettre de la lumière à l'état solide. Ces résultats impliquent que, pour sonder l'émission intrinsèque des GNRs uniques, un problème majeur consiste à individualiser les GNRs en suspension. Pour les GNRs synthétisés sur une surface d'or, l'échantillon a été transféré sur des substrats isolants afin d'effectuer les mesures PL. Les résultats de microRaman ont confirmé que les GNRs ont bien été transférés sur les substrats cibles. On observe la PL à haute énergie sur tout le film de GNR transféré, au lieu d'une émission correspondant à la bande interdite. Nous attribuons cette PL à l'émission des défauts, qui pourraient être créés lors de la synthèse et le transfert. Donc, dans la prochaine étape, la synthèse et le transfert devraient être améliorés. À la fin de cette partie, nous avons également discuté de l'origine des raies Raman distinctes observées sur GNRs : le mode RBLM (acronyme anglais of radical-breathing-like mode) qui est spécifique à la largeur de GNRs, le mode D intrinsèque et les modes D et G de l'ordre élevé qui sont intenses et résolus de manière inattendue. Les résultats présentés dans cette partie montrent les propriétés optiques des GNRs synthétisés par l'approche ascendante et ces propriétés n'ont pas été observées dans les GNRs fabriqués par l'approche descendante en raison de l'absence de contrôle structurel. Bien que l'émission intrinsèque des GNRs uniques n'ait pas encore été observée, nos résultats fournissent une orientation claire pour y parvenir.

Dans la deuxième partie, les propriétés optiques des GQDs synthétisées par en solution ont été étudiées. Les résultats de la spectroscopie de photoluminescence stationnaire et résolue en temps indiquent que les GQDs sont effectivement individualisées dans la dispersion. Une étude de la microphotoluminescence a été réalisée pour explorer directement les propriétés intrinsèques des GQDs uniques. L'émission intrinsèque de GQDs au niveau de l'objet unique est observée. Des mesures de corrélation de photons de second ordre ont révélé que les GQDs présentent une émission de photons uniques à température ambiante avec une grande pureté, une brillance élevée et une bonne photo-stabilité. De plus, une analyse photo-dynamique sur une GQD unique a été réalisée pour comprendre la dynamique des états excités. Ces mesures ont fourni une forte indication de l'existence d'un état de triplet avec un court temps de vie et un faible rapport de branchement qui expliquent que la brillance du GQD est peu affectée. Enfin, par une chloration précise des bords, nous avons observé que la longueur d'onde d'émission des GQDs chlorés uniques était décalée de 100 nm. C'est le premier exemple de l'accordabilité optique des GQDs grâce au contrôle de leur structure. Les résultats présentés dans cette partie démontrent que le potentiel des GQDs révélés par la théorie est maintenant accessible expérimentalement.

université PARIS-SACLAY | ÉCOLE DOCTORALE Ondes et Matière (EDOM)

Titre : Propriétés optiques de nanorubans et de boites quantiques de graphène
Mots clés : photoluminescence, graphène, semiconducteurs

Résumé :
Ce manuscrit présente une étude expérimentale sur les propriétés optiques des nanorubans de graphène (acronyme anglais : GNRs) et des boites quantiques de graphène (acronyme anglais : GQDs) synthétisés par la chimie ascendante.
Pour la partie sur les GNRs, les spectres d'absorption et de photoluminescence ainsi que les mesures de la durée de vie sur la dispersion impliquent la formation d'états excimères résultant de l'agrégation des GNRs. Au moyen de la microscopie confocale et de la microscopie à force atomique, nous observons l'émission de petits agrégats de GNRs confirmant leur capacité à émettre de la lumière à l'état solide. D'autre part, les caractérisations optiques des GNRs synthétisés sur une surface d'or présentent des caractéristiques de Raman remarquables, impliquant les propriétés vibrationnelles spécifiques des GNRs par rapport au graphène et aux nanotubes de carbone. La PL observée est spectralement large avec une énergie plus élevée que celle de la bande interdite des GNRs. Cela pourrait être lié aux défauts créés lors de la préparation de l'échantillon.
Pour la partie sur les GQDs, les résultats de spectroscopie optique indiquent que les GQDs sont individualisées en dispersion plutôt que sous la forme d'agrégats. Ensuite, grâce à la microphotoluminescence, nous abordons directement les propriétés intrinsèques des GQDs uniques. Des mesures de corrélation de photons de second ordre révèlent que les GQDs présentent une émission de photons uniques avec une grande pureté. De plus, l'émission de GQD présente une bonne photo-stabilité avec une brillance élevée. Comme premier exemple de l'accordabilité optique des GQDs via le contrôle de la structure, nous observons que l'émission de GQDs fonctionalisés avec des atomes de chlore est décalée de près de 100 nm tout en maintenant une émission de photons uniques.

Title: Optical properties of graphene nanoribbons and quantum dots
Keywords: photoluminescence, graphene, semiconductors

Abstract:
This manuscript presents an experimental study on the optical properties of graphene nanoribbons (GNRs) and graphene quantum dots (GQDs) synthesized by bottom-up chemistry.
For the part on GNRs, the optical absorption and photoluminescence spectra as well as the life-time measurements on the dispersion of solution-mediated synthesized GNRs implies the formation of excimer states as a result of aggregation of GNRs. By means of confocal fluorescence microscopy and atomic force microscopy, we observe the emission of small GNR aggregates confirming the ability of GNRs to emit light in the solid state. On the other hand, the optical characterizations of on-surface synthesized GNRs shows remarkable Raman features, implying the distinct vibrational properties of GNRs compared to graphene and carbon nanotubes. The observed PL is spectrally broad with higher energy instead of a bright bandgap emission, which might be related to the defects created during the sample preparation.
For the part on GQDs, the optical spectroscopy results indicate that GQDs are individualized in dispersions rather than in the form of aggregates. Then by means of microphotoluminescence, we directly address the intrinsic properties of single GQDs. Second-order photon correlation measurements reveal that GQDs exhibit single-photon emission with a high purity. Notably, the emission of GQDs has good photo-stability with high brightness. As a first example of the optical tunability of GQDs through the control of their structure, we observe that the emission of single edge-chlorinated GQDs is redshifted by almost 100 nm while maintaining the single-photon emission.